2019

Interface Engineering of Nanostructured Metal Catalysts for Improved C02 Electrochemical Reduction

Yong Zhao
University of Wollongong

Australian Research Council Centre of Excellence for Electromaterials Science

Intelligent Polymer Research Institute

Australian Institute for Innovative Materials

Interface Engineering of Nanostructured Metal Catalysts for Improved CO_2 Electrochemical Reduction

Yong Zhao

B. Eng., M. Eng.

This thesis is presented as part of the requirements for the

Award of the Degree of Doctor of Philosophy of

The University of Wollongong

February 2019

Certifications

I, Yong Zhao, declare that this thesis, submitted in fulfilment of the requirements for the award of Doctor of Philosophy, at the Australian Institute for Innovative Materials, University of Wollongong, is wholly my own work except where specific references or acknowledgements are made. The thesis has not been submitted for a degree to any other university or institution.

Yong Zhao

February 2019

Acknowledgements

I would like to express my gratitude to my supervisors, Professor Gordon G. Wallace and Dr. Caiyun Wang for the opportunity of being an ACES member to carry out my doctoral research at IPRI, and for their committed mentorships during my journey into the world of CO_2 electrocatalysis. Gordon and Caiyun, thank you for your drive and commitment to excellence. Your guidance and feedback are crucial for me to carry out solid and impactful research. The personal and professional reflections from our discussions will remain with me as an invaluable part of my research career. I am very grateful for your support and the trust you placed in me to move this challenging project forward with a high degree of freedom. Thank you very much.

I owe a deep debt of gratitude to my collaborators, Miss Jiaojiao Liang and Prof. Jianmin Ma at Hunan University, Prof. Douglas R. Macfarlane at Monash University, Prof. Long Hao and A/Prof. Jing Ning at Qingdao Agricultural University, and Dr. Chong-Yong Lee and Dr. Yuqing Liu at IPRI, for their contributions to experiments, ideas or manuscript revising. This research project also benefited tremendously from the input and expertise of many staff members in AIIM. In particular, I would like to thank Dr. Patracia Hayes for her help with NMR, Raman and FTIR analyses. The Electron Microscopy Centre (EMC) is kindly acknowledged for access to its facilities, and I would like to thank Dr. Gilberto Casillas Garcia for his assistance with STEM imaging, and Dr. Tony Romeo for his help with SEM training. Also, many thanks to Dr. Adam Fahy at the University of Newcastle for his help with XPS tests. Besides the great results obtained, I greatly appreciate the learning opportunities that my interactions with each of them presented.

I would also like to thank my teammates, Chen Zhao, Kewei Su, Xiaoteng Jia, Yu Ge, Yunfeng Chao, Amuruthalakshimi Vijayakumar, Changchun Yu, Yan Han, and Zan Lu, with whom I have had gainful and pleasant working experience in Lab 209. To my friends at IPRI, Christina Puckert, Chunyan Qin, Dandan Cui, Dan Yang, Guanran Zhang, Inseong Cho, Jeacheol Choi, Jianfeng Li, Lei Feng, Liang Wu, Qijie Wu, Qi Gu, Long Zhang, Long Zhao, Tian Zheng, Yang Xiao, Yu Chen, Yan Zong and Zhi Chen, thank you all for providing kind help for my experiments and making my life in Australia wonderful and cheerful. To my friends at ISEM, Haipeng Guo, Jian Hong, Lei Zhang, Li Wang, Weihong Lai and Yajie Liu, thanks to you for your help with reagent sharing and equipment using. To my friends Fengwang Li and Ying Zhang at Monash University, thank you for your

knowledge sharing in electrocatalysis. During the past four years, I have become friends with many great researchers. These friendships have become a vital part of my PhD study, and I will sincerely miss working alongside or discussing with all of them.

Besides, I am very grateful to my old friends who have stood by my side through difficult times. A special mention goes to Shu Tu and Xinfeng Zhang whose company and support, irrespective of distance, have been a source of encouragement and confidence. I am uniquely indebted to them.

Last but not least, I am infinitely grateful to my parents and my sisters. Their love, unwavering support, and constant encouragement have been key ingredients for the successful completion of this dissertation overseas.

Yong Zhao

September 5, 2018

Abstract

Electrochemical reduction of CO_2 (CO_2ER) into value-added chemicals and liquid fuels using renewable energy is a promising route for CO_2 recycling. The realization of inexpensive and efficient metal-based electrocatalysts is crucial for improving its reaction kinetics for high energy efficiency and product selectivity; driving this technique to large-scale industrial application. Apart from the commonly used surface structural and compositional regulation, engineering the interfaces of metal catalysts is an alternative and effective strategy for increasing the activity of reactive sites leading to enhanced electrocatalytic reactivity.

The goal of this thesis work is the utilization of this strategy to develop low-cost and efficient CO_2ER electrocatalysts; exploring the interfacial effects between metal catalysts and supporting materials or adsorbates on this reaction. In this context, three different kinds of hybrid catalysts have been developed by engineering the metal-metal interface, metal-carbon interface and metal-organic ligands interface, respectively. The influence of these interactions on CO_2ER has been revealed accordingly.

First, a one-dimensional Sn nanoparticle modified Cu nanowire catalyst is developed for improved CO_2ER by engineering the nanoscale Cu-Sn interface. This hybrid catalyst is fabricated by facile electrochemical anodization and electroless deposition techniques. It can catalyze the CO_2-to-CO conversion with high selectivity and current density compared with the bare Cu nanowires and Sn nanoparticles. Besides, the catalytic performance can be tuned by regulating the coverage of Sn nanoparticles on the Cu nanowire surface and introducing a third metal component in-between. These findings reveal that the synergistic effect between Cu and Sn at the nanoscale interfaces affords improved kinetics for the CO_2-to-CO conversion.

Second, a Sn modified nitrogen-doped carbon nanofiber catalyst is developed by manipulating the interactions between Sn species (Sn nanoparticles or atoms) and carbon nanofiber supports. This hybrid catalyst is prepared via a straightforward electrospinning technique combined with a pyrolysis method. It has been found that the electronic interaction between Sn species and N-doped carbon nanofibers plays an important role in tuning the catalytic activity and selectivity of the hybrid catalyst. The effect from the electron-rich pyridinic-N-doped carbon nanofiber promotes formate formation at low

overpotentials on the Sn nanoparticles in comparison with that from graphitic-N-doped carbon nanofibers. Moreover, the atomically dispersed Sn species that remained on the nanofiber after removing the Sn nanoparticles switches to selectively reduce CO_2 to CO at low overpotentials. The interaction between Sn and N-doped carbon at the atomic level may lead to the formation of the active Sn-N_x moieties and thus improve the reaction kinetics for the CO_2-to-CO conversion.

Finally, the interfacial strategy is extended from the metal-support interface to the metal-organic ligand interface. An rGO sheet supported ultrasmall Au nanoparticles catalyst is developed via a facile wet chemistry technique and used as the starting material. Five primary amines are used to modify the Au-rGO composite for CO_2ER. An amine-structure-dependent effect is revealed: the linear amines promote the CO_2-to-CO conversion whereas the branched polyamine greatly depresses it; the increasing alkyl chain length boosts the promotion effect of linear amines. The alkyl chain induced amine coverage is the major contributor to the different promotion effects. Among the five modifiers, the linear oleylamine with optimal coverage on ultrasmall Au nanoparticles exhibits the best promotion effect in CO selectivity whilst not deteriorating the catalytic activity.

This thesis work demonstrates that the nanoscale interfacial interactions between metals and supporting materials or organic molecular adsorbates can be modulated to tune the electrocatalytic properties of nanostructured metals for improved CO_2ER. The combination of facile synthesis techniques with excellent performance affords three different types of electrocatalysts, developed in this thesis, that have great potential for practical large-scale application.

Abbreviations

BET	Brunauer-Emmett-Teller
CO_2ER	CO_2 Electrochemical Reduction
CV	Cyclic Voltammetry
DFT	Density Functional Theory
EDS	Energy-Dispersive X-ray Spectroscopy
EIS	Electrochemical Impedance Spectroscopy
FE	Faradaic Efficiency
FID	Flame Ionization Detector
FTIR	Fourier Transform Infrared Spectroscopy
GO	Graphene Oxide
GC	Gas Chromatography
HAADF	High-Angle Annular Dark-Field
HER	Hydrogen Evolution Reaction
HRTEM	High Resolution TEM
LSV	Linear Sweep Voltammetry
NMR	Nuclear Magnetic Resonance
NPs	Nanoparticles
NWs	Nanowires
PTFE	Polytetrafluoroethylene
RGO	Reduced Graphene Oxide
RHE	Reversible Hydrogen Electrode
SHE	Standard Hydrogen Electrode
SEM	Scanning Electron Microscope

STEM	Scanning Transmission Electron Microscope
TEM	Transmission Electron Microscope
TGA	Thermo-gravimetric Analysis
TCD	Thermal Conductivity Detector
XRD	X-ray Diffraction
XPS	X-ray Photoelectron Spectroscopy
A	Ampere
C	Coulomb
cm	Centimeter
F	Faraday
h	Hour
MHz	Megahertz
M	Mole per liter
mA	Milliampere
mV	Millivolt
min	Minute
nm	Nanometer
ppm	Parts per million
psi	Pounds per square inch
S	Siemens
s	Second
V	Volt
Ω	Ohm
µ	Micro

Table of Contents

Chapter 1 Introduction

1.1 Background

1.1.1 Increasing Atmospheric CO_2 Concentration

Since the industrial revolution in the 19th century, fossil fuels including coal, petroleum and natural gas have been the main energy sources to sustain the global economy.[1-3] The excessive depletion of fossil fuels has given rise to a series of problems. Fossil fuels are non-renewable resources and have limited reserves on the earth. They cannot keep up with the huge energy demand arising from the rapidly growing population and industrialization, which may eventually result in an energy crisis.[4] Moreover, the intense consumption of fossil fuels has led to a continuous accumulation of carbon dioxide (CO_2) in the atmosphere. The concentration of atmospheric CO_2 has now surpassed 400 parts per million (ppm) from a pre-industrial level of about 280 ppm (**Figure 1.1**).[5] CO_2 is a notorious greenhouse gas that absorbs infrared radiation and traps the sun's heat. Its over-accumulation in the atmosphere is believed to be a major contributor to the environment and climate changes such as desertification, ocean acidification and global warming.[4] Finding solutions to alleviate the energy and environmental crisis has become a pressing issue for the sustainable development of human society.[6,7]

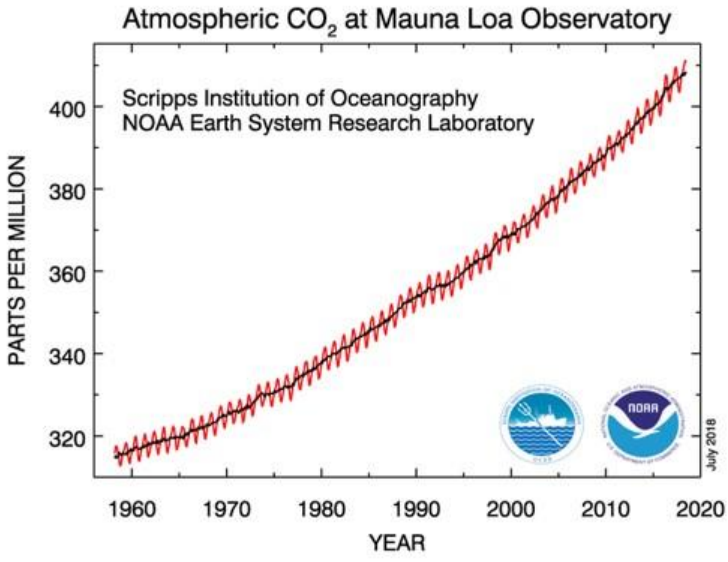

Figure 1.1 Trend of atmospheric CO_2 concentration in recent 60 years observed at the Mauna Loa Observatory. Adapted from reference.[5]

1.1.2 CO_2 Capture and Utilization

During the past several decades, various technologies have been proposed and designed to solve these problems. Capturing CO_2 from the emission sources such as power plants, transporting it to a storage site, and sequestrating it into geological formations is an effective way to prevent the release of large quantities of CO_2 into the atmosphere.[8-10] However, these technologies require large amounts of energy, reducing the overall plant efficiency. It has been estimated that the CO_2 capture and storage technology may use 10%-40% of the energy produced by a power station.[11] Wide-scale adoption may erase efficiency gains in coal power plants and increase resource consumption by one third. It is possible for this technology to induce net negative emission of CO_2 when combined with biomass.[12] Another major concern regards the permanence of CO_2 storage. The safe and permanent storage of CO_2 cannot be guaranteed, and even very low leakage rates could undermine any climate effect and result in fatalities.[11]

An attractive alternative to CO_2 sequestration is to make profits from CO_2, namely, using it as a reagent for producing useful and value-added chemicals through either chemical or electrochemical means. In fact, CO_2 has already been used in the production of chemicals such as urea, salicylic and polycarbonates. However, the demand for these products is too limited and the amount of fixed CO_2 is no more than 100 Mt per year, which is far less than the amount of CO_2 produced from the consumption of fossil fuels (> 25 Gt per year).[13, 14] Therefore, these industrial processes are unlikely to make a significant impact on the CO_2 emissions and its increasing concentration in the atmosphere.[15] CO_2 can also react with hydrogen (H_2) to yield a mixture of water and carbon monoxide (CO) via the reverse water gas shift reaction or to directly produce water and methanol;[16,17] however, this process is highly difficult to drive to completion.

1.1.3 Promising CO_2 Electrochemical Reduction

Electrochemical conversion of CO_2 (CO_2ER) into fuels and feedstocks is an appealing and promising strategy to closing the carbon cycles when powered by renewable energy.[18] In this process, CO_2 can be converted to hydrocarbons and oxygenates using water and renewable electricity. The produced formic acid, carbon monoxide, methane, and ethylene can be used as commodity chemicals in more complex chemical production; and those high-energy-density liquid fuels such as methanol, ethanol and propanol may be integrated into the existing transportation system.[19] This offers the prospect of long-term and large-scale

renewable energy storage. From a capital equipment perspective, the systems for CO_2 electrochemical reduction are analogous to commercialized hydrogen electrolyzers, taking advantage of their already-built infrastructures.

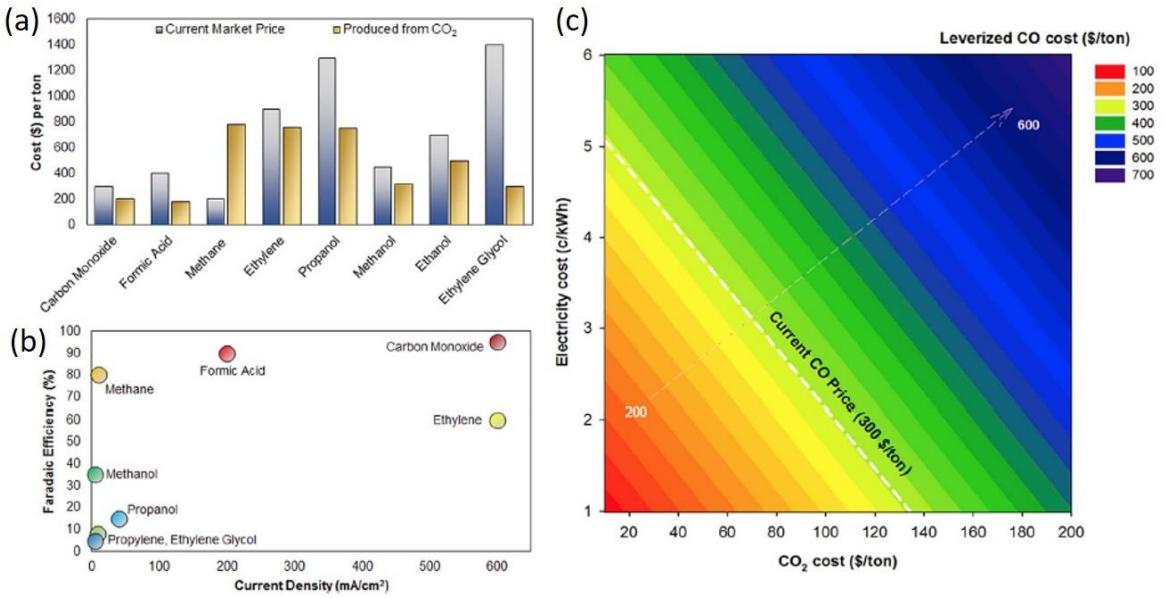

Figure 1.2 Techno-economic analysis of CO_2ER. (a) Comparison of the cost of various chemicals between the current market price and the levelized cost from CO_2 reduction assuming an electrolyser cost of $500/kW, energy conversion efficiency of 60%, Faradaic efficiency of 90%, electricity cost of 2¢/kWh, and CO_2 cost of 30$/ton; (b) Comparison of CO_2-derived molecules based on technical parameters of Faradaic efficiency and current density; (c) Contour plot of economics of CO production based on electricity and CO_2 cost. Adapted from reference.[19] Copyright 2018, Cell Press.

Based on a techno-economic analysis by Sargent et al.[19], the electrochemical transformation of CO_2 to certain target chemicals is highly competitive in comparison with current production technologies (**Figure 1.2**a). The currently achievable combination of key performance parameters (Faradaic efficiency and current density) suggests a focus on C1 and C2 products including formic acid, CO, methane and ethylene (Figure 1.2b). Recent market force analyses point to CO and formic acid as economically viable and atom-economic targets. The cost of CO_2, such as capture and transportation expenses, serves as another crucial input parameter for economical CO_2ER. From the preliminary analysis of the interplay between the costs of electricity and input CO_2 on reduction of CO_2 to CO (Figure 1.2c), it can be concluded that, even at the current level of CO_2ER technology, CO_2 reduction could potentially be made economical with access to low-cost renewable electricity.

Advances in CO_2 reduction to higher value products such as ethylene glycol and propanol holds even greater economic promise.

1.1.4 Research Status of CO_2 Electrochemical Reduction

CO_2 is a notoriously inert and thermodynamically stable molecule.[20] The electrochemical reduction of CO_2 is a kinetically sluggish process. High-performance electrocatalysts are essentially needed to accelerate the activation of CO_2 and promote this reaction to achieve a considerable reaction rate, high energy efficiency, and high product selectivity.

CO_2 contains two polar C=O bonds with two sets of orthogonal π orbitals. The carbon atom with a Lewis acid character can be an electrophilic centre, whereas the oxygens with weak Lewis bases can be nucleophilic centres. Transition metals have vacant orbits and active d electrons, which are believed to be able to energetically facilitate the bonding between the metal and the CO_2 for intermediate formation and also facilitate the desorption of reduction products.[21] This may be the major reason that the most commonly explored electrocatalysts for CO_2ER are transition metal elements and their compounds. Based on the catalysts used, CO_2 electroreduction can be categorized into two different types, homogeneous catalysis[18,22] and heterogeneous catalysis[4,6].

Homogeneous CO_2ER catalysts generally consist of transition metal coordination complexes with appropriate redox states and molecular structures.[23] Under the external bias, the homogeneous CO_2ER usually starts with an initial reduction of metal complexes to an appropriate reduced state, and the reduced metal complexes subsequently react with CO_2 molecules and protons to form product intermediates. Finally, the product molecules detach from the catalytic sites and the reduced state of metal complexes is restored for the next catalysis cycle. This process is clearly demonstrated using the classical Re(bipyridine)$(CO)_3$X catalyst in **Figure 1.3**.[24,25] Due to their unique active centres and molecular structures, homogeneous electrocatalysts can interact with CO_2 molecules efficiently and exhibit excellent catalytic activity and selectivity.[22,26] The pioneering work was done by Fisher and Eisenberg on Ni and Co macrocyclic complexes in 1980.[27] Following it, various transition metals, by coordinating Re, Mn, Fe, Co or Ni with appropriate ligands such as bipyridine, cyclam, tetraazamacrocycle, corrole, phthalocyanine or porphyrin have been used for this purpose.[21,23,28] However, most of these metal complex catalysts have poor solubility, activity and stability in the aqueous environment, and thus have to be used in organic environments. This often makes the homogeneous CO_2ER suffer

from high cost, toxicity and complicated post-separation; which hinder its large-scale industrial application.[4]

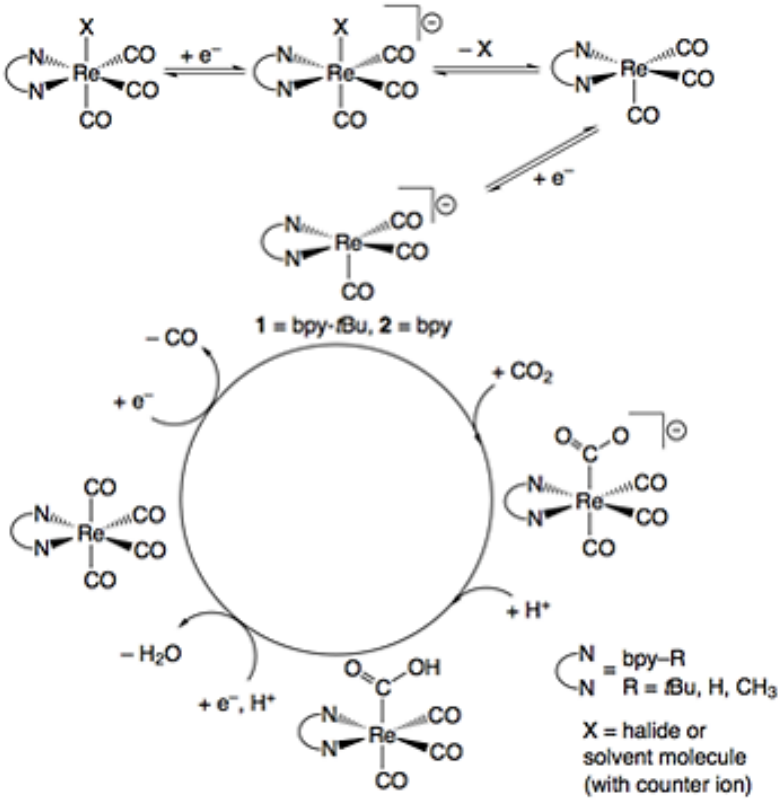

Figure 1.3 A simplified homogeneous CO_2ER process using a classical Re(bpy)$(CO)_3$X (X = halide or solvent molecule) molecular catalyst. Adapted according to references[24,25] with the permission of American Chemical Society and Elsevier.

In contrast, heterogeneous CO_2 electroreduction is more attractive owing to the facile preparation of electrocatalysts, environmental friendliness and outstanding efficiency. Moreover, compared with metal complexes, heterogeneous catalysts can be much more easily incorporated into a gas-diffusion type of electrolyser stacks to reach high current densities as required for massive production or commercialization.[29] A pioneering work was done by Hori and co-workers in the early 1990s, who scrutinized the bulk transition and post-transition metals and revealed their intrinsic activities for CO_2ER in aqueous solution. With the development of nanoscience and nanotechnology, heterogeneous nanostructured catalysts attract much attention. The major heterogeneous electrocatalysts developed in the recent two decades include nanostructured metals, metal-oxide-derived catalysts and other novel catalysts such as single-atom catalysts and heteroatom doped carbon materials. To date, the performance of electrocatalysts are still far from satisfying when considering the

catalyst cost, catalytic activity and selectivity. Searching for robust, low cost and efficient electrocatalysts is still a great challenge.

1.2 Fundamentals of Heterogeneous CO_2ER

1.2.1 Thermodynamics and Kinetics of CO_2ER

A heterogeneous CO_2ER reaction system generally includes a cathode, an anode and electrolyte, as shown in **Figure 1.4**. Reduction of CO_2 occurs at the cathode, while the oxygen evolution reaction takes place at the anode. An ion exchange membrane is often adopted to separate the cathode and anode compartments to prevent further oxidation of the products formed from the CO_2 reduction, only allowing the transfer of corresponding ions.[4]

The CO_2ER is a multi-step proton-assisted reaction which occurs on the surface or near-surface of heterogeneous catalysts.[21] The surface properties of electrocatalysts determine the electron transfer, proton transfer and product formation processes. Depending on the number of electrons and protons transferred, CO_2 can be reduced to tens of different products such as carbon monoxide (CO), formic acid (HCOOH) or formate ($HCOO^-$), methane (CH_4), ethylene (C_2H_4), methanol (CH_3OH) and ethanol (C_2H_5OH). Some thermodynamic electrochemical half-reactions of CO_2 reduction and their associated standard electrode potentials (E^0, versus standard hydrogen electrode, SHE) are listed in **Table 1.1**.[4] It should be noted that the potentials are for aqueous solutions only (pH=7, 25 °C, 1 atm and 1 M concentration of solutes). These half-reaction potentials only reflect each reaction's tendency and possibility; and not the kinetics, such as reaction rate and mechanism.

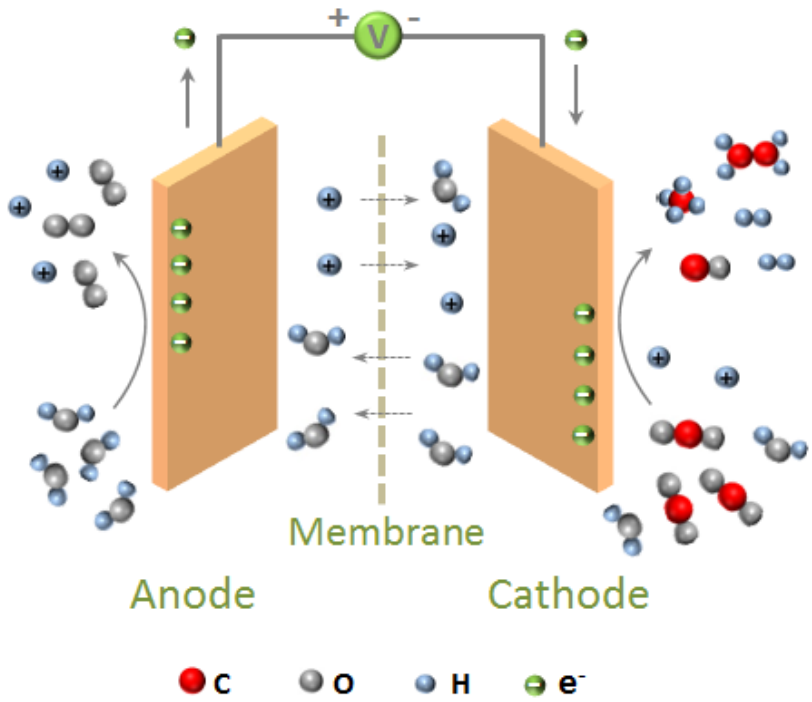

Figure 1.4 Schematic illustration of a typical reaction system of CO_2ER in aqueous solution.

The CO_2ER interfacial reaction involves four major steps: i) CO_2 molecule is chemically adsorbed on a surface active site of the heterogeneous electrocatalyst; ii) one electron is injected into the adsorbed CO_2 molecule to break the C=O bond and form a $CO_2^{\cdot -}$ radical ion; iii) a product molecule is formed on the active site via multiple electron transfer and/or proton transfer coupled with intermediate rearrangement; iv) the product desorbs from the active site and diffuses into the electrolyte.[4] Due to the large reorganizational energy involved from changing a linear molecule to the bent radical anion, the single electron reduction of CO_2 in aqueous solution occurs at a highly negative potential, -1.9 V (vs. SHE).[22] However, the radical anion is highly reactive, and can subsequently form thermodynamically more favourable intermediates through multiple proton-coupled electron-transfer steps.[30] This one-electron transfer to CO_2 to form a key intermediate species $CO_2^{\cdot -}$ is usually considered as the rate-limiting step of a CO_2ER reaction. Due to the high energetic barrier of this step, the actual electrode potentials required to drive the CO_2 reductions are much more negative than the corresponding standard equilibrium ones. To reduce the energetic barriers, an efficient catalyst needs to be applied to bypass the formation of $CO_2^{\cdot -}$ through proton-assisted multiple-electron transfer.

In addition, thermodynamically, a reduction reaction with a more positive E^0 is more favourable according to the Gibbs free energy and potential relationship, $\Delta G = -nFE^0$, where

n is the number of electrons transferred during the redox reaction and F is the Faraday constant. Based on the E^0 values (**Table 1.1**), reductions of CO_2 to form hydrocarbon or alcohol products should be more favourable than CO, HCOOH, HCHO, and H_2 production. However, that is actually not the case, because apart from the thermodynamic barrier, CO_2 reduction also has a kinetic dependence on the catalytic sites and the available protons in solution.[31] It implies that a preferred catalyst affords catalytic sites for fast electron and proton transfer to form preferable intermediates. The hydrogenation of adsorbed C_1 intermediates is kinetically easier than the formation of C-C bonds, limiting the rate and selectivity of C_2 and higher hydrocarbon production. The maximum selectivity for C_2H_4, the simplest C_2 product, was reported to be 70%, whereas that of C_3 product such as C_3H_7OH is no more than 30%.[32]

Table 1.1 Selected thermodynamic electrochemical half-reactions of CO_2ER and their associated standard electrode potentials in aqueous solution (pH = 7, 1 M solute) at 25 °C and 1 atm.[4]

Electrochemical thermodynamic half-reactions	Electrode potentials (V vs. SHE) in aqueous solution (pH = 7)
$CO_2 + e^- = CO_2^{\cdot -}$	-1.90
$CO_2 + 2H^+ + 2e^- = CO + 2H_2O$	-0.52
$CO_2 + 2H^+ + 2e^- = HCOOH$	-0.61
$CO_2 + 8H^+ + 8e^- = CH_4 + 2H_2O$	-0.24
$2CO_2 + 12H^+ + 12e^- = C_2H_4 + 4H_2O$	-0.34
$CO_2 + 6H^+ + 6e^- = CH_3OH + H_2O$	-0.38
$2CO_2 + 12H^+ + 12e^- = C_2H_5OH + 3H_2O$	-0.33
$2H^+ + 2e^- = H_2$	-0.42

1.2.2 Electrocatalytic Figures of Merit

To benchmark the electrocatalytic ability of catalysts for CO_2ER, several key figures of merit are typically reported including Faradaic efficiency, current density, overpotential and Tafel slope.

Faradaic efficiency (FE). It is also called current efficiency, which refers to the percentage of electrons consumed for the formation of a given product during a specific period of time. It can be calculated according to the equation $FE_A = n_A z_A F/Q_{total}$, where n_A is the molar amount of product A, z_A is the number of electrons transferred to form one A molecule, F refers to Faraday's constant (96485 C mol^{-1}) and Q is the total charge consumed. The FEs of different products are directly related with the selectivity of electrocatalysts, and hence they are the most important parameters to evaluate the performance of CO_2ER.

Current density (j). The overall current density (j_{total}) in areal or gravimetric unit can be calculated by dividing the current by the surface area of the working electrode or mass of the catalysts. It is directly related to the reaction rate. Due to the competence of HER and poor selectivity in aqueous electrolyte, it is necessary to get the partial current densities of all CO_2ER products by the equation $j_A = FE_A \times j_{total}$. The active-site dependent current density can be calculated based on the electrochemical active surface area (ECSA), revealing the real reactivity of electrocatalysts. The ECSAs are usually evaluated by different electrochemical methods such as the electrochemical double-layer capacitance (EDLC) method and underpotential deposition (UPD) method. The EDLC can be measured by performing a cyclic voltammetry scan in a narrow potential range without surface redox reactions. The UPD method utilizes the surface charge delivered by an underpotential deposition of a metal on the electrode. Both methods can be applied for the ECSA analysis of pure catalysts without conductive additives, while only the UPD method can be used for hybrid catalysts with non-reactive additives.

Overpotential (η). The overpotential for a catalyst is the absolute value of the difference between the potential required for product formation (E) and the equilibrium potential (E^0), $\eta = |E\text{-}E^0|$. The overpotential and faradaic efficiency together determines the overall energy utilization toward the product. The energy efficiency (ε) of a CO_2ER reaction can be calculated by the equation, $\varepsilon = FE \times E^0/(E^0 + \eta)$. It can be concluded that a high ε arises from a low overpotential as well as a high FE.

Tafel slope. Tafel plot is a function of overpotentials and logarithm of partial current density of one product. The slope of a Tafel plot is a useful parameter to evaluate the reaction kinetics for the product formation. Generally, a Tafel slope of ~120 mV dec^{-1} indicates that the rate-determining step (RDS) is a one-electron transfer to CO_2 to form $CO_2^{\bullet-}$ intermediate.[33] Whereas, a slope of ~59 mV dec^{-1} indicates that the one-electron transfer step followed by a

subsequent proton (H^+) transfer to the formed $CO_2^{\bullet-}$ is the RDS.[34] A smaller Tafel slope indicates a faster kinetic of CO_2 reduction.

1.2.3 Challenges

The last decade has witnessed the rapid development of heterogeneous CO_2ER catalysts, but up to now none of the reported electrocatalysts have met the requirements for practical and technological commercialization (current density ~ 200 mA cm^{-2}, lifetime ~100 hours)[35, 36]. Big challenges still remain, which are summarized as follows.

Low energy efficiency. The CO_2ER process involves protons, and there should be proton sources in the electrolyte. However, the hydrogen evolution reaction (HER) has a similar equilibrium potential as for CO_2ER but requires a much lower overpotential to occur on most electrode surfaces.[37] In the aqueous electrolyte, the CO_2ER has to compete with the intense HER and needs much higher overpotentials to obtain appreciable amounts of products. This leads to a low energy efficiency of CO_2ER. Taking the HCOOH formation as an example, the maximum energy efficiency for this conversion over the promising Sn-based electrocatalysts is still less than 60%.[38]

Low selectivity and high post-separation cost. Due to the similarity of the equilibrium potentials of the above half-reactions, the product of CO_2ER often comprises a mixture of several species. This selectivity issue incurs high cost for the products' separation.

Low current density. Due to the low solubility of CO_2 in aqueous electrolyte solutions (~30 mM in H_2O at atmospheric pressure), the diffusion-limited current densities typically do not exceed 30 mA cm^{-2}, which is one order of magnitude lower than the technical requirements for practical application.[35]

Short lifetime. CO_2ER is very sensitive to the surface composition and structure of electrocatalysts. Any surface contamination can lead to a variation of electrocatalytic behaviour. The active sites are easily blocked or poisoned by the reaction intermediates or the impurities from the electrolytes, resulting in severe deactivation of catalysts during the electrolysis process.[39] Up to now, the lifetime reported is far less than the 100 h that is required for industrial application.

Overall, a promising catalyst should be able to minimize the energy barrier of CO_2 activation and facilitate the kinetic process for targeted product formation. It should feature

a low overpotential, a high current density, and long-term stability, while simultaneously suppress the HER effectively to yield targeted products with high selectivity.[15,21]

1.3 Catalysts for Heterogeneous CO_2ER

Over the past several decades, much efforts in heterogeneous CO_2ER studies have been devoted to exploring efficient electrocatalysts. To date, there are mainly five types of heterogeneous electrocatalysts that have been investigated with appreciable performances. They include metals, metal oxides, transition-metal dichalcogenides, metal-free carbon materials, atomically dispersed metal catalysts. In this section, some representative catalysts are summarized and tabulated to give a general view of catalyst development. The influential factors of electrocatalytic properties will be discussed systematically in the next section.

1.3.1 Metals

1.3.1.1 Bulk Metals

The early studies of CO_2ER catalysts were focused on bulk transition and post-transition metals. The formation of CO_2 reduction products significantly depends on the properties of metals. For example, high purity polycrystalline Cu produced CH_4 and C_2H_4 with a FE of 33.3% and 25.5%, at -1.44 V (vs. SHE).[40] Zn metal showed high selectivity for CO with a FE of 79.4% at -1.54 V, while Sn metal showed excellent selectivity for HCOOH with a FE of 88.4% at -1.48 V.[30] According to Hori and his co-workers, these metal electrodes may be divided into four groups in accordance with the product selectivity (in aqueous electrolyte) as indicated in **Table 1.2**.[40] Group 1 includes Pb, Hg, In, Sn, Cd and Tl, giving HCOOH or $HCOO^-$ as the major product. Au, Ag, Zn, Pd and Ga belong to Group 2, forming CO as the major product. Cu is the only metal of Group 3 with the ability of producing hydrocarbons (e.g., CH_4, C_2H_4, C_2H_6) and alcohols in appreciable amounts. For Group 4 metals that include Ni, Fe, Pt, and Ti, the HER occurs dominantly.

Table 1.2 FEs of different products from CO_2ER using bulk metal electrodes in 0.1 M $KHCO_3$ at 18.5 °C (± 0.5). Adapted according to reference[40].

Group	Metal	Potential	j_{total}	FE / %							
		V vs. RHE	mA cm^{-2}	CH_4	C_2H_4	EtOH	PrOH	CO	$HCOO^-$	H_2	Total
1	Pb	-1.23	5.0	-	-	-	-	-	97.4	5.0	102.4
	Hg	-1.11	0.5	-	-	-	-	-	99.5	-	99.5
	Tl	-1.20	5.0	-	-	-	-	-	95.1	6.2	101.3
	In	-1.15	5.0	-	-	-	-	2.1	94.9	3.3	100.3
	Sn	-1.08	5.0	-	-	-	-	7.1	88.4	4.6	100.1
	Cd	-1.23	5.0	1.3	-	-	-	13.9	78.4	9.4	103.0
	Bi	-1.16	1.2	-	-	-	-	-	77	-	-
2	Au	-0.74	5.0	-	-	-	-	87.1	0.7	10.2	98.0
	Ag	-0.97	5.0	-	-	-	-	81.5	0.8	12.4	94.6
	Zn	-1.14	5.0	-	-	-	-	79.4	6.1	9.9	95.4
	Pd	-0.80	5.0	2.9	-	-	-	28.3	2.8	26.2	60.2
	Ga	-0.84	5.0	-	-	-	-	-	-	79.0	102.0
3	Cu	-1.04	5.0	33.3	25.5	5.7	3.0	1.3	9.4	20.5	103.5
4	Ni	-1.08	5.0	1.8	0.1	-	-	-	1.4	88.9	92.4
	Fe	-0.51	5.0	-	-	-	-	-	0.0	94.8	94.8
	Pt	-0.67	5.0	-	-	-	-	-	0.1	95.7	95.8
	Ti	-1.20	5.0	-	-	-	-	-	tr.	99.7	99.7

The difference in product selectivity among these metals can be explained according to their tendency to bind various reaction intermediates and products (**Figure 1.5**).[30] As mentioned above, the first step in CO_2ER is the one-electron transfer to CO_2 forming intermediate $CO_2^{\bullet-}$. For the metals like Sn and In (Group 1), the $CO_2^{\bullet-}$ radical anions cannot be strongly adsorbed on the surface active sites, and therefore only formic acid or formate ($HCOO^-$) is formed through an outer-sphere mechanism at the electrode-electrolyte interface.[41] The metals in the other three groups can stabilize the $CO_2^{\bullet-}$ intermediates on their surface and subsequently convert them to other intermediates such as *COOH and *CO. For Group 2 metals, the obtained *CO is weakly adsorbed and easily released without further

reduction, leading to the predominant CO formation. However, the *CO is bound too strongly on the surface of Group 4 metals (e.g., Pt, Ni, Fe, etc.) to be desorbed, poisoning the catalyst and inhibiting the further reduction of CO_2. In contrast, Cu has an optimal binding energy for the *COOH and *CO intermediates. These intermediates can be stabilized without poisoning the Cu surface, and are further converted to *COH or *CHO intermediates and finally to hydrocarbons or alcohols.

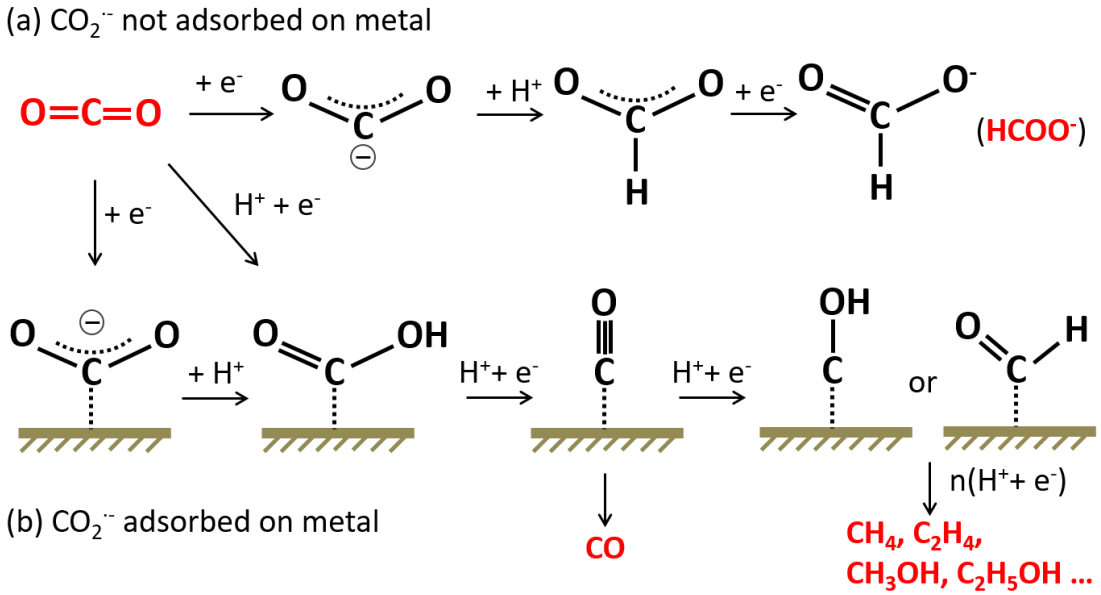

Figure 1.5 Schematic simplified reaction mechanism of CO_2ER on metal catalysts in aqueous solution. Redrawn according to reference[30]. Species in black are intermediates, while those in red are reactants or products.

In fact, the actual surface chemistry of transition metals during CO_2ER is more complicated than the aforementioned theories.[4] Recently, Kuhl et al.[42] performed CO_2 reduction on seven transition metal foils using a home-designed electrolyser with high product sensitivity. Both methane and methanol were formed on Ag, Zn, Cu, Ni, and Pt metals. Only methane was generated on Fe, and methanol was produced on Au. In addition to the dependence on the CO binding strength, they also suggested that the different oxophilicities between Au and Fe contributed to those results. Fe could break the second C-O bond of CO_2 leading to the formation of methane due to its strong binding affinity for O. In contrast, less-oxophilic Au preferred to keep the second C-O bond intact, and methanol is the only product. Therefore, tuning the binding strength of adsorbed O species can produce the designated hydrocarbon or alcohol product.

Although bulk metals exhibit interesting performances for CO_2ER, they are easily poisoned by impurities due to their low specific surface area.[41,43] Their electrocatalytic selectivity, activity and stability are far below the requirements for practical applications. Moreover, early works on bulk metal catalysts mainly reported the selectivity. Limited information was available about the reaction rate and stability, together with limited catalyst fabrication methods and characterization techniques.[30] Therefore, it is highly desirable to evaluate the comprehensive performances of these electrocatalysts; aiming at large scale applications.

1.3.1.2 Nanostructured Metals

With the rapid development of nanoscience and nanotechnology, recent CO_2ER studies have extensively focused on nanostructured metals. Compared with their bulk counterparts, nanostructured metals have several unique properties.[37] First, they have more surface active sites than bulk metals due to the enhanced surface areas. This improves not only the current density but the tolerance to the impurities or contaminations in the electrolyte. In addition, nanostructured metals usually contain a large portion of grain boundaries, edges and low-coordinated sites that afford different catalytic behaviours compared with the flat surfaces and fully-coordinated sites in bulk materials. It has been experimentally revealed that the structural parameters of nanostructured metal catalysts such as morphology, crystal-facets, roughness and particle size have dramatic influence on the activity and product selectivity of CO_2ER.[44,45] **Table 1.3** summarizes the performance of some representative nanostructured single-element metal catalysts for CO_2ER, which clearly demonstrates the influences from the structural parameters of morphology, size and chemical state (please see detailed discussion in Section 1.4).

Table 1.3 The CO_2ER performance of some representative nanostructured single-element metal catalysts.

Metal	Morphology	Electrolyte	Major Product	FE / %	η / V	$j_{partial}$
Sn	Nano-SnO_2 particles (5 nm)[46]	0.1 M $NaHCO_3$	$HCOO^-$	86	1.13	4.6 mA cm^{-2}
	Sn quantum-sheets/graphene[47]	0.1 M $NaHCO_3$	$HCOO^-$	85	1.13	18.0 mA cm^{-2}
	Sn particles/SnO_x layers (3.5 nm)[48]	0.1 M $KHCO_3$	$HCOO^-$	64	1.2 $_{cell}$	1.9 mA cm^{-2}
	Electrodeposited thin film[49]	0.1 M [BMIM]OTf	CO	77	1.28	5.0 mA cm^{-2}
	Mesoporous SnO_2 nanosheets[50]	0.5 M $NaHCO_3$	$HCOO^-$	87	0.88	50 mA cm^{-2}
	Reduced porous SnO_2 NWs[38]	0.1 M $KHCO_3$	$HCOO^-$	78	0.60	4.8 mA cm^{-2}
	Carbon nanotubes/Sn microspheres[51]	0.5 M $KHCO_3$	$HCOO^-$	82.7	0.76	26.7 mA cm^{-2}
	SnO_2 wire-in-tube[52]	0.1 M $KHCO_3$	$HCOO^-$	63	0.8	4.4 mA cm^{-2}
	N-carbon supported Sn NPs[53]	0.5 M $KHCO_3$	$HCOO^-$	63	0.69	11 mA cm^{-2}
Bi	Bi NPs (36 nm)[54]	0.1 M [BMIM]OTf	CO	96	0.25	15.6 A g^{-1}
	Nanoporous thin film[55]	0.1 M [BMIM]OTf	CO	73	0.22	31.0 mA cm^{-2}
	Electrodeposited thin film[49]	0.1 M [BMIM]OTf	CO	78	0.20	8.4 mA cm^{-2}
	Bi nanosheets[56]	0.5 M $NaHCO_3$	$HCOO^-$	80	0.92	24 mA cm^{-2}
	Ultrathin Bi nanosheets[57]	0.5 M $NaHCO_3$	$HCOO^-$	>90	0.89	~12 mA cm^{-2}
	Bi NPs [58]	0.5 M $KHCO_3$	$HCOO^-$	98.4	0.73	9.7 mA cm^{-2}
In	In nanocrystals[59]	0.3 M $BMIMPF_6$	CO	99	0.13	15.0 mA cm^{-2}
	Reduced In_2O_3 nanocatalyst[60]	0.5 M K_2SO_4	$HCOO^-$	85	1.05	NA
	Dendritic In foam[61]	0.5 M $KHCO_3$	$HCOO^-$	86	0.75	5.8 mA cm^{-2}
	Nanocubic $In(OH)_3$/Carbon[62]	0.5 M K_2SO_4	$HCOO^-$	77	0.875	3.8 mA cm^{-2}
	Anodized In foil[63]	0.5 M K_2SO_4	$HCOO^-$	80	1.0	NA
Co	Partially oxidized Co atomic layer[64]	0.1 M Na_2SO_4	$HCOO^-$	90	0.24	10.0 mA cm^{-2}
	Ultrathin Co_3O_4 layer (1.72 nm)[65]	0.1 M $KHCO_3$	$HCOO^-$	63	0.27	0.67 mA cm^{-2}

	Co_3O_4 nanocubes on N-doped graphene[66]	0.1 M $KHCO_3$	$HCOO^-$	83	0.235	10.5 mA cm^{-2}
Au	Ultrathin Au NWs (3 nm)[67]	0.5 M $KHCO_3$	CO	94	0.24	1.96 A g^{-1}
	Au NPs (8 nm) [68]	0.5 M $KHCO_3$	CO	90	0.56	5.6 A g^{-1}
	Oxide-derived rough Au[34]	0.5 M $KHCO_3$	CO	98	0.29	6.0 mA cm^{-2}
	Grain-boundary-rich Au NPs[69]	0.5 M $NaHCO_3$	CO	94	0.39	14 A g^{-1}
	Sphere-like Au_{25} clusters (1 nm)[70]	0.1 M $KHCO_3$	CO	73.7	0.46	NA
	Au NPs on graphene nanoribbons[71]	0.5 M $KHCO_3$	CO	92	0.55	~35 A g^{-1}
	Nano-needles[72]	0.5 M $KHCO_3$	CO	95	0.24	15 mA cm^{-2}
	Ultrasmall Au NPs on RGO sheets	0.1 M $KHCO_3$	CO	75	0.59	257 A g^{-1}
Ag	Ag NPs (5 nm)[73]	0.5 M $KHCO_3$	CO	84	0.63	~3 A g^{-1}
	Cl^- induced Ag nano-corals[74]	0.1 M $KHCO_3$	CO	95	0.37	2.0 mA cm^{-2}
	Nano-porous Ag[75]	0.5 M $KHCO_3$	CO	90	0.39	9.0 mA cm^{-2}
	Ultrathin Ag NWs (35 nm)[76]	0.5 M $KHCO_3$	CO	80	0.79	~5.5 mA cm^{-2}
	Ag_2CO_3-derived Ag corals[77]	0.1 M $KHCO_3$	CO	92	0.29	~1.0 mA cm^{-2}
	Triangular Ag nanoplates[78]	0.1 M $KHCO_3$	CO	96.8	0.746	1.2 mA cm^{-2}
Pd	Pd NPs (3.7 nm)[79]	0.1 M $KHCO_3$	CO	91.2	0.78	23.9 A g^{-1}
	Pd NPs[80]	2.8 M $KHCO_3$	CO	99	0.10	7 A g^{-1}
	Nano-needles[72]	0.5 M $KHCO_3$	$HCOO^-$	91	0.20	10 mA cm^{-2}
	Pd icosahedra NPs[81]	0.1 M $KHCO_3$	CO	91.1	0.69	2 mA cm^{-2}
	Pd octahedral NPs[81]	0.1 M $KHCO_3$	CO	52	0.69	1 mA cm^{-2}
	Pd NPs with high-index facets[82]	0.5 M $KHCO_3$	$HCOO^-$	97	0.09	22 mA cm^{-2}
Zn	Zn dendrites[83]	0.5 M $NaHCO_3$	CO	79	0.9	13.5 mA cm^{-2}
	Reduced nanoporous ZnO[84]	0.25 M K_2SO_4	CO	92	1.1	15.1 mA cm^{-2}
	Nanoscale Zn (~40 nm)[85]	0.5 M NaCl	CO	93	0.98	15 mA cm^{-2}
	Hexagonal Zn nanoplates[86]	0.5 M KCl	CO	95	0.94	5.6 mA cm^{-2}

Cu	Cu NPs (7 nm)[29]	0.1 M $NaHCO_3$	CH_4	76	1.5	10 mA cm^{-2}
	CuO derived NWs[87]	0.1 M $KHCO_3$	CO	50	0.49	0.3 mA cm^{-2}
	Nano-flowers[88]	0.1 M $KHCO_3$	CH_4, C_2H_4	5, 14	-1.2 V vs RHE	NA
	Nano-foam[89]	0.5 M $NaHCO_3$	C_2	56	-0.8 V vs RHE	NA
	Oxide-derived rough Cu[33]	0.1 M $KHCO_3$	CO	45	0.2	NA
	Nanocubes (44 nm)[90]	0.1 M $KHCO_3$	C_2H_4	41	-1.1 V vs RHE	NA
	Cu NWs (8.1μm)[91]	0.1 M $KHCO_3$	C_2H_4	20	-1.1 V vs RHE	NA
	Plasma-activated Cu nanocubes[92]	0.1 M $KHCO_3$	C_2H_4, C_2H_5OH	45, 22	-1.0 V vs RHE	35 mA cm^{-2} total current
	Cu nano-dendrites[93]	0.1 M KBr	C_2H_4	57	NA	170 mA cm^{-2}
	Onion-like carbon/Cu NPs[94]	0.1 M $KHCO_3$	C_2H_4	60	-1.2 V vs RHE	NA
	Cu nanoporous ribbons[95]	0.1 M $KHCO_3$	C_2H_4, C_2H_6, C_2H_5OH	40	-0.81V vs RHE	~11 mA cm^{-2} total current
	Cu nanocrystals[96]	0.1 M $KHCO_3$	n-C_3H_7OH	10.6	-0.95V vs RHE	1.74 mA cm^{-2}
	5-fold twinned Cu NWs[97]	0.1 M $KHCO_3$	CH_4	55	-1.25V vs RHE	~ 3.7 mA cm^{-2}
	Cu nanocubes[98]	0.1 M $KHCO_3$	C_2H_4, C_2H_5OH, C_3H_7OH	60	-0.96V vs RHE	40 mA cm^{-2}
	3D porous hollow fibre Cu[99]	0.3 M $KHCO_3$	CO	72	0.29	10 mA cm^{-2}

Note: NPs is the abbreviation for nanoparticles, NWs for nanowires, and CB for carbon black. If the FE, η and j values were not specifically stated, they were derived from graphical results or calculated with the available information in the references.

1.3.1.3 Metal Alloys

The reaction activity and product selectivity of CO_2ER are highly dependent on the binding strength of key intermediates such as *COOH, *CO and *H (for the competing HER) on the surface of metals. Changing the composition of a metallic catalyst by alloying with other metal(s) may enhance the performance over that of solo metal by tuning their binding ability towards key intermediates.[100]

Cu is the only metal that can bind the key *CO intermediate properly and promote its further reduction to form high-value hydrocarbons and oxygenates such as ethylene, methanol and ethanol.[30] It also brings in a challenge of poor product selectivity. Alloying Cu with other metals has been proven to be an effective approach to tune the binding strength of *CO and *COOH intermediates on Cu surfaces for enhanced reaction kinetics. For instance, Watanabe et al.[101] found that the selectivity of Cu-based alloys could be easily tuned by the second metal component: Cu-Ni alloys produced CH_3OH and HCOOH, whereas Cu-Sn, Cu-Pb, and Cu-Cd alloys produced HCOOH and CO. Xu et al.[102] found that incorporating Au into Cu NPs could positively shift the onset potential of CO_2 reduction. Jia et al.[103] reported a nanoporous Cu-Au alloy catalyst which exhibited enhanced methanol and ethanol production with a total FE of 28%. In order to better understand the effects of alloying, Yang et al.[104] investigated the CO_2ER performance of a series of bimetallic Au-Cu NPs with different Cu/Au ratios. They found that the incorporation of Au promoted CO evolution and suppressed the formation of $HCOO^-$, CH_4, C_2H_4, and H_2. The Au_3Cu NPs showed the optimal activity for the formation of CO. Recently, Takanabe et al.[105] developed a Cu-In alloy nanolayer (~3 nm) by electrochemically reducing an oxide-derived Cu electrode in an In-containing solution, which efficiently converted CO_2 to CO with a high FE of 90% at -0.5 V vs. RHE.

The computational research on Cu-alloy catalyzed CO_2ER has also been reported.[106-108] The electrocatalytic activity of Cu-based alloys did not follow the volcano-type relationship for pure metals. Different Cu-alloy surfaces favour the formation of different intermediates, that is, the activity and selectivity of CO_2ER can be tuned by alloying Cu with different transition metals (**Figure 1.6**a).[108] Additionally, theoretical work of non-copper alloys has shown that six among 34 stable binary alloys may be capable of reducing CO into methanol with an activity order of $PtIn_2(111) > PtHg_2(201) > PtPb_4(001) > PdBi_2(111) > IrSn_2(111)$ (Figure 1.6b).[109]

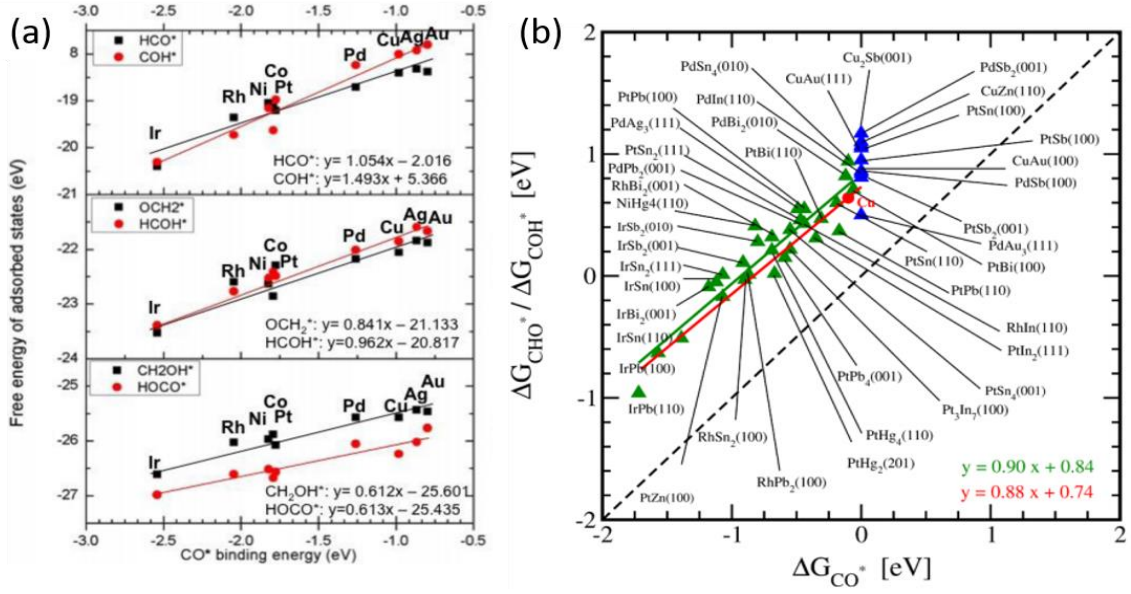

Figure 1.6 (a) Linear scaling correlations of the free energy of different intermediates on Cu_3X surfaces as a function of CO* binding energy; Only the X element is shown. (b) Free binding energies of *CHO or *COH plotted against the corresponding energies for *CO adsorption. Adapted from references[108,109] with permission of the American Chemical Society.

Experimentally, non-copper alloys were also widely investigated. For example, Koper et al.[110] combined a metal that binds CO strongly (Pd) with a metal with weakly binding of CO (Au) to tune the binding energy of *CO. The Pd-Au alloy with an optimal composition realized the production of a mixture of C_1-C_5 hydrocarbons and soluble oxygenates starting from an onset potential of -0.8 V vs. RHE. Lewis et al.[111] reported that the Ni-Ga alloy films with different compositions (NiGa, Ni_3Ga, and Ni_5Ga_3) were able to reduce CO_2 into a range of products, including methane, ethane and ethylene at low overpotentials. Jaramillo et al.[112] synthesized a thin film of Au-Pd alloy that was more active and selective for $HCOO^-$ production than either pure Au or Pd. Sun et al.[113] reported a Pd-Sn alloy catalyst whose catalytic activity and selectivity were highly dependent on the surface electronic structure of the alloy. With an optimal surface Pd, Sn and O distribution, the Pd-Sn alloy could preferably produce formic acid with nearly 100% FE at a low overpotential of 0.26 V. **Table 1.4** lists some recently reported alloy catalysts for CO_2ER, giving some insights into the development of this kind of catalysts.

Table 1.4 Some representative metal alloy catalysts and their optimal CO_2ER performances.

Alloys	Morphology	Electrolyte	Product	FE / %	E vs. RHE	$j_{partial}$
$Cu_{64}Au_{36}$	Nanoporous film[103]	0.5 M $NaHCO_3$	C_2H_5OH, CH_3OH	12 15.9	-0.41	NA
$CuAu_3$	NPs[104]	0.1 M $NaHCO_3$	CO	65	-0.73	230 A g^{-1}
Cu_3Pd_7	Mesoporous film[114]	0.1 M $KHCO_3$	CO	80	-0.8	0.5 mA cm^{-2}
$Cu_{11}In_9$	Nanolayer[105]	0.1 M $KHCO_3$	CO	95	-0.6	0.6 mA cm^{-2}
Cu-Sn	Rough, grain-like film[115]	0.1 M $KHCO_3$	CO	90	-0.6	1.0 mA cm^{-2}
Cu_2Cd	Alloy on Cu foil[116]	0.1 M $KHCO_3$	CO	84	-1.0	8.0 mA cm^{-2}
Cu_3Pt	Nanocrystal[117]	0.5 M $KHCO_3$	CH_4	21	-0.93	NA
Cu-Ag	Alloy nanowire film[118]	1 M KOH	C_2H_4, C_2H_5OH	60 25	-0.7	300 mA cm^{-2} total current
Cu-Pd	Phase-separated particles[119]	1 M KOH	C_2H_4, C_2H_5OH	47 15	-0.74	360 mA cm^{-2} total current
Cu_4Zn	Spherical particles film[120]	0.1 M $KHCO_3$	C_2H_5OH	29.1	-1.05	8.2 mA cm^{-2}
Cu-Ag	Ultrasmall bimetal NPs[121]	0.5 M $KHCO_3$	CH_3COOH	21.2	-1.33	NA
Cu_2O-Ag	Surface alloyed NPs[122]	0.1 M $KHCO_3$	C_2H_5OH	34.2	-1.2	0.6 mA cm^{-2}
$Cu_{0.2}Zn_{0.4}Sn_{0.4}$	Thin films[123]	0.5 M $KHCO_3$	CO	86	-0.4	3 mA cm^{-2}
$Cu_{0.2}Sn_{0.8}$	Thin film[123]	0.5 M $KHCO_3$	$HCOO^-$	85	-0.35	3 mA cm^{-2}
Au-Fe	8 nm core-shell NPs[124]	0.5 M $KHCO_3$	CO	97.6	-0.4	11.1 mA cm^{-2}
$Ag_{76}Sn_{24}$	20 nm core-shell NPs[125]	0.5 M $NaHCO_3$	CO	80	-0.8	16.0 mA cm^{-2}
$Au_{55}Pd_{45}$	Thin film[112]	0.1 M $KHCO_3$	$HCOO^-$	10	-1.0	0.33 mA cm^{-2}
$In_{90}Sn_{10}$	Nano & micro-particles[126]	0.1 M $KHCO_3$	$HCOO^-$	92	-1.2	13.8 mA cm^{-2}
Mo-Bi	300 nm sheet-like structure[127]	0.5 M [EMIM]BF_4/ MeCN	CH_3OH	71.2	-0.7 vs. SHE	12.1 mA cm^{-2}
Pd-Sn	1-5 nm alloy NPs[113]	0.5 M $KHCO_3$	$HCOO^-$	99	-0.43	1.8 mA cm^{-2}

1.3.2 Metal Oxides

Although a variety of metal electrodes have been investigated for CO_2 electrolysis, only a few metal oxides such as TiO_2, FeO_x, and Cu_2O have been reported for CO_2ER.[128-131] This is mainly attributed to the fact that most metal oxides such as Cu_xO, SnO_x and ZnO can be readily reduced to metals under moderately negative potentials in neutral or near-neutral aqueous solutions. Recently, Ma et al.[132] reported a TiO_2 supported Ag NPs catalyst for CO_2 reduction which exhibited excellent catalytic selectivity (FE_{CO} > 90%) and activity (j_{CO} > 100 mA cm^{-2}) in aqueous solution. They also proposed that the formed Ti^{4+}/Ti^{3+} redox couple stabilized the key reaction intermediate $CO_2^{\bullet-}$, making the Ag-TiO_2 composite to outperform the Ag-carbon counterpart.

Most of the reported metal oxides exhibited reasonable electrocatalytic properties only in the presence of organic salts or ionic liquids. For example, Chu et al.[133] reported that a nanostructured TiO_2 film was able to convert CO_2 to low-density polyethylene (LDPE) with a moderate FE of 14% in 1-ethyl-3-methylimidazolium tetrafluoroborate ([EMIM]BF_4) aqueous solution. The authors proposed that Ti^{4+} was reduced to Ti^{3+} species first, then it reacted with CO_2 to form $CO_2^{\bullet-}$ intermediates. The local high pressure induced by the unique nanoporous structure of TiO_2 film helped to polymerize the $*CH_2$ intermediates to LDPE. Kamat et al.[134] obtained methanol as the major product (FE, ~ 90%) when using a nanostructured TiO_2 film as catalyst in 0.1 M tetraethylammonium perchlorate (TEAP)/acetonitrile (0.33 M H_2O). They also identified that Ti^{3+} species formed at negative potentials were the active sites for CO_2 reduction.

MoO_2 was identified as an electrocatalyst for CO_2 reduction in organic solutions as well.[135] Its catalytic activity and product selectivity were highly dependent on the temperature and water content of the electrolyte. In a solution with an optimal content of water, formate and oxalate were shown to be the major products at room temperature, whereas CO and oxalate were generated with greatly enhanced current densities at -20 °C. Sekimoto et al.[136] found that doped gallium oxide (Ga_2O_3) with Sn and Si could efficiently convert CO_2 to formic acid with high FEs exceeding 80% in an aqueous solution of KCl and NaOH. Those dopants mainly contributed to the improved conductivity, while Ga_2O_3 itself possessed the intrinsic ability of catalysing the CO_2ER.

1.3.3 Transition-Metal Dichalcogenides

Compared with metal and metal oxide catalysts, to date there are only a few reports about the use of transition-metal dichalcogenides (TMCDs) for CO_2 reduction. It was firstly reported by Yamaguchi and coworkers in 2014.[137] They synthesized iron sulphide and Ni-containing iron sulfides via a hydrothermal method and evaluated their energetics for CO_2ER in a slightly acidic solution. Pure FeS could not efficiently reduce CO_2, whereas the amine-modified and Ni-substituted compound $FeNi_2S_4$ showed much better efficiency and selectivity for CO and CH_4 formation. In the same year, Nørskov et al.[138] demonstrated the feasibility of using MoS_2, $MoSe_2$ and Ni-doped MoS_2 for CO_2 reduction by use of density functional theory (DFT) calculations. They demonstrated that the edge sites of these materials could selectively bind *COOH and *CHO to bridging S or Se atoms and bind *CO to Mo atoms. All edges are active for the conversion of CO_2 to CO, while the Ni-doped S edge of MoS_2 and Mo edge of $MoSe_2$ could reduce CO further to produce hydrocarbons and/or alcohols.

Later in the year 2014, Asadi et al.[139] experimentally reported that layer-stacked bulk MoS_2 with Mo-terminated edges exhibited an excellent CO_2ER performance in terms of electrocatalytic activity and product selectivity (65 mA cm^{-2}, FE_{CO} ~ 98% at -0.764 V vs. RHE) in ionic liquid [EMIM]BF_4-H_2O electrolyte (**Figure 1.7**a-d).Their DFT calculations revealed that the superior catalytic performance could be attributed to the high d-electron density on the Mo-terminated edges of MoS_2 and metal-like low work function. To prove it, they synthesized vertically aligned MoS_2 nanosheets with more Mo atoms on the edges as active sites (Figure 1.7e). As expected, a further improvement in CO_2ER reaction rate (130 mA cm^{-2} at -0.764 V vs. RHE) was observed (Figure 1.4f). They also pointed out the important role of ionic liquid EMIM-BF_4, which could transport CO_2 to the catalyst surface by complexation under acidic conditions with increased local CO_2 concentration, and reduce the reaction barrier for electrons passing into CO_2 as well.

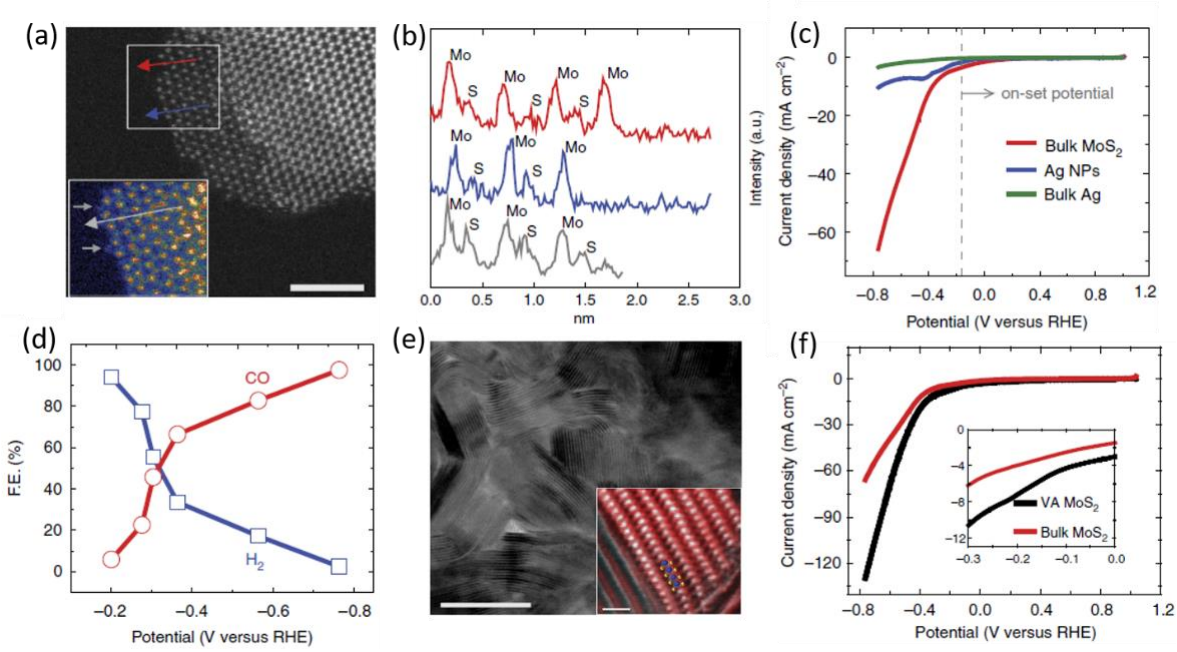

Figure 1.7 (a) Raw grayscale high-angle and low-angle annular dark-field image (inset) of MoS_2 edges (scale bar, 5 nm); (b) The line scans identifying Mo atoms to be the terminating atoms; (c) LSV curves for bulk MoS_2, Ag NPs, and bulk Ag performed in CO_2-saturated EMIM-BF_4 (4 mol%) aqueous solution; (d) FE_{CO} and FE_{H2} at different applied potentials; (e) Bright-field STEM images of vertically aligned MoS_2, inset is high-resolution HAADF-STEM image, scale bar are 20 nm and 2 nm respectively; f) LSV curves of the bulk MoS_2 and vertically aligned MoS_2 nanosheets. Adapted with permission.[139] Copyright 2014, Nature Publishing Group.

The same group further synthesized a series of nanostructured TMDCs including MoS_2, WS_2, $MoSe_2$, and WSe_2 nanoflakes, and studied their electrocatalytic properties for CO_2ER in the same ionic liquid solution.[140] Among them, WSe_2 with the lowest work function exhibited the best catalytic performance for the formation of CO. The superior electronic properties of W edge atoms led to faster electron transfer and thus higher catalytic activity. Their DFT calculations revealed that the formation of *COOH and *CO intermediates on TMDCs was exergonic because of their strong binding to TMDC metal edge sites, and the d-band centres of metal edges were much closer to the Fermi level than those of Ag(111) surface, further supporting this strong binding interaction.

Li et al.[141] also reported an effective TMDC catalyst, polyethylenimine (PEI) modified and graphene oxide supported amorphous molybdenum sulphide (MoS_x). This composite was capable of producing CO at a low overpotential of 140 mV, and it could achieve a

maximum FE_{CO} of 85.1% at an overpotential of 540 mV. The PEI was revealed to suppress the competing HER and stabilize the intermediates in the CO_2ER process, providing a synergistic effect with MoS_x for the CO_2-to-CO conversion. It should be noted that this efficient electrolysis was realized in an aqueous electrolyte without use of expensive ionic liquids. It implies that the surface modification may be an effective strategy to tune the electrocatalytic properties of TMDCs and realize its application for aqueous CO_2ER.

1.3.4 Metal-Free Carbon Materials

1.3.4.1 Carbon Catalysts for CO Formation

Recently metal-free carbon-based catalysts have become more and more attractive due to their distinct properties in comparison with conventional metallic catalysts. First of all, carbon atoms can be assembled into a variety of nanoscale carbon materials with different dimensions and structures such as quantum dots, fullerene, carbon nanotubes (CNTs) and graphene.[142] These carbon materials usually possess many intrinsic advantages including high surface area, high conductivity, excellent chemical stability and remarkable mechanical strength, which may be beneficial for the CO_2 electroreduction. Furthermore, their structure and surface chemical state can be easily modulated by introducing heteroatoms such as B, N, P and S in the synthesis process or post-treatment to tune their electrocatalytic properties to improve the CO_2ER performance. In addition, they are inexpensive, environment-friendly and available at large quantities, and thus have great potential for practical applications.

In 2013, Kumar et al.[143] firstly reported the remarkable catalytic ability of polyacrylonitrile-derived N-doped carbon nanofibers (CNFs) to catalyze CO_2 reduction into CO at a low overpotential (0.17 V) in [EMIM]BF_4-H_2O electrolyte. This catalyst exhibited a high current density that was ~13 times and ~4 times larger than those of bulk Ag film and 5-nm Ag NPs under similar experimental conditions (**Figure 1.8**a-d). The catalytic ability of CNFs was attributed to the positively charged carbon atoms adjacent to pyridinic N rather than the pyridinic N atoms themselves based on the unchanged XPS peak of pyridinic N after experiments. They proposed a reaction mechanism as shown in Figure 1.8e. Initially, the naturally oxidized carbon atoms were reduced by a redox cycling process. Then the [EMIM-CO_2] complex intermediates would adsorb on the reduced carbon atoms and re-oxidize them to their initial state, and finally the produced CO was released. The cyclic reduction and oxidation process maintained the catalytic activity of these carbon atoms.

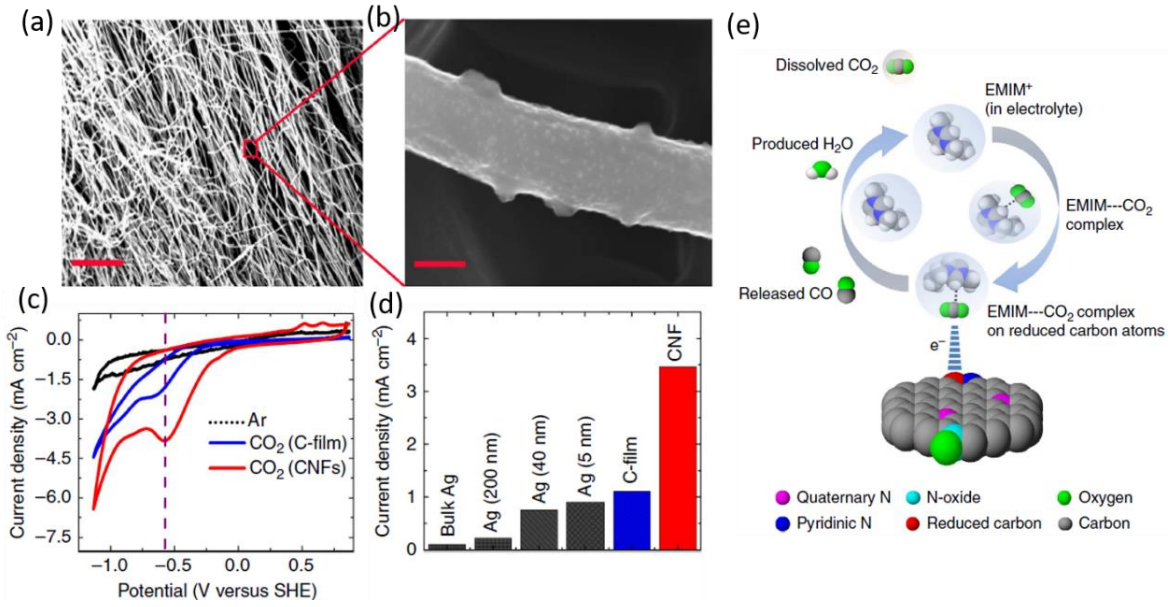

Figure 1.8 (a-b) SEM images of the N-doped CNFs; (c) CVs for CO_2ER in Ar- and CO_2-saturated pure EMIM-BF_4 at a carbon film electrode and CNFs electrode, respectively, at a scan rate of 10mV s^{-1}; (d) Absolute current density for CO_2ER at different (bulk Ag, Ag nanoparticles and CNF) electrodes in pure EMIM-BF_4 electrolyte; (d) Schematic illustration of the CO_2 reduction mechanism. Adapted with permission.[143] Copyright 2013, Nature Publishing Group.

In 2014, Meyer et al.[144] demonstrated that a polyethylenimine (PEI) modified N-doped carbon nanotubes catalyst could selectively convert CO_2 to formate in aqueous solution. A maximum FE of 87% was reached with a high current density of 9.5 mA cm^{-2}. It was revealed that the PEI could significantly reduce the overpotential and increase the current density and efficiency, which were attributed to the improved stabilization of $CO2^{\bullet-}$ intermediates via the H-bond interaction between these radical anions on the N-sites of carbon nanotubes and the amine functionality on PEI.

In 2015, Ajayan et al.[145] reported on nitrogen-doped carbon nanotubes (NCNTs) synthesized by liquid chemical vapour deposition for CO_2 electroreduction. The NCNTs have bamboo-shaped morphology in a multi-walled nature with uniform N distribution and high N content up to 5 at% (**Figure 1.9**a-c). The N configurations were identified as pyridinic, pyrrolic, and graphitic N (Figure 1.9d). This catalyst exhibited unprecedented onset overpotential (0.18 V) and selectivity (80%) for the CO_2-to-CO conversion in 0.1 M $KHCO_3$. By tuning the precursor and growth temperature, they synthesized a series of NCNTs with different defect densities and N contents exhibiting different catalytic properties (Figure

1.9e).[146] They found that the onset potential for CO formation were positively correlated with the contents of pyridinic and graphitic N (Figure 1.9f), and proposed that these two N moieties were active sites for CO_2ER since it was difficult to experimentally distinguish the catalytic activity of pyridinic or graphitic N site. Their DFT calculations (Figure 1.9g) showed that pyridinic defects retained a lone pair of electrons that were capable of binding CO_2, whereas the geometry of pyrrolic-N defects moved the N atom towards the centre of the CNT making these electrons harder to access for CO_2 binding. Although graphitic N exhibited a 1 eV higher barrier than pyridinic N for *COOH formation, it still lowered the overpotential by 1V in comparison with pristine CNTs.

They also developed a N-doped three-dimensional graphene foam with increased active sites and easy access of electrolyte.[147] The catalyst required a low onset overpotential (0.19 V) for CO formation, and exhibited superior activity over Au and Ag, achieving similar maximum FE_{CO} (~85%) to NCNTs but at a lower overpotential (0.47 V). They also discovered that the metal-free N-doped graphene quantum dots were able to reduce CO_2 to high-value oxygenates and hydrocarbons such as ethanol and ethylene at low overpotentials with high faradaic efficiencies and high current densities in a flow cell system using alkaline electrolyte.[148] A high total FE of over 90% was achieved for CO_2ER, with a selectivity of 45% for the conversion of ethylene and ethanol at -0.75V vs. RHE. Although active sites were recognized as pyridinic-N atoms, the formation mechanism of high-carbon products remained elusive.

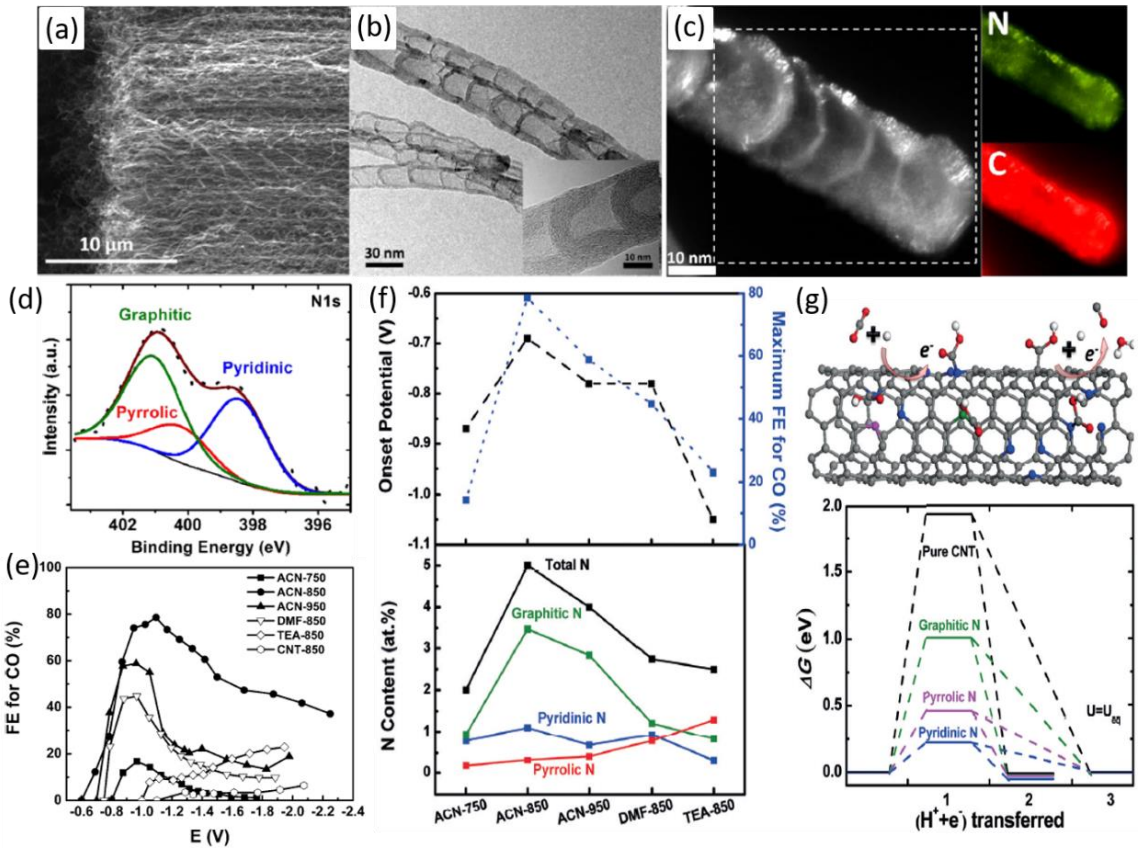

Figure 1.9 (a) SEM, (b) TEM and (c) Electron energy loss spectroscopy elemental mapping of N and C of NCNTs; (d) Representative XPS of N 1s for NCNTs. (f) The onset potential and maximum FE_{CO} as a function of N content in NCNTs. (g) Schematic illustration of CO formation on NCNTs and free-energy diagram at equilibrium potential for CO_2 reduction on different N defects in comparison with pristine CNTs. Reproduced from references[145,146] with permission from the American Chemical Society and Wiley-VCH.

1.3.4.2 Carbon Catalysts for Oxygenates Formation

Apart from the traditional carbon forms, Quan et al.[149] developed a Si nanorod supported N-doped nanodiamond catalyst (NDD/Si RA) that preferentially and rapidly converted CO_2 to acetate over formate with an onset potential of -0.36 V vs. RHE, overcoming the usual limitation of low selectivity for C_2 products (**Figure 1.10**a-c). A high FE of 71% was achieved for acetate formation in the potential range of -0.8 to -1.0 V. A pathway towards acetate formation, $CO_2 \rightarrow CO_2^{\bullet-} \rightarrow (COO)_2^{\bullet} \rightarrow CH_3COO^-$, was proposed based on their electrokinetic and in-situ infrared spectra analyses. The high performance of this catalyst was attributed to its high overpotential for H_2 evolution, high N doping, and large fraction of N-sp^3 C species which was highly active for CO_2ER.

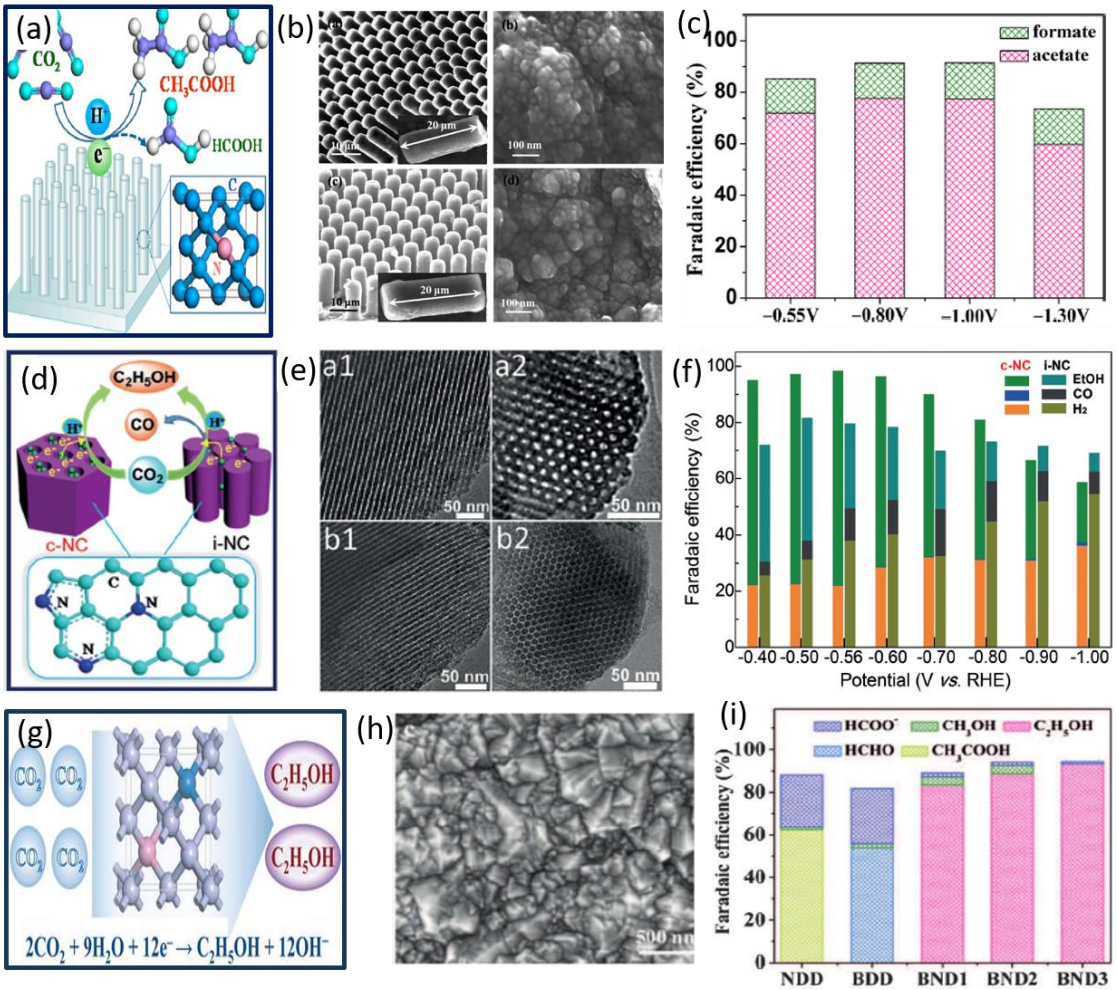

Figure 1.10 (a) Illustrations of CO_2ER over N-doped nanodiamond/Si nanorod arrays (NDD/Si RA); (b) SEM images of NDD/Si RA prepared at 450 ^oC and 500 ^oC; (c) FEs for acetate and formate production on NDD/Si RA electrode at different potentials in CO_2-saturated 0.5 M $NaHCO_3$ solution. (d) Illustration of inverse (i-NC) and cylindrical (c-NC) mesoporous N-doped carbon for CO_2ER; (e) TEM images of c-NC (a1, a2) and i-NC (b1, b2); (f) FEs of CO_2ER products over c-NC and i-NC catalysts at various applied potentials. (g) Illustrations of CO_2ER over B,N-doped diamond (BND); (h) SEM images of BND; (c) FEs of formate, methanol and ethanol for different diamonds samples at -1.0 V vs. RHE. Reproduced from references[149-151] with permission from the American Chemical Society and Wiley-VCH.

Very recently, Sun et al.[150] developed an N-doped ordered cylindrical mesoporous carbon as a robust metal-free catalyst for CO_2 electroreduction, enabling the efficient production of ethanol with nearly 100% selectivity and a high FE of 77% at -0.56 V vs. RHE in aqueous solution (Figure 1.10d-f). Their DFT calculations demonstrated that the

cylindrical channel surface of N-doped carbon with high electron density could stabilize the *CO intermediates that were preferentially formed on the pyridinic N sites and facilitate the C-C coupling and subsequent proton-electron transfer reactions, resulting in superior electrocatalytic performance for ethanol formation.

In addition to N-doped carbons, boron doped carbons were also effective for CO_2ER. Nakata et al.[152] reported that boron-doped diamond (BDD) was capable of reducing CO_2 to HCHO with a high FE of 74%. They attributed this high performance to the presence of sp^3-bonded carbon on the BDD which were effective in converting the as-formed HCOOH to HCHO and suppressing the competing H_2 evolution. Sreekanth et al.[153] reported that B-doped graphene was able to reduce CO_2 to formate in aqueous electrolyte, in which boron-doping could introduce asymmetric spin density and make it suitable for CO_2 adsorption and formate formation.

Most recently, Quan et al.[151] investigated the impact of co-doping with B and N on CO_2 reduction using diamond as the starting material (Figure 1.10g-i). The B,N-co-doped diamond (BND) catalyst could reduce CO_2 to ethanol with a high FE of 93.2% at -1.0 V vs. RHE. By comparing the N-doped diamond (NDD), B-doped diamond (BDD) and BND with different N ratios, they found that the superior performance for ethanol production on BND mainly originated from the synergistic effect of B and N co-doping, high N content and high overpotential for H_2 evolution. A possible pathway for ethanol formation was revealed by DFT calculation, $CO_2 \rightarrow$ *COOH $\rightarrow$ *CO $\rightarrow$ *COCO $\rightarrow$ *$COCH_2OH$ $\rightarrow$ *CH_2OCH_2OH $\rightarrow$ CH_3CH_2OH, where the coupling of *CO intermediates on BND easily occurred.

Table 1.5 summarizes some representative metal-free carbon catalysts for CO_2ER. Together with the above discussion, it can be clearly seen that the electrocatalytic properties of heteroatom-doped carbon materials are highly dependent on the carbon structures as well as the introduced heteroatoms. Manipulating the carbon/heteroatom-containing precursors and synthetic methods may produce the designated metal-free carbons for targeted products. However, big challenges remain. An obvious shortcoming of these metal-free carbon catalysts is their low reactivity, i.e., low catalytic current density. Introducing transition metal sites into the heteroatom-doped carbons has been verified as an effective way to further improve the CO_2ER performances, which will be discussed in the next section.

Table 1.5 Some representative metal-free carbon catalysts and their optimal CO_2ER performances.

Metal-free carbons	Proposed active sites	Electrolyte	Product	FE / %	Potential vs. RHE	j_{total}
N-CNT[154]	Graphitic N	0.5 M $NaHCO_3$	CO	90	-0.9	~ 5.5 mA cm^{-2}
Porous N-C[155]	Pyridinic-N	0.5 M $NaHCO_3$	CO	83.7	-0.82	~ 8 mA cm^{-2}
N-graphene-like carbon[156]	N sites	BMIM-BF_4	CH_4	91.8	-1.4 vs. SHE	~ 1.4 mA cm^{-2}
N-CNFs[143]	C adjacent to pyridinic-N	[EMIM]BF_4	CO	98	-0.573	3.5 mA cm^{-2}
PEI-modified N-CNT[144]	Pyrrolic- and pyridinic-N	0.1 M $KHCO_3$	$HCOO^-$	87	-1.16	9.5 mA cm^{-2}
HNCM-CNT[157]	C next to pyridinic-N	0.1 M $NaHCO_3$	$HCOO^-$	81	-0.9	~ 3.8 mA cm^{-2}
N-MWCNT[145]	Pyridinic-N	0.1 M $KHCO_3$	CO	80	-0.39	0.75 mA cm^{-2}
N-graphene foam[147]	Pyridinic-N	0.1 M $KHCO_3$	CO	85	-0.58	1.9 mA cm^{-2}
N-GQDs[148]	Edge sites, pyridinic-N	1 M KOH	C_2H_5OH, C_2H_4	14, 31	-0.75	~ 40 mA cm^{-2}
N-diamond[149]	N-sp^3 C	0.5 M $NaHCO_3$	CH_3COO^-	71	-0.8	~ 6.2 mA cm^{-2}
B-diamond[152]	sp^3 C	1 M CH_3OH	HCHO	74	-1.7 vs. Ag/Ag^+	NA
B-graphene[153]	Positive charged C	0.1 M $KHCO_3$	$HCOO^-$	66	-1.4	NA
B,N-diamond[151]	B,N synergy	0.1 M $KHCO_3$	C_2H_5OH	93.2%	-1.0	NA

1.3.5 Atomically Dispersed Metal Catalysts

Atomically dispersed metal (ADM) catalysts have well-defined metal active sites that are atomically stabilized on or embedded in supporting materials and have exhibited excellent catalytic activity for CO_2ER. The contained metal sites play an essential role in the adsorption and activation of CO_2 molecules in the CO_2ER process. The ADM catalysts are commonly prepared by incorporating transition metal atoms into N-doped carbon materials to form M-N_x sites, or by immobilizing effective molecular complex or metal sites on electrically conductive supports to form immobilized catalysts. They can maximize the exposure of reactive metal sites to the reactants (CO_2 and proton sources) to facilitate the mass transport and electron transfer at the interface. Moreover, their local structure such as metal-ligand interplay, bond length and coordination number can be easily modulated to tune the binding strength of intermediates and thus their catalytic performance.

1.3.5.1 Metal-Nitrogen Doped Carbons

This kind of ADM catalysts usually contain the unit of single-atom transition metal coordinated with nitrogen (M-N_x) which is similar to metal-porphyrin catalysts. Homogeneous catalysts based on metal porphyrins are known to be active catalysts for reducing CO_2 to CO, and so are heterogeneous catalysts containing the M-N_x centre. Solid metal-nitrogen doped carbon materials (M-N-C) have been demonstrated to be promising low-cost catalysts for CO_2ER, because they can efficiently produce CO at low overpotentials (**Table 1.6**). In the following context, some representative work will be discussed to provide insights into the M-N-C catalyst.

In 2015, Strasser et al.[158] reported the first exploration of transition metal doped carbon-based catalysts for CO_2 electroreduction. They functionalized the commercial carbon blacks with N and Fe and/or Mn ions using pyrolysis and acid leaching. The formed solid powder catalysts were found to be very active and highly selective for CO_2 to CO conversion, outperforming a low-area polycrystalline Au benchmark. They revealed that CO production occurred on the M-N_x moieties, unspecific with respect to the nature of metal dopants. The interaction between CO and metal centres were sufficiently strong, and even could enable the protonation of CO and the formation of CH_4.

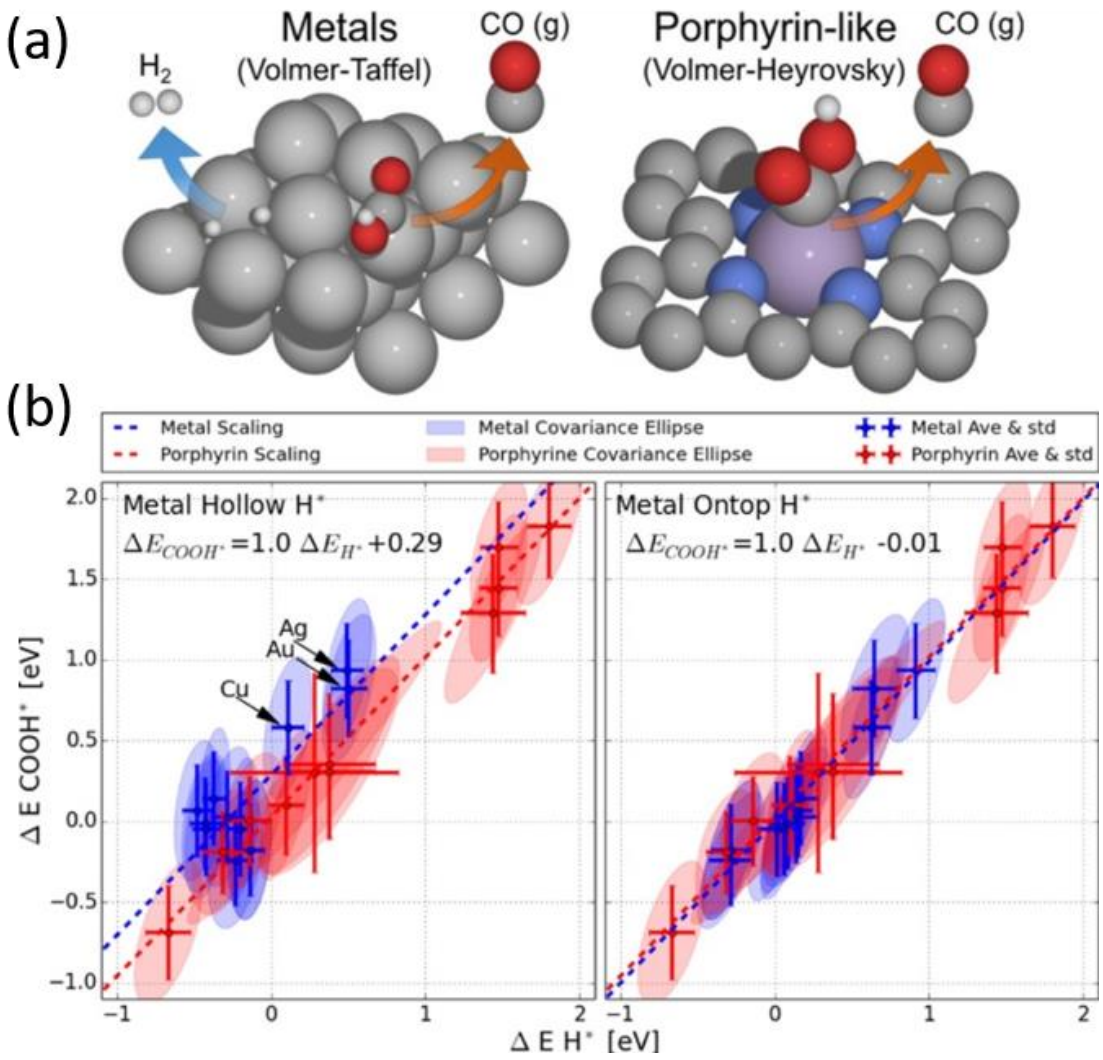

Figure 1.11 (a) Illustration of a metal surface and a porphyrin-like structure; the H* binding is at the hollow site for the metal, and the H* is forced on top of the metal atom for the porphyrin-like structure. (b) DFT energy relation between H* and COOH*. In the left figure the porphyrin-like structure has a scaling relation advantage over the metal scaling relation. Reproduced from reference[159] with the permission of Elsevier.

In 2017, they computationally explored the origin of CO_2ER activity and selectivity of the M-N_x motifs using a simple metalloporphyrin structure model (**Figure 1.11**). They found that the single metal site in a porphyrin-like structure had a simple advantage of limiting the competing H_2 evolution reaction (HER).[159] This structure required an ontop site binding of H, compared to the hollow site binding of H on a metal catalyst surface. The difference in binding site structure gave a fundamental energy-shift in the scaling relation of ~0.3 eV between the *COOH vs. H* intermediate (CO_2ER vs. HER). As a result, metal coordinated

porphyrin-like catalysts had the advantage over their metal counterparts of suppressing HER and enhancing CO_2ER selectivity.

The Fe-N-C, Co-N-C and Ni-N-C catalysts prepared by use of different N-C precursors and synthesis methods all exhibited excellent performance for CO formation, as can be seen in Table 1.6. For example, Yan et al.[160] developed a Ni-N-C catalyst, coordinatively unsaturated Ni-N sites doped porous carbon, by pyrolysis of Zn/Ni bimetallic zeolitic imidazolate framework-8 (ZIF-8). Their extended X-ray absorption fine structure (EXAFS) analysis revealed the coordinatively unsaturated state of Ni species in the Ni-N composites. Over these catalysts, the CO current density increased with the overpotential and reached 71.5 mA cm^{-2} at -1.03 V vs. RHE, while maintaining a high CO faradaic efficiency of 92-98% over a wide potential range of -0.53 to -1.03 V (**Figure 1.12**a-b). DFT calculations suggested that the key intermediates (*COOH and *CO) were more easily formed on coordinatively unsaturated NiN_3, NiN_3V and NiN_2V_2 sites than the coordinatively saturated NiN_4 sites, indicating that the excellent CO_2ER performance arose from the coordinatively unsaturated Ni-N sites (Figure 1.12c-e).

To strengthen the understanding of the reaction intermediates and reactive sites at a molecular level, Li et al.[161] fabricated a series of atomically dispersed Co catalysts with different N coordination numbers by modulating the pyrolysis temperature, and studied their catalytic performance for CO_2ER. Atomically dispersed Co with two-coordinated N atoms, achieving both high selectivity and superior activity: a FE_{CO} of 94 % and a current density of 18.1 mA cm^{-2} at an overpotential of 520 mV. They found that the decreased coordinating N resulted in more unoccupied 3d orbitals which benefited the adsorption of $CO_2^{\bullet-}$ and increased the reaction rate of CO_2 reduction. They also developed a robust electrocatalyst with atomically dispersed Co-N_5 sites anchored on polymer-derived hollow N-doped porous carbon spheres, which exhibited high CO faradaic efficiency above 90% over a wide potential range of -0.57 to -0.88 V.[162] Experiments and DFT calculations demonstrated that the single-atom Co-N_5 site was the dominating active centre simultaneously for CO_2 activation, the rapid formation of key intermediate *COOH as well as the desorption of CO.

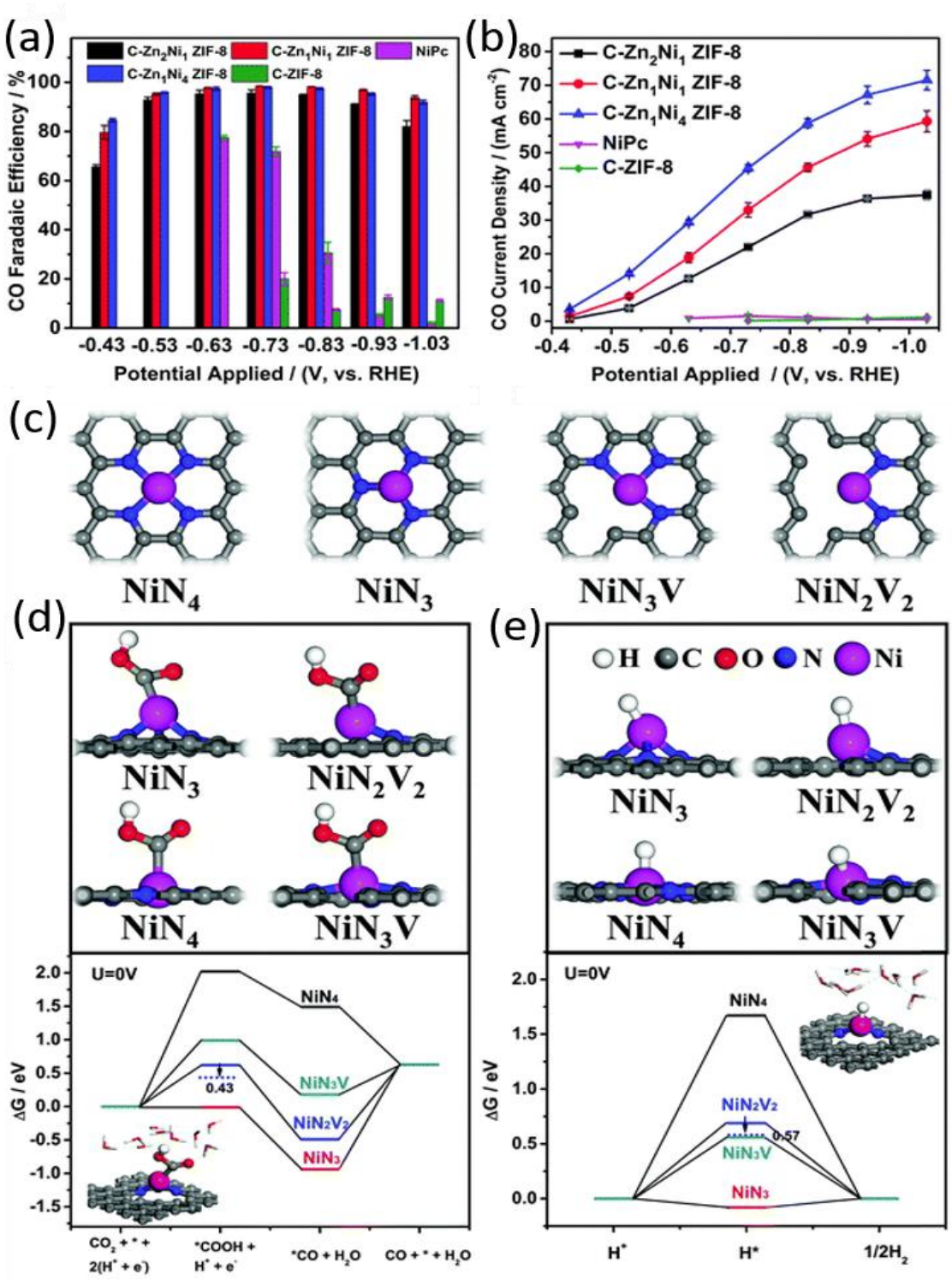

Figure 1.12 (a) Applied potential dependence of FE_{CO}; (b) CO partial current density measured in CO_2-saturated 1 M $KHCO_3$ solution; (c) Optimized atomic structures of different Ni-N structures with Ni atoms coordinated with 4 N atoms (NiN_4), 3 N atoms (NiN_3 and NiN_3V), 2 N atoms (NiN_2V_2); Free energy diagrams with implicit (solid lines) and explicit (dashed lines) solvation effect corrections for the CO_2ER (d) and HER (e) pathways on Ni-N sites at 0 V. Reproduced from reference[160] with the permission of Royal Society of Chemistry.

Table 1.6 Some representative metal-nitrogen doped carbon catalysts and their optimal CO_2ER performances.

Catalysts	**N-C precursor**	**Electrolyte**	**Product**	**FE** / %	**Potential** vs. RHE	$j_{partial}$
Fe-N-C[158]	PANI	0.1 M $KHCO_3$	CO	80	-0.5	~ 3 A g^{-1}
Fe-N-C[163]	4,4'-Dipyridyl	0.1 M $KHCO_3$	CO	65	-0.55	~ 3.8 A g^{-1}
FeN_x-CNT[164]	Melamine, CB	0.1 M Na_2SO_4	CO	85	-0.6	NA
FeN_4-C[165]	ZIF-8	0.5 M $NaHCO_3$	CO	90	-0.6	5.4 mA cm^{-2}
Fe-N-CNT/CNS[166]	FePc, CNT	0.1 M $KHCO_3$	CO	69	-0.59	0.82 mA cm^{-2}
Fe-N-C nanofibers[167]	PAN, NH_3	0.1 M $KHCO_3$	CO	95	-0.53	4.71 mA cm^{-2}
Fe-N-C[168]	ZIF-7, NH_3	1 M $KHCO_3$	CO	85	-0.43	~ 8 mA cm^{-2}
Ni-N-C[163]	4,4'-Dipyridyl	0.1 M $KHCO_3$	CO	85	-0.78	~ 12.5 A g^{-1}
Ni single atom[169]	ZIF-8	0.1 M $KHCO_3$	CO	70	-1.0	7.37 mA cm^{-2}
Ni-N_4-C[170]	g-C_3N_4, glucose	0.5 M $KHCO_3$	CO	99	-0.81	28.6 mA cm^{-2}
Ni atoms on graphene[171]	GO, NH_3	0.5 M $KHCO_3$	CO	95	-0.73	11 mA cm^{-2}
Ni-single atoms[172]	Amino acid, melamine, GO	0.5 M $KHCO_3$	CO	95	-0.72	22 mA cm^{-2}
Ni-N-graphene[173]	Pentaethylene-hexamine, GO	0.1 M $KHCO_3$	CO	90	-0.7	NA
C-Zn_1Ni_4 ZIF-8[160]	ZIF-8	1 M $KHCO_3$	CO	92	-0.53	~15 mA cm^{-2}
Ni^{2+}@N-G[174]	g-C_3N_4, glucose	0.5 M $KHCO_3$	CO	92	-0.68	9.38 mA cm^{-2}
Co-N_2-C[161]	ZIF-8	0.5 M $KHCO_3$	CO	94	-0.63	18.1 mA cm^{-2}
Co-N_5-C[162]	Melamine-polymer, CoPc	0.2 M $NaHCO_3$	CO	99	-0.73	6.2 mA cm^{-2}
Co-N-C[175]	CTF	0.1 M $KHCO_3$	CO	85	-0.7	~ 1 mA cm^{-2}

1.3.5.2 Immobilizing Molecular Complexes on Carbon Supports

Immobilizing effective molecular complexes onto electrically conductive supports can combine the advantages of homogeneous catalysts (high product selectivity and structure tunability) and heterogeneous catalysts (easy product separation and catalyst regeneration).[176,177] Their advantages mainly include: control over the active site environment; prevention of aggregation or dimerization of the molecular complex; efficient electron transfer to molecular complex; and stabilization of the catalyst.[45,176,178] The molecular complexes are usually linked to the conductive supporting materials such as active carbon, carbon nanotubes (CNTs), graphene, metallic organic frameworks (MOFs) and covalent organic frameworks (COFs) via either non-covalent (e.g., π-π interaction, electrostatic interaction) or covalent approaches.

The first work was reported in 1974 by Meshitsuka et al.[179], who dip-coated Ni- or Co-phthalocyanine (Pc) onto a graphite electrode to catalyze the CO_2ER. Thereafter, different kinds of molecular catalysts have been employed to link onto various substrates. For example, Chardon-Noblat et al.[180] reported a polymeric $[Ru(bpy)(CO)_2]_n$ film by electroreduction of *trans*(Cl)-$[Ru(bpy)(CO)_2Cl_2]$ complexes, which mainly produced CO with a FE_{CO} of 94% at a potential of -1.20 V vs. Ag/AgCl. Yao et al.[181] reported on a covalent attachment of cobalt porphyrin complexes onto boron-doped p-type conductive diamond by a click reaction, which exhibited good stability and electrocatalytic activity for the CO_2-to-CO conversion in 0.1 M Bu_4NPF_6/acetonitrile solution. Kang et al.[182] immobilized a pyrene-modified Ir pincer dihydride complex onto multi-walled carbon nanotubes (MWCNTs) coated gas diffusion electrodes, which exhibited current densities up to ~15 mA cm^{-2} and a turnover number of 15.1 for the CO_2-to-formate conversion. Koper et al.[183] reported a Co protoporphyrin immobilized on a pyrolytic graphite electrode which could reduce CO_2 to CO in an aqueous acidic solution at relatively low overpotential (0.5 V) with an efficiency and selectivity comparable to the benchmarking porphyrin-based electrocatalyst[184].

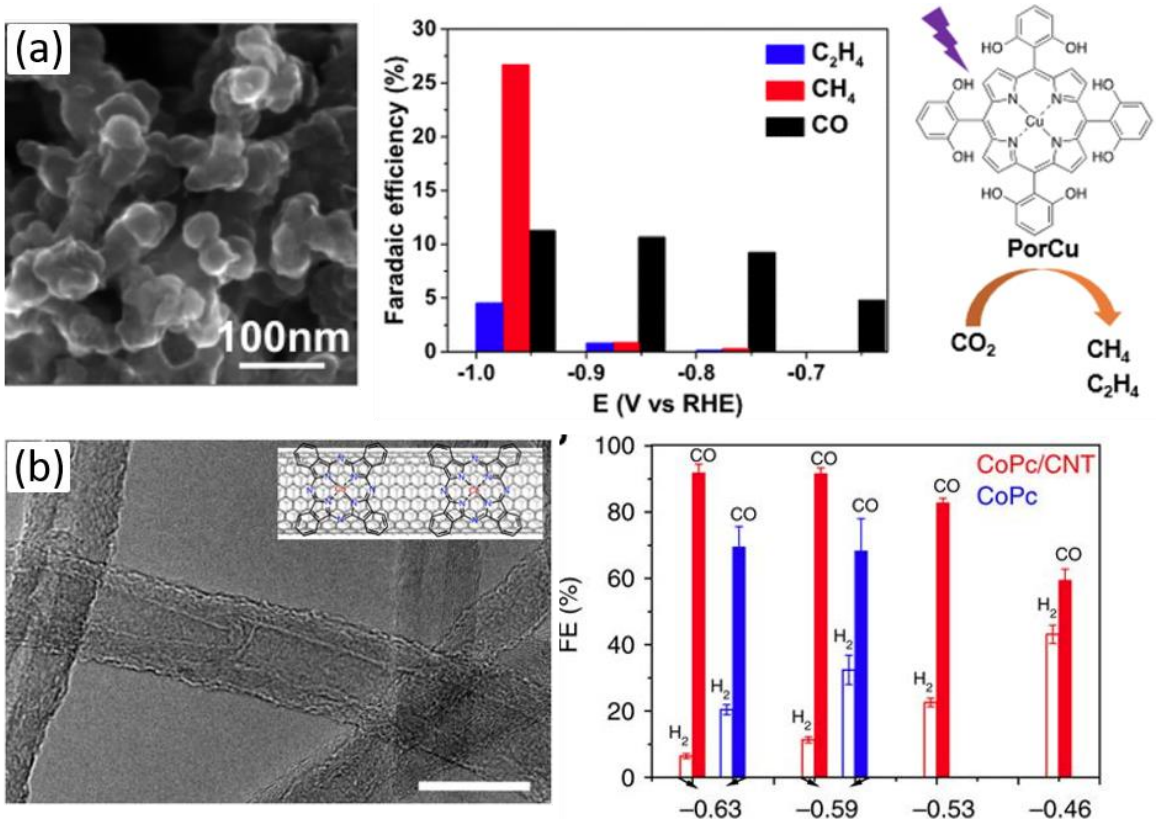

Figure 1.13 (a) SEM images of Cu porphyrin complex deposited carbon electrode and the distribution of CO_2ER products in the gas phase at various potentials; (b) TEM images of CoPc/CNT hybrid, and the FE_{CO} and FE_{H2} for CoPc/CNT (red) and CoPc (blue) at various potentials. Reproduced from references[185,186] with the permission of the American Chemical Society and Nature Publishing Group.

In 2017, Wang et al.[185] reported a molecular Cu-porphyrin complex deposited on carbon fibre paper which could electrochemically reduce CO_2 to hydrocarbons (CH_4 and C_2H_4) in aqueous media (**Figure 1.13**a). With a mass loading of 0.25 mg cm^{-2} at an applied potential of -0.976 V vs. RHE, a partial current density of 21 mA cm^{-2} and a FE of 44% for hydrocarbons were achieved. The catalytic performance was attributed to the Cu^I being the active centre and built-in hydroxyl groups in the porphyrin structure facilitating binding of certain reaction intermediates or providing an intramolecular source of protons.[45] Later, they reported on cobalt-phthalocyanine (CoPc) complexes uniformly anchored on CNTs to afford highly active and selective production of CO from CO_2 reduction in aqueous solution (Figure 1.13b).[186] They found that the hybridization with CNTs improved not only the catalytic activity but also the product selectivity and catalytic stability of CoPc complex. The excellent performance was attributed to the strong interactions between the molecular complex and CNTs, which allowed a uniform distribution of molecules on the highly

conductive carbon support and thus enabled a high degree of catalytic site exposure and rapid electron transfer from the electrode to surface immobilized molecules.

Reisner et al.[187] assembled a [MnBr(bpy)(CO)$_3$] complex onto MWCNTs as an effective electrocatalyst for CO_2 reduction (**Figure 1.14**). In addition to the high electrocatalytic activities at low overpotentials, they found that the CO_2ER product selectivity could be fine-tuned by controlling the surface loading of catalyst on the CNT sidewalls. Low Mn catalyst loadings afforded a selectivity for the generation of dissolvable formate, whereas high loading resulted in a higher selectivity for gaseous CO production. They identified two different intermediates responsible for the change in selectivity. The formation of a dimeric Mn^0 species at higher surface loading was shown to preferentially lead to CO formation, whereas at lower surface loading the electrochemical generation of a monomeric Mn-hydride was suggested to greatly enhance the production of formate.

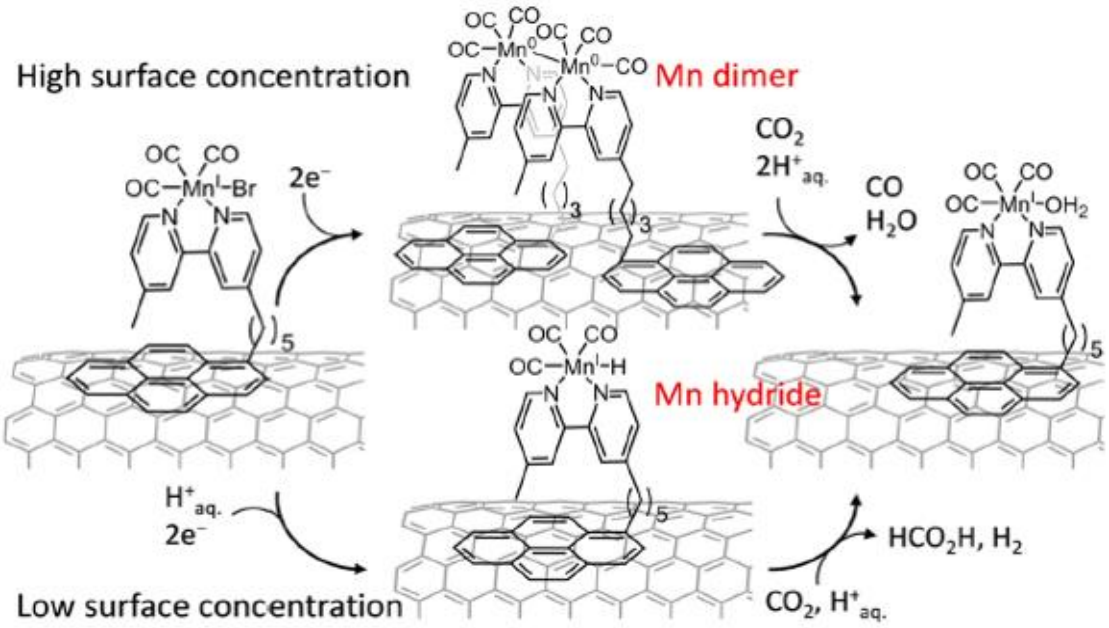

Figure 1.14 Schematic representation of [MnBr(bpy)(CO)$_3$] immobilized on a CNT sidewall, concentration-dependent dimerization or Mn-H formation, and intermediate-dependent reduction of CO_2 to CO or HCOOH. Adapted with permission.[187] Copyright 2017, American Chemical Society.

Recently, Sato et al.[188] investigated a Mn-complex/MWCNT hybrid electrocatalyst, which reduced CO_2 to CO at a constant rate for 48 h with a current density of >2.0 mA cm^{-2} at -0.39 V vs. RHE in aqueous solution. They revealed the key role of MWCNTs support and K^+ ions in the electrolyte. The MWCNTs with electron accumulation properties along

with the surface adsorbed K^+ ions, could help to stabilize the CO_2 molecules adjacent to the Mn-complex and significantly lower the overpotential for CO_2 reduction in an aqueous solution.

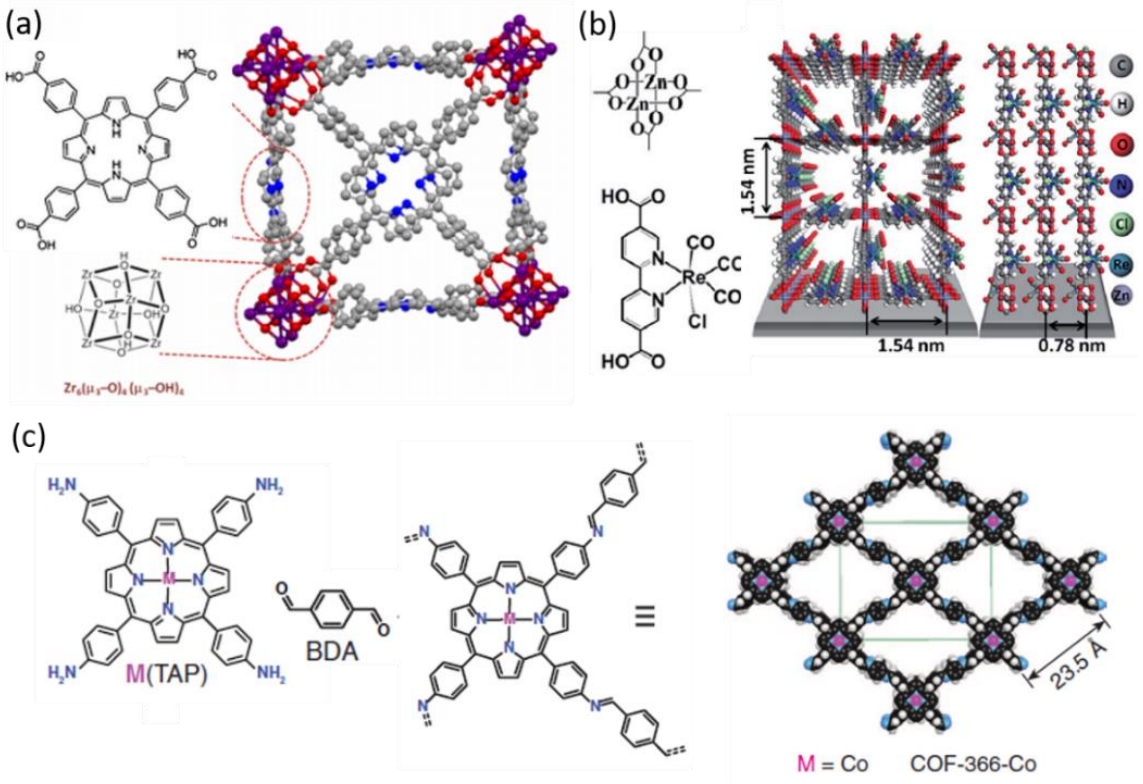

Figure 1.15 Illustration of a portion of the crystal structure of MOF-525 (a), Re-MOF (b) and Co-porphyrin based COF (c), and the chemical structure of their precursors. Reproduced from references[189-191] with permissions from the American Chemical Society, Royal Chemistry of Society and American Association for the Advancement of Science.

Without using traditional carbon supports, Hod et al.[190] reported on an electrophoretic deposition of Fe-porphyrin MOF thin films on a conductive fluorine doped tin oxide (FTO) substrate as an effective catalyst for CO_2ER (**Figure 1.15**a). This approach yielded a high effective surface coverage of electrochemically addressable catalytic sites (~1015 sites cm^{-2}) for the CO_2-to-CO conversion, affording an average CO turnover frequency of 64 h^{-1}. Ye et al.[191] incorporated the active Re complex onto the linker and constructed a Re(bpy)$(CO)_3$Cl-based MOF thin film on FTO, which exhibited an extremely high FE of 93% and a current density of > 2 mA cm^{-2} for reducing CO_2 to CO (Figure 1.15b), outperforming the benchmark Fe-porphyrin and Co-porphyrin based MOF thin films[190,192]. Apart from MOFs, COFs were also used as host to immobilize the electrocatalytic sites. Lin

et al.[189] reported modular optimization of COFs, in which the building units were Co-porphyrin complexes linked by organic struts through imine bonds, to prepare a catalyst for electrochemical reduction of aqueous CO_2 to CO (Figure 1.15c). The catalysts exhibited high faradaic efficiency (90%) and turnover numbers (up to 290,000 at pH 7) with an overpotential of 0.55V, equivalent to a 26-fold improvement in activity compared with the molecular Co complex.

1.4 Surface and Interface Engineering of Metal Catalysts

Heterogeneous CO_2ER is an interfacial process that occurs at the catalyst/electrolyte interface. The electrocatalytic activity and selectivity of this reaction strongly depends on the interfacial properties related with catalyst surface, electrolyte, and mass transportation. Among them, the surface and interface of electrocatalysts are closely correlated with the adsorption and stabilization of reactants and intermediates. They are critical factors in the heterogeneous CO_2ER process. In this section, various surface factors and interfacial factors will be discussed. Considering the large variety of heterogeneous catalysts presented above, the discussion will only focus on metal-based catalysts. Other factors such as electrolyte and mass transport are beyond the scope of this thesis.

1.4.1 Surface Engineering of Metal Catalysts

Altering the surface structure and composition of metal electrocatalysts is a straightforward strategy for tuning the adsorption binding strength of CO_2 molecules and intermediates, leading to the change of intrinsic activity. It mainly includes the engineering of particle morphology, grain-boundary, crystal facet, and surface chemical state.

1.4.1.1 Crystal Facet Effects

The intrinsic electronic properties of the catalyst surface strongly govern the kinetics and product selectivity of CO_2 reduction by affecting the binding energies and activation barriers of intermediate species. A fundamental study using single-crystal metal electrodes is ideal to reveal the electrocatalytic properties of different crystal facets. The early studies on low-index Pt[193-196], Ag[197] and Pd[198] single crystals have shown that their electrocatalytic activity for CO_2 to CO reduction highly depends on the orientation of single crystals. Ag and Pd showed the activity trend of (100) < (111) < (110), whereas Pt exhibited a trend of (111) < (100) < (110).

Besides these noble metals, the reactivity and selectivity of Cu electrodes are also highly dependent on the crystal facets.[199-202] The ratio between the products CH_4 and C_2H_4 depends strongly on the crystal orientation: Cu(111) facets favour the formation of CH_4, and Cu(100) facets favour the C_2H_4. Hori et al.[199] optimized the Cu single-crystal surface by introducing (111) steps onto Cu(100) basal plane, which significantly promoted C_2H_4 formation and suppressed CH_4 formation. The mechanism behind the selectivity change on Cu(111) and (100) surfaces was unravelled by Koper and Nørskov et al. by using both experimental and theoretical studies.[203-206] It was found that Cu(100) surfaces facilitated the formation of C_2H_4 through *CO dimerization, whereas Cu(111) surfaces favoured the *CO protonation which was a key step towards CH_4 formation.

1.4.1.2 Particle Size and Shape Effects

Advances in colloidal chemistry has enabled controllable synthesis of abundant metal nanostructures with specific shape and size, making it possible to independently investigate these structural factors of catalysts for CO_2ER. For example, Zhu et al.[68] investigated the size-dependent electrocatalytic reactivity for the CO_2-to-CO conversion over monodispersed Au NPs with different sizes (4, 6, 8 and 10 nm) (**Figure 1.16**a-c). Among them, the 8 nm Au NPs exhibited the highest FE_{CO} values at different potentials. Their DFT calculations suggested that corner sites bound *H strongly favour H_2 evolution whereas edge sites stabilized the *COOH intermediates facilitating CO formation. The 8 nm Au NPs with 4 nm crystalline diameter provided a near-optimal number of edge sites while minimizing the number of corner sites, and thus exhibited the best performance. They further demonstrated the importance of edge sites using ultrathin Au NWs with different aspect ratios.[67] The Au NW with the largest aspect ratio (500 nm length, 2 nm width) exhibited a low onset overpotential (90 mV) and a high FE_{CO} of 94% at a low overpotential (0.24 V) for CO production (Figure 1.16d-f). Their DFT calculations revealed that the NWs with maximal edge sites maintained the activation of CO_2 to *COOH and facilitated the release of CO.

Strasser et al.[207] reported that a decrease in the size of Cu NPs, especially down to 5 nm, was beneficial for the enhancement of the total current density and selectivity toward H_2 and CO (Figure 1.16g-i). Their DFT calculation revealed that smaller Cu NPs could produce more under-coordinated atoms to realize strong binding energies for *H and *COOH intermediates, thus facilitating the reduction of CO_2 to CO and simultaneously restraining further recombination reactions that produce other hydrocarbons. By comparison, larger Cu

nanoparticles exhibited much higher selectivity for hydrocarbons due to a decrease of under-coordinated sites. This size effect was also confirmed by other reports using glassy carbon supported Cu NPs (the original 7 nm NPs grew to 23 nm during reaction)[29] and Vulcan carbon-supported Cu NPs (12 nm; 40% by weight)[208].

Wang et al.[79] also reported a size-dependent activity/selectivity on Pd-NPs catalysed CO_2ER. Electrochemical analyses showed that the FE_{CO} increased from 5.8% to 91.2% with a decrease in the size from 10.3 to 3.7 nm. The enhanced catalytic performance was attributed to the additional corner, edge, and terrace sites produced by varying the size of Pd NPs, which can facilitate CO_2 adsorption and COOH* formation. However, there is an optimal size of Pd NPs. Too small particles are not beneficial for the CO_2ER because of their preference for the HER over the CO_2ER.

Apart from the size effect, the shape of metal NPs also has a remarkable influence on CO_2ER. This effect is particularly obvious on Cu-based catalysts because of its special facet-dependent product selectivity for CO_2ER. Nanosized Cu catalysts with a dominant exposure of (100) facets and step sites have been revealed to facilitate C_2H_4 or even C_3 product formation.[98,209-211] Buonsanti et al.[90] found that the cube-shaped NPs were more intrinsically active than spheres, and the cubic NPs showed a non-monotonic size-dependence of the product selectivity (Figure 1.16j-l). The cubes with 44 nm edge length exhibited the highest selectivity towards CO_2ER (80%) and FE (41%) for C_2H_4 formation, which was related to its optimal ratio of edge/facet (100).

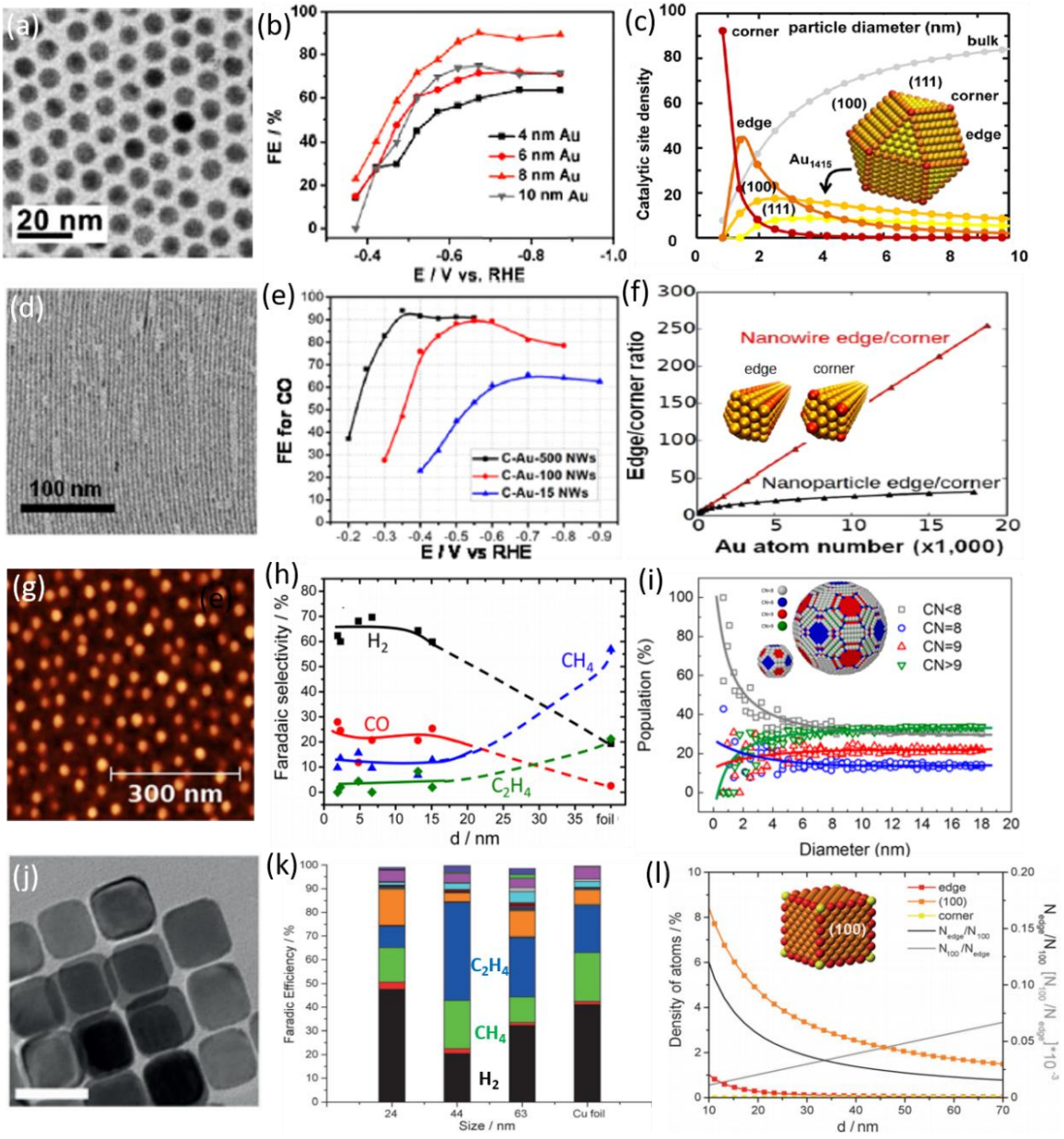

Figure 1.16 (a, d, j) TEM and (g) AFM image of 8 nm Au NPs, 500 × 2 nm ultrathin Au NWs, Cu NPs, and 44 nm Cu nanocubes; (b, e, h, k) Particle size dependent faradaic efficiencies at different potentials; (c, f, i, l) Density of catalytic sites, edge/corner ratios, population of surface atoms with specific coordination numbers (CN), density of adsorption sites on a cuboctahedral Au cluster model, an Au NW model, a Cu spherical model and a Cu cube model, respectively. Adapted from references[67,68,90,207] with the permission of American Chemical Society and Wiley-VCH.

Huang et al.[81] demonstrated a remarkable shape effect using Pd octahedra and icosahedra with similar particle sizes as catalysts for CO_2ER. The Pd icosahedra catalyst exhibited a maximum FE_{CO} of 91.1% at -0.8 V vs. RHE, 1.7-fold higher than that of Pd octahedra at -

0.7 V. By combining molecular dynamic simulations, DFT calculations and surface valence-band photoemission spectra, they revealed that the shape effect arose from their different surface strains. The tensile strain on the surface of Pd icosahedra boosted the catalytic activity by shifting up the d-band centre and thus strengthening the adsorption of key intermediate *COOH. By contrast, the Pd octahedron showed slightly compressive strain on the surface without obvious change of surface electronic state.

The size and shape effects were also reported for Bi NPs[54], Sn NPs[46], Ag NPs[73], Ag triangular nanoplate[78] and Zn hexagonal nanoplate[86] catalysts. The reasons behind these effects are similar, which are an optimal ratio of specific edges, corner and terrace sites. Tuning the particle size or shape affords an appropriate binding strength of the intermediates such as *COOH and *CO. These well-understood effects can be combined to explain the excellent CO_2ER performance of irregularly nanostructured catalysts (e.g., nanoporous Ag[75], Zn dendrites[83], Cu nanoflowers[88], concave Au NPs[212] etc.).

1.4.1.3 Grain-Boundary Effects

Apart from the regular sites such as edges and facets, grain boundaries (GBs) were revealed as highly active sites for CO_2ER as well. In 2012, Kanan's group proposed that the high densities of GBs in the nanocrystalline "oxide-derived" catalysts were responsible for their improved CO_2-to-CO and CO-to-fuels electrocatalytic activity.[34,213,214] Later, they quantitatively correlated electrocatalytic activity and GB density for the catalysts composed of discrete Au and Cu NPs.[69,215] Most recently, they proved that grain-boundary surface terminations in Au electrodes were more active for the CO_2-to-CO rather than the competing H_2 evolution compared with grain surfaces; by using a combination of bulk electrochemical measurements and scanning electrochemical cell microscopy (SECCM) with a submicrometre resolution (**Figure 1.17**).[216] They found that the catalytic footprint of GBs was commensurate with its dislocation-induced strain field, and proposed two possible explanations for the increase in CO_2ER activity at regions with high dislocation densities. They suggested that lattice strain at the surface induced by dislocations could alter the binding energies for CO_2 reduction intermediates in a way that reduces the overall barrier. Alternatively, dislocation surface terminations may create high step densities that are more active than terraces.

Kim et al.[217] theoretically revealed the mechanistic role of GBs during CO_2ER using DFT calculations on the Au surface. The broken local spatial symmetry near a GB tunes the

Au metal-to-adsorbate π-backbonding ability, thereby stabilizing the key *COOH intermediate. This stabilization leads to a decrease of ~200 mV in the overpotential and a change in the rate-determining step. The important role of GBs was also revealed experimentally on reduced SnO_2 NWs catalysts for CO_2-to-HCOOH conversion.[38]

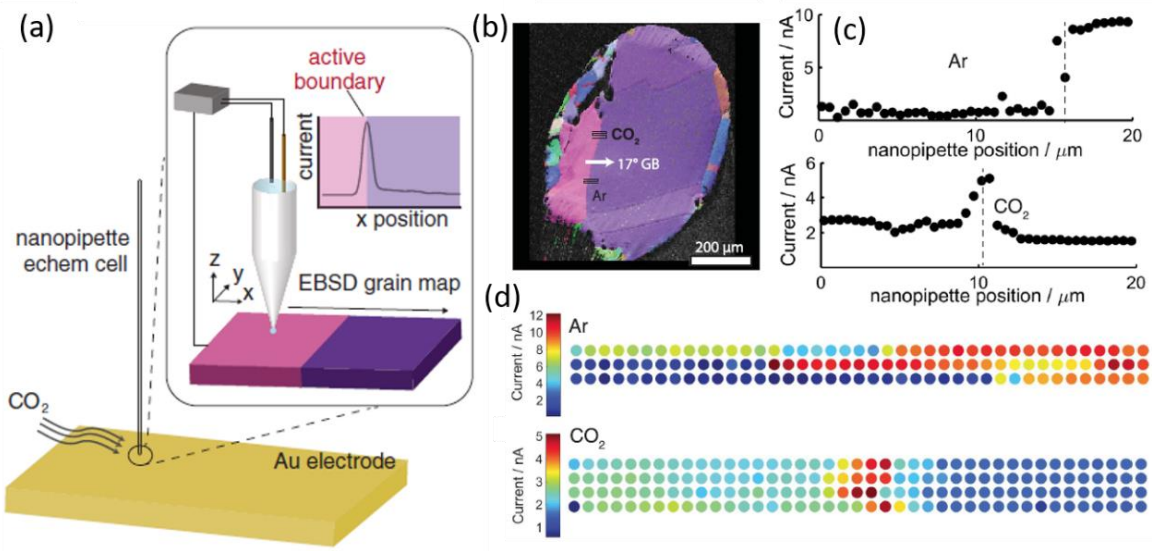

Figure 1.17 (a) Schematic illustration of the SECCM using a ~300-nm nanopipette electrochemical cell. (b) Electron backscatter diffraction orientation map of sample; inset text and paths indicate location where line scans and maps were collected. (c) Line scan generated from individual constant potential electrolysis across the GB under 1 atm Ar and CO_2, respectively; dashed lines indicate location of GBs. (d) Electrocatalytic heat map composed of multiple line scans across the GB under Ar and CO_2 environments. Adapted from reference[216]. Copyright 2017, American Association for the Advancement of Science

1.4.1.4 Morphology Induced Effects

The above size, shape and grain boundary effects are related to the intrinsic properties of metal surfaces. Morphologies of catalysts themselves may have additional influence on the electrocatalytic performance induced from the local mass transport process or local electrical field.

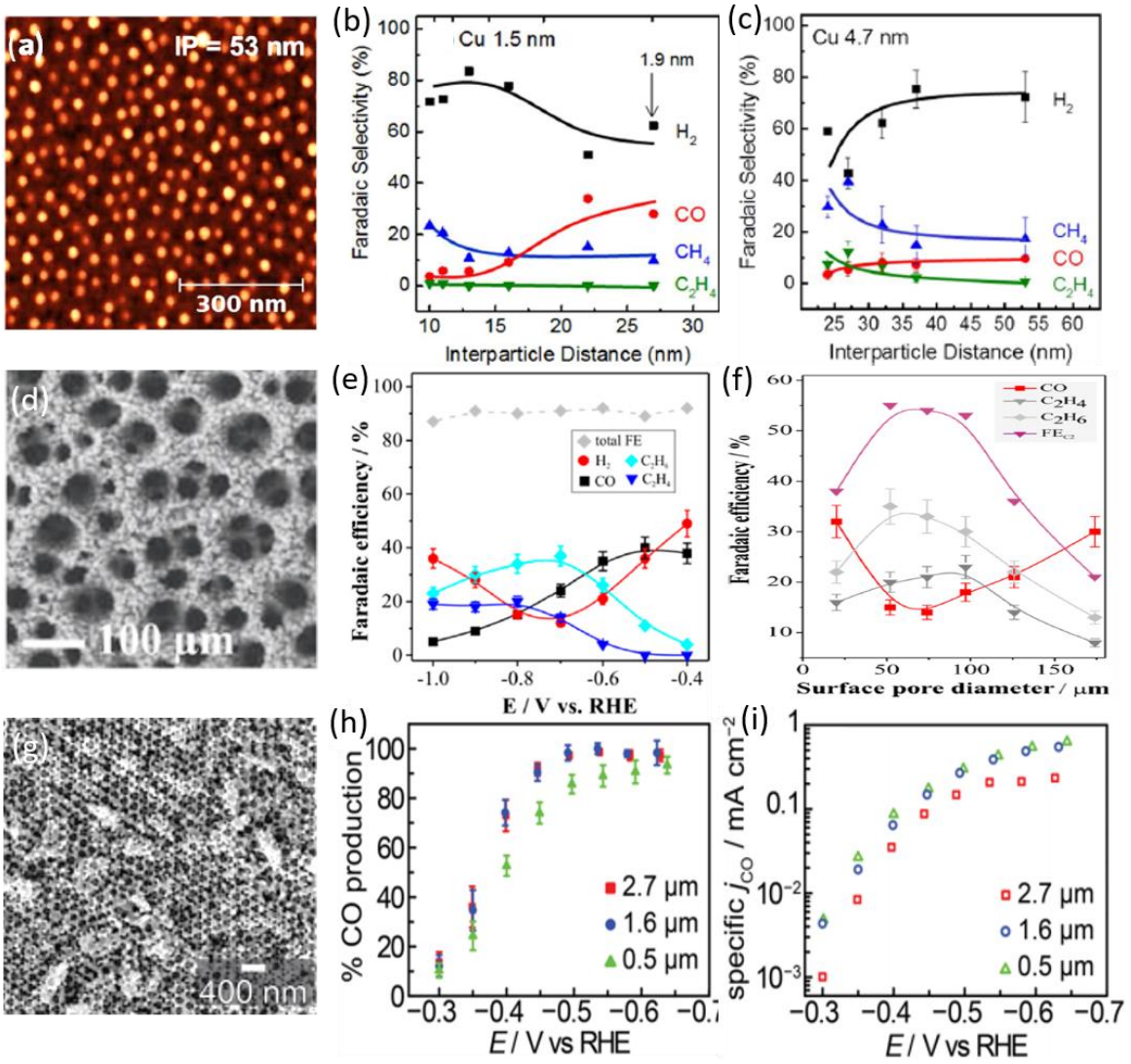

Figure 1.18 (a) AFM images of 4.7 nm Cu NPs dip-coated onto SiO_2/Si(111) acquired after ligand removal, corresponding to an IP distance of 53 nm; (b-c) FE as a function of inter-particle distance at -1.1 V vs RHE over 1.5 nm and 4.7 nm Cu NPs. (d) SEM image of Cu foam; (e) FEs for the Cu foam catalyst; (f) Analysis of the products depending on the surface pore size of Cu foam at -0.8 V vs. RHE. (g) SEM image of Au-inverse opals; (h) FE_{CO} and FE_{H2} for 0.5, 1.6, 2.7 µm thick Au porous films. Reproduced from references[89,218,219] with the permission of American Chemical Society.

Strasser et al.[218] found that decreasing the inter-particle (IP) spacing between Cu NPs could increase the selectivity for CH_4 and C_2H_4 from CO_2 reduction (**Figure 1.18**a-c). By combining the experimental results with a reaction-diffusion model, they revealed that the improved hydrocarbon selectivity over Cu NPs with small IP distance originated from the mesoscale phenomena, i.e., the increased likelihood of the re-adsorbing of CO intermediates on a neighbouring particle and being further reduced.[202,218] Dutta et al.[89] found a strong

dependence of the FE_{C2} (C_2H_4 and C_2H_6) on the surface pore size of Cu form catalysts, as shown in Figure 1.18d-f. Besides the presence of active sites favouring *CO dimerization, they identified that the temporal trapping of gaseous intermediates (CO, H_2, and C_2H_4) inside the mesoporous Cu foam acted as a key factor in optimizing the selectivity towards the fully reduced C_2 product (C_2H_6). Surendranath et al.[219,220] found that increasing the thickness of porous Ag and Au inverse opal thin films could highly decrease the specific activity for H_2 evolution while maintaining the CO evolution activity (Figure 1.18g-i). The H_2 suppression in these mesoporous films stemmed from the generation of diffusional gradients within the pores of this mesostructured electrode rather than changes in surface active sites. This confining effect was also reported for N-doped carbon catalysts. Mesopores may help to trap or stabilize the *CO intermediates and further convert it to high-carbon product such as ethanol.[150]

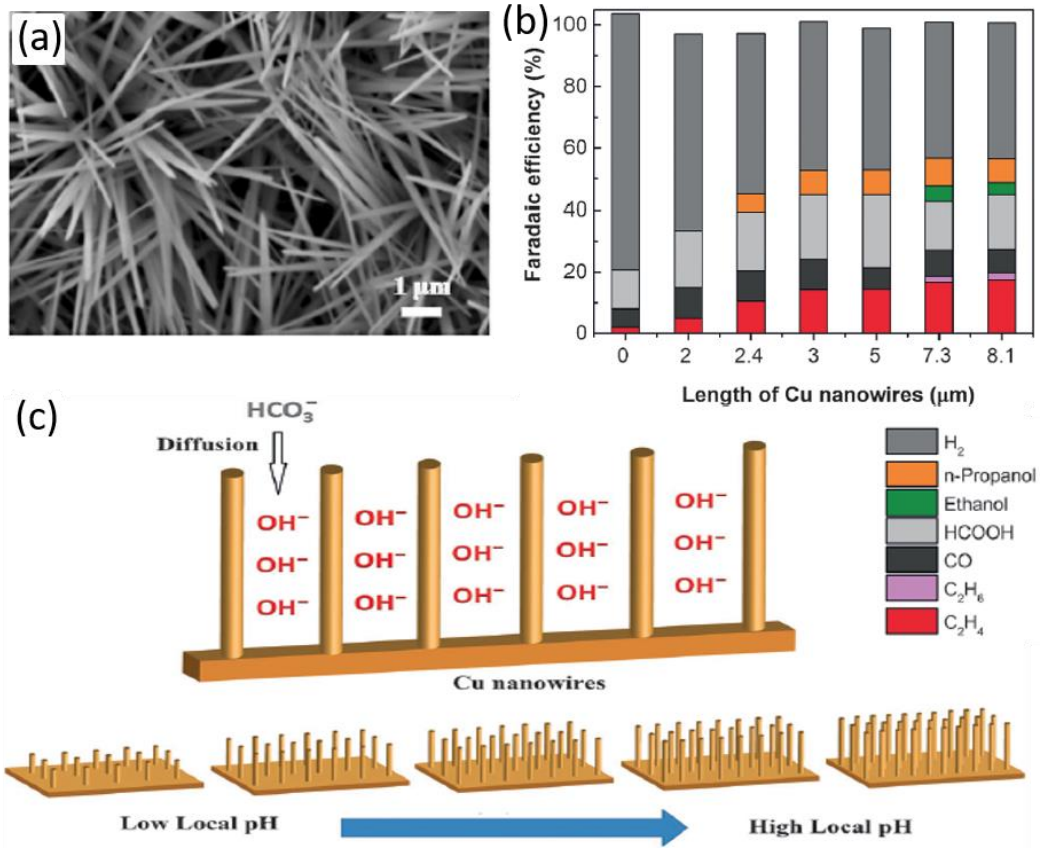

Figure 1.19 (a) SEM image of $Cu(OH)_2$ NWs with an average length of 8.1 μm. (b) FEs for C_2H_4, C_2H_6, CO, HCOOH, ethanol, n-propanol, and H_2 on Cu NW arrays with different lengths at -1.1 V vs. RHE in CO_2-saturated 0.1 M $KHCO_3$ solution (0 μm NWs represent Cu foil). (c) Schematic illustration of the diffusion of electrolytes into Cu NW arrays. Adapted with permission from reference[91]. Copyright 2016, Wiley-VCH.

Smith et al.[91] studied the effects of Cu NW morphology on the selectivity of CO_2ER by investigating samples with different lengths and densities (**Figure 1.19**). They found that the selectivity for hydrocarbons and oxygenates (e.g., ethylene, n-propanol, ethane, ethanol) on Cu NW arrays at a fixed potential could be tuned by altering the NW length and density, which was related to the resultant local pH values. Higher local pH near the surface of longer and denser Cu NW arrays favoured the formation of C_2H_4 and alcohols, whereas lower local pH values near the surface of shorter and sparser arrays favoured H_2 evolution.

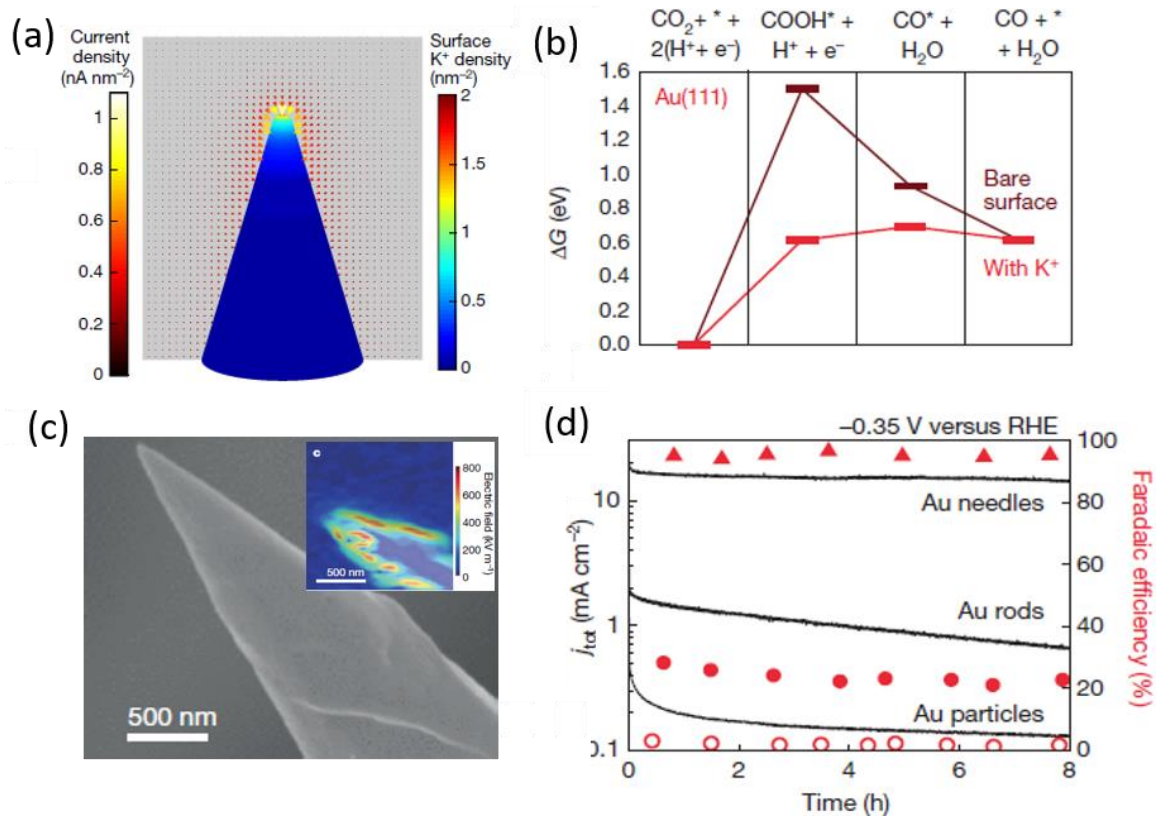

Figure 1.20 (a) Surface K^+ density and current density distributions on the surface of Au needles (tip radius is 5 nm); (b) Thermodynamic barriers for the CO_2-to-CO reduction reaction on Au(111) surface under conditions with and without K^+; (c) SEM image and electric field distribution of Au needles deduced using Kelvin probe AFM; (d) CO_2 reduction current density and FE_{CO} of Au needles, rods and particles at -0.35 V vs. RHE. Reproduced from reference[72] with the permission of Nature Publication group.

Nano-morphology induced electrical field effect has a remarkable influence on CO_2ER as well. By applying theoretical modelling and calculations, Sargent et al.[72] predicted that a high-curvature nanoneedle could locally enhance electrostatic field intensity that led to tens of folds increased surface-adsorbed K^+ ion concentration at the needle tip (**Figure 1.20**a-c).

With concentrated K^+, CO_2 could be quickly stabilized on the tip. The thermodynamic energy barrier for CO_2ER could be lowered due to the improved stabilization of *COOH and *CO intermediates. This was verified by using Au electrodes with different radius of curvature (140 nm particles, 60 nm rods, 5 nm needles) for CO_2ER. At a low overpotential of -0.35 V vs. RHE, the CO partial current density on Au nanoneedles was 63 times higher than that on rods and 112 times higher than that on particles, indicative of the higher intrinsic CO_2ER activities of Au needles. Similarly, Pd nanoneedles produced formate with a FE of > 90% and an unprecedented current density of 10 mA cm^{-2} at -0.2 V vs. RHE. The Au nanoneedles supported sulphide-derived Sn catalyst also accelerated the CO_2-to-formate conversion at a current density of 55 mA cm^{-2} at -0.75 V with a FE of 93%.[221] These results demonstrated the wide applicability of the field-induced reagent concentration concept for CO_2ER.

1.4.1.5 Surface Oxidation State

The surface oxidation state has been the subject of numerous studies since the pioneering work of Frese[222] who first reported significant yields of methanol on thermally oxidized Cu electrodes. In 2012, Kanan and colleagues[33] introduced oxide-derived Cu (OD-Cu) as a new class of catalyst for CO_2ER with considerably improved product selectivity at low overpotentials (**Figure 1.21**a-b). They later suggested that grain boundaries may stabilize strong CO-binding sites on oxide-derived catalysts, thereby enabling the efficient reduction of CO to hydrocarbons.[214,215] Koper et al.[223] and Yeo et al.[224] demonstrated that the initial oxide film thickness played a key role in determining the selectivity of oxide-derived Cu as well. They also suggest that Cu^+ sites might still remain on the catalyst surface during the reaction and work as active sites.[225,226]

This claim was confirmed by Cuenya et al.[92,227] through combining electrochemical measurements with operando microscopic and spectroscopic techniques over a plasma-treated oxide-derived Cu catalyst (Figure 1.21c-d). Their OD-Cu displayed a high selectivity towards C_2H_4 (60%) production at -0.9 V vs. RHE. The operando X-ray absorption spectroscopy and cross-sectional scanning transmission electron microscopy showed that copper oxides were surprisingly resistant to reduction and Cu^+ species remained on the surface during the reaction. The roughness of OD-Cu played only a partial role in determining the catalytic performance, while the presence of Cu^+ species was the key for lowering the onset potential and enhancing C_2H_4 selectivity. Recently, Nilsson et al.[228]

observed a substantial amount of residual oxygen in nanostructured OD-Cu electrocatalysts using in-situ XPS and quasi in-situ electron energy loss spectroscopy (EELS) analyses. They proposed that residual subsurface oxygen might change the electronic structure of catalyst surface and create sites with higher CO binding energy, which was the key for reducing CO_2 into multi-carbon compounds.

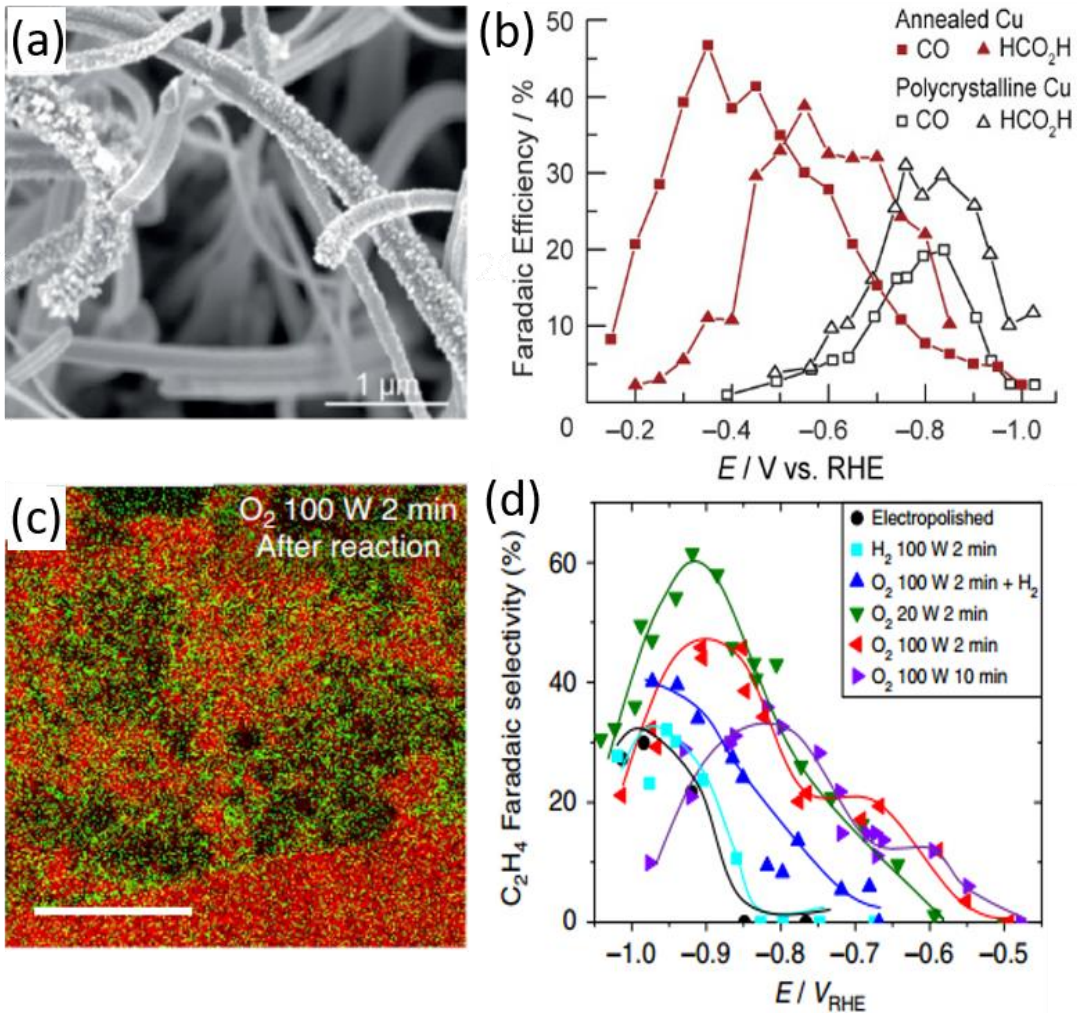

Figure 1.21 (a) SEM image of oxide-derived Cu after electrolysis; (b) Comparison of the FEs for CO and formic acid on polycrystalline Cu and Cu annealed at 500 °C for 12 h. (c) EDS elemental maps of Cu foils treated with O_2 plasma after electrolysis; (d) FE of C_2H_4 at various applied potentials. Reproduced from references[33,227] with the permission of American Chemical Society and Nature publication group.

The unique electrocatalytic properties of oxide-derived metal catalysts have been extended to other metals such as Au[34], Ag[229], Sn[230], Zn[231], Pb[232] and Pd[80] in which product distributions are unequivocally different from those observed on the corresponding

metal surfaces. Although oxide-derived metallic catalysts are very promising in terms of CO_2ER efficiency, key questions remain about the fundamental mechanism behind this improvement. In-situ and operando studies, instead of ex-situ studies which currently provide the majority of available characterization data for this reaction, are essential to solve these questions and ultimately gain an insight into the chemical state of the active catalyst under reaction conditions.[202]

1.4.2 Interface Engineering of Metal Catalysts

Apart from tuning the intrinsic surface property, engineering the interfaces is an alternative method for increasing the activity of active sites and leading to significantly enhanced electrocatalytic reactivity. The key interfaces reported for CO_2ER mainly include metal-metal, metal-metal oxide, metal-carbon, and metal-ligand.[233] The first three kinds of interfacial effects can be categorized as metal-support effects, and the last one can also be denoted as metal-adsorbate interfacial effect.

1.4.2.1 Metal-Support Interfacial Effects

A well-defined interface between metal and supporting component is advantageous for producing synergistic effects at the nanoscale interfaces. Many hybrid catalysts using the metal-metal (or metal oxide) and metal-carbon interactions have demonstrated improved electrocatalytic activity. For example, Bao et al.[234] constructed Au NP-CeO_x interfaces that exhibited much higher activity and selectivity than Au NPs or CeO_x alone for CO_2ER (**Figure 1.22**a). In-situ STM and XPS analyses revealed that the Au-CeO_x interface was the dominant site for enhancing CO_2 adsorption and activation. DFT calculations indicated that the Au-CeO_x interface could improve the stability of *COOH intermediate and thus facilitate the CO_2ER. Zheng et al.[235] synthesized a 2D hierarchical Pd/SnO_2 structure, ultrathin Pd nanosheets partially capped by SnO_2 NPs, which enabled a high selectivity (FE ~ 55%) for reducing CO_2 to CH_3OH at a low overpotential (-0.24 V vs. RHE). They demonstrated that this hybrid structure not only enhanced the adsorption of CO_2 on SnO_2, but also weakened the binding strength of *CO on Pd due to the Pd-O-Sn interfaces, which was critical to improving the electrocatalytic selectivity and stability of the Pd catalyst.

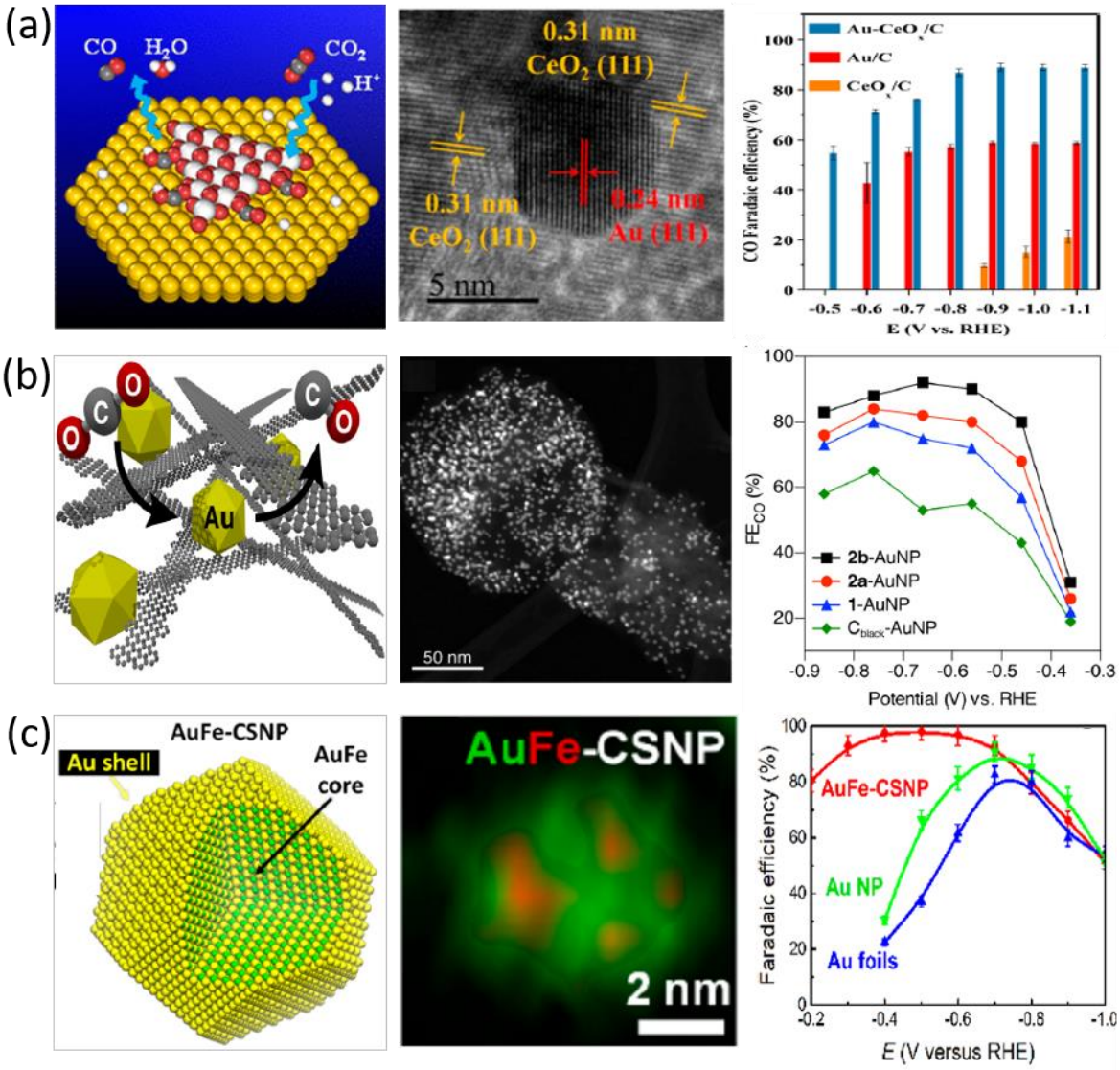

Figure 1.22 Catalyst models, TEM images and potential-dependent FE_{CO} profiles for three different catalysts: CeO_x supported Au NPs (a), graphene nanoribbon supported Au NPs (b) and Au-Fe core-shell NPs (c). Adapted from references[71,124,234] with the permission of American Chemical Society.

Fischer et al.[71] synthesized a hybrid catalyst composed of Au NPs embedded in a graphene nanoribbon (GNR) matrix (Figure 1.22b), which exhibited an excellent CO_2ER performance: an onset overpotential of ~0.09 V, a maximum FE_{CO} > 90% and a superior stability of over 24 hours. They demonstrated that the GNR could facilitate the dispersion of Au NPs and electron transport to Au NPs, thereby reducing the catalytic onset potential compared with that for bare Au NPs or carbon black supported Au NPs. The authors also proposed that the methyl carboxylates along the graphene edges introduced by the bottom-up synthetic strategy, could stabilize the intermediate during the CO_2ER and therefore shift

the rate-determining step, altering the electrocatalytic mechanism. Sun et al.[236] assembled monodisperse Cu NPs on a pyridinic-N rich graphene support for CO_2ER, and found that pyridinic-N in the composite functioned as a CO_2 and proton adsorber, facilitating hydrogenation and carbon-carbon coupling reactions on Cu for the formation of C_2H_4. Gogotsi et al[94] found that onion-like carbon (OLC) supported Cu NPs also exhibited higher C_2H_4 selectivity compared with CNTs and RGO supported ones. They suggested that the intrinsic ability of OLC for CO_2-to-CO conversion could afford a higher CO surface concentration. These generated CO could transfer to the neighbouring Cu surface for further reduction and yield more C_2H_4. Meanwhile, the formation of CO on OLC could lead to an increase of local pH which was also beneficial for the formation of C_2H_4.

In addition, constructing core-shell structures offer another effective way of tailoring the electrocatalytic activity of metals, which can be rationalised in terms of ligand and strain effects.[237,238] For example, Wang et al.[124] synthesized an Au-Fe core-shell NPs catalyst by leaching the surface Fe atoms on the AuFe NPs (Figure 1.22c), which exhibited exclusive selectivity, higher mass activity, and lower onset overpotential for CO_2-to-CO conversion. Their DFT calculations showed that the Fe-leaching-induced surface defects contributed significantly to the enhanced performance, and the core-shell structure was the key to stabilize such surface defects. Fermin et al.[239] investigated Au-Pd core-shell NPs with different shell thicknesses, and found that the products generated during CO_2ER were related to the Pd shell thickness. CO and H_2 were the only products generated at those NPs with 1 nm thick shells, whereas $HCOO^-$, CH_4 and C_2H_6 were produced on the NPs with shells of 5 and 10 nm. They concluded that the collisions between the adsorbed H at relaxed Pd lattices (thicker shell) and the strongly bound "CO-like" intermediates might promote the complete hydrogenation to C_1 and C_2 alkanes.

1.4.2.2 Metal-Adsorbate Interfacial Effects

The interaction between metal catalysts and functional adsorbates can induce significant electronic effects that affect the intrinsic properties of catalysts, or steric effect that affects the catalytic environments; they all may tune the electrocatalytic properties of metal catalysts.[240] This process is also known as surface modification or surface functionalization. The adsorbates have the functionalities such as improving CO_2 concentration, facilitating CO_2 stabilization and tuning the electronic structure of the metal surface. The widely used

adsorbates include organic ligand molecules, inorganic ion ligands and functional quantum dots.

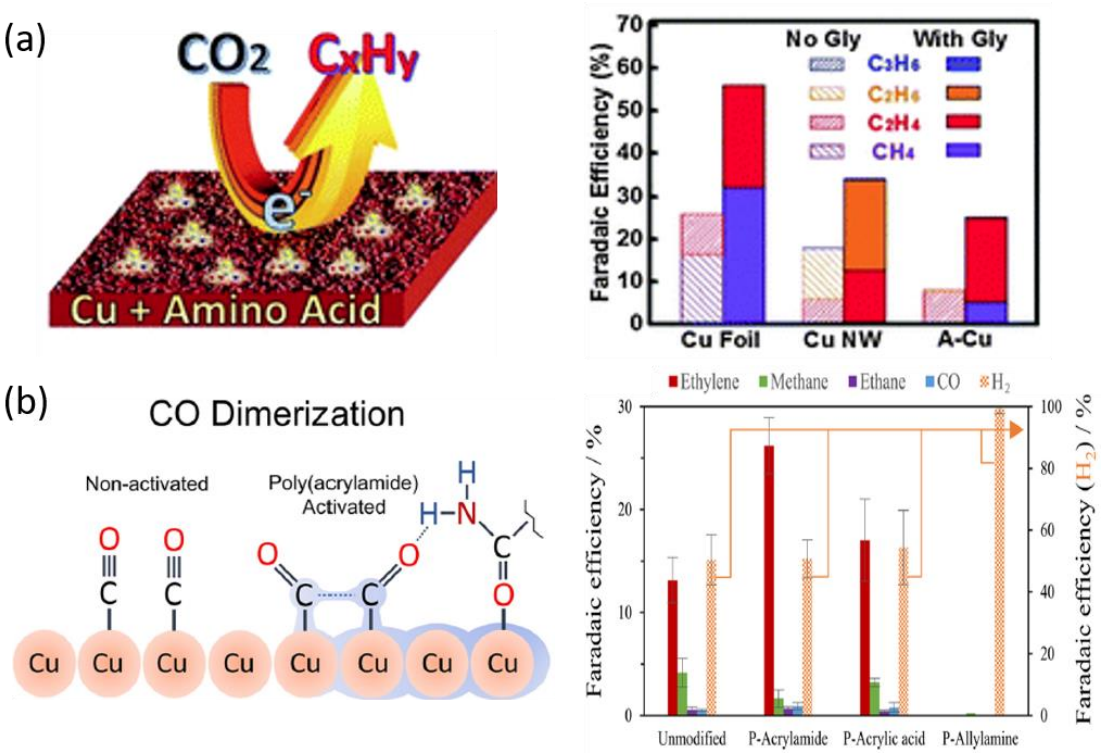

Figure 1.23 Catalyst models and corresponding hydrocarbon selectivity of amino acids (a) and poly(acrylamide) (b) functionalized Cu electrodes for CO_2 electroreduction. Adapted from references[241,242] with the permission of American Chemical Society.

In 2012, by DFT calculation, Nørskov et al.[243] proposed that effective CO_2ER catalysts must be capable of efficiently catalyzing the protonation of the adsorbed *CO to *CHO and simultaneously exhibit poor activity for the competitive H_2 evolution. The presence of certain ligands on the catalyst surface might help to stabilize the key adsorbed intermediates and facilitate the CO_2ER. This theory was evidenced by Wang et al.[241] through investigating the amino acid modified Cu electrodes (**Figure 1.23**a). They observed a remarkable enhancement in the FE and current densities of C_2 and C_3 hydrocarbon generation on the modified Cu electrodes regardless of the electrode morphology (Cu foil, roughened Cu, and Cu NWs). Their DFT calculations revealed that the key intermediate *CHO for hydrocarbon formation was stabilized by the hydrogen-bond like strong interaction with $-NH^{3+}$ of the adsorbed zwitterionic glycine. Recently, Andreoli et al.[242] modified the electrodeposited Cu foam with poly(acrylamide), which led to a significant enhancement in FE for ethylene production from 13% to 26% at -0.96 V vs. RHE (Figure 1.23b). Their DFT calculations

suggested that poly(acrylamide) on Cu surface acted as a multipoint binding catalytic system, where the interplay between activation and stabilization of intermediates resulted in an enhanced selectivity towards C_2H_4 formation.

Chang, Yang and coworkers[244] reported that N-heterocyclic carbene-functionalized Au NPs exhibited greatly improved selectivity, activity and kinetics for the CO_2 reduction to CO compared with the parent Au NPs (**Figure 1.24**a). They proposed that the carbene coordination may influence the Au surface through a combination of electronic and geometric effects. The strong σ-donation from the carbenes made the Au NP surface highly electron rich, affording a fast electron transfer to CO_2 molecules prior to the rate-determining step (Tafel slope, 72 mV dec^{-1}). From geometric aspects, the strong carbene-Au bond could destabilize Au-Au bonding with neighbouring atoms, which may lead to a restructuring of Au NP surface and thereby increasing the number of defect sites with better kinetics for CO_2ER. In another study, Chang et al.[245] functionalized Pd with tris-N-heterocyclic carbene ligands, enabling a 32-fold increase in activity for C_1 product formation with high selectivity (FE ~ 86%) compared with the parent Pd foil (FE ~23%); this study further revealed the contributions of chelate effect for tailoring and maintaining the reactivity at the molecular level. Flake et al.[246] used different thiol-tethered ligands to functionalize Au electrode, and found that a proton-induced desorption mechanism associated with the pKa of ligands was responsible for the selectivity changes over various ligand functionalized Au catalysts.

Similar molecular functionalization effect was also reported using amine modifiers. For example, Hwang et al.[247] found that the amine molecules on Ag NPs were highly effective in improving the selectivity for CO production by suppressing H_2 evolution. The role of amine modifiers was mainly attributed to the following two aspects: amine functionality is intrinsically effective in depresssing the H_2 evolution reaction,[247,248] and enhancing the competing CO_2ER; where the amine group may help to stabilize the key intermediates in CO_2 reduction by forming hydrogen bonds or electrostatic interactions,[144,242] and thus improve the reaction kinetics.

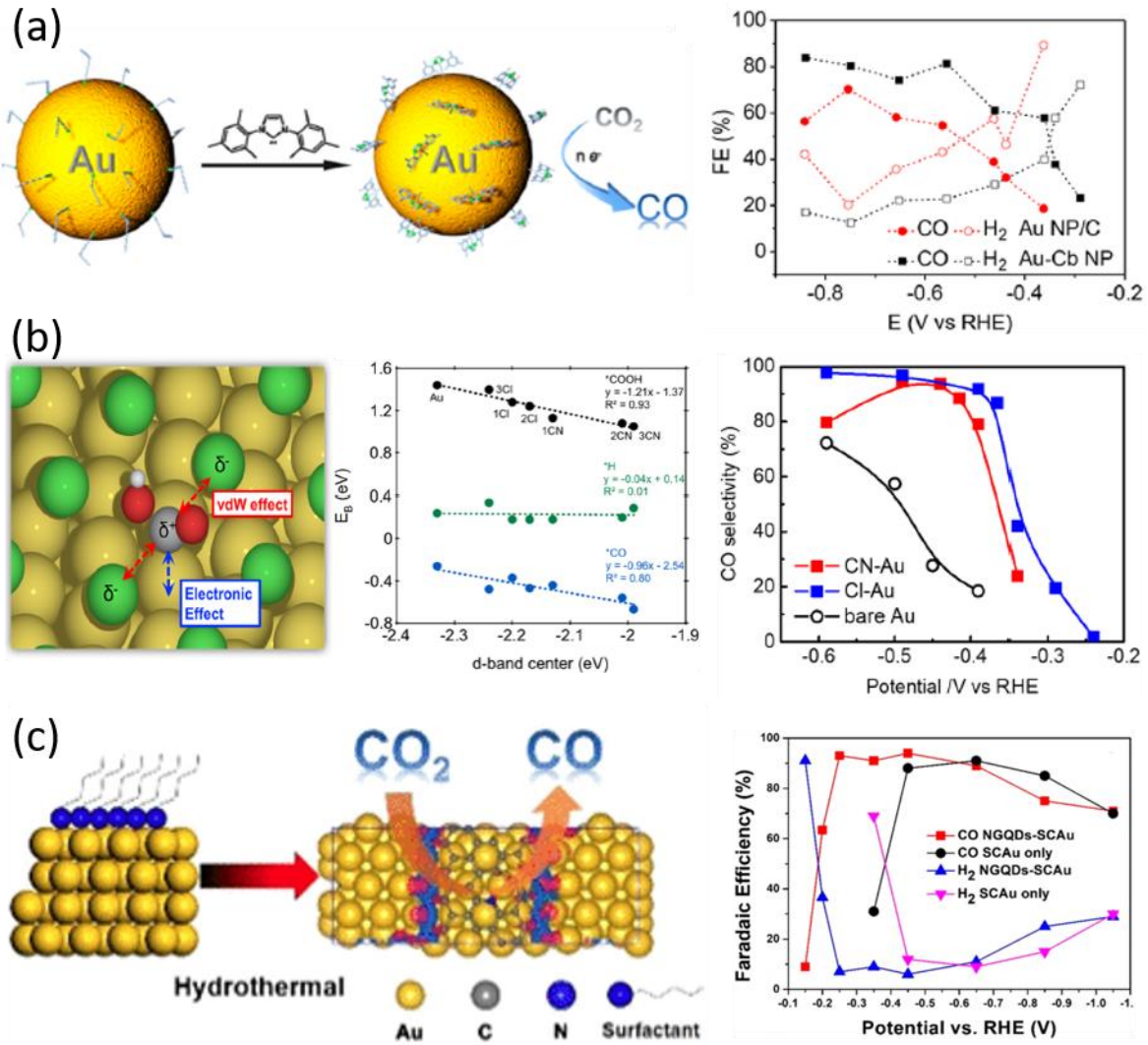

Figure 1.24 Three different surface modifications on Au electrodes for CO_2 to CO conversion and the corresponding potential-dependent FE_{CO} profiles. (a) N-heterocyclic carbene-functionalized Au; (b) Cl^- and CN^- ions modified Au electrodes; (c) N-doped graphene quantum dots modified Au NPs. Adapted from references[244,249,250] with the permission of the American Chemical Society.

Apart from molecular functionalization, the surface adsorbed ions or elements may also affect the activity and selectivity of CO_2ER. For example, Cho et al.[249] found that the CN and Cl anions functionalized Au electrodes could efficiently reduce CO_2 to CO at low overpotentials in comparison with pristine Au (Figure 1.24b). Their DFT calculation indicated that the adsorbed anions could stabilize the *COOH intermediates by physical interaction and electronic effect with an appropriate coverage of these anions, and thus enhance the kinetics of CO_2ER. A similar role of Cl^- was also reported for nanostructured Ag catalysts[74, 251]. Surface adsorbed sulfur were able to promote the CO_2-to-HCOOH

conversion on Sn-based catalysts.[221,252] Besides, the halide ions can enhance the reduction of CO_2 to CH_4 on Cu electrodes via a covalent Cu-halide interaction[253] and the increased negative charge on the surface[254]. On plasma-activated Cu catalysts, the halides could lower the overpotential and increase the CO_2ER rate without sacrificing their intrinsically high selectivity for C_2-C_3 products. This enhancement was mainly attributed to the specific adsorption of halides on the Cu surface during the reaction, which could facilitate the formation and stabilization of *COOH intermediates by charge donation from halide ions to CO_2.[254,255] Most recently, Sargent et al. reported the use of boron to tune the ratio of $Cu^{\delta+}$ to Cu^0 active sites and improve both stability (~40 hours) and C_2-product generation (79%). Simulations showed that the ability to tune the average oxidation state of copper enables the control of CO adsorption and dimerization, and makes it possible to implement a preference for the electrosynthesis of C2 products.

Recently, Zhu et al.[250] reported that modifying single-crystalline Au NPs with N-doped graphene quantum dots was also able to enhance the catalytic activity for the CO_2-to-CO conversion (Figure 1.24c). A FE_{CO} of 93% was achieved at a very low overpotential of 0.14 V, and the onset overpotential for CO production was only 0.04V. This excellent performance was attributed to the synergistic effect between Au NPs and N-doped graphene in enhancing the adsorption of *COOH over the pyridinic N sites. The modification of Au NPs with carbon dots-C_3N_4 demonstrated a similar promotion effect on CO formation.[256]

1.5 Thesis Objective

As presented, the atmospheric CO_2 concentration has reached an unprecedentedly high level, which is considered as the major cause for global warming and other environmental issues. Reducing CO_2 emissions and its atmospheric content has become more and more pressing for the sustainable development of human society. Electrochemical reduction of CO_2 to value-added chemicals or fuels using renewable electricity is very promising to curb anthropogenic CO_2 emissions and solves these environmental problems. However, converting CO_2 into carbon products is a sluggish reaction, and catalysts are required to activate and promote its completion. Heterogeneous metal electrocatalysts with outstanding intrinsic activity have great potential for practical application. Over recent decades, a large number of nanostructured metal catalysts have been developed, and a variety of parameters have been revealed in determining the electrocatalytic activity and selectivity. However, to date the performance of metal catalysts cannot meet the economic and technical

requirements for large scale applications. They still suffer from complicated fabrication procedures, poor metal utilization, poor selectivity, low energy efficiency and limited stability.

Rationally designing inexpensive, efficient and robust catalysts holds the key to realizing CO_2-to-targeted product conversion with high current density and selectivity at low overpotentials. Engineering the surface structure and/or the composition of electrocatalysts is a commonly adopted strategy to improve the electrocatalytic activity. However, this strategy usually suffers from complicated fabrication procedures and incompatible relationships between the structure and performance. For example, reducing the size of metal catalysts may enhance the current densities and material utilizations but with deteriorated product selectivity due to the increase of low-coordinated atoms. Controlling the facets, shapes and surface composition of nanostructured catalysts may improve product selectivity but requires complicated and costly state-of-the-art synthesis. Performing interfacial engineering of metal catalysts can simply manipulate their catalytic properties by utilizing interfacial interaction or external functionality, providing an effective strategy to overcome these challenges.

The primary goal of this thesis is to develop high-performance catalysts for CO_2 electroreduction via engineering the interface of nanostructured metals. To this end, three types of low-cost and efficient hybrid catalysts have been developed, which include Sn NPs decorated Cu NWs, N-doped carbon nanofiber supported Sn NPs, and amine modified ultrasmall Au NPs on rGO sheets. The fabrication methods applied are facile wet chemistry techniques that can be easily scaled up. Within this context, three kinds of metal-based interfacial effects including metal-metal interaction, metal-carbon interaction and metal-organic ligand have been investigated. A brief introduction of these works is described below.

In chapter 3, a one-dimensional nanowire catalyst, Sn NPs modified Cu NWs, is developed to improve electrocatalytic activity. This hybrid catalyst has been fabricated by use of a facile and scalable electrochemical anodization method in combination with electroless deposition techniques. The formed nanoscale Cu-Sn interfaces are revealed to be the major factor contributing to the significantly improved selectivity and activity for CO_2-to-CO conversion at moderate overpotentials. It can be attributed to the increased energy barrier for the competitive H* adsorption at the Cu-Sn interfaces. The electrocatalytic performance can be further tuned by the coverage of Sn species on Cu NWs surface and

introduction of a third metal component Au. However, the Cu nanowire supports suffer from a relatively low chemical and structural stability under CO_2ER conditions. To develop an efficient and robust catalyst, it is essential to search for a chemically stable and electrically conductive supporting material. Moreover, this kind of hybrid catalyst is directly formed on a Cu substrate and is not suitable for integration into gas-diffusion type electrolyzers that can generate high current densities aimed at practical applications.

To address these problems, in Chapter 4, Sn NPs are deliberately anchored on chemically stable and freely dispersed conductive carbon supports. A powder-like hybrid catalyst, one-dimensional Sn modified N-doped carbon nanofibers, is fabricated using a straightforward and simple electrospinning technique in combination with a pyrolysis method. It is found that the presence of pyridinic-N on the N-doped carbon nanofiber is able to promote the formate formation with higher selectivity at low overpotentials. The strong electronic interaction between Sn NPs and pyridinic-N-doped carbon is proposed as the major contributor. Interestingly, atomically dispersed Sn species remained after a simple acidic leaching treatment could drive the CO_2-to-CO conversion with high selectivity and current density. The pyridinic N is the key to stabilizing these Sn atoms on the carbon nanofibers for the promotion of CO_2ER performance. This further reveals the important role of metal-carbon substrate interaction in tuning the electrocatalytic properties of Sn catalysts.

To explore more interfacial strategies for developing high-performance and low-cost metal electrocatalysts, Chapter 5 transfers the interface engineering from metal-support interfaces to metal-organic ligand interfaces. A simple but effective molecular modification strategy is adopted to tune the surface properties and catalytic environment of metal active sites. A two-dimensional rGO sheet supported ultrasmall Au NPs catalyst is developed via a facile and surfactant-free chemistry technique. Five common primary amines with different structures are used to surface modify this catalyst in order to investigate the metal-organic ligand interaction on the CO_2ER performance. An amine-structure-dependent effect has been revealed: linear amines promote the CO_2-to-CO conversion whereas the branched polyamine greatly depresses it; the increasing alkyl chain length boosts the promotion effect of linear amines. The strong Au-amine interaction and molecular configuration induced amine coverage on the ultrasmall Au NPs are revealed to contribute to this effect. This work not only demonstrates an efficient Au catalyst with high atom utilization and mass specific catalytic activity, but also may shed light on the rational design of high-performance catalysts for CO_2 conversion by engineering the catalyst surface at a molecular level.

The studies in this thesis work have clearly demonstrated that the electrocatalytic performance of nanostructured metal catalysts can be tuned by engineering the metal-metal interfaces, metal-carbon interfaces and metal-organic ligands interfaces. These interfacial engineering strategies provide low-cost and facile alternatives to the conventional surface engineering strategies for improved CO_2ER catalysts. This thesis work may not only deepen the understanding of the interfacial process of CO_2ER, but also provide useful guidelines in the rational design of inexpensive and efficient electrocatalysts for targeted products from the CO_2 reduction.

Chapter 2 Experimental Methods

In this chapter, chemicals, materials, material characterization methods, and catalyst fabrication and CO_2ER analysis methods used in this doctoral work are summarized and briefly introduced.

2.1 Chemical Reagents and Materials

Chemicals and materials used in this work are listed below according to their applications. They were used as-received unless otherwise stated.

Table 2.1 Chemicals and materials used in this thesis.

Reagent name	Purity or Property	Supplier	Application
Tin(II) sulphate	95%	Sigma-Aldrich	Synthesis of Cu-Sn NWs and Cu-Au-Sn NWs (Chapter 3)
Sodium hydroxide	99%	Chem-Supply	
Sodium citrate dihydrate	99%	Sigma-Aldrich	
Monosodium phosphate	99%	Chem-Supply	
Gold(III) chloride trihydrate	99.9%	Sigma-Aldrich	
Potassium bicarbonate	99.95%	Sigma-Aldrich	
Copper foil	99.9%, 0.127 mm	Alfa Aesar	
N,N-Dimethylformamide	99.5%	Sigma-Aldrich	Sn/N-carbon nanofibers preparation (Chapter 4)
Tin(II) chloride dehydrate	98%	Sigma-Aldrich	
Polyacrylonitrile	Mw ~ 150000	Sigma-Aldrich	
Polymethylmethacrylate	Mw ~ 35000	Sigma-Aldrich	
Ethylenediamine	99.5%	Sigma-Aldrich	Synthesis and modification of rGO-Au NPs (Chapter 5)
Propylamine	99%	Sigma-Aldrich	
Hexylamine	99%	Sigma-Aldrich	
Oleylamine	90%	Sigma-Aldrich	
Polyethylenimine	Mw ~ 800	Sigma-Aldrich	
Graphite flakes	200 mesh	Sigma-Aldrich	
Hydrochloric acid	32%	Chem-Supply	

Potassium permanganate	97%	Sigma-Aldrich	(Chapter 5)
Hydrogen peroxide	30%	Chem-Supply	
Ammonia	28%	Chem-Supply	
Toluene	99.5%	Sigma-Aldrich	
Nafion® 117 solution	5 wt%	Sigma-Aldrich	Gas diffusion electrode preparation (Chapter 4 & 5)
Carbon paper (GDL 38AA)	225 ± 30 μm thick	SGL Carbon	
Carbon black	Vulcan XC72	Cabot Corp.	
PTFE aqueous dispersion	60 wt%	Sigma-Aldrich	

2.2 Material Characterizations

Material characterizations are involved in the whole process of CO_2 reduction to fully understand the catalysts and electrodes used. By combining the structural analyses and electrochemical analyses, the structure-property relationship of electrocatalysts may be revealed, facilitating the rational design of efficient catalysts for targeted products. In this section, those main techniques used are briefly discussed.

2.2.1 Structural Characterizations

The material structure was analysed by X-ray diffraction (XRD), scanning electron microscopy (SEM), transmission electron microscopy (TEM), scanning transmission electron microscopy (STEM) in conjunction with energy-dispersive X-ray spectroscopy (EDS), X-ray photoelectron spectroscopy (XPS), and Raman spectrometer, Fourier transform infrared spectroscopy (FTIR), thermal gravimetric analysis (TGA), and specific surface area (SSA) analysis.

2.2.1.1 SEM

Scanning electron microscopy (SEM) is a microscopy technique that produces images of a sample by scanning the surface with a focused beam of electrons.[257] The electrons interact with atoms in the sample, producing various signals that contain information about the sample's surface topography and composition. The most common SEM mode is detection of secondary electrons emitted by atoms excited by the electron beam. By scanning the sample and collecting the secondary electrons, an image displaying the topography of the surface is created.

In this work, all the samples were electrically conductive and directly anchored on an aluminium sample holder using carbon tape for SEM observation. All the SEM images were taken on a JEOL JSM7500 FA cold-field-gun scanning electron microscope under a working voltage of 5 or 10 kV and an emission current of 10 μA.

2.2.1.2 TEM, STEM and EDS

Transmission electron microscopy (TEM) is a microscopy technique in which a beam of electrons is transmitted through an ultrathin specimen (less than 100 nm thick) to form an image.[258] The image is magnified and focused onto an imaging device, such as a fluorescent screen and a charge-coupled device. A TEM can be modified into a scanning transmission electron microscope (STEM) by adding a system that rasters the beam across the sample to form the image and combining with suitable detectors such as an energy-dispersive X-ray spectroscopy (EDS) detector and a high-angle annular-dark-field (HAADF) detector.

In this study, the bright-field TEM images were taken on a 200 kV conventional LaB_6 TEM (JEOL JEM-2010) with a spatial resolution of 0.16 nm. The HAADF-STEM images and EDS mapping images were taken on a 200 kV probe corrected STEM (JEOL JEM-ARM200F) with the capability of imaging at atomic resolution. The sample was well dispersed in ethanol and loaded onto a lacy carbon film supported on a copper or gold grid.

2.2.1.3 XPS

X-ray photoelectron spectroscopy (XPS) is a surface-sensitive quantitative spectroscopic technique that measures the elemental composition, chemical state and electronic state of the elements within a material.[259] XPS spectra are obtained by irradiating a material with a beam of X-rays while simultaneously measuring the kinetic energy and number of electrons that escape from the top 0 to 10 nm of the material being analysed.

All the XPS spectra in this study were collected by an SES2002 analyser (Scienta) using Al Kα (1486.6 eV) radiation. Survey scans and regions scans were carried out with a pass energy of 200 eV and 20 eV, respectively. All of them were aligned by fitting a peak to the maximum for C1s spectra and setting this position to 284.5 eV. Samples were fixed on the sample holder using carbon conductive tape and analysed directly without any pre-treatment.

2.2.1.4 Raman

Raman spectroscopy is a spectroscopic technique used to observe vibrational, rotational, and other low-frequency modes in a material system.[260] It is commonly used to provide a structural fingerprint by which molecules can be identified. It relies on inelastic scattering or Raman scattering of monochromatic light. The laser light interacts with molecular vibrations, phonons or other excitations in the system, resulting in the energy of the laser photons being shifted up or down. The shift in energy gives information about the vibrational modes in the system.

In this study, Raman spectra were collected by use of a Jobin-Yvon Horiba 800 using a 632.8 nm laser. Samples were attached on a clean glass slide and analysed.

2.2.1.5 FTIR

Fourier transform infrared spectroscopy (FTIR) is a technique which is used to obtain an infrared spectrum of absorption or emission of a sample.[260] The absorption peaks represent a molecular 'fingerprint' and can be used to identify different chemical structures, which are particularly for identification of organic and polymer materials. In this work, the FTIR spectra were acquired using a Shimadzu FTIR Prestige-6821 (Shimadzu Scientific Instruments).

2.2.1.6 TGA

Thermo-gravimetric analysis (TGA) is a method of thermal analysis in which changes in the properties of materials (monitored as weight loss) are measured as a function of the increasing temperature (at a constant heating rate), or as a function of time (at constant temperature and/or constant mass loss).[261] The weight percentage of each component in composites may be evaluated by referencing known reactions. In this study, TGA was carried out in air using Q500 (TA Instruments) at a heating rate of 5 °C min^{-1}.

2.2.1.7 SSA Analysis

The specific surface area (SSA) can be analysed by applying the Brunauer-Emmett-Teller (BET) theory to the systems with multilayer adsorption. It usually utilizes probing gases, that do not chemically react with the material surfaces, as adsorbates to quantify surface area.[262] Nitrogen is the most commonly employed gaseous adsorbate.

The N_2 adsorption/desorption experiments in this work were conducted by BET measurements using a TriStar II 3020 surface area and porosity analyzer (Micromeritics).

2.2.2 Electrochemical Characterizations

The electrocatalytic performances were evaluated by linear sweep voltammetry (LSV), cyclic voltammetry (CV), constant potential amperometry (CPA), and electrochemical impedance spectroscopy (EIS).

2.2.2.1 LSV and CV

LSV and CV employ a linearly varying potential between the working electrode and a reference electrode, and the generated current response at the working electrode is recorded. In LSV measurements, the applied potential is ramped to the set potential, while the potential is ramped in the opposite direction to return to the initial potential after the set potential for CV experiments (**Figure 2.1**). Oxidation or reduction of species is registered as a peak in the current signals at the potential the species are oxidized or reduced. Heterogeneous CO_2ER is usually an irreversible reduction process, and thus LSV analysis is commonly used to evaluate its electrocatalytic performance. CV analysis is widely used in homogeneous CO_2ER to reveal the redox reactivity of molecular catalysts.

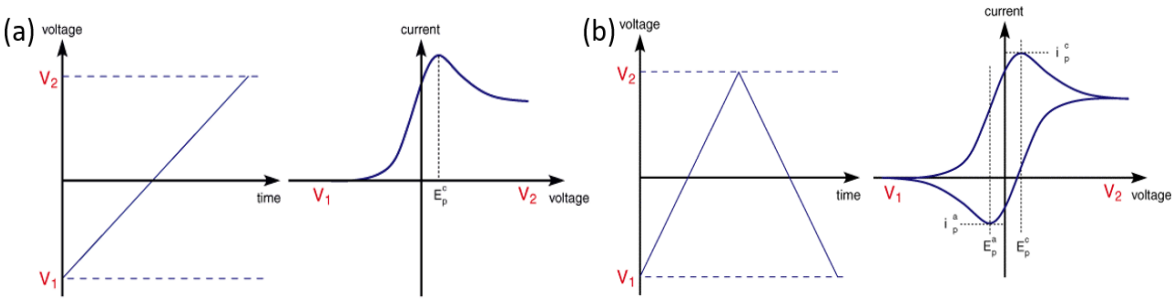

Figure 2.1 Applied potential profiles (left) and the corresponding voltammetry profiles (right) of LSV (a) and CV (b) techniques.

2.2.2.2 CPA

Constant-potential amperometry (CPA) is an electrochemical technique where the current response is measured whilst the potential difference between the working electrode and reference electrode is held at a constant value. In the CO_2ER, this technique is used for bulk electrolysis to investigate the products formed at the applied potentials.

2.2.2.3 EIS

Electrochemical impedance spectroscopy (EIS) is achieved by measuring the current responses through an electrochemical cell by applying an AC potential at different frequencies. The applied sinusoidal potential leads to a sinusoidal current response at the same frequency in shifted phase. Changes in the phase shift at different frequencies provide data associated with an electrochemical process within the electrochemical cells. It is a useful tool for the study of charge transfer and transport processes occurring at the interface between a heterogeneous catalyst and electrolyte.

In this work, EIS tests were conducted using a Bio-logic workstation (VSP model) in the frequency range of 100 kHz to 0.01 Hz with an AC amplitude of 10 mV at given potentials.

2.2.2.4 Experimental Measurements

In this work, all the electrochemical measurements except EIS were performed on a potentiostat (CH Instrument 650D) in a standard three-electrode configuration. The working electrodes (WE) are the copper foil or carbon paper supported catalysts. In Chapter 3, the catalysts were generated on the Cu foil and used as working electrodes directly. For the powder-like catalysts developed in Chapter 4 and 5, they were deposited on the carbon paper to form the working electrodes. A piece of platinum gauze (2 cm × 2 cm) and an Ag/AgCl (3 M NaCl, BASi) electrode served as counter electrode (CE) and reference electrode (RE), respectively. All the potentials were measured against the reference electrode and converted to the reversible hydrogen electrode (RHE) reference scale by the following equation: $E_{RHE} = E_{Ag/AgCl} + 0.21 + 0.0591 \times pH$. The pH value of CO_2-saturated 0.1 M $KHCO_3$ aqueous solution was 6.8. CV and LSV curves were recorded at a specific scan rate without iR compensation. CPA measurements were performed with automatic iR compensation (100%) on the potentiostat. The current density reported in this study was normalized to the geometric surface area.

2.3 CO_2 Reduction and Product Analysis

Product detection and analysis is the core of the CO_2 reduction research. During bulk electrolysis at various potentials, gas and liquid products may be produced. The gaseous products are usually detected and analyzed by gas chromatography (GC) technique, while the liquid products are commonly analyzed using nuclear magnetic resonance (NMR) technique.

2.3.1 Gas Product Detection and Analysis

In this study, an on-line gas analysis system was designed and established by integrating electrocatalysis with a GC (SRI 8610C 3#), gas purification, and flow rate control, as illustrated and shown in **Figure 2.2**. The H_2 carrier gas for the flame ionization detector (FID) is purified by a moisture trap and hydrocarbon trap; and the Ar carrier gas for the thermal conductivity detector (TCD) is purified by a moisture trap and oxygen trap. Gas purification is used to improve the sensitivity of these two detectors. A low-pressure needle valve and a mass flowmeter are used to control the flow-rate of Ar and CO_2, respectively. A bubble flowmeter is used to calibrate the gas flow-rates at the outlet of the GC sampling loop. This design can be used to give different CO_2 partial pressures by mixing with Ar. The moisture in the gas mixture vented to the GC is removed by a low-temperature chiller (AI C15 series recirculating chillers) to minimize its negative impact on the molecular sieve column.

This SRI GC was equipped with a packed MolSieve 5A column and a packed Haysep D column. Argon was used as the carrier gas. The FID with methanizer was used to quantify CO, CH_4, C_2H_4 and C_2H_6 concentration; and the TCD was used to quantify H_2 concentration. The TCD detector could detect H_2 with a concentration of ~100 ppm, while the FID detector could detect the hydrocarbons with a lowest concentration of ~1 ppm.

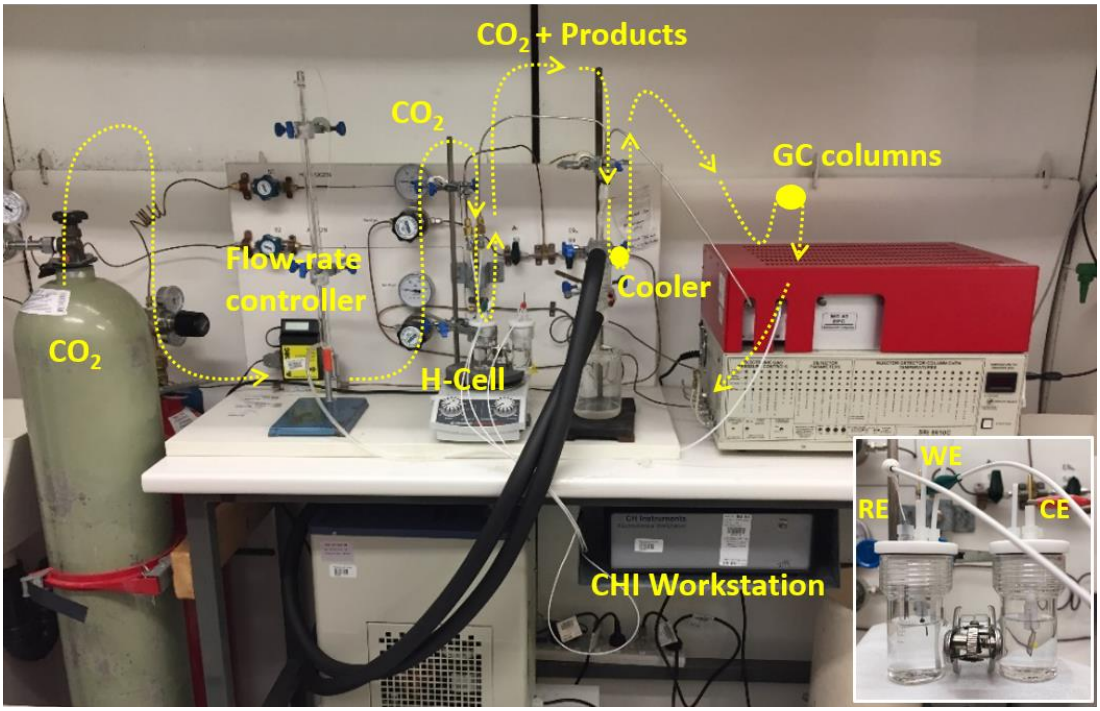

Figure 2.2 Digital image and the illustrated gas flow path of the on-line gas analysis system used for CO_2 reduction; inset is an enlarged image of the two-compartment H-cell.

A two-compartment gas-tight glass cell (inset of Figure 2.2) was used for CO_2 electrochemical reduction. The cathodic and anodic compartments were separated by a piece of Nafion membrane to prevent the product from CO_2ER being oxidized on the anode. Each compartment contained 30 mL of electrolyte. The volume of the headspace in every compartment was approximately 20 mL. Prior to CO_2 reduction, the electrolyte in the cathodic compartment was purged with CO_2 (99.99%, BOC) for 30 min. The electrolyte was stirred using a Teflon-coated magnetic stirring bar at 500 rpm to enhance the mass transport of CO_2 to the working electrodes. During the electrolysis, CO_2 was continuously bubbled into the cathodic compartment at a rate of 20.0 mL/min controlled by a mass flow controller (GFC17, Aalborg®) and vented directly into the gas-sampling loop (1 mL) of the GC. The flow-rate was calibrated with a manual soap-film flowmeter at the outlet of the GC. The GC run was initiated every 15 min. The average of three or four measurements was used in data analysis.

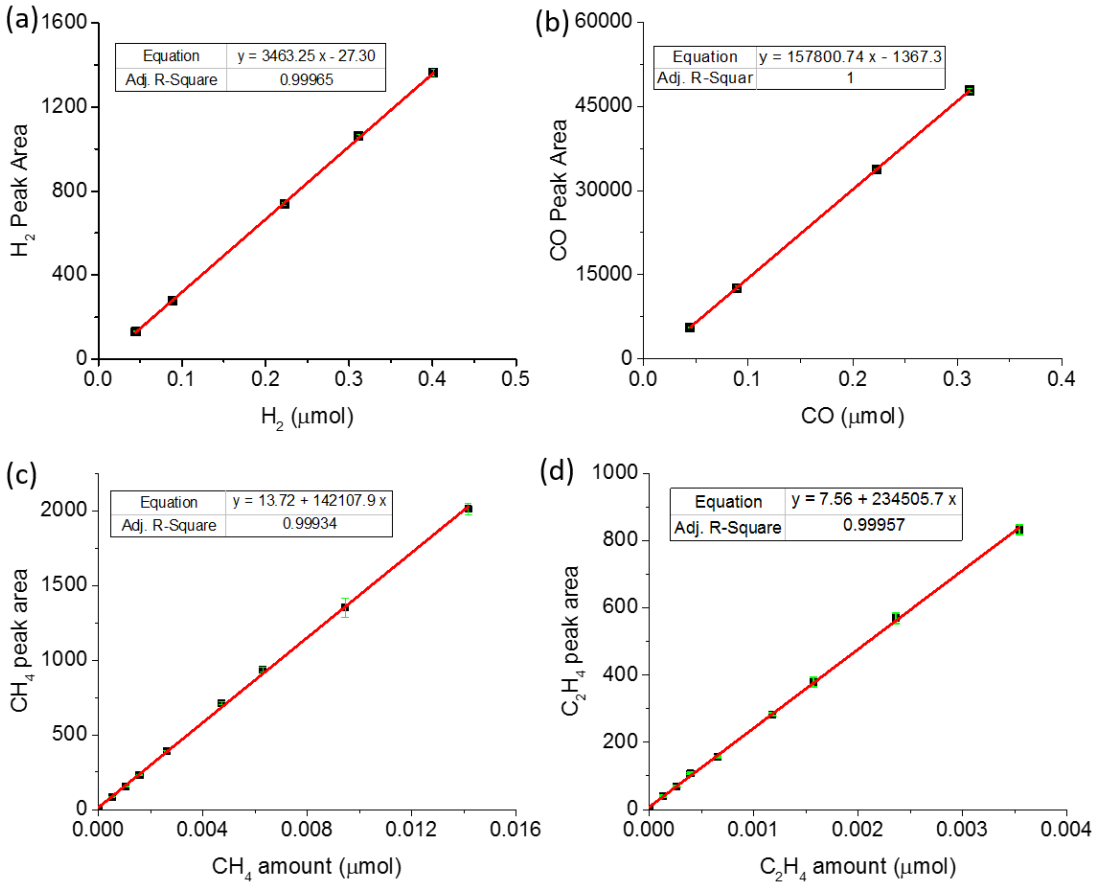

Figure 2.3 GC calibration curves for (a) H_2, (b) CO, (c) CH_4 and (d) C_2H_4.

External standard method was adopted with a standard gas mixture composed of H_2 (10%), CO (10%), CH_4 (4%), C_2H_4 (1%), C_2H_6 (1%) and CO_2 (74%) to quantify every gaseous

component. A gas-tight syringe (SGC, 50 µL range) was used to sample different volumes (V) of the standard gas for injection analyses on the GC. The molar amount of each component injected (n = V/22.411) was plotted relative to the corresponding peak area, generating their calibration curves. **Figure 2.3** shows the typical calibration curves of H_2, CO, CH_4 and C_2H_4. It should be noted that the calibration curves need to be re-plotted at least every two months.

For on-line automatic valve sampling, the injected volume (V_0, mL) of mixed gas is a constant, 1 mL. The molar amount of each component (n_A) can be derived according to the fitted calibration curves. The Faradaic efficiency (FE_A) of gas products can be calculated according to the following equations:

$$FE_A = \frac{n_A \times z_A \times F}{Q} \quad (1)$$

$$Q = I \times t = I \times \frac{V_0}{\vartheta} \quad (2)$$

where z_A is the number of electrons transferred to form one A molecule, F refers to Faraday's constant (96485 C mol^{-1}), υ is the flow-rate (mL min^{-1}) obtained at the outlet of GC sampling-loop, and I is the current (mA) at the time when valve-sampling starts.

2.3.2 Liquid Product Detection and Analysis

Liquid products (formate and ethanol in this work) were analysed on a 400 MHz NMR spectrometer (Bruker Avance) at 30 ℃. 0.5 mL of product-containing electrolyte was syringed out from the cathodic compartment at the designated time. It was mixed with 100 µL internal standard (1-Propanesulfonic acid 3-(trimethylsilyl) sodium salt, DSS, 99.7%, Sigma-Aldrich) and 100 µL D_2O (99.9 %, Cambridge Isotope Lab), and then transferred to a NMR sample tube. The 1D ^1H spectra were measured with water suppression by a pre-saturation method.

The calibration curves of formate and ethanol were prepared by using sodium formate (99.999%, Sigma-Aldrich) and ethanol (99.5%, Sigma-Aldrich) together with the internal standard and D_2O. Relative area rather than absolute area was used. The relative areas of formate (singlet peak area at 8.44 ppm) and ethanol (triplet peak area at 1.17 ppm) with respect to DSS (peak area at 0.00 ppm) were plotted against the corresponding

concentrations to obtain their calibration curves as shown in **Figure 2.4**. The amount of produced formate and ethanol (n_B) was thus calculated based on their calibration curves and the known volume of electrolyte. It should also be noted that the calibration curves need to be re-plotted at least every two months. The Faradaic efficiency (FE_B) of liquid products can be obtained according to the following equations:

$$FE_B = \frac{n_B \times z_B \times F}{Q_{total}} \quad (3)$$

$$Q_{total} = \int I(t)\, dt \quad (4)$$

where z_B is the number of electrons transferred to form one formate or ethanol molecule, F refers to Faraday's constant (96485 C mol^{-1}), and Q_{total} (C) is obtained by integrating the corresponding i-t curve.

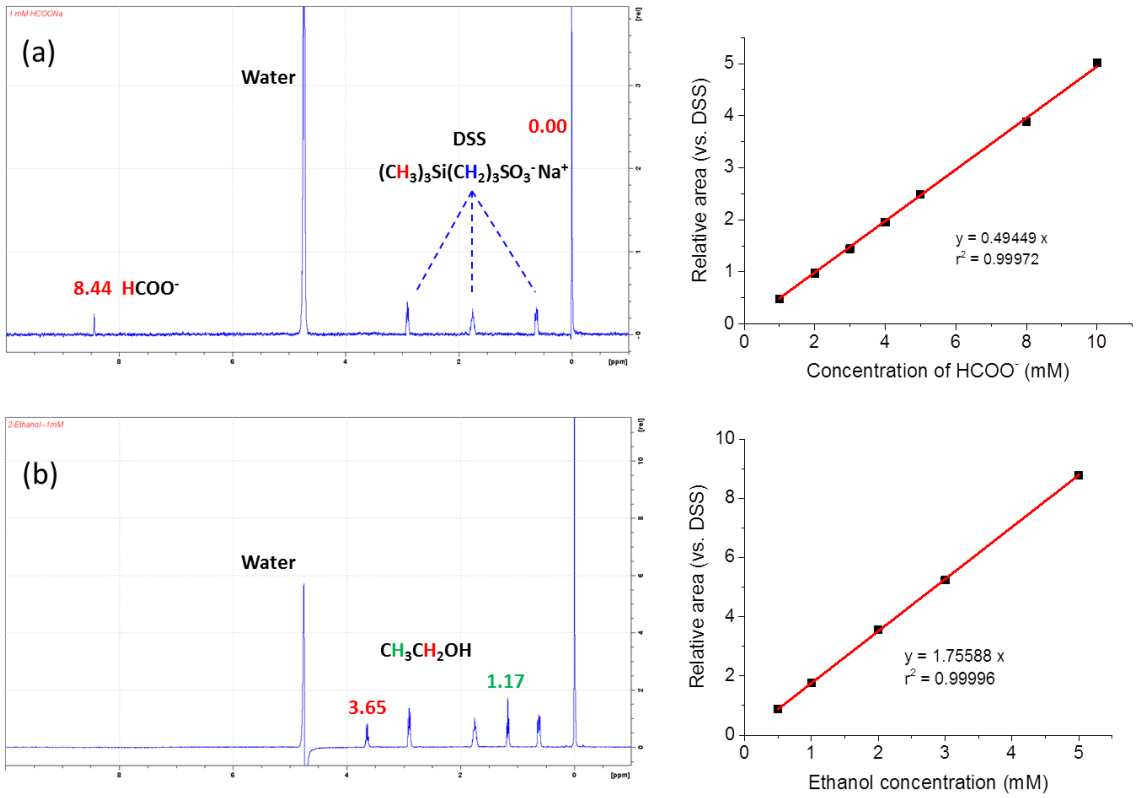

Figure 2.4 (a) ^{1}H-NMR spectrum for formate (1 mM) and the linear relationship between the formate concentration and relative area vs. DSS; (b) ^{1}H-NMR spectrum for ethanol (1 mM) and the linear relationship between the ethanol concentration and relative area vs. DSS.

Chapter 3 Engineering Cu-Sn Interfaces on Copper Oxide Nanowire for Enhanced CO_2 Electroreduction to CO

This chapter is adapted from the article, "Tin Nanoparticles Decorated Copper Oxide Nanowires for Selective Electrochemical Reduction of Aqueous CO_2 to CO", by Yong Zhao, Caiyun Wang and Gordon G. Wallace, which was published in J. Mater. Chem. A (2016, 4, 10710-10718), with permission from the Royal Society of Chemistry.

3.1 Introduction

Electrochemical reduction of CO_2 to CO is a process of fundamental significance.[158,263,264] CO is an industrial gas that has many applications in bulk chemicals productions such as the synthesis of methanol, urea, salicylic and polycarbonates.[265,266] Moreover, this reduction process is accompanied by a hydrogen evolution reaction (HER). The gas product mixture of H_2 and CO is also known as syngas, a critical feedstock for the Fischer-Tropsch process to produce synthetic fuels such as liquid hydrocarbons.[267-269] Thus, it is highly desirable to develop electrocatalysts capable of efficiently converting CO_2 to CO.

Some nanostructured noble metals such as Au, Ag and Pd have been demonstrated to promote the CO_2-to-CO process with high FEs above 80% and high current densities at modest overpotentials. They are among the most efficient electrocatalysts for CO formation. However, their high cost and low abundance in nature limit large-scale application. Some earth-abundant and inexpensive metals such as Zn and Cu are promising alternatives.[30,270] Dendrite-like Zn[83], reduced nanoporous ZnO[84] and nanoscale Zn[85] have been developed for aqueous CO_2 electroreduction. However, they need large overpotentials (> 900 mV) to achieve high FEs (> 80%). Oxide-derived Cu catalysts can drive this process at low overpotentials (< 500 mV), but suffer from low FEs (< 60%) and low current densities (< 1 mA cm^{-2}).[33,87]

Experimental[104,271-273] and theoretical[108,109,274] studies have revealed that alloying Cu with other metals is an effective way to improve the CO_2-to-CO conversion. By alloying, the binding strength of the *CO intermediate can be tuned to enhance the reaction kinetics, and thus enhance the CO production.[104] For example, Akihiro et al.[272] demonstrated that electroplated Cu-Sn alloy could deliver a CO faradaic efficiency of 67% and a CO partial current density of 0.6 mA cm^{-2} at an applied potential of ~ -0.87 V vs. RHE. Takanabe et

al.[273] developed a Cu-In alloy catalyst by electrodepositing expensive In on reduced oxide-derived Cu surface, which selectively converted CO_2 to CO with a FE of 95% at -0.7 V vs RHE. Recently, they reported a similar Cu-Sn alloy catalyst by electrodepositing Sn on the Cu surface, demonstrating high FE_{CO} values > 90% in a broad potential range from - 0.5 V to - 0.8 V vs. RHE.[115] Their DFT calculations suggested that the presence of In or Sn greatly affected the adsorption ability of neighbouring Cu to intermediates. The H adsorption became unfavourable while the CO adsorption energy was nearly unchanged, leading to higher selectivity towards CO.

However, most of the Cu-based alloys studies only focus on the effect of composition (ratio of two metals) at atom scale. Few studies focus on the effect of nanoscaled metal-metal interfaces. The lack of knowledge on this aspect has prevented the full understanding of the structural effects on CO_2ER. Moreover, the alloys usually contain large amounts of bulk components without access to electrolyte, greatly reducing the materials utilization efficiency. The alloying process is also time- and energy-consuming, requiring either state-of-the-art synthesis methods[104,275] or large amounts of energy (i.e., thermal energy[276] and electricity[272,273]) to form desirable atomic arrangements. Constructing Cu-metal nanoscale interfaces via a simple surface modification method can not only overcome the above limitations in the alloying process and reduce the cost of catalyst fabrication, but also may provide an excellent platform to study the effect of nanoscale metal interfaces on CO_2ER.

This chapter is focused on this topic and the adoption of a simple strategy to construct nanoscale Cu-Sn interfaces to explore the influence of Cu-Sn nanoscale interfaces on CO_2ER. A Sn NPs-decorated copper oxide nanowire (Cu_xO-Sn) catalyst has been developed. The Cu_xO NWs are anchored on Cu foil and modified by inexpensive Sn NPs via a facile, scalable and low-cost electroless deposition method. After a five-second deposition of Sn NPs, the resulting hybrid NWs demonstrated a significantly improved FE_{CO} from 6% to 82%, and a CO partial current density increase from 0.3 to 4.5 mA cm^{-2} at an overpotential of 690 mV. Its selectivity and activity towards CO formation were easily tuned by the Sn deposition time.

3.2 Experimental

3.2.1 Catalyst Preparation

Synthesis of Cu_xO NWs: $Cu(OH)_2$ NWs were firstly synthesized on Cu foils by an electrochemical anodization method in an alkaline solution. The Cu foil (1 cm × 1 cm) with a rectangular tip (0.3 cm × 0.5 cm) cut by a laser engraver was polished to a mirror-like finish using sand paper (Grit 1200), while the back side was fully covered with commercial tape (3M Company). After being cleaned with DI water and dried by N_2, the Cu foil was immediately immersed into a 1 M NaOH solution for the anodization at a current density of 2 mA cm^{-2} for 10 min with an Ag/AgCl (3 M KCl) reference electrode and a platinum gauze (2 cm × 2 cm) counter electrode. The resultant Cu foil with a cyan layer of $Cu(OH)_2$ NWs was rinsed with copious amounts of DI water and dried by N_2, followed by peeling off the tape. The $Cu(OH)_2$ NWs were dehydrated by annealing them at 200℃ for 2 h in an air atmosphere. The brown dehydrated $Cu(OH)_2$ NWs were electrochemically reduced to dark-red Cu_xO NWs in a 0.1 M $KHCO_3$ solution at a constant potential of -1.4 V vs Ag/AgCl for 10 min. The related electrochemical anodization and reduction curves are shown in **Figure 3.1**. The Cu foil was anodized at an almost constant rate within 10 min, while the reduction of Cu_xO NWs was completed within 2 min.

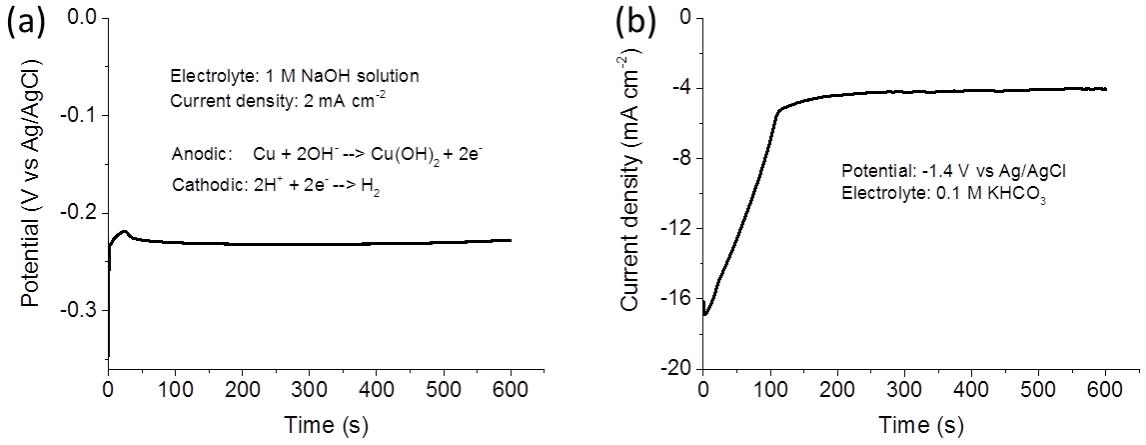

Figure 3.1 Chronopotentiometry curves for anodizing Cu foil at a current density of 2 mA cm^{-2} in 1 M NaOH (a) and reducing CuO NWs for 10 min at -1.4 V in 0.1 M $KHCO_3$ under Ar atmosphere (b).

Synthesis of Cu_xO-Sn NWs: Cu_xO NWs on Cu foil with the back side covered with epoxy was immersed into a Sn electroless plating bath[43] to deposit Sn NPs at 80℃. The plating bath was composed of 0.3 M $SnSO_4$, 2.8 M NaOH, 0.9 M NaH_2PO_4 and 0.6 M sodium citrate. After the deposition, it was rinsed thoroughly with ethanol and DI water to remove any residue and dried by N_2. An elapsed time of 5 s, 10 s, 20 s, 40 s, 60 s or 80 s was applied.

The corresponding samples are referred as Cu_xO-Sn5, Cu_xO-Sn10, Cu_xO-Sn20, Cu_xO-Sn40, Cu_xO-Sn60 or Cu_xO-Sn80.

Synthesis of Cu_xO-Au-Sn NWs: Gold was coated on the surfaces of Cu_xO NWs by the simple displacement reaction between Cu metal and $AuCl_4^-$ ions. The freshly-prepared dark red Cu_xO NWs were immersed into a 0.5 mM $HAuCl_4$ aqueous solution for 20 s. No obvious colour change was observed after this reaction. The as-obtained samples, referred to as Cu_xO-Au20, were rinsed with copious amounts of DI water and dried by N_2. Tin NPs were finally deposited onto these Cu_xO-Au20 NWs following the same method as that on Cu_xO NWs.

3.2.2 Electrochemical Measurements and Product Analysis

All the electrochemical measurements, and product analysis of bulk electrolysis experiments were performed according to the methods and procedures presented in Chapter 2.

3.3 Results and Discussion

3.3.1 Structural Characterizations

The Cu_xO-Sn hybrid NWs were fabricated on the Cu foil using a facile and scalable method, as illustrated in **Figure 3.2**a. Briefly, $Cu(OH)_2$ NWs were synthesized on Cu foil via electrochemical anodization. They were transformed into Cu_xO NWs via a dehydration process and a subsequent electrochemical reduction process. The electroless deposition of Sn NPs on Cu_xO NWs resulted in the final product, Cu_xO-Sn hybrid nanowires. Figure 3.2b shows four representative X-ray diffraction (XRD) patterns of the materials used or formed during this fabrication process. They can be assigned to the standard substances, Cu (JCPDS 04-0836), $Cu(OH)_2$ (JCPDS 13-0420), Cu_2O (JCPDS 65-3288) and CuO (JCPDS 48-1548). It is clear that a mixture of Cu_2O and CuO, denoted as Cu_xO, was formed after the dehydration of $Cu(OH)_2$ and the subsequent reduction. The colour of the material changed concomitantly from cyan to brown and finally to dark-red (Figure 3.2c). After the tin deposition, a sharp peak appeared at 51.9º corresponding to the (211) plane of SnO_2 (JCPDS 41-1445), indicating the successful deposition of tin on the Cu_xO nanowires.

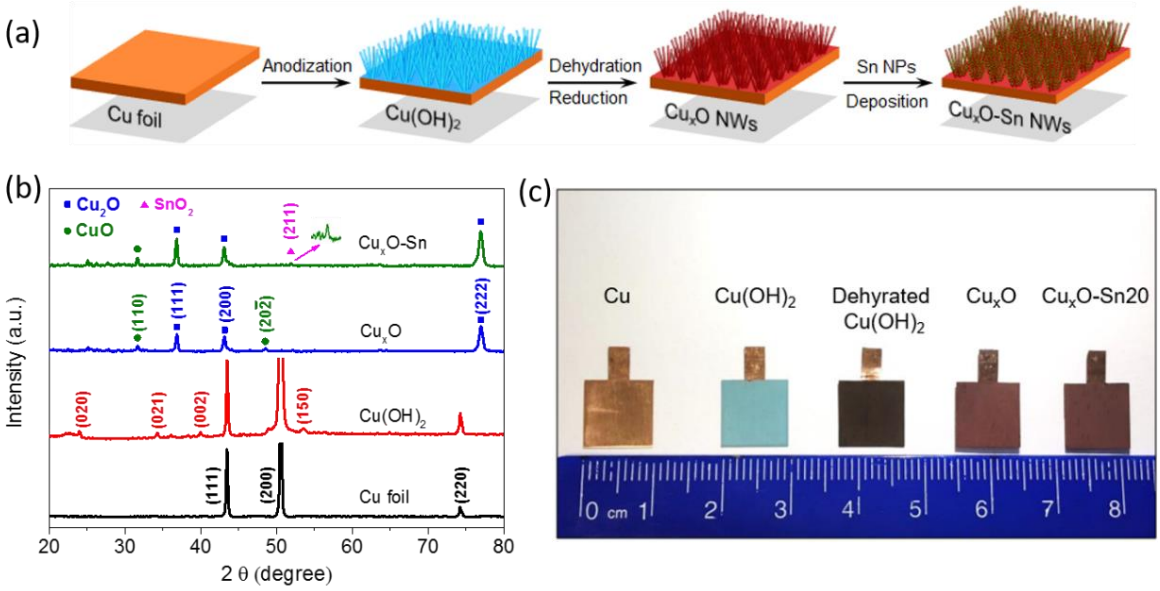

Figure 3.2 (a) Illustration of the fabrication process of Cu_xO-Sn NWs; (b) XRD patterns of Cu foil, $Cu(OH)_2$, Cu_xO and Cu_xO-Sn20; (c) Digital images of these samples.

The corresponding morphology changes were investigated by scanning electron microscopy (SEM) as shown in **Figure 3.3**a-c. After dehydration by annealing at 200 ℃ in air, the thin nanowires tend to aggregate, forming nanowire bundles. After the electrochemical reduction in 0.1 M $KHCO_3$ solution for 10 min, Cu_xO NWs were formed with nanowire buddles being bent and a rough surface. The Cu_xO-Sn20 (Sn deposition for 20 s) exhibited a three-dimensional open porous structure composed of nanowires. These hybrid nanowires typically have a diameter of 50~100 nm with a length of several microns. They have a slightly rough surface. With the increased deposition time, this architecture remained unchanged, but the surface of nanowires became rougher (Figure 3.3d-f).

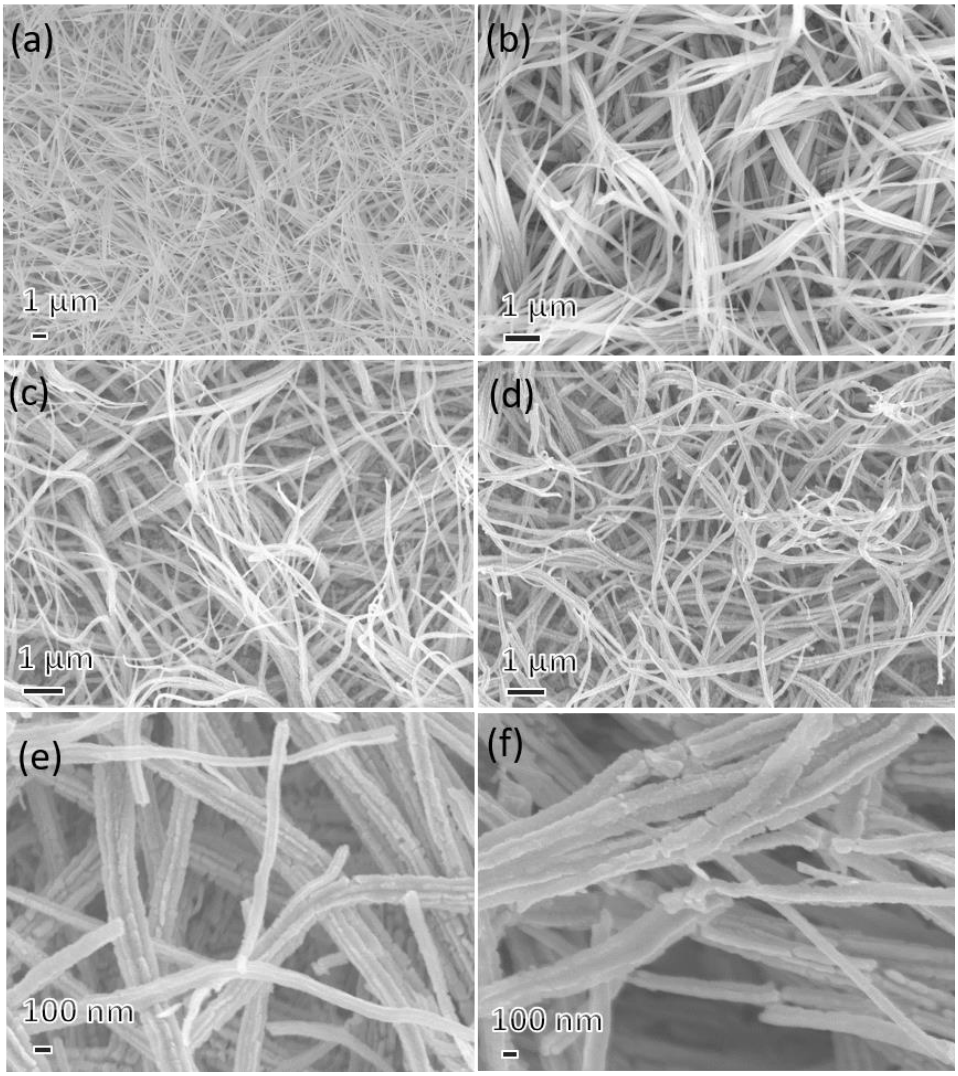

Figure 3.3 SEM images of (a) $Cu(OH)_2$, (b) dehydrated $Cu(OH)_2$, (c) Cu_xO, (d) Cu_xO-Sn20, (e) Cu_xO-Sn40 and (f) Cu_xO-Sn60 NWs.

The morphology and structure of these hybrid nanowires were further investigated by transmission electron microscopy (TEM). **Figure 3.4**a shows a typical high-angle annular dark-field scanning transmission electron microscopy (HAADF-STEM) image of Cu_xO-Sn20 hybrid NWs. These NWs had rough surface, and their diameters range from 50 nm to 100 nm, consistent with SEM observations. In addition, pores or gaps were observed in the bulk or at the edges of these NWs. This may arise from the collapse of the $Cu(OH)_2$ crystals during dehydration. Figure 3.4b shows a typical bright-field TEM image of these hybrid NWs with tin or tin oxide NPs (small black dots, ~ 20 nm) deposited on the surface. In the high-resolution TEM image (Figure 3.4c), two different sets of lattice spacing, 0.175 nm and 0.211 nm, were observed and they can be assigned to the (211) and (210) planes of SnO_2 (JCPDS 41-1445).

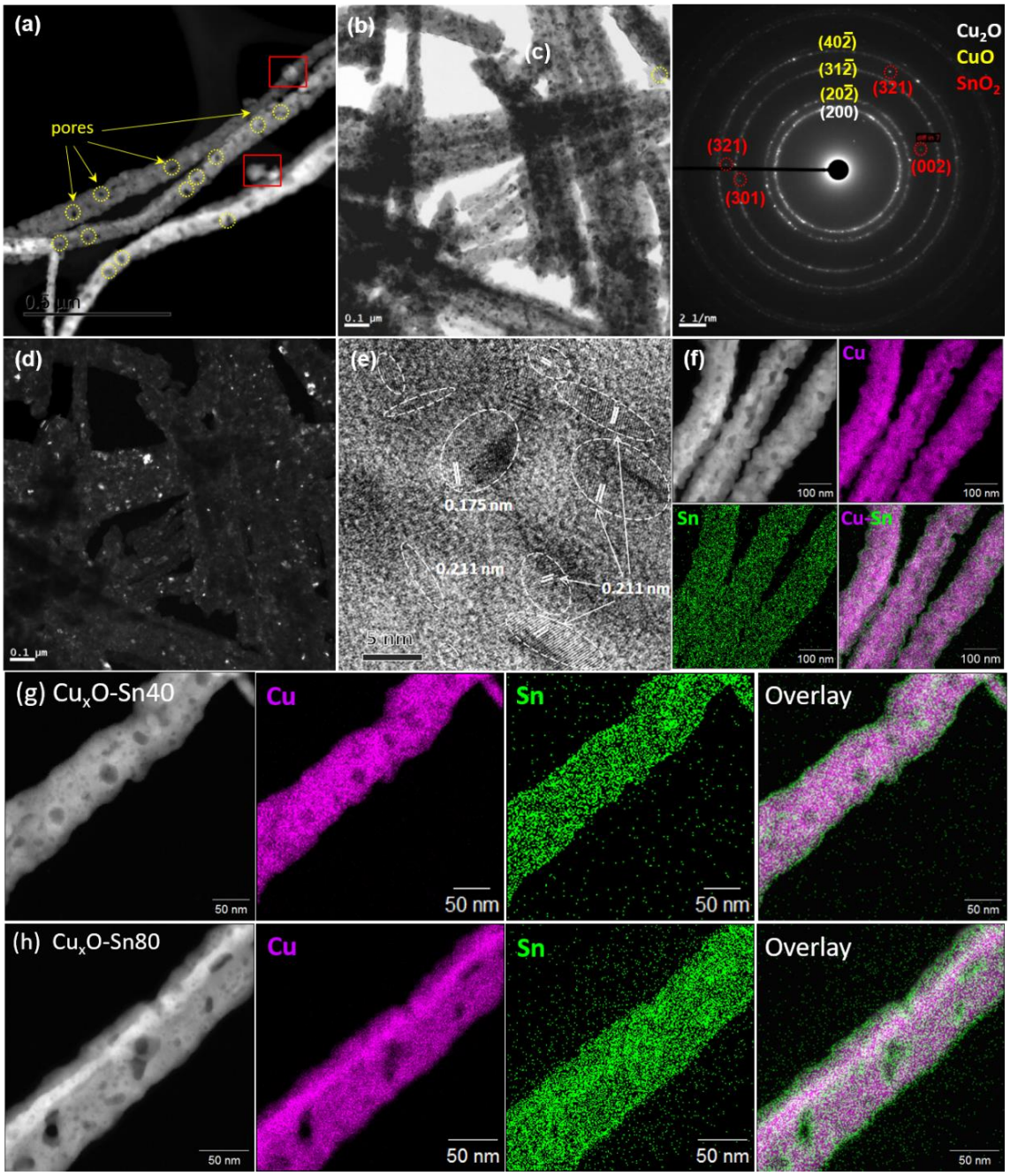

Figure 3.4 (a) HAADF-STEM and (b) bright-field TEM image of Cu_xO-Sn20 NWs; (c) HRTEM image of the hybrid NWs; (d) SAED pattern of the hybrid NWs in figure (b); (e) Dark-field image from the bright spot pinpointed by the red arrow in (d); STEM elemental mapping results of Cu_xO-Sn20 (f), Cu_xO-Sn40 (g) and Cu_xO-Sn80 (h) hybrid NWs.

In addition to those relatively big SnO_2 NPs (~ 20 nm, Figure 3.4b), the Cu_xO NWs were also decorated with irregular small SnO_2 nanocrystals with a size of less than 10 nm. The presence of tin species can be verified by the selected area electron diffraction (SAED) analysis as well. In the SAED pattern (Figure 3.4d), the obvious diffraction rings were

derived from Cu_2O and CuO, indicating the polycrystalline structure of Cu_xO NWs. Those four selected bright spots were indexed to the various planes of standard SnO_2. They are consistent with the XRD and HRTEM analyses. The dark-field image in Figure 3.4e derived from the selected diffraction spot provides further evidence for the presence and particular shape of SnO_2 on the nanowires. In addition, the element mapping results of Cu_xO-Sn20 (Figure 3.4f) clearly reveal the uniform and conformal deposition of Sn on the surface of Cu NWs. The mapping results of Cu_xO-Sn40 and Cu_xO-Sn80 are provided in Figure 3.4g-h. Clearly the coverage of Sn on the surface of Cu_xO NWs increased with the prolonged deposition time. Although some Sn aggregates were formed on some nanowire bundles as shown in the SEM images of Figure 3.3d-e, the coverage of Sn NPs was still uniform.

3.3.2 Surface Chemical State Analysis

To confirm the surface chemical states of Cu_xO-Sn hybrid nanowires, X-ray photoelectron spectroscopy (XPS) analysis was performed. **Figure 3.5**a shows the XPS spectra for Cu_xO and Cu_xO-Sn, evidencing the presence of Sn species on the hybrid NWs. Figure 3.5b shows the high-resolution Cu 2p spectra of three different Cu_xO samples. They all exhibited two main peaks at or near the binding energies of 932.6 eV and 952.4 eV that can be assigned to the $Cu2p_{3/2}$ and $Cu2p_{1/2}$ peaks of $Cu^{0/1+}$, respectively.[33,87] The surface layer (< 10 nm) of the dehydrated $Cu(OH)_2$ NWs was mainly dominated by CuO, as evidenced by the presence of the characteristic Cu^{2+} satellite peaks and the shift of $Cu2p_{3/2}$ peak towards higher binding energy[87]. After the reduction, only the peaks of $Cu^{0/1+}$ were detected. Taking the XRD and SAED results into consideration, it can be concluded that only the surface of dehydrated $Cu(OH)_2$ NWs were reduced to Cu_2O and/or Cu, while CuO still persisted within the core of the NWs. In addition, the Cu2p peaks were nearly unchanged after Sn deposition, manifesting that the presence of Sn species does not significantly affect the electronic structure of Cu. Figure 3.5c shows the detailed $Sn3d_{5/2}$ XPS spectrum of the Cu_xO-Sn20 hybrid nanowires. It consists of two peaks at the binding energies of 486.5 eV and 484.8 eV corresponding to Sn^{4+} and Sn^0, respectively.[44] The Sn^{4+} can be ascribed to SnO_2 formed by the spontaneous oxidation of Sn NPs in air.

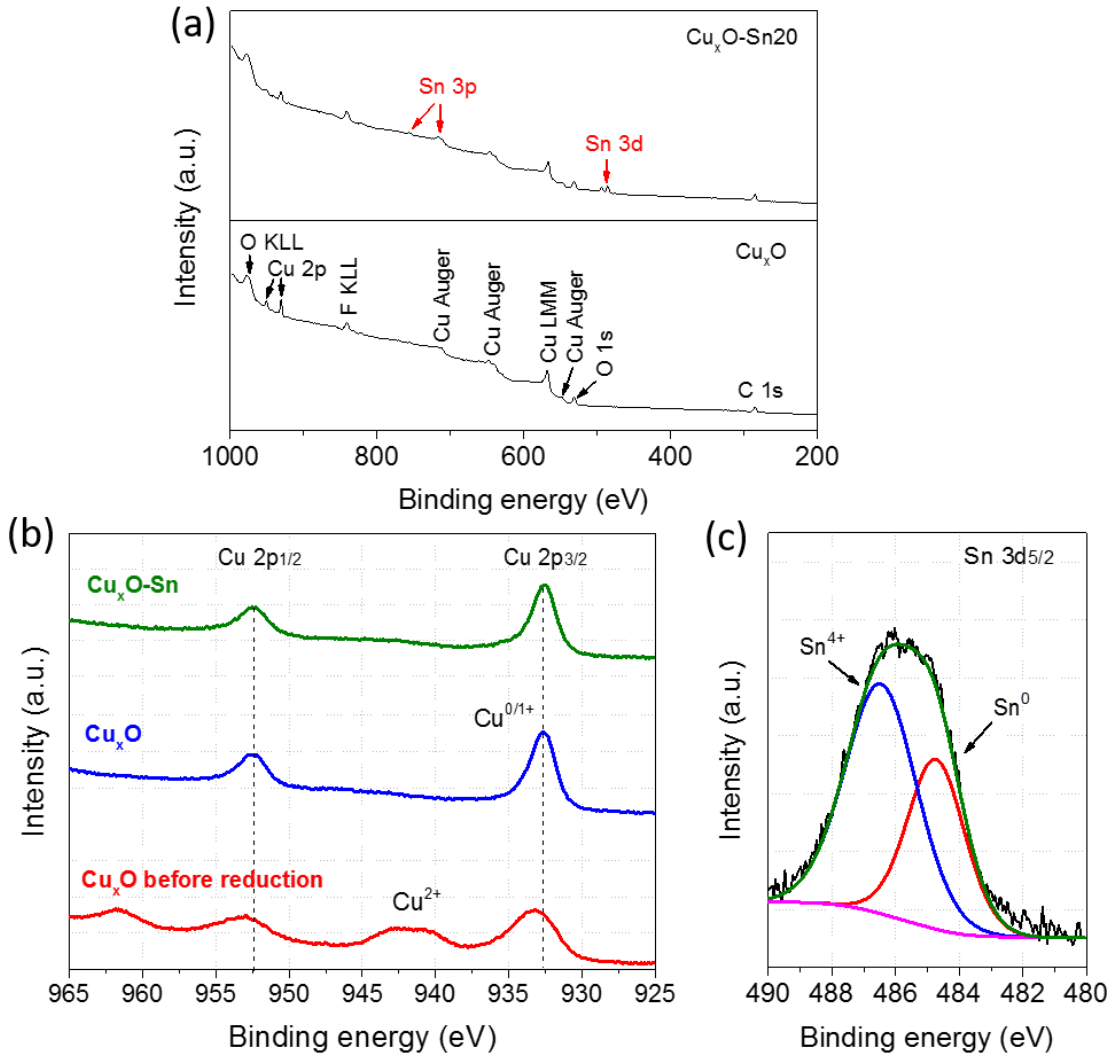

Figure 3.5 (a) XPS survey spectra of Cu_xO NWs and Cu_xO-Sn20 hybrid NWs, (b) Cu 2p XPS spectra of Cu_xO-Sn20, Cu_xO and dehydrated $Cu(OH)_2$; (c) High resolution Sn 3d XPS spectra and the fitting results.

3.3.3 Electrochemical Analysis

Electrochemical reduction of CO_2 using the Cu_xO-Sn20 NW electrode was evaluated first. Prior to CO_2 reduction, the surface oxides were electrochemically reduced by holding the electrodes at -1.4 V (vs. Ag/AgCl) for 30 min in Ar-purged electrolyte (**Figure 3.6**). For the Cu NWs, the oxide peak was totally removed after the pre-reduction. For the Cu-Sn20 NWs, the oxide peak still persisted after the pre-reduction, and became gradually decreased with further increases in cathodic scanning times. It indicates that copper oxide and tin oxide might still persist beneath the catalyst surface. However, the residual oxides presumably do

not contribute to CO_2 reduction due to the limited access afforded to the electrolyte.[46] To simplify, Cu_xO-Sn nanowire catalysts are cited as Cu-Sn NWs in the following discussion.

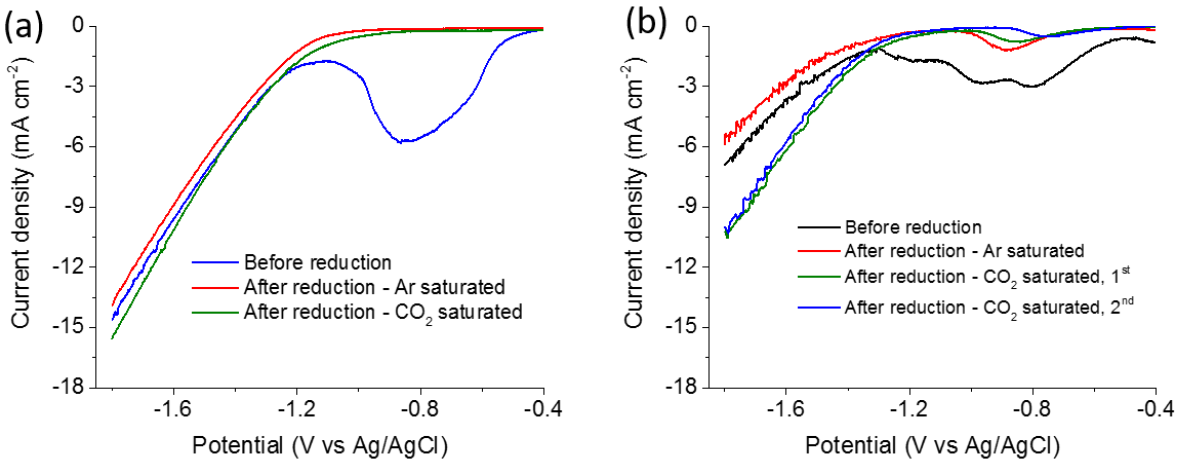

Figure 3.6 LSV curves of Cu NWs (a) and Cu-Sn20 NWs (b) before and after pre-reduction at -1.4 V vs. Ag/AgCl in Ar-saturated 0.1 M $KHCO_3$ solution.

Figure 3.7a-b shows the iR-corrected controlled-potential electrolysis curves on Cu NWs and Cu-Sn20 NWs. Both the catalysts exhibited almost stable current densities during the electrolysis at the potentials positive to -1.0 V vs. RHE. An obvious current increase was detected with electrolysis time at the potentials more negative than -1.0 V, which may be caused by the enhanced electron transfer due to the gradual reduction of Cu_xO at the core of nanowires under such high overpotentials. Figure 3.7c shows the potential dependent average total current densities (j_{total}) for these two catalysts. The Cu NWs exhibited higher j_{total} values at a potential region from -0.5 to -1.0 V (vs. RHE), and a more positive onset potential compared with Cu-Sn20 NWs. These results indicate that the overall catalytic activity is depressed after introducing Sn NPs onto Cu NWs. This effect became more obvious with the increase of Sn deposition time, as reflected by the LSV curves in Figure 3.7d.

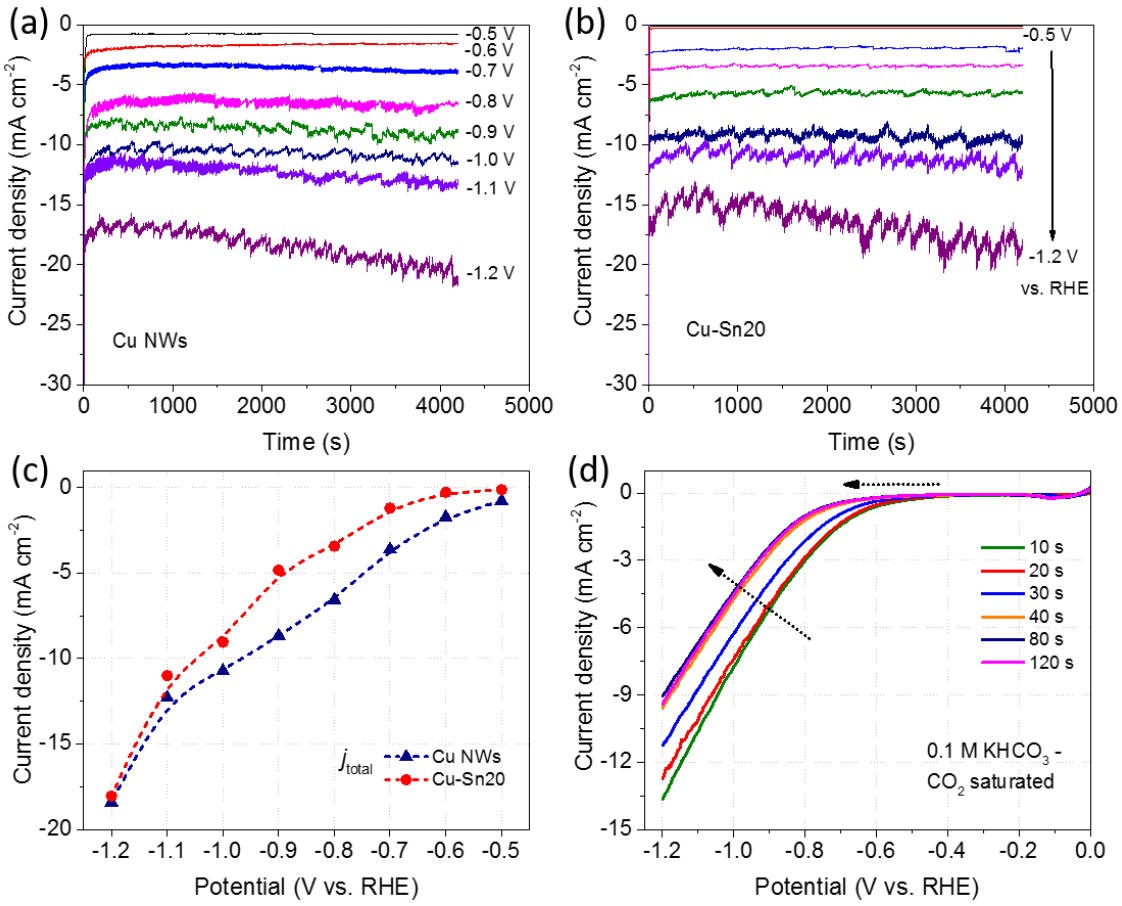

Figure 3.7 Controlled-potential electrolysis curves for CO_2 reduction using Cu NWs (a) and Cu-Sn20 NWs (b) electrodes in CO_2-saturated 0.1 M $KHCO_3$ solution; (c) Average total current densities at different potentials for Cu and Cu-Sn20; (d) LSV curves of Cu-Sn NWs with different Sn deposition times ranging from 10 s to 120 s in CO_2-saturated 0.1 M $KHCO_3$ at a scan rate of 20 mV s^{-1}.

3.3.4 CO_2ER Performance Analysis

Detailed product analysis for CO_2 reduction on these two electrodes at various applied potentials is shown in the **Figure 3.8**a-b. The products from the CO_2ER for Cu NWs included H_2, HCOOH, CO, CH_4, C_2H_4, C_2H_6 and C_2H_5OH, consistent with the previous report[33], while only H_2, HCOOH and CO were detected for Cu-Sn20 catalysts; clearly demonstrating the change of catalytic nature after the Sn decoration. The potential dependent CO and H_2 selectivity for these two catalysts were compared and are displayed in Figure 3.8c-d. The Cu NWs showed low faradaic efficiencies for CO (FE_{CO} < 20%), while primarily generating H_2 (FE_{H2} > 60%) and HCOOH (FE ~ 30%) at the potential from -0.6 V to -1.0 V. In contrast, Cu-Sn20 electrode demonstrated a much higher CO selectivity and a suppressed H_2

evolution, especially at the middle cathodic region (-0.7 to -1.0 V vs. RHE). The CO selectivity exhibited a typical volcano shape over the potential range of -1.0 V to -0.5 V, reaching a maximum FE_{CO} value of 82% at -0.7 V vs. RHE (corresponding to an overpotential of 590 mV relative to the CO_2/CO equilibrium potential, -0.11 V vs. RHE).

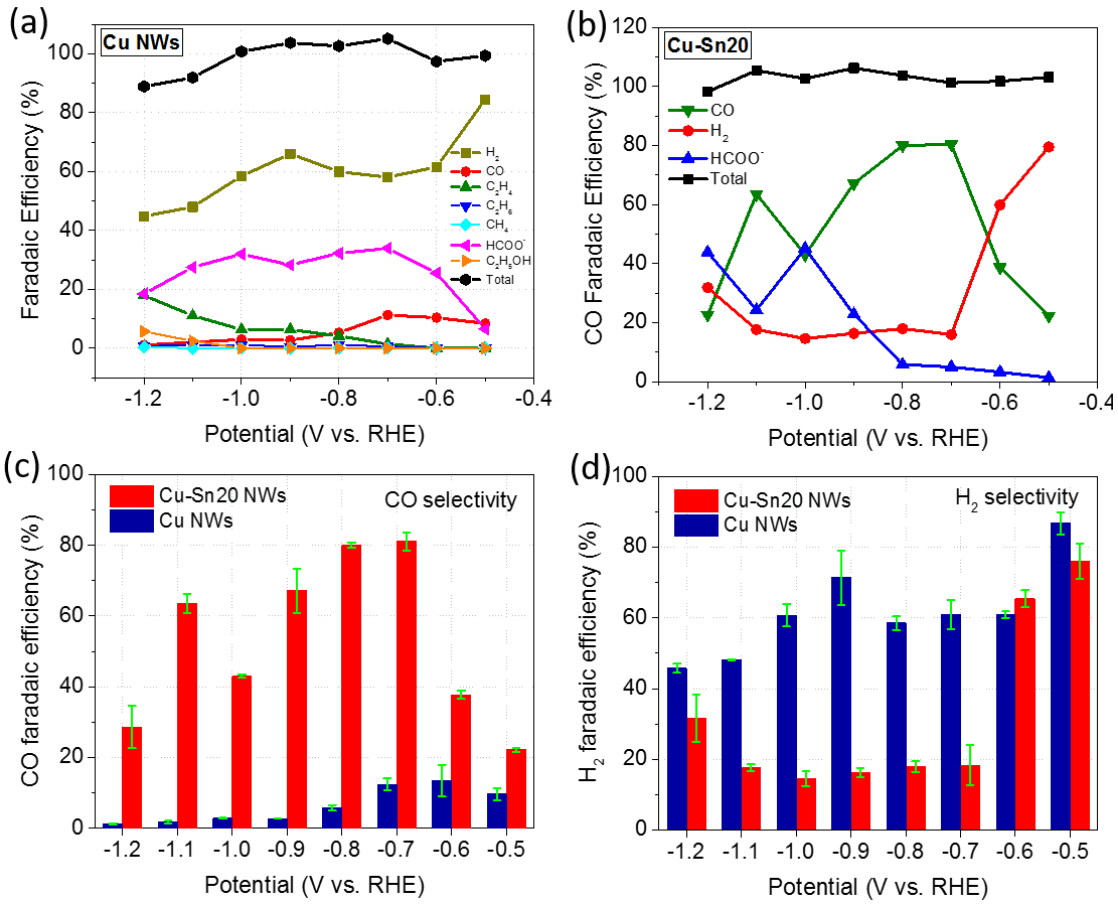

Figure 3.8 (a-b) Product analysis of the CO_2ER on Cu NWs and Cu-Sn20 NWs; (c-d) Comparison of the faradaic efficiency of CO and H_2 at different potentials. The error bars in (c-d) represent one standard deviation based on three independent sample measurements.

Moreover, the hybrid catalyst demonstrated a much higher reaction rate for CO_2-to-CO conversion, as evidenced by its high CO partial current density (j_{CO}), as shown in **Figure 3.9**a. The j_{CO} values of Cu-Sn20 NWs significantly surpassed that of Cu NWs at all potentials, and reached a maximum of ~ 6.7 mA cm^{-2} at -1.1 V compared with that of only 0.24 mA cm^{-2} for Cu NWs. Notably, at -0.8 V vs. RHE (an overpotential of 690 mV) the FE_{CO} reached ~ 80% yet with a significantly enhanced j_{CO} of 2.74 mA cm^{-2}, nearly three times higher than that at -0.7 V vs. RHE (0.96 mA cm^{-2}). This indicates that an applied overpotential of 690 mV is the optimal potential to drive the CO_2-to-CO with excellent selectivity and activity.

The Tafel plot of Cu-Sn20 electrode (Figure 3.9b) exhibited a slope of 136 mV per decade close to that 120 mV per decade over the overpotential range of 300 mV to 700 mV, indicating that an initial single-electron transfer to CO_2 to form surface adsorbed $CO_2^{\cdot-}$ intermediates is the rate-determining step.[33,87]

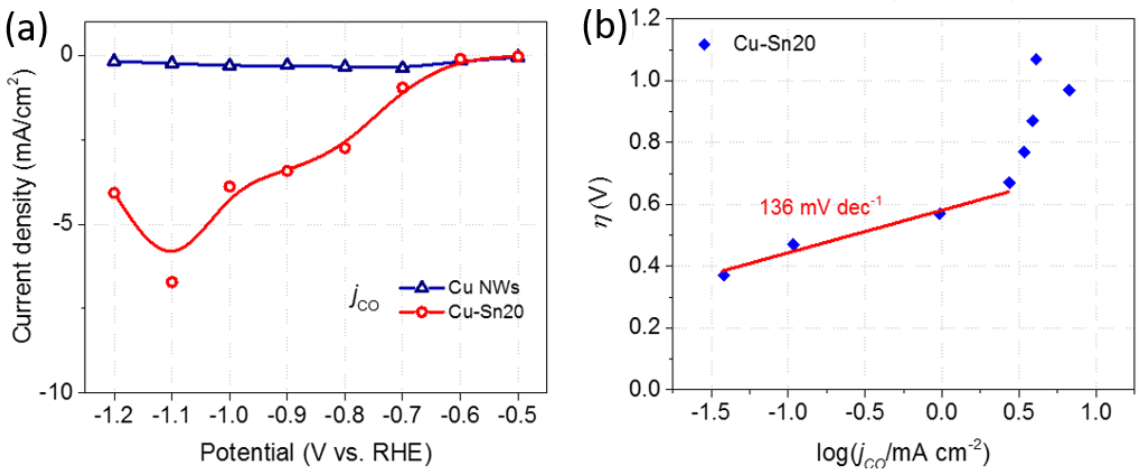

Figure 3.9 (a) CO partial current densities of the Cu NWs and Cu-Sn20 NWs catalysts; (b) Tafel plot for Cu-Sn20 NWs.

The durability of Cu-Sn20 hybrid catalyst was evaluated under the optimal overpotential, as shown in **Figure 3.10**a. During the first 6 h of electrolysis, the current density was nearly steady, and the real-time CO faradaic efficiency fluctuated around 82%, consistent with the quasi-steady-state FE_{CO} (80%, averaged over 70 min) in Figure 3.8c. The FE_{H2} gradually increased from ~10% to ~20%. Although the FE_{CO} exhibited a slight decay with further electrolysis, it still retained a high FE of 78% after 12 h of electrolysis, revealing its excellent stability towards aqueous CO_2 reduction. SEM analysis was performed on the electrode before and after the prolonged bulk electrolysis (Figure 3.10b-e). The nanowire structure remained very well intact; however, large amounts of nanoparticles were formed on the hybrid nanowire surface. This might have arisen from the aggregation of Sn nanocrystals on the surface of Cu NWs during the electrolysis, as illustrated in the schematics (insets of Figure 3.10c and e). With the increasing aggregation of Sn NPs, more and more Cu active sites that facilitates the H_2 generation were released, which may lead to the decay of FE_{CO} and the increase of FE_{H2} in Figure 3.10a.

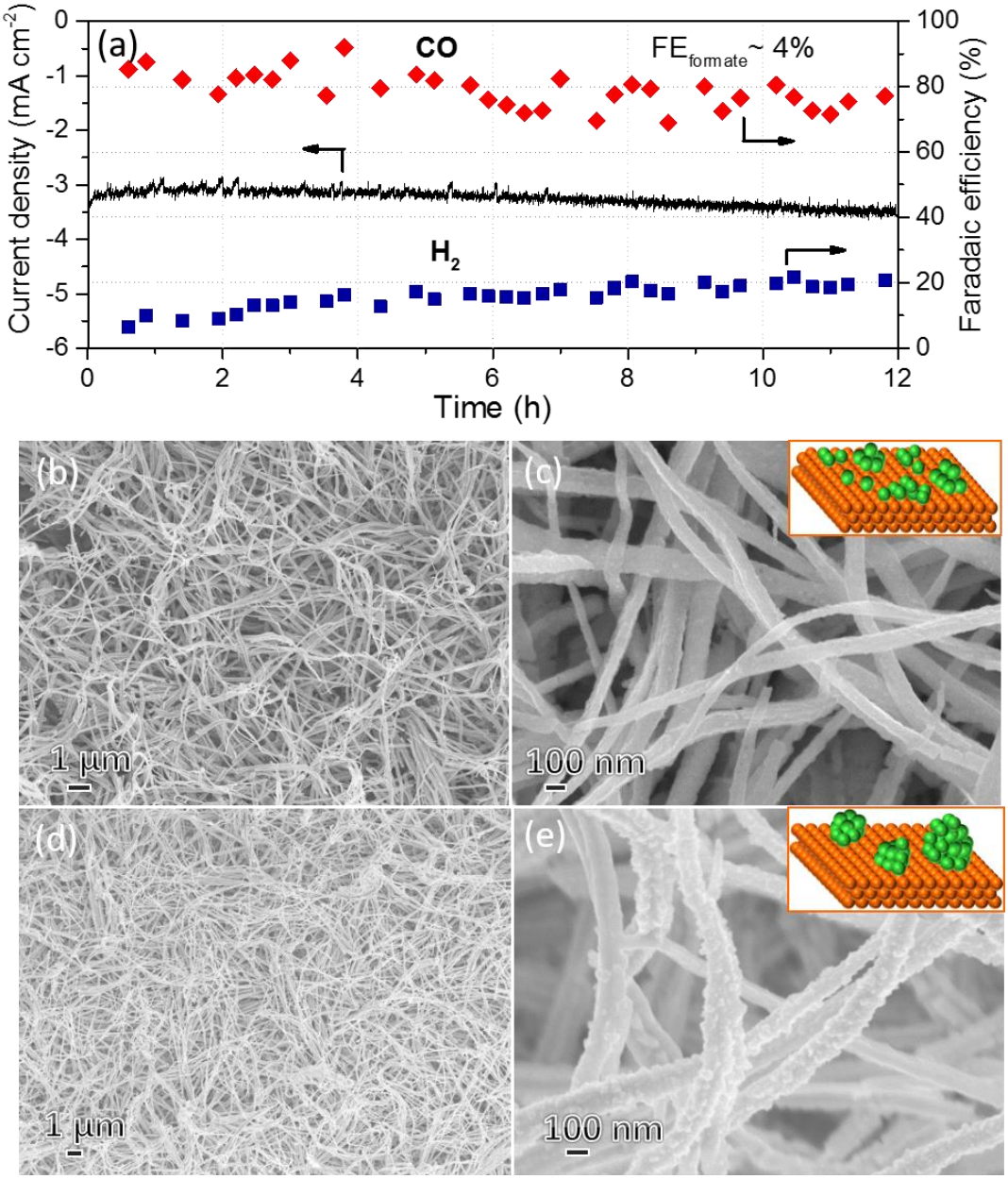

Figure 3.10 (a) Long-term stability test of Cu-Sn20 NWs at -0.8 V vs. RHE for 12 h in CO_2-saturated 0.1 M $KHCO_3$ solution; SEM images of the Cu-Sn20 NWs before (b, c) and after (d, e) the prolonged electrolysis.

3.3.5 Influence of Sn Coverage on CO_2ER

The hybrid Cu-Sn NWs electrodes exhibited strikingly different CO_2 reduction activities at -0.8 V vs. RHE, depending on the coverage of Sn NPs. The faradaic efficiencies and the partial current densities of CO, H_2 and $HCOO^-$ significantly changed with the increase of Sn deposition time (Figure 3.11). Both FE_{HCOO^-} and FE_{H2} increased with the increasing Sn deposition time. FE_{CO} experienced a sharp increase within a deposition time of 10 s, and a

decrease with the prolonged deposition time. When the deposition time was longer than 40 s, the evolution of $HCOO^-$ and H_2 prevailed.

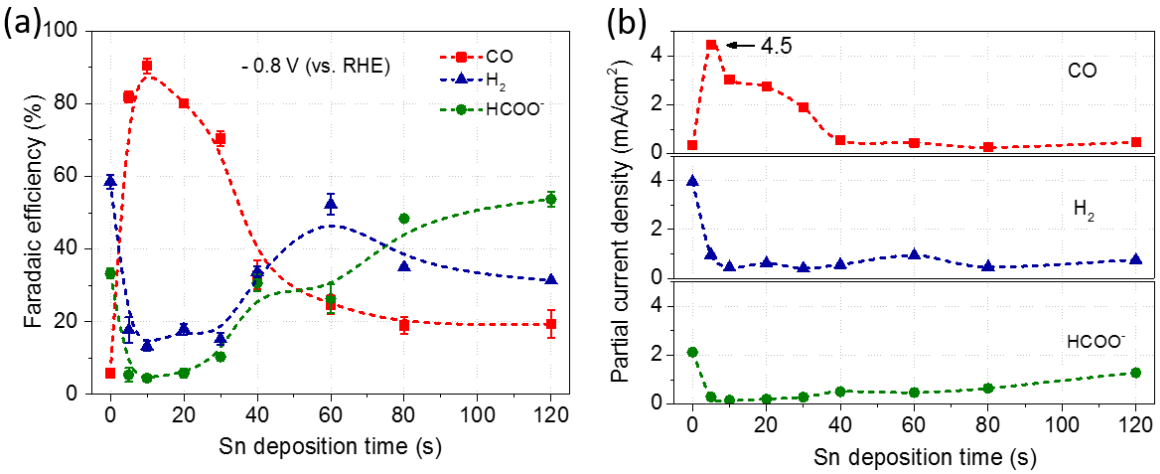

Figure 3.11 Comparison of (a) product selectivity and (b) partial current density of CO, H_2 and $HCOO^-$ for the Cu-Sn catalysts with different Sn deposition times ranging from 0 s to 120 s at -0.8 V vs. RHE in CO_2-saturated 0.1 M $KHCO_3$ solution. The error bars represent one standard deviation based on three independent measurements.

The electrochemical surface areas of these Cu-Sn hybrid NWs can be reflected by their double-layer capacitance (**Figure 3.12**a-e). The capacitance experienced an increase within a Sn deposition time of 60 s (Figure 3.12f). This trend is consistent with that for FE_{H2}, FE_{HCOO-}, j_{H2} and j_{HCOO-}, but contrary to that of FE_{CO} and j_{CO} in Figure 3.11. It indicates that the increased surface area mainly consists of active interfaces for H_2 and $HCOO^-$ formation. For Cu-Sn120, the FE_{HCOO-} reached a maximum of ~ 54% with a FE_{H2} of ~32%, whereas the FE_{CO} was only ~17%. This result is very close to that on a Sn electrode with a native 3.5 nm SnO_x layer[48]. Notably, the highest FE_{CO} of ~ 90% was achieved on Cu-Sn10 electrode (Figure 3.11). A maximum CO partial current density of 4.5 mA cm^{-2} together with a FE_{CO} of 82% was reached on the Cu-Sn5 NWs. The catalytic performance is much better than that from Cu-Sn alloy[272] or N-doped carbon nanotubes[145], Cu-Pd alloy[114], and even comparable to polycrystalline gold[30] and Pd NPs[79].

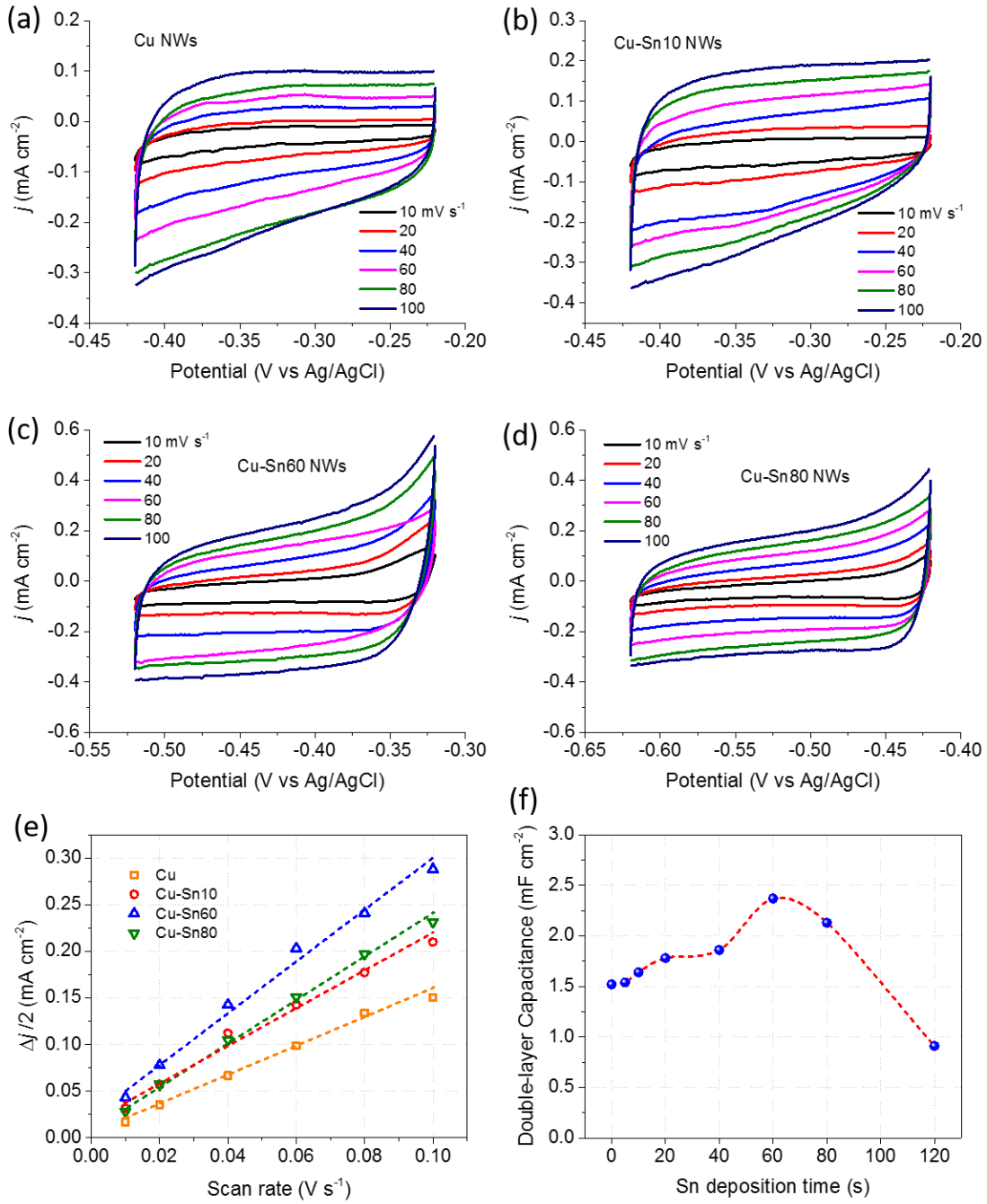

Figure 3.12 Determination of double-layer capacitance (C_{dl}) of Cu NWs and Cu-Sn NWs in Ar-saturated 0.1 M $HClO_4$ solution. CVs were taken over a range of scan rates in a potential window where only double-layer charging and discharging is relevant. The C_{dl} was estimated by plotting the $\Delta j/2$ against scan rates, in which the slope was C_{dl}. The Δj is the difference between j_a and j_c, where j_a and j_c are the anodic and cathodic current densities at the midpoint of the applied potential window, respectively.

All the above evidence suggests that the intrinsic activity for the CO_2-to-CO conversion on Cu-Sn hybrid nanowires most likely arises from the synergistic interaction between Sn

NPs and Cu NWs. This effect can be elucidated based on the DFT calculations for the recently reported Cu-Sn alloy catalysts.[115] The Sn atom can discompose the multi-fold sites on the surface of Cu, disfavouring the adsorption of H and leaving the adsorption of CO relatively unperturbed. Thus, the hydrogenation processes (H_2 and $HCOO^-$ formation) are inhibited while CO productivity is hardly affected, resulting in an improved FE_{CO}. This effect can be optimized by tuning the density of Cu-Sn interfaces to an optimal value (corresponding to a deposition time of ~ 10 s in this work). When the active sites on Cu NWs are fully covered by Sn NPs (~ 80 s), the effect from Sn metal prevails. As revealed in the STEM mapping results in **Figure 3.13**; when the deposition time was 10 s, only a small amount of Sn species was scattered on the surfaces of Cu NWs. When the time increased to 40 s, a sparse thin Sn layer (~ 3 nm) was formed, and the Sn content concomitantly increased from 2.0 wt% to 5.6 wt%. The FE_{CO} suffered from a sharp drop from 90% to 33%. These results clearly demonstrate that the improved CO selectivity is from the Cu-Sn interface. When the Sn coverage increased from 2.0 wt% to 5.6 wt%, the Cu sites responsible for CO production might mostly get occupied by Sn NPs, resulting in the significant decline of FE_{CO}. When the deposition time was prolonged to 80 s, the Sn layer became denser and fully covered the Cu NWs; therefore it exhibited the prevailing catalytic performance of pristine Sn metal with a FE_{HCOO^-} of ~50%.

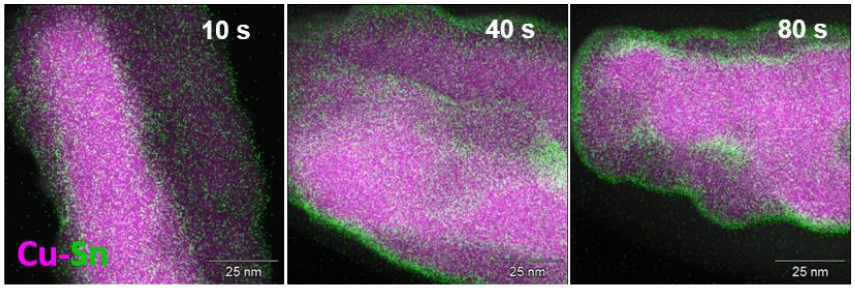

Deposition time	Cu wt.%	Sn wt.%
10 s	97.92	2.08
40 s	94.39	5.61
80 s	91.15	8.85

Figure 3.13 STEM mapping results of three representative Cu-Sn NWs with various Sn deposition time (10 s, 40 s and 80 s).

It should be noted that the performance of this optimized Cu_xO-Sn electrode (high FE_{CO} of ~ 90% at -0.8 V vs RHE) is inferior to that of the recently reported Cu-Sn alloy catalyst (FE_{CO} > 90% in a broad potential range from -0.5 to -0.8 V).[115] This difference can be attributed to the microstructure of Cu_xO-Sn electrode. Compared with the uniform Cu-Sn atomic arrangement in the alloy, the nanoscale non-uniform distribution of Sn NPs from electroless deposition may leave some Cu sites unaffected by Sn species. The catalytic

behaviour of pristine Cu or Sn still persists in the Cu_xO-Sn electrode, leading to its relatively low performance compared with the Cu-Sn alloy catalyst. However, this electroless deposition method is much more efficient and cost-effective than electrochemical deposition. Only through a five-second deposition of Sn NPs, the resulting hybrid nanowire electrode demonstrated a FE_{CO} of 82% and a j_{CO} of 4.5 mA cm^{-2} at -0.8 V; surpassing the optimized Cu-Sn alloy catalyst (electrodeposition of ~ 15 min, FE_{CO} ~ 91% and j_{CO} ~ 3.1 mA cm^{-2}).

3.3.6 Influence of Au NPs on Cu-Sn NW Catalyst

To further verify the synergistic effect between adsorbed Sn NPs and Cu NWs, a third metal, Au, was introduced as an interference factor to change the properties of Cu NWs. Au NPs were *in situ* anchored on the surfaces of Cu NWs via a facile redox reaction between copper and chloroauric acid. The coverage of Au NPs was simply controlled by the reaction time. The structure of Cu-Au20 NWs (Au deposition time was 20 s) was characterized by SEM and TEM (**Figure 3.14**). The structural analysis revealed that a large amount of small Au nanocrystals (< 10 nm) were decorated on the surfaces of Cu NWs. However, the Cu NW surface was not fully covered by Au NPs, creating large amounts of Cu-Au interfaces (Figure 3.14h). Then the Sn species was deposited on the Cu-Au20 NWs to form the Cu-Au20-Sn20 NWs and investigated for CO_2ER under the same conditions in comparison with Cu NWs and Cu-Sn20 NWs. It is reasonable to infer that a Cu-Au-Sn three-phase interface can be formed after Sn electroless deposition. Due to the intrinsic CO_2ER property and excellent electronic conductivity of Au NP interlayer, the electrocatalytic performance for CO_2-to-CO conversion may be further improved.

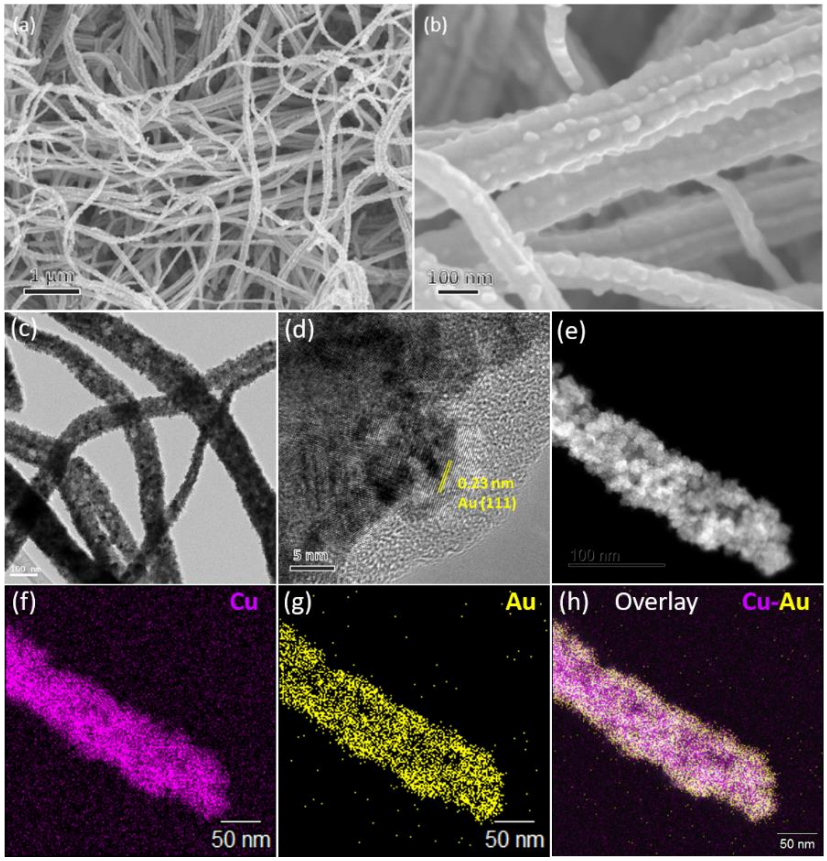

Figure 3.14 (a-b) SEM images of Cu-Au20 NWs; TEM (c), HRTEM (d), HAADF-STEM images and the corresponding elemental mapping results (e-h) of Cu-Au20 NWs.

Figure 3.15a-b shows the iR-corrected controlled-potential electrolysis curves on Cu-Au20 NWs and Cu-Au20-Sn20 NWs. Both of them exhibited almost stable current densities during the electrolysis at different potentials, which are very similar to those of Cu NWs and Cu-Sn20 NWs. Detailed product analysis is shown in Figure 3.15c-d. For Cu-Au20 NWs, H_2, $HCOO^-$, CO, C_2H_4, C_2H_6 and C_2H_5OH (trace amount) were detected, which was almost same as the polycrystalline Cu NWs (Figure 3.8a). The CO faradaic efficiency (FE_{CO}) and partial current density (j_{CO}) of Cu-Au20 showed a slight increase compared to bare Cu NWs, and the peak FE_{CO} positively shifted from -0.7 V to -0.6 V vs. RHE. This may be attributed to the increased electronic conductivity from Au. It is also noticed that changes in FE_{CO} and j_{CO} were limited. It clearly demonstrates that the introduction of Au NPs on Cu NWs did not obviously change the surface properties, namely, Cu-Au interfaces are not efficient for CO formation. After a rapid Sn modification of 20 s on the Cu-Au20 NWs, the FE_{CO} was intensely increased, while the FE_{H2} was evidently depressed. This is almost similar to the effect on bare Cu NWs. Figure 3.15e-f highlights the potential dependent FE_{CO} and j_{CO} of these four electrodes. It is clear that Cu-Au20 NWs displayed similar CO_2-to-CO behaviour

as Cu NWs. The introduction of Au did not obviously change the FE_{CO}. However, the FE_{CO} changed dramatically after introducing Sn (20s) onto Cu-Au20 NWs, as observed for Cu NWs. It can be deduced that the introduction of Sn is the key to improve the CO selectivity.

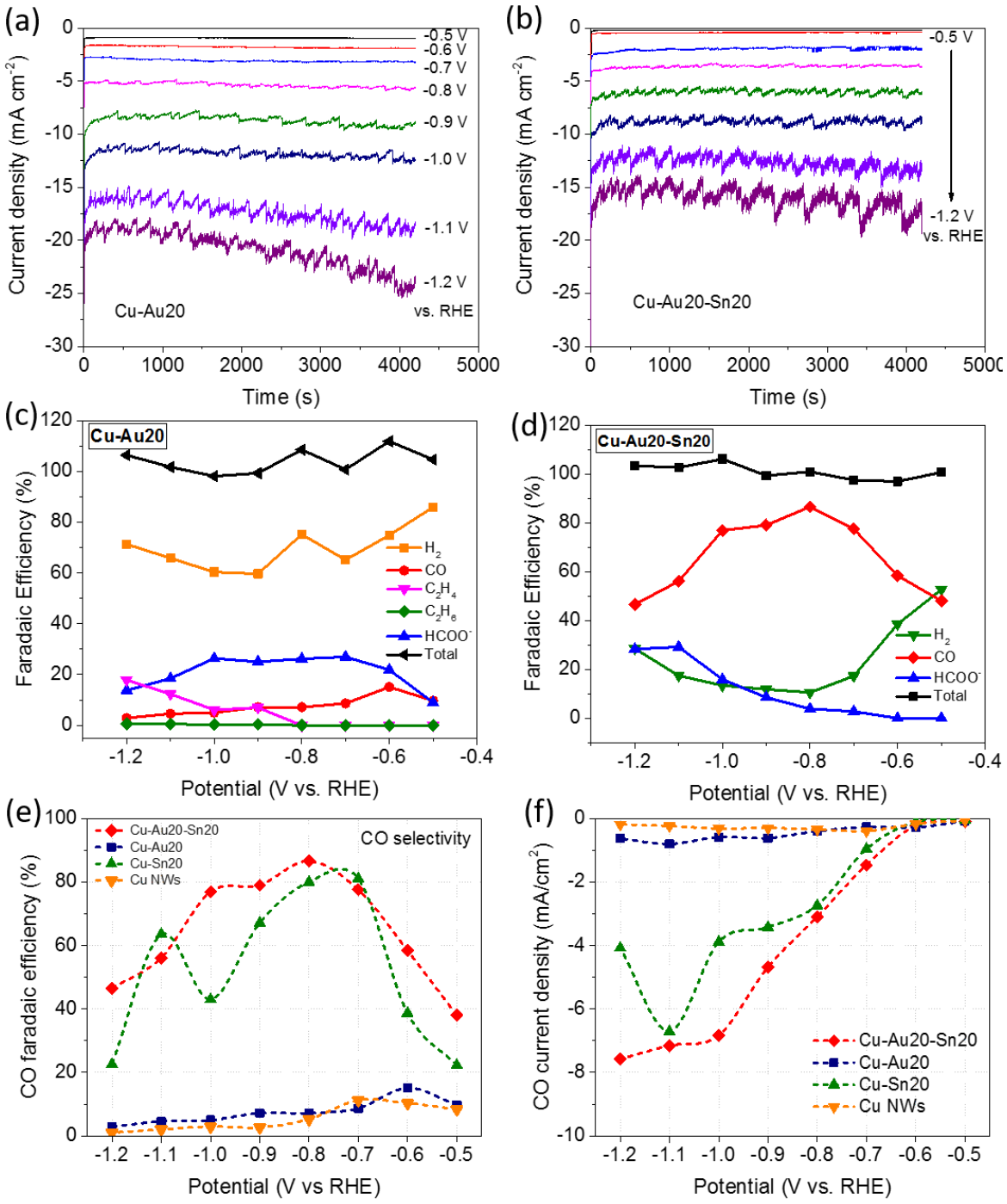

Figure 3.15 Controlled-potential electrolysis curves in CO_2-saturated 0.1 M $KHCO_3$ solution and the product analysis for Cu-Au20 NWs (a, c) and Cu-Au20-Sn20 NWs (b, d). Potential dependent CO faradaic efficiency (e) and CO partial current density (f) for Cu, Cu-Sn20, Cu-Au20 and Cu-Au20-Sn20 NWs.

It is also noticed that Cu-Au20-Sn20 shows higher FE_{CO} and j_{CO} values than Cu-Sn20, and exhibits an obvious change of FE_{CO} and j_{CO} trends at the low potential region between -1.0 V and -1.2 V vs. RHE. It reveals that the presence of Au affects the interactions between Cu and Sn, and the Cu-Au-Sn interfaces are more efficient for CO production than the Cu-Sn interfaces. This may be mainly attributed to the increased electrocatalytic surface area (**Figure 3.16**a-c). The Au interlayer may also reduce the electron transfer barrier at the catalytic interfaces, which is reflected by the decreased electron transfer resistance (Figure 3.16d). These results clearly demonstrate that the addition of a third element Au can interfere the CO formation at the Cu-Sn interfaces, further evidencing the efficient catalytic capability from the Sn NPs-Cu NWs interface.

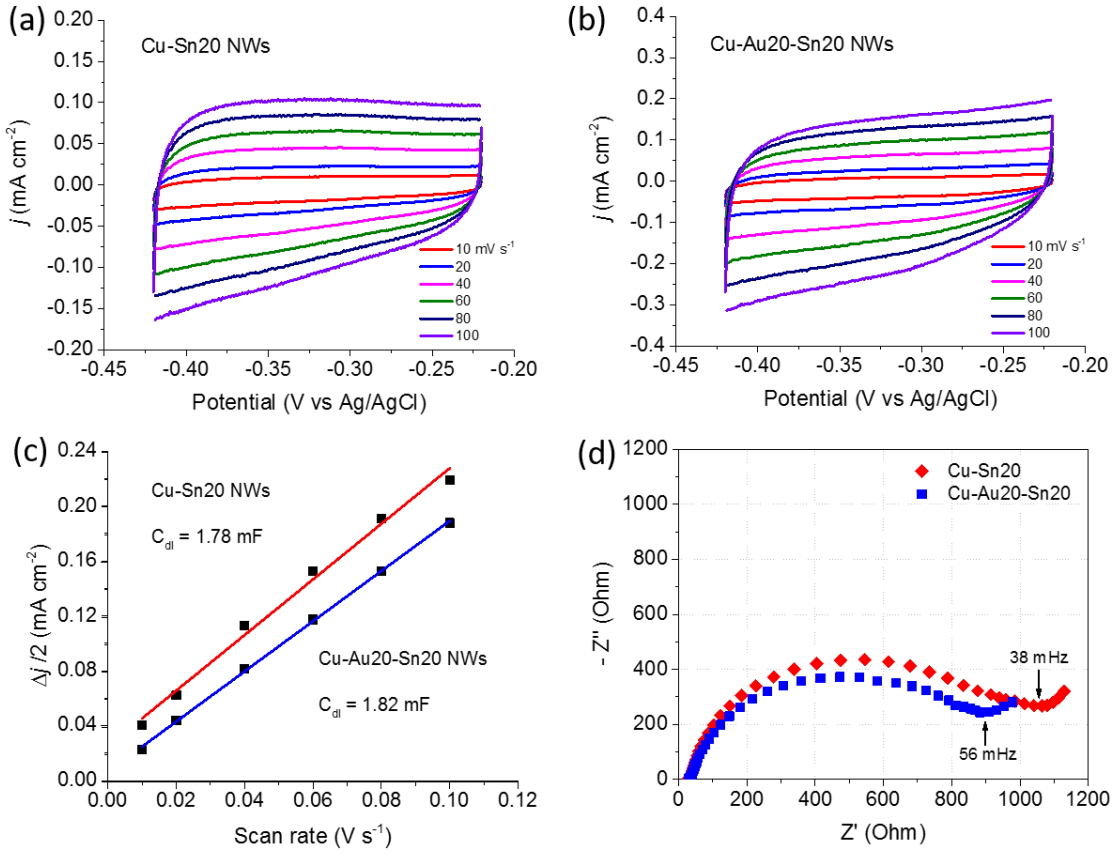

Figure 3.16 (a-c) Comparison of the double-layer capacitances for Cu-Sn20 NWs and Cu-Au20-Sn20 NWs in Ar-saturated 0.1 M $HClO_4$ solution. The slightly larger C_{dl} value of Cu-Au20-Sn20 indicates its higher electrochemical active surface area compared with Cu-Sn20. (d) Electrochemical impedance spectroscopy (EIS) investigation of these two electrodes in CO_2-saturated 0.1 M $KHCO_3$ solution by applying an AC voltage with 5 mV amplitude in a frequency range from 0.02 Hz to 100 kHz.

The synergistic effect of Cu-Sn or Cu-Au-Sn interfaces was further investigated by tuning the Au and Sn deposition time separately, that is, changing the Au coverage under a specific Sn deposition time [Cu-Au(t)-Sn10] or varying the Sn coverage under a specific Au deposition time [Cu-Au20-Sn(t) or Cu-Au10-Sn(t)]. These results are presented in **Figure 3.17**. When the Sn deposition time was the optimal value of 10 s, the FE_{CO} constantly decreased while the FE_{H2} increased with the increasing deposition of Au interlayer particles (Figure 3.17a). The CO partial current density exhibited an obvious decrease when the Au deposition time was less than 20 s (Figure 3.17b). This may be caused by the decreasing density of Cu-Au-Sn interfaces which was efficient for CO production with the increased coverage of Au interlayer NPs. When extending the Au deposition time to > 40 s, the surface of Cu NWs might be almost covered by Au NPs. The low selectivity of these Au NPs may cause the constant decrease of FE_{CO}; however, the intrinsic activity of Au NPs was much higher than Cu or Cu-Sn, probably leading to the increase of total current density and CO partial current density.

In addition, the selectivity and activity of Au modified Cu NWs (Cu-Au20 and Cu-Au10) for CO production varied with the Sn coverage (Figure 3.17c-d). The influence of Sn modification was related with the coverage of Au interlayer NPs as well. The electrode with more Cu-Au interfaces (Cu-Au20) required more Sn (20 s deposition) to achieve a peak FE_{CO} of ~90%, while the one with less Cu-Au interfaces (Cu-Au10) only needed a Sn deposition time of 10 s to achieve the similar peak FE_{CO}. This further reveals that the Cu-Sn interfaces were the major active sites for efficient CO_2-to-CO formation.

However, it should be noted that the influence of Au on reaction rate (j_{CO}) is not totally consistent with its influence on CO selectivity (FE_{CO}). This is revealed by a study on Cu-Au10 electrode with deficient Au coverage for transforming all the Cu sites into Cu-Au interfaces. On this electrode, increasing the Sn deposition time from 10 s to 20 s led to an increase of j_{CO} but with a reduced FE_{CO}. It indicates that the Sn coverage is another key to generate highly active Cu-Au-Sn interfaces. Optimizing the coverage of Au and Sn on Cu surface is essential for optimizing the reaction rate and product selectivity for CO production.

All the above results verified that the Cu-Sn interfaces were responsible for the promotion of CO production in Cu-Sn hybrid catalyst system. They also highlight the importance of engineering Cu-Sn interface by introducing the third interlayer metal to improve the electrocatalytic properties of Cu.

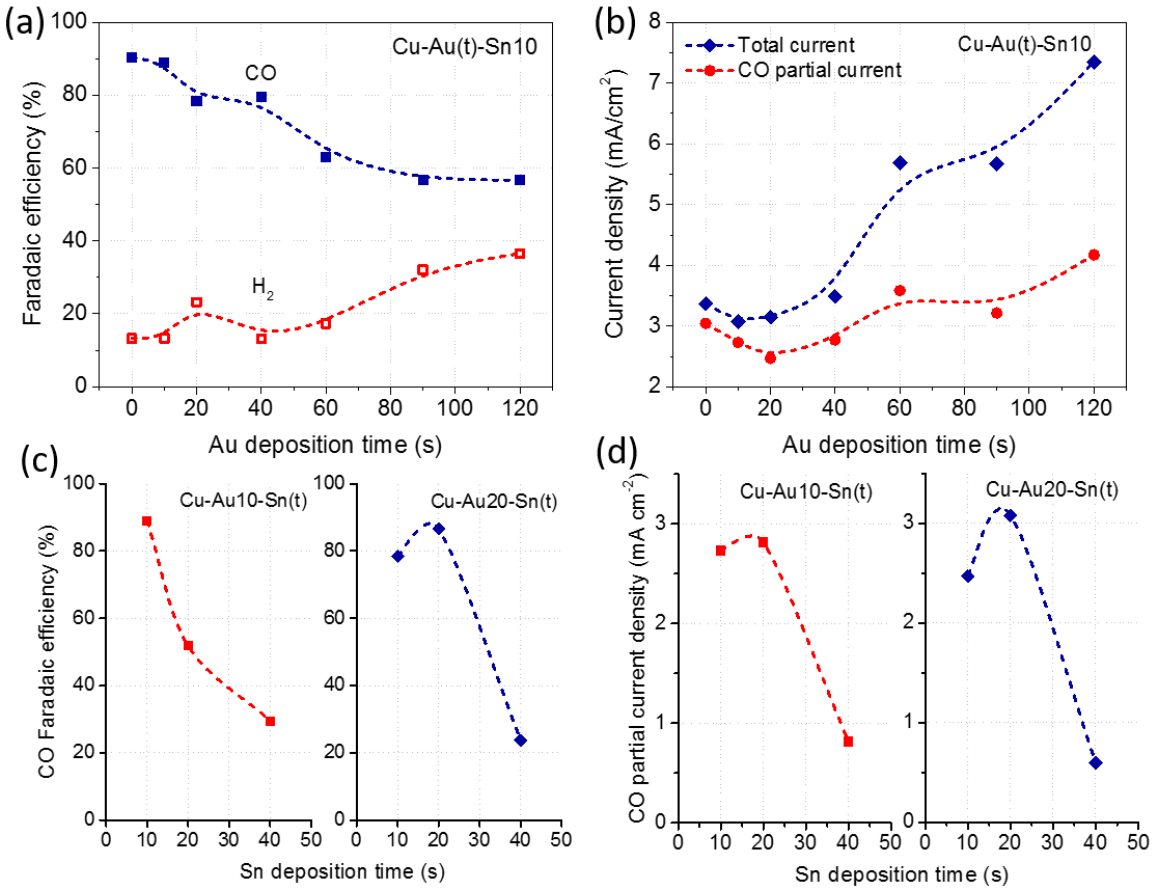

Figure 3.17 Comparison of (a) product selectivity and (b) partial current density of CO and H_2 for the Cu-Sn10 catalysts with different Au deposition times ranging from 0 s to 120 s at -0.8 V vs. RHE in CO_2-saturated 0.1 M $KHCO_3$ solution. (c) The dependence of CO selectivity and activity on Sn deposition time over two different substrates Cu-Au10 and Cu-Au20 NWs.

3.4 Conclusion

In this chapter, a novel kind of Sn NPs decorated Cu_xO NWs hybrid catalyst has been developed to explore the influence of Cu-Sn nanoscale interfaces on CO_2 electroreduction. This catalyst was fabricated by facile and low-cost electrochemical anodization and electroless deposition techniques, and exhibited excellent electrocatalytic activity towards the electroreduction of CO_2 to CO. A high FE_{CO} of 90% and a high j_{CO} of 4.5 mA cm^{-2} were reached under a moderate overpotential of 690 mV by simply tuning the coverage of Sn NPs. The performance could be further improved by introducing a third metal Au in-between Cu and Sn. These results evidenced that the interaction between the nanoscale Cu and Sn phases was the major factor for the improved CO_2-to-CO conversion. Moreover, the performance

of this Cu-Sn hybrid catalyst is highly similar to that of the reported Cu-Sn intermetallic alloy catalyst[115], indicating that the electrocatalytic property of the Cu-Sn bimetallic system is not sensitive to the mixing patterns of two metal elements as reported for Cu-Pd[119], Cu-Ag[118] and Cu-Au[104] systems. This study provides not only a facile and scalable way to fabricate non-precious metal hybrid catalysts but also guidance towards the rational design of Cu-based bimetallic catalysts for improved CO_2 electroreduction by modulating the metal-metal interfaces at the nanoscale.

Chapter 4 Engineering Tin Species on Nitrogen-Doped Carbon Nanofibers for Improved CO_2 Electroreduction

This chapter is adapted from the article, "Tunable and Efficient Tin Modified Nitrogen-doped Carbon Nanofibers for Electrochemical Reduction of Aqueous Carbon Dioxide", by Yong Zhao, Jiaojiao Liang, Caiyun Wang, Jianmin Ma, Gordon G. Wallace, which was published in Adv. Energy Mater. (2018, 8, 1072524). Adapted with permission from Wiley-VCH.

4.1 Introduction

Tin, a nontoxic earth-abundant metal, has great potential for practical CO_2ER application due to its high selectivity for producing formate or formic acid. In recent years, a number of nanostructured Sn-based catalysts have been developed by modulating the surface structural factors such as particle size,[46] grain-boundary density,[38] oxide layer thickness,[48] and morphology.[277] However, their performance is not satisfactory yet. It remains a challenge to achieve high formate selectivity and current density at low overpotentials for pure Sn catalysts due to the intrinsically low reactivity of Sn metal.

The local electronic environment from the supporting materials has been identified as an important factor to tune the intrinsic activity of Sn catalysts.[46] In Chapter 3, the investigations revealed that the synergistic interaction between Sn NPs and Cu NW supports is responsible for the realization of efficient CO_2-to-CO conversion. However, this kind of substrate-directed nanostructured catalysts usually suffer from limited loading capacity and difficulty in their incorporation to gas diffusion electrodes for generating high current densities. To overcome this limitation, it is necessary to anchor Sn NPs on a kind of freely dispersed supporting materials to develop efficient powder-like Sn-based catalysts.

Carbon materials are the most commonly used supporting materials for nanoscale metal catalysts. Meyer et al.[46] found that compared with carbon black support, graphene sheet with a stronger electron donating ability could promote the adsorption of CO_2 and $CO_2^{\bullet -}$ and thus facilitate formate formation on the supported Sn NPs. Nitrogen-doping can tailor the electronic structure of graphitic carbons,[278] leading to increased electronic conductivity, high surface energy and tunable chemisorption ability favouring electrochemical reactions

such as oxygen reduction reaction and HER.[279] However, the research on the interaction between N-doped carbons and p-block metal Sn is limited. On the other hand, N-doped carbons themselves can act as active sites for CO_2-to-CO conversion due to their capability of binding CO_2 and protons.[146] The introduction of active transition metal atoms such as Fe,[158,165] Mn,[158] Ni,[160,169] or Co[161,162] can further improve catalytic activity by turning the pyridinic-N sites into more active metal-N moieties for CO production. However, the effect of p-block element doping remains unexplored.

To address this knowledge gap, in this chapter, a Sn modified N-doped porous carbon nanofiber (Sn-CF) catalyst has been developed using a straightforward electrospinning technique in combination with a pyrolysis method. The electrocatalytic activity of this hybrid catalyst can be tuned by manipulating the interactions between Sn species and carbon nanofiber supports. The electron-rich pyridinic-N-doped carbon nanofibers have an obvious promotion effect on the supported Sn NPs for CO_2-to-formate conversion compared with the graphitic-N-doped nanofibers. This catalyst drove an efficient formate formation at a high current density of 11 mA cm^{-2} and a faradaic efficiency of 62% with a moderate overpotential of 600 mV in 0.5 M $KHCO_3$ solution. After a simple acidic leaching treatment, atomically dispersed Sn species remained on the surface of nanofibers that might be stabilized by the pyridinic-N sites. This kind of Sn coordinated pyridinic-N-doped carbon nanofibers switched to a selective reduction of CO_2 to CO with a FE of 91% at a low overpotential of 490 mV in 0.1 M $KHCO_3$.

4.2 Experimental

4.2.1 Synthesis of Sn Modified Nitrogen-Doped Carbon Nanofibers

The hybrid nanofibers (Sn-CFs) were prepared via an electrospinning method. Briefly, polyacrylonitrile (PAN, 0.35 g) and polymethylmethacrylate (PMMA, 0.35 g) were dissolved in DMF (7 g) forming a homogeneous colloidal solution. After adding 0.68 g of $SnCl_2 \cdot 2H_2O$, the solution was magnetically stirred for 4 h at 50 °C to form a clear solution. Then it was transferred into a plastic syringe (10 mL) equipped with a capillary and needle head (0.5 mm in diameter). Under a high voltage of ~ 8.5 kV, the content of the syringe was propelled by a peristaltic pump at a speed of 0.4 mL h^{-1}, and the fibres were electrospun from the metallic needle and collected at an aluminium collector. The distance between the needle and collector was 12 cm. The fibres were then dried in a vacuum oven at 60 °C for 12 h.

Finally, they were subjected to a pyrolysis process in a tube furnace at three different temperatures, 900, 1000 and 1100 °C for 2 h in Ar/H_2 gas (8% H_2) to form the Sn decorated N-doped carbon nanofibers. The heating rate was 3 °C min^{-1}.

To prepare the Sn atoms modified nitrogen-doped carbon nanofibers (AD-Sn/N-C1000), the Sn-CF1000 powder was immersed in 3 M HCl solution for 8 h at 90 °C, and collected by centrifugation and washed with copious amounts of water to reach a neutral pH. The catalyst was dried at 60 °C for 12 h in a vacuum oven.

4.2.2 Fabrication of Working Electrode

The catalyst inks were prepared by mixing 15 mg of the obtained carbon nanofiber samples, ethanol/water (2:3 v/v, 1.9 mL) solution and Nafion solution (5 wt%, 0.1 mL) under sonication for 90 min. An aliquot of the catalyst ink (130 µL) was dropped uniformly onto one side of a carbon paper (1 cm × 1 cm), and kept at room temperature overnight to evaporate most of the solvents. After being annealed in an oven at 70 ℃ for 3 h, these catalyst covered carbon papers were used as working electrodes.

4.2.3 Electrochemical Measurements and Product Analysis

All the electrochemical measurements, and product analysis of bulk electrolysis experiments were performed according to the methods and procedures presented in Chapter 2. It should be noted that the influence of the concentration of electrolyte was investigated in this chapter. The pH of CO_2-saturated 0.1 M, 0.3 M, 0.5 M, 0.7 M and 1.0 M $KHCO_3$ was measured by using a pH meter (Aqua-CP/A, TPS) and determined to be 6.8, 7.2, 7.4, 7.6 and 7.7, respectively.

4.3 Results and Discussion

4.3.1 Structural Analysis of Sn-CFs Catalysts

The fabrication of Sn-CFs catalysts involved an electrospinning process from a precursor solution containing PAN, PMMA and $SnCl_2$; followed by a pyrolysis process at the designated temperature in the range of 900-1100 °C in Ar/H_2 atmosphere to form a Sn-containing fibre membrane (**Figure 4.1**a). During the pyrolysis, the PAN was transformed to N-doped carbon; $SnCl_2$ was reduced to Sn; and PMMA was decomposed to create pores

on the nanofibers.[280,281] The resultant material was denoted as Sn-CF1000 for example when 1000 was the annealing temperature.

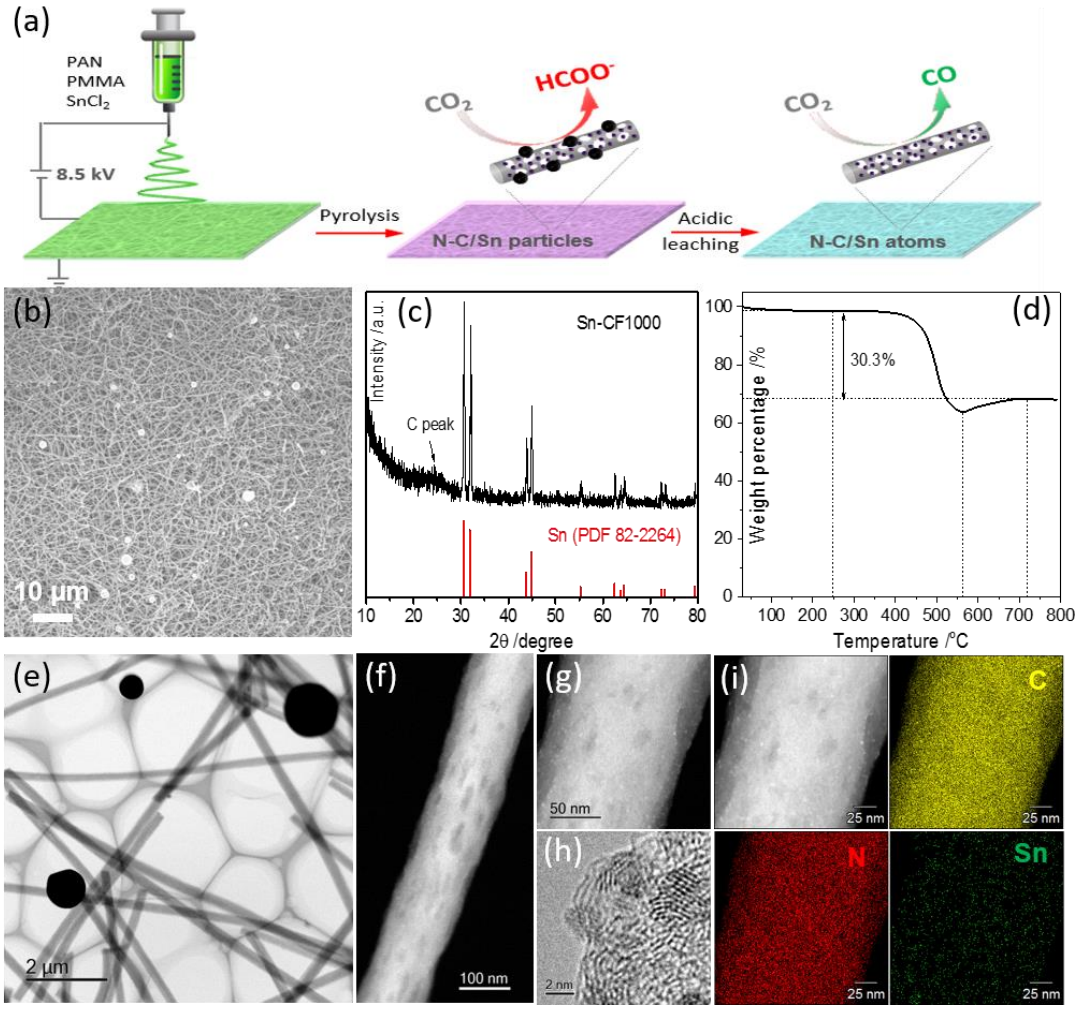

Figure 4.1 (a) Schematic illustration of the fabrication process of Sn modified N-doped carbon nanofiber electrocatalysts for $HCOO^-$ and CO production; (b) SEM image, (c) XRD pattern, (d) TGA curve and (e) bright field TEM image of Sn-CF1000 composite; (f-g) Dark field STEM images under different magnifications, (h) HRTEM image and (i) STEM-EDS mapping results of a single nanofiber.

The Sn-CF1000 composite consists of nanofibers decorated with microspheres (Figure 4.1b,e). These nanofibers had a typical diameter of ~ 250 nm and a length of tens of microns. They were interconnected into a porous three-dimensional (3D) network favouring the mass transport. Those microspheres were in a diameter of 0.5-3 μm with smooth surfaces. They were identified as Sn (JCPDS 82-2264) by the XRD analysis (Figure 4.1c), which were formed due to the phase separation between Sn and carbon at high temperatures. The Sn content was evaluated from TGA analysis by assuming Sn was oxidized to SnO_2 (Figure

4.1d), and it was ~ 53 wt%. In addition, a large number of nanosized pores (dark parts) and nanoparticles (bright dots) were observed on the nanofiber surface, as revealed by dark field scanning transmission electron microscope (STEM) (Figure 4.1f-g). These nanodots with a diameter of ~ 2.5 nm were tightly anchored on the surface. A set of fine lattice fringes with a space of 0.34 nm was identified (Figure 4.1h), which can be ascribed to the (110) plane of SnO_2 (JCPDS 41-1445). The SnO_2 may be formed from the spontaneous oxidation of Sn in air. No obvious lattice fringes of carbon can be observed, indicating its amorphous nature. The elements Sn and N species were uniformly distributed along the carbon nanofiber, as revealed by the STEM energy-dispersive X-ray spectroscopy (EDS) mapping (Figure 4.1i).

The N_2 adsorption/desorption isotherm exhibited a typical type-IV hysteresis loop at the relative pressure $P/P_0 > 0.5$ (**Figure 4.2**a), suggesting the existence of mesopores in the nanofibers.[282] This material presented a hierarchical mesoporous structure, as evidenced by the presence of three different peaks at ~ 4.0 nm, 6.5 nm and 11.7 nm on the Barrett-Joyner-Halenda (BJH) pore-size-distribution curve (inset of Figure 4.2a). These results are consistent with the TEM observations (Figure 4.1f). According to the Brunauer-Emmett-Teller (BET) method, the specific surface area was calculated to be 286 $m^2 g^{-1}$ with a pore volume of 0.25 $cm^3 g^{-1}$ (for pores smaller than 330 nm). The hierarchical mesoporous structure and large surface area may provide more open channels and active sites for CO_2 reduction.

The structure and chemical state of Sn and N species on Sn-CF1000 were further analysed by high-resolution XPS. The $Sn3d_{3/2}$ and $Sn3d_{5/2}$ spectra (Figure 4.2b**)** fit into three groups at binding energies of 495.6 and 487.4 eV for Sn^{4+}, 495.0 and 486.7 eV for Sn^{2+}, and 493.2 and 484.7 eV for Sn^0;[283] indicating a mixture of SnO_x and Sn. The presence of Sn^{4+} is consistent with the observed SnO_2 in the HRTEM analysis. As revealed by the deconvoluted N1s spectrum (Figure 4.2c**)**, the N-doped carbon was mainly ascribed to pyridinic-N (398.0 eV) and graphitic-N (400.8 eV) with abundance of 24.8% and 75.2%, respectively.[280] The relative N content evaluated from the X-ray photoelectron spectroscopy (XPS) analysis was 2.35 atm% (Table 4.1). It exhibited two broad peaks at 1346 and 1585 cm^{-1} in the Raman spectrum (Figure 4.2d), corresponding to the defect-induced band (D) and graphitic-induced band (G) of carbon.[280,284] The intensity ratio of D/G band (I_D/I_G) was ~ 1.30, reflecting a disordered carbon structure and agreeing with the HRTEM result.

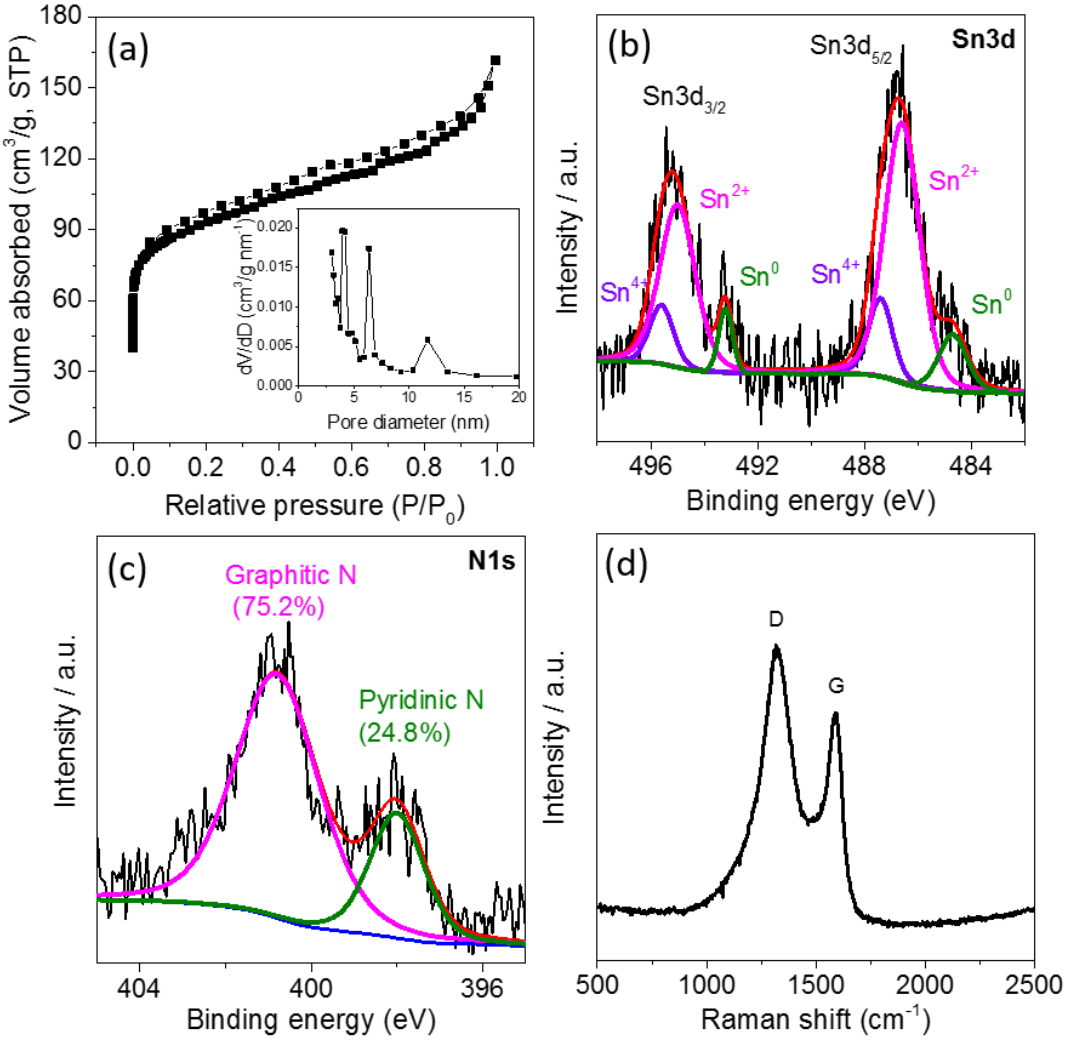

Figure 4.2 (a) N_2 adsorption/desorption curve of Sn-CF1000, inset is the corresponding Barrett-Joyner-Halenda (BJH) pore distribution curve. (b,c) High-resolution Sn3d and N1s XPS spectra of Sn-CF1000; (d) Raman spectrum of Sn-CF1000.

The effect of pyrolysis temperature on the structure of Sn and N species in Sn-CF composites was investigated. Two more samples were obtained after annealing the Sn-containing fibre membrane at 900 and 1100 ˚C. The resulting Sn-CF900 and Sn-CF1100 were fully characterized using XRD, TGA, SEM, TEM and XPS. They displayed similar structure to Sn-CF1000: interconnected carbon nanofibers with microspheres decoration and uniform distribution of Sn and N species along the nanofiber (**Figure 4.3**).

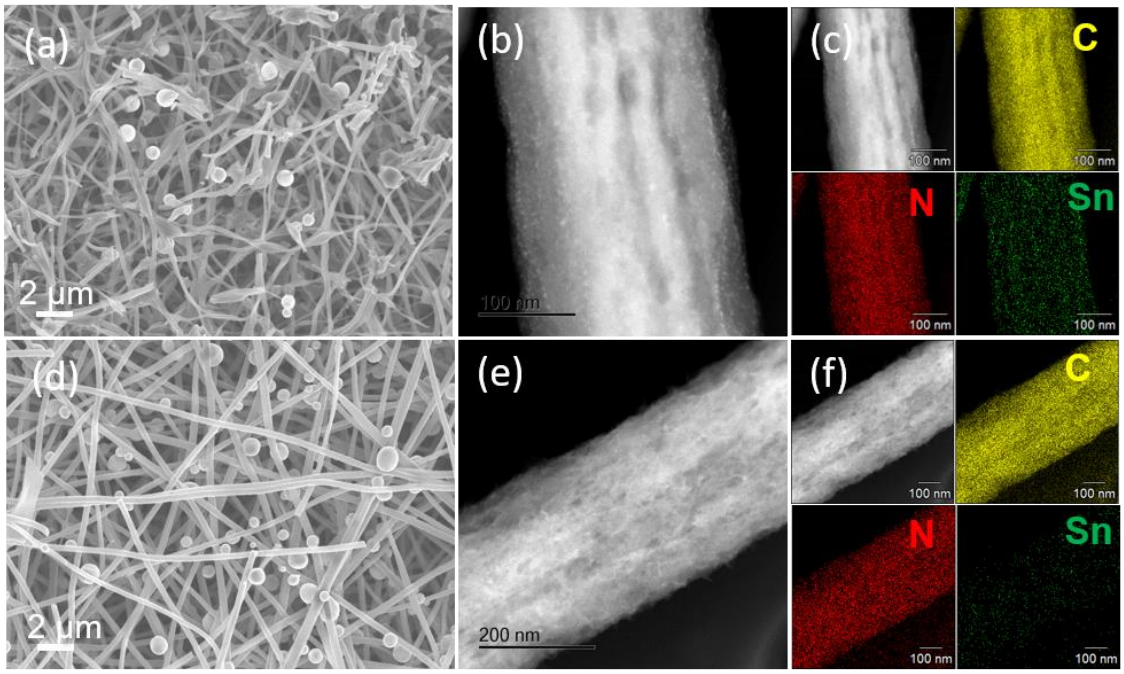

Figure 4.3 SEM and TEM characterizations of Sn-CF900 (a-c) and Sn-CF1100 (d-f): (a, d) are SEM images; (b, e) are dark field STEM images; (c, f) are the EDS mapping results.

The crystalline phase of the composites was also assigned to Sn (JCPDS 82-2264) (**Figure 4.4**a). However, the density of Sn nanodots on Sn-CF1100 was lower than that on Sn-CF900. It can be concluded that the density of Sn species on the nanofiber surface decreased with the increase of pyrolysis temperature from 900 to 1100 °C. This tendency is consistent with the XPS result in **Table 4.1**. Based on the TGA analyses (Figure 4.4b), the weight percentages of Sn in Sn-CF900 and Sn-CF1100 were ~ 50% and ~ 43%, respectively, which was slightly less than that of Sn-CF1000. The BET surface areas of the Sn-CF900 and Sn-CF1100 composites were calculated to be 230.4 m^2 $g^{-1}$and 423.2 m^2 g^{-1}, respectively (Figure 4.4c-d).

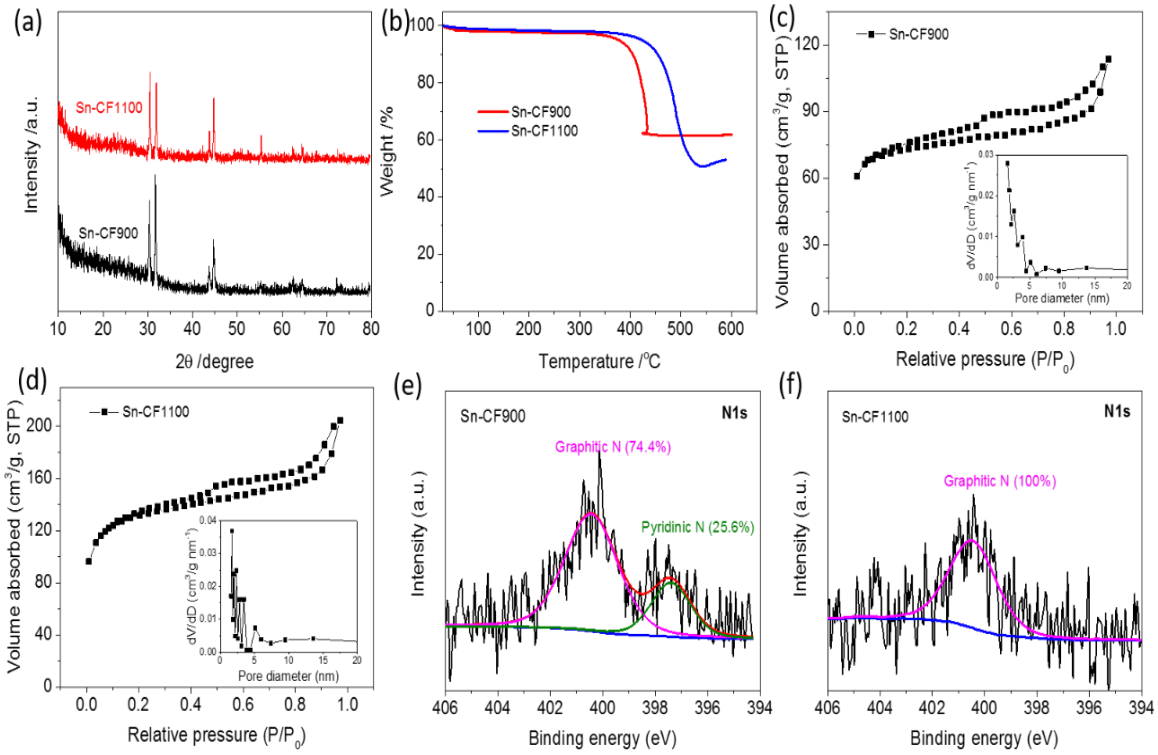

Figure 4.4 (a) XRD patterns, (b) TGA curves, (c, d) N_2 adsorption/desorption curves and (e, f) N1s XPS peaks of Sn-CF900 and Sn-CF1100 composites.

In addition, the content of N, particularly the pyridinic-N, decreased with the increased temperature (Table 4.1). The Sn-CF900 exhibited similar N-doping forms to the Sn-CF1000, whereas no pyridinic-N was detected on Sn-CF1100 (Figure 4.4e-f). Instead, small graphite nanosheets with a thickness of ~ 2 nm and a lateral size of ~ 20 nm were formed on Sn-CF1100 (Figure 4.3e). The pyridinic-N defects have been demonstrated to be active for the CO_2-to-CO conversion due to the ability to bind CO_2 and protons.[146] The abundance of pyridinic-N in Sn-CF900 and Sn-CF1000 may promote the electrocatalytic activity for CO_2ER.

Table 4.1 Relative content of Sn, O, N and C in Sn-CFs estimated from XPS analysis.

Atomic content (%)	C	N	O	Sn
Sn-CF900	62.81	2.83	28.56	5.79
Sn-CF1000	71.77	2.35	23.98	1.90
Sn-CF1100	94.41	1.21	4.22	0.16

4.3.2 CO_2ER Performance of Sn-CFs Catalysts

The CO_2ER performance of three different Sn-CFs hybrid catalysts was firstly evaluated by linear sweep voltammetry (LSV) studies (**Figure 4.5**a). All the catalysts exhibited similar current-voltage profile with a weak reduction peak at around -0.2 V vs. RHE which could be ascribed to the reduction of surface tin oxide. The Sn-CF900 and Sn-CF1000 showed higher current densities and more positive onset potentials compared with Sn-CF1100. The iR-corrected total current densities under stationary bulk electrolysis conditions exhibited the same trends as the LSV results (Figure 4.5b). The positive shift in the defined onset potential (the potential where current density reached 0.5 mA cm^{-2}) for Sn-CF900 and Sn-CF1000 indicates higher catalytic capability for CO_2ER. These three electrodes all generated H_2, CO and formate ($HCOO^-$) but with different faradaic efficiencies (FEs) (Figure 4.5c-e). At - 0.5 V, the HER prevailed and the dominant product from CO_2ER was CO. The FE for H_2 evolution (FE_{H2}) decreased with the negatively shifting potential and reached a minimum at ~ - 0.8 V. Meanwhile, the dominant CO_2ER product changed from CO to formate. This selectivity change may be attributed to the potential-dependent formation of different intermediates HCOO* and COOH* (respectively for $HCOO^-$ and CO formation) on the N-doped carbon with active Sn sites.[285] Sn-CF1100 displayed a catalytic behaviour typical of Sn metal: the formate production was promoted by the increased overpotential, as demonstrated for Sn NPs,[46] Sn NWs,[38] and Sn dendrites.[277] Sn-CF900 and Sn-CF1000 demonstrated a FE_{HCOO-} maximum at - 0.9 V and - 0.8 V, respectively. At - 0.8 V (corresponding to an overpotential of 600 mV, E^{Θ} for the $CO_2/HCOO^-$ reaction is -0.2 V vs. RHE in aqueous media[38]), a maximum FE_{HCOO-} of 65% was reached on Sn-CF1000, and the H_2 evolution was highly suppressed (FE_{H2} ~ 12%). The $HCOO^-$ partial current density (j_{HCOO-}) for Sn-CF900 and Sn-CF1000 was similar, much higher than that for Sn-CF1100 (Figure 4.5f). Sn-CF1000 exhibited a j_{HCOO-} of 4.7 mA cm^{-2}, about five times larger than that obtained using Sn-CF1100 (0.97 mA cm^{-2}).

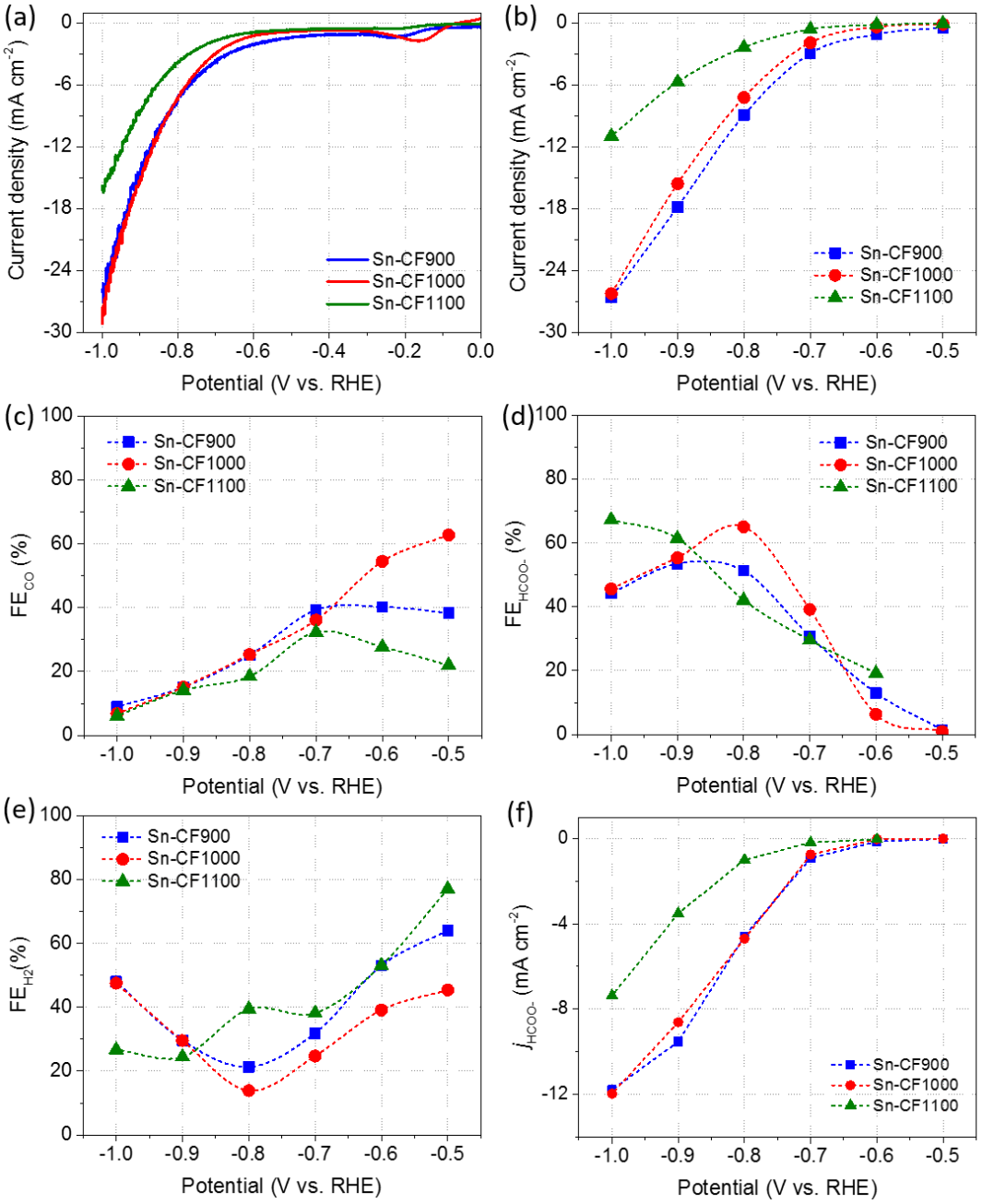

Figure 4.5 (a) LSV curves, (b) stationary CO_2ER average current densities, (c) FE_{HCOO^-}, (d) FE_{CO}, (e) FE_{H2}, and (f) j_{HCOO^-} during 50 min of electrolysis in CO_2-saturated 0.1 M $KHCO_3$ for three different Sn-CFs catalysts at different applied potentials.

To confirm that the products $HCOO^-$ and CO were generated from CO_2 rather than from the carbonaceous catalysts, electrolysis using Sn-CF1000 catalyst was carried out in an Ar-saturated CO_2-free electrolyte at a potential of - 0.8 V vs. RHE (**Figure 4.6**a). Only H_2 was detected, ruling out the possibility of decomposition or transformation of carbon structures into $HCOO^-$ and CO. It should be noted that the Faradaic efficiencies for CO and H_2 formation tested in phosphate buffer (KPi) was different from those tested in $KHCO_3$,

particularly the FE_{H2}. This may be caused by the chemically adsorbed phosphate ions on Sn sites during the electrolysis which were able to accelerate the catalytic HER rate. This was verified by the decreased FE_{H2} and increased FE_{CO} after transferring the electrode used in KPi to $KHCO_3$ for further CO_2ER electrolysis (Figure 4.6b).

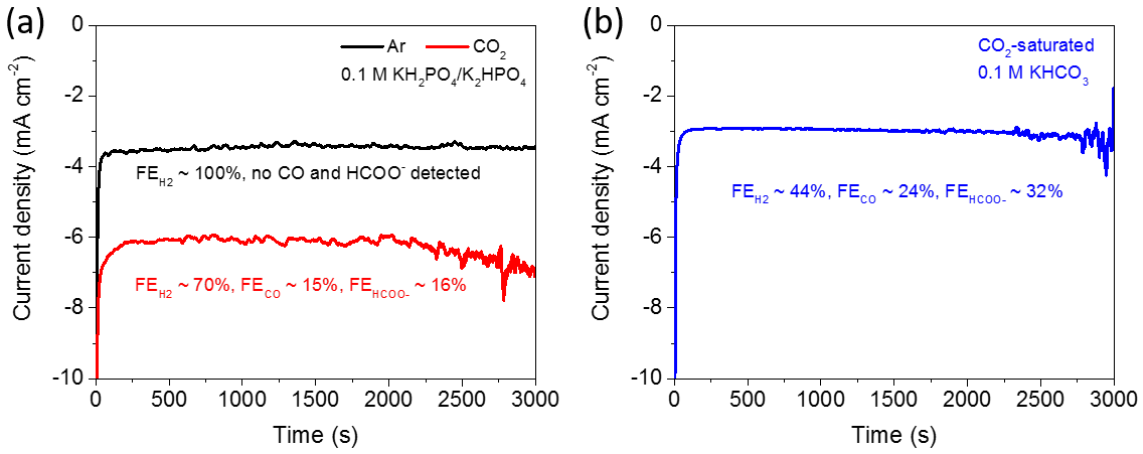

Figure 4.6 (a) Electrolysis curves of Sn-CF1000 in Ar-saturated (pH ~ 7.0) and CO_2-saturated (pH ~ 6.4) 0.1 M K_2HPO_4/KH_2PO_4 (KPi) at - 0.8 V vs. RHE. (b) The subsequent electrolysis in 0.1 M $KHCO_3$ (pH ~ 6.8) using the same electrode at - 0.8 V vs. RHE.

The effect of electrolyte concentration on the rate of formation of $HCOO^-$ (j_{HCOO-}) at the Sn-CF1000 electrode was investigated (**Figure 4.7**a-b). At -0.8 V, the j_{HCOO-} increased from 7.1 mA cm^{-2} to 12.1 mA cm^{-2} when the bicarbonate concentration ($[HCO_3^-]$) was increased from 0.1 M to 1.0 M, with the FE_{HCOO-} decreasing slightly from 65% to 57%. The plot of log (j_{HCOO-}) versus log ($[HCO_3^-]$) showed a slope of 0.27 (Figure 4.7c), indicating that HCO_3^- may be involved in the rate determining step for $HCOO^-$ formation. The rate and FE for H_2 evolution was also improved with increased $[HCO_3^-]$, whereas the CO production was not much affected; as previously reported.[286,287] Notably, a high j_{HCOO-} of 11.0 mA cm^{-2} can be obtained in 0.5 M $KHCO_3$ while maintaining a high FE_{HCOO-} of 62%. The reduction potential (- 0.8 V vs. RHE) and j_{HCOO-} are comparable to some state-of-the-art Sn-based catalysts such as Sn porous NWs,[38] Ag-Sn core-shell NPs,[125] and even some Sn-based gas-diffusion electrodes (**Table 4.2**).[287-289] This demonstrates the intrinsic high catalytic activity of Sn-CF1000 and excellent mass transport in the electrodes. The electrocatalytic performance of Sn-CF1000 may be further improved by using rationally designed gas diffusion electrodes in a flow-cell electrolyser, owing to the improved mass transport and reaction kinetics obtained.[290-292]

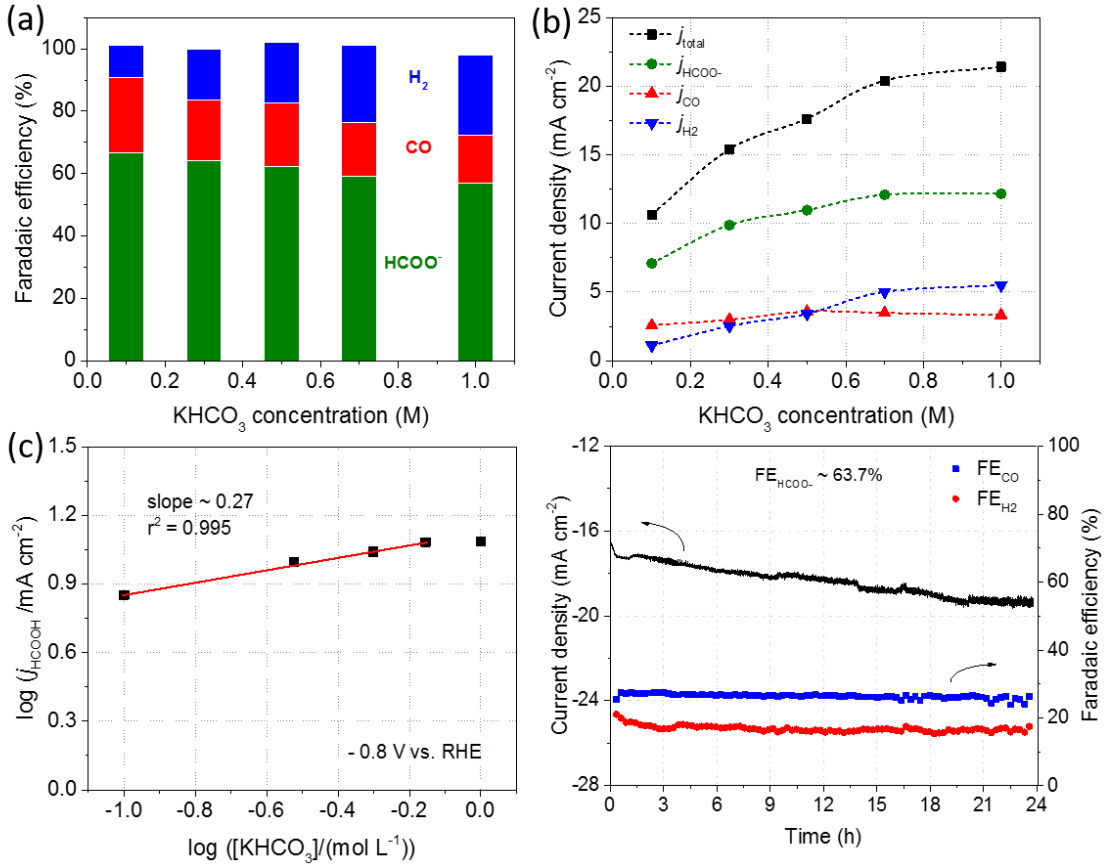

Figure 4.7 Faradaic efficiencies (a) and partial current densities (b) of three products on Sn-CF1000 at - 0.8 V vs. RHE in CO_2-saturated $KHCO_3$ solution with different concentrations; (c) The relationship between log ($[HCO_3^-]$) and log (j_{HCOO-}) for the Sn-CF1000 electrode; (d) Stability of Sn-CF1000 at - 0.8 V for 24 h in CO_2-saturated 0.5 M $KHCO_3$.

The stability of the Sn-CF1000 electrode for CO_2ER was evaluated under optimal conditions: electrolyte concentration was 0.5 M $KHCO_3$ and using a potential of - 0.8 V vs. RHE (Figure 4.7d). In the first 20 h of electrolysis, the current density slowly increased from 16.6 to 19.3 mA cm^{-2}. This may be mainly attributed to an increased local pH due to the fast consumption of protons at the electrode/electrolyte interface, which could further improve the reaction kinetics. Moreover, the increased accessibility of electrolyte containing reactants (proton and CO_2) to Sn active sites, the enhanced electron transport related to the reduction of tin oxide, and the electric-field-induced increase of cation concentration in the cathode compartment may also contribute. The FE_{H2} and FE_{CO} were almost uninfluenced and stabilizing around 16% and 26%, respectively over this 20 hr period. The FE_{HCOO-} at the end of the electrolysis was 63%, which is slightly higher than 62% for the first 50 min of

electrolysis. No obvious changes in electrode surface morphology were observed after the electrolysis for 24 h (**Figure 4.8**), indicating the structural stability of the Sn-CF1000 catalyst.

Table 4.2 Comparison of different Sn-based catalysts for the CO_2-to-$HCOO^-$ conversion

Catalysts	**Loading mass** ($mg\ cm^{-2}$)	**Electrolyte**	**Potential** (V vs. RHE)	**FE_{HCOO^-}**	**j_{HCOO^-} ($mA\ cm^{-2}$)**
Sn/SnO_x /Ti foil[230]	N/A	0.5 M $NaHCO_3$	-0.7	58%	1.04
Electrodeposited Sn GDE[293]	3.0	0.5 M $NaHCO_3$	-1.1	71%	5.77
SnO_2 GDE	N/A	0.5 M $KHCO_3$	-1.28	68%	4.08
Sn GDE[294]	5.0	0.5 M $KHCO_3$	-1.1l	~ 73%	~ 9.82
Sn foil[295]	N/A	0.5 M $KHCO_3$	-1.37	63.5	17.78
Sn/Nafion GDE[288]	0.7	0.5 M $NaHCO_3$	-1.17	70%	18.9
SnO_x/graphene [46]	0.21	0.1 M $NaHCO_3$	-1.16	93.6%	9.55
SnO_x/CB[46]	0.21	0.1 M $NaHCO_3$	-1.16	86%	4.64
Porous Sn NWs[38]	4.0	0.1 M $KHCO_3$	-0.8	80.1%	4.81
Sn NPs[38]	4.0	0.1 M $KHCO_3$	-0.8	58%	1.39
SnO_x dendrite /Sn foil[277]	N/A	0.1 M $NaHCO_3$	-1.16	56.9%	7.97
Ag-Sn core-shell NPs[125]	1.0	0.5 M $NaHCO_3$	-0.8	80%	15.6
Sn-CF1000 (this work)	0.97	0.5 M $KHCO_3$	-0.8	62%	11.0

Notes: 1) GDE, gas-diffusion electrode. 2) The potentials were converted to RHE scale based on the equation, E (vs. RHE) = E (vs. Ag/AgCl) + E (Ag/AgCl) + 0.0591×pH, by assuming the pH of CO_2-saturated 0.5 M and 0.1 M $NaHCO_3$ or $KHCO_3$ is 7.2 and 6.8, respectively. 3) If the FE_{HCOO^-} and j_{HCOO^-} values were not specifically stated, they were derived from graphical results or calculated from the available information.

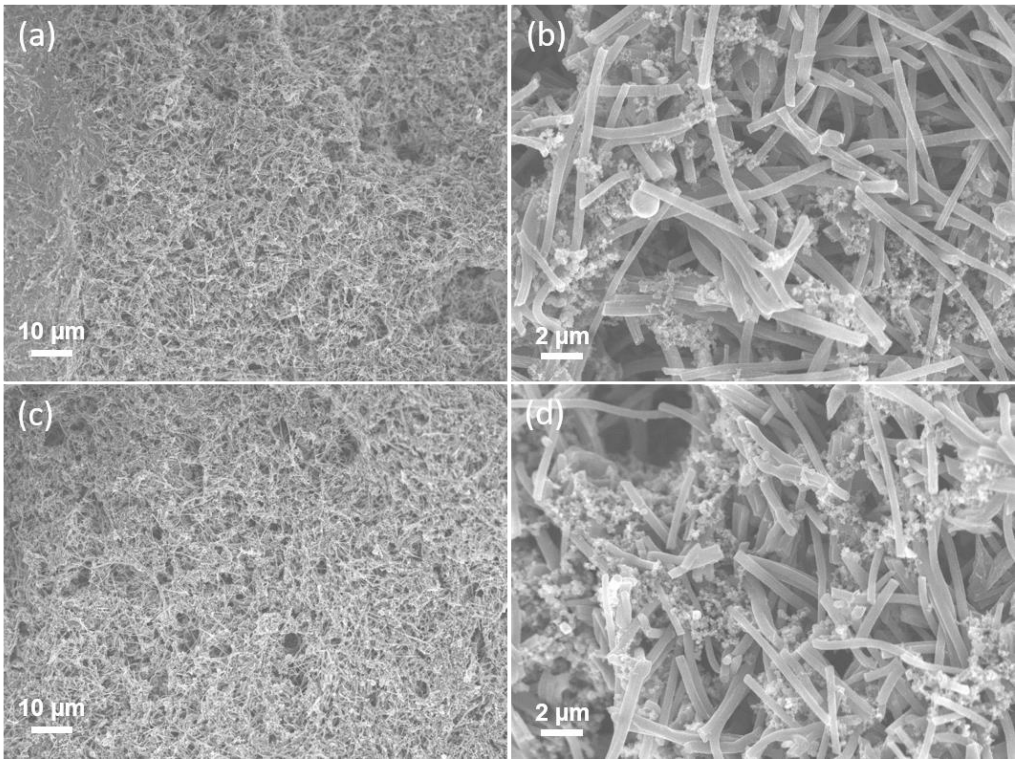

Figure 4.8 SEM images of Sn-CF1000 electrode before (a,b) and after (c,d) 24 h of electrolysis in CO_2-saturated 0.5 M $KHCO_3$ solution at - 0.8 V vs. RHE. The small particles are carbon blacks.

To gain some insight into the mechanism of formate formation on these three electrodes, Tafel plots were performed (**Figure 4.9**). Five elementary steps (Equation 1-5 in Figure 4.9) are proposed based on the previous reports[46,69]. The slope of the Tafel curve for Sn-CF900 and Sn-CF1100 was respectively 105 and 134 mV dec^{-1}, close to the 120 mV dec^{-1} expected for a rate determining step (RDS) of one-electron transfer forming adsorbed $CO_2^{\bullet -}$ (Equation 2).[30] In comparison, Sn-CF1000 exhibited a Tafel slope of 79 mV dec^{-1}, which is close to the theoretical value of 59 mV dec^{-1} for a rapid one-electron transfer step followed by a RDS.[30,50] This RDS may be the protonation of adsorbed $CO_2^{\bullet -}$ (Equation 3). These results suggest that Sn-CF1000 can bind the $CO_2^{\bullet -}$ intermediates much more strongly than the other two electrodes. This may account for the increased formate formation at relatively low overpotentials. However, it should be noted that this assignment of RDS has to be tentative given the experimentally determined Tafel slope value and the complexity of CO_2ER.[30] Future mechanistic studies are required to determine the reaction kinetics.

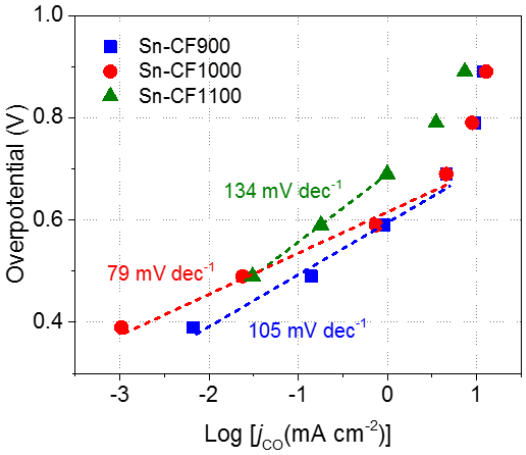

$$CO_2\ (solution) \rightarrow CO_2\ (ads) \quad (1)$$

$$CO_2\ (ads) + e^- \rightarrow CO_2^{\bullet-}\ (ads) \quad (2)$$

$$CO_2^{\bullet-}\ (ads) + HCO_3^- \rightarrow HCOO^{\bullet}\ (ads) + CO_3^{2-} \quad (3)$$

$$HCOO^{\bullet}\ (ads) + e^- \rightarrow HCOO^-\ (ads) \quad (4)$$

$$HCOO^-\ (ads) \rightarrow HCOO^-\ (solution) \quad (5)$$

Figure 4.9 Tafel plots of the three Sn-CF electrodes and a proposed reaction mechanism for formate formation.

The different catalytic performance of these three electrodes may mainly be attributed to the coverage of Sn species on the nanofiber surface and their interaction with N-doped carbon supporting. Compared with Sn-CF1100, the higher content of Sn in Sn-CF900 and Sn-CF1000 and a larger coverage of Sn nanodots on the nanofiber surface (Figure 4.3 and 4.4b, Table 4.1), may contribute to the higher catalytic current density observed. The low Sn coverage in Sn-CF1100 may afford big Sn particles a dominant role in formate production, leading to a typical Sn-like catalytic behaviour. The pyridinic-N defects can improve the electron donating ability of graphitic carbon frameworks due to the lone pair of electrons present.[146, 278] Due to the abundance of pyridinic-N, carbon nanofibers in Sn-CF900 and Sn-CF1000 would have stronger electronic interactions with the anchored Sn nanodots, making Sn nanodots more negatively charged than those in Sn-CF1100. The enhanced electron donation capability of Sn nanodots may promote the adsorption of CO_2 and $CO_2^{\bullet-}$, thus facilitating CO_2 reduction at relatively low overpotentials.[46,296] The Sn-CF1000 has a relatively low Sn coverage on the nanofiber surface compared with Sn-CF900; however, it may have a stronger Sn-N interaction, as reflected by its smaller Tafel slope (Figure 4.9). A balance between Sn coverage and Sn-N interaction may lead to the increased formate selectivity of Sn-CF1000.

4.3.3 Structural Analysis of Atomically Dispersed Sn-N-C Catalysts

To demonstrate the role of atomically dispersed Sn species on the N-doped carbon nanofibers for CO_2ER, the Sn particles were removed via a simple acidic leaching process.

The Sn-CF1000 composite with the best CO_2ER performance was chosen as a case study. The resultant atomically dispersed Sn catalyst (denoted as AD-Sn/N-C1000), exhibited only two distinct peaks at ~ 26.1° and 43.2° in the XRD pattern (**Figure 4.10**a), which can be ascribed to the (002) and (101) planes of the graphitic carbon frameworks.[297] No peaks attributable to Sn or SnO_x were detected. The weight loss was remarkable after being annealed at 650 °C in air (Figure 4.10b). The weight percentage of Sn in AD-Sn/N-C1000 was evaluated to be approximately 1%. These results indicated that big Sn particles were effectively removed.

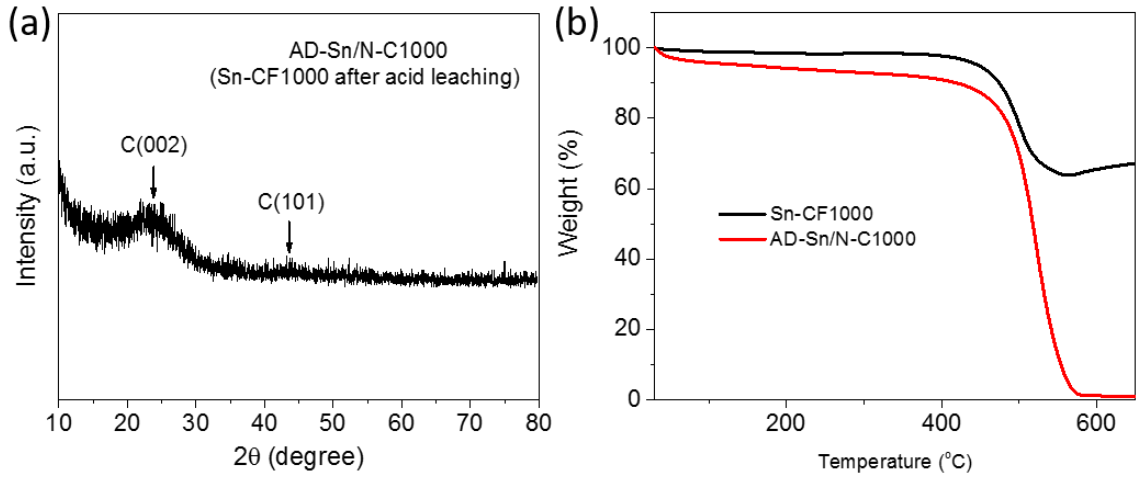

Figure 4.10 (a) XRD pattern of the AD-Sn/N-C1000, (b) TGA curves of Sn-CF1000 and AD-Sn/N-C1000.

Scanning transmission electron microscope (STEM) imaging was also used to analyse the sample after acidic leaching. No Sn NPs were detected in the bright field and dark field STEM images (**Figure 4.11**a-b). Under the aberration-corrected high-angle annular dark field STEM (HAADF-STEM) mode, a number of atomically dispersed bright spots were observed in-between the carbon layers or on the surface (Figure 4.11c-d), which may be ascribed to Sn atoms or clusters. The isolated Sn atoms can be discerned in the carbon support because of the different Z contrasts of Sn, N and C. The elements Sn and N were homogeneously dispersed along the carbon nanofiber (STEM-EDS analysis, Figure 4.11e). Moreover, the AD-Sn/N-C1000 demonstrated a different binding energy in the Sn3d XPS spectrum compared with Sn-CF1000 (Figure 4.11f). The binding energy of the $Sn3d_{5/2}$ peak (486.3 eV) was higher than that for Sn^0 (484.7 eV) and lower than that for Sn^{2+} (486.7 eV), revealing the ionic $Sn^{\delta+}$ ($0 < \delta < 2$) nature of Sn in AD-Sn/N-C1000. This unique valence state is similar to that recently reported for the Ni in pyridinic-N coordinated Ni-single-atoms

catalyst.[169] In light of the abundance of pyridinic-N defects in Sn-CF1000, it may be reasonable to propose that Sn atoms in AD-Sn/N-C1000 are coordinated by pyridinic-N, and the formed Sn-N moieties may act as new active sites for CO_2ER.

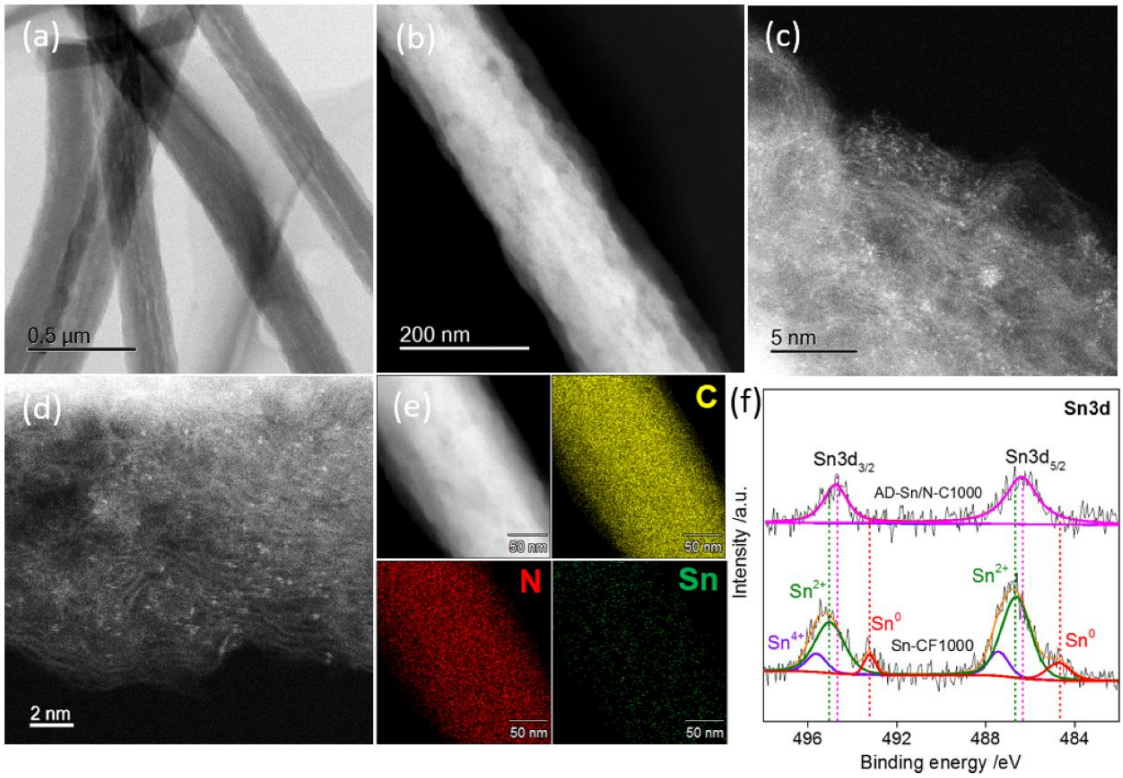

Figure 4.11 (a) Bright field STEM image of the AD-Sn/N-C1000; (b-d) HAADF-STEM images of AD-Sn/N-C1000 under different magnifications; (e) EDS mapping results of the nanofiber in (b); (f) Sn3d XPS spectra for AD-Sn/N-C1000 and Sn-CF1000.

4.3.4 CO_2ER Performance of Atomically Dispersed Sn-N-C Catalysts

The CO_2ER activity of the AD-Sn/N-C1000 catalyst is summarized in **Figure 4.12** with N-doped carbon nanofibers (N-C1000) as control. The AD-Sn/N-C1000 catalyst exhibited a much larger current density, and a more positive onset potential of ~ - 0.4 V (vs. RHE) compared with ~ - 0.8 V for N-C1000 (Figure 4.12a). At - 0.8 V, the current density of AD-Sn/N-C1000 reached 5.12 mA cm^{-2}, ~ 7.6 times larger than 0.67 mA cm^{-2} for N-C1000. These results indicate that the incorporation of Sn atoms enhanced the electrocatalytic activity of N-doped carbon nanofibers. The primary products produced using AD-Sn/N-C1000 and N-C1000 were CO and H_2. They showed a similar volcano-like FE_{CO} dependence on the applied potentials, peaking around - 0.6 V (Figure 4.12b), yet the AD-Sn/N-C1000 exhibited substantially higher FE_{CO} and j_{CO}. At - 0.6 V (corresponding to an overpotential

of 490 mV for CO formation), the AD-Sn/N-C1000 attained a maximum FE_{CO} of 91% and a j_{CO} of 1.75 mA cm^{-2} (Figure 4.12c), much higher than those (64%, 0.2 mA cm^{-2}) for N-C1000. This performance is comparable to the recently reported 3D N-doped graphene foam,[147] Fe-N-C,[165] Mn-N-C,[158] Ni-N-C,[169] and Cu-Sn catalysts[298]. It may be further improved by promoting the mass transport via the use of rationally designed electrode and reactor structures (i.e., use of a gas diffusion electrode in a flow-cell).[299] Due to the low content of Sn doping (1 wt%), the mass specific CO partial current density of AD-Sn/N-C1000 was over 16 times larger than that of N-C1000 over a moderate overpotential range of - 0.6 to - 0.8 V (Figure 4.12d).

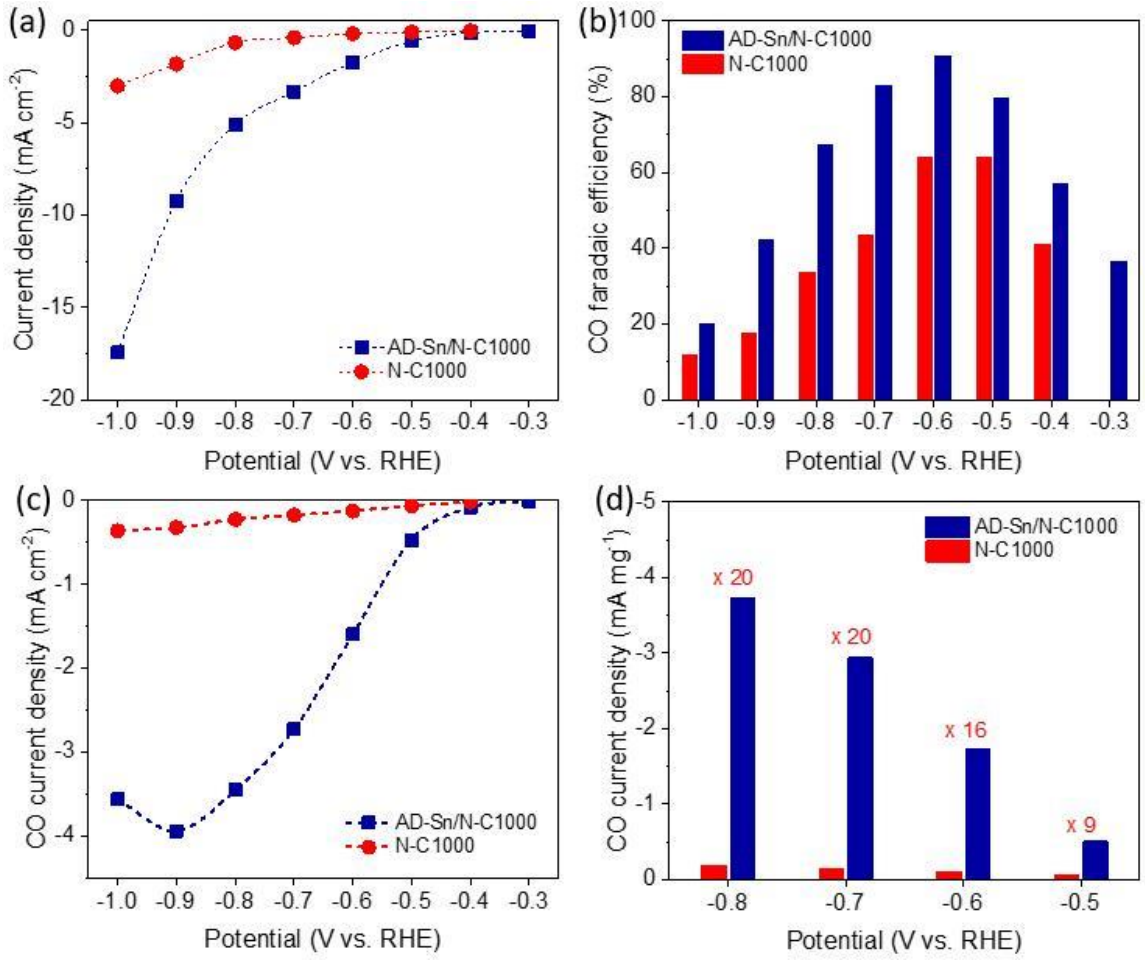

Figure 4.12 The catalytic profile of AD-Sn/N-C1000 and N-C1000 catalysts: (a) Stationary CO_2ER average current densities at different potentials in CO_2-saturated 0.1 M $KHCO_3$; (b) CO faradaic efficiency and (c) partial current density for these two catalysts; (d) Comparison of the mass specific CO partial current densities under four different potentials.

In addition, the AD-Sn/N-C1000 catalyst exhibited an excellent stability. During electrolysis over a 24 h period, the current density was kept almost stable at around 1.55 mA

cm^{-2}, and the FE_{CO} only slightly decreased from 91% to 84% (**Figure 4.13**a). After the prolonged electrolysis, the electrode was further characterized by SEM. No obvious morphological changes were observed compared with the sample before electrolysis (Figure 4.13b-d). This implies that the structure of this catalyst was stable under the operating conditions.

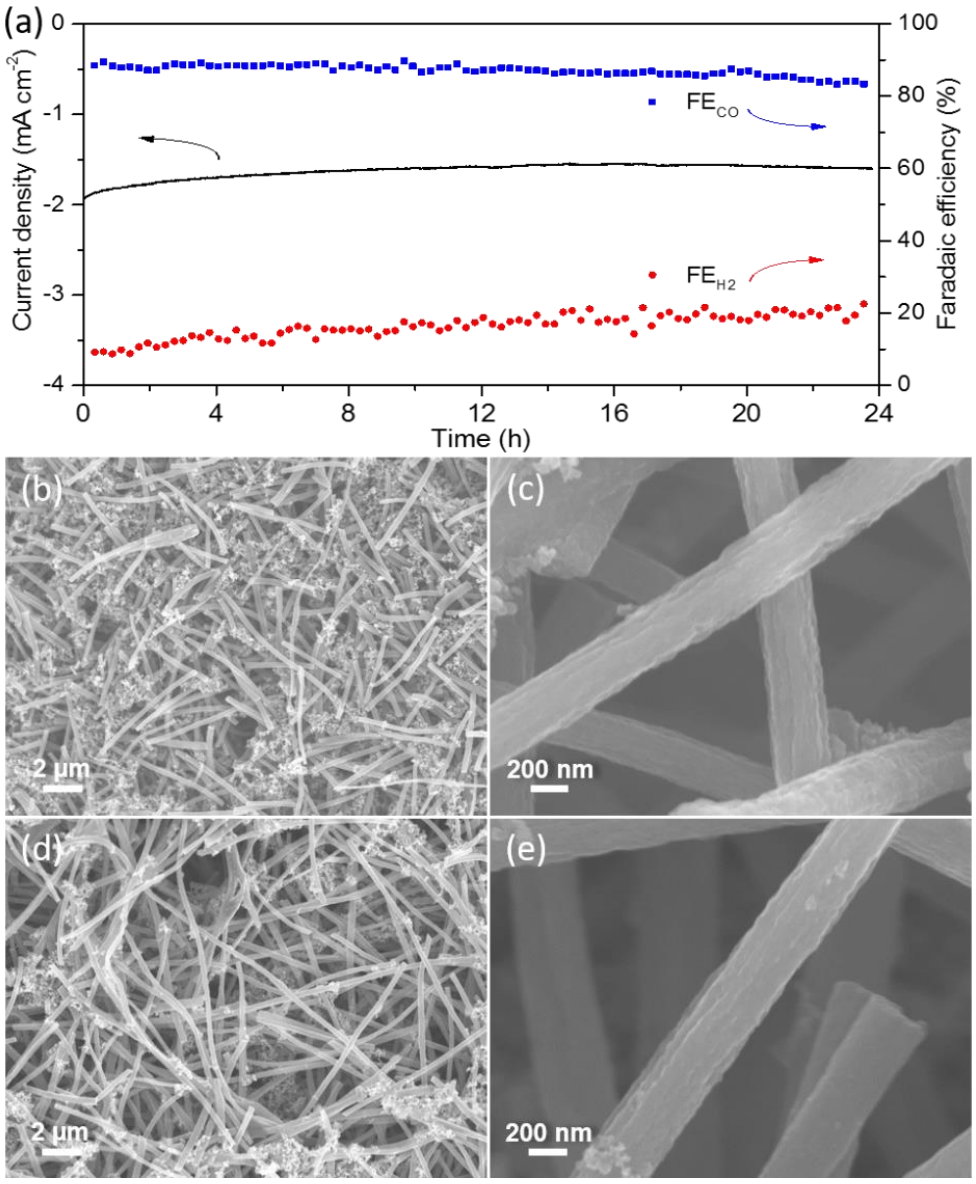

Figure 4.13 (a) Prolonged electrolysis of AD-Sn/N-C1000 in CO_2-saturated 0.1 M $KHCO_3$ solution at - 0.6 V vs. RHE for 24 h and the corresponding product analyses. SEM images of AD-Sn/N-C1000 electrode before (b, c) and after (d, e) 24 h of electrolysis; the small particles are carbon blacks.

To obtain some insight into the mechanism of CO formation on this AD-Sn/NC1000, Tafel plots were performed with NC-1000 as control (**Figure 4.14**a). The AD-Sn/N-C1000

catalyst demonstrated a Tafel slope of 140 mV dec^{-1}, which was close to the theoretical 120 mV dec^{-1} for a mechanism where the initial single-electron transfer forming $CO_2^{\bullet-}$ intermediates is the rate-determining step for the CO_2-to-CO conversion.[30] In contrast, N-C1000 exhibited a slope of 239 mV dec^{-1}, evidencing its sluggish kinetics. This result is in agreement with other reported N-doped carbons.[145-147] It should be noted that the catalytic behaviours and structure of AD-Sn/N-C are very similar to active transition metal doped N-carbons,[146,165,169] in which metal-N moieties are active sites for CO formation. It is reasonable to infer that Sn-N moieties are the active centres in the AD-Sn/N-C1000 catalyst.

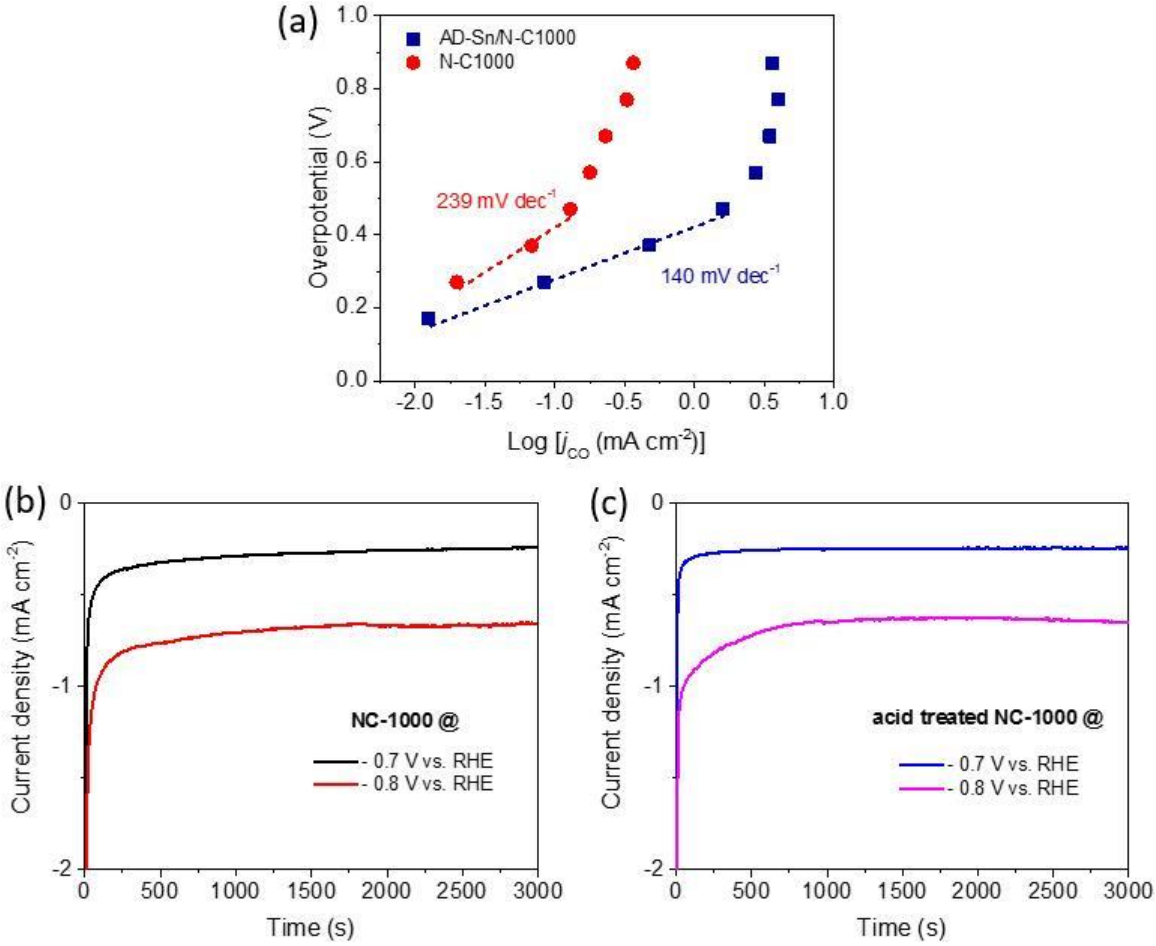

Figure 4.14 (a) Tafel plots of AD-Sn/N-C1000 and N-C1000 catalysts for CO production. Electrolysis curves of N-C1000 (b) and acid treated N-C1000 (c) at - 0.7 V and - 0.8 V vs. RHE in CO_2-saturated 0.1 M $KHCO_3$.

To reveal the origin of the promoted CO formation on AD-Sn/NC1000, a series of control experiments and structural analyses were carried out. Firstly, the N-C1000 control was treated with acids same as that for the AD-Sn/NC1000 and investigated for CO_2ER under the same conditions. The acid treated N-C1000 showed nearly identical catalytic current

densities to the untreated samples, ruling out any contribution to the improved performance on AD-Sn/N-C1000 from functional groups generated during the acidic treatment (**Figure 4.14**b-c).

XPS analyses showed that both the AD-Sn/NC1000 and NC-1000 had almost the same content and structure of N species (**Figure 4.15**a-b). Moreover, the NC-1000 catalyst had a larger specific surface area (Figure 4.15c-d), thus excluding that the promoted catalytic performance of AD-Sn/NC1000 arose from the influence of surface area and N-doping structures. Therefore, Sn doping was considered as the major contributor. The improved kinetics for CO formation on AD-Sn/N-C1000 were mainly attributed to the enhanced stabilization of $CO_2^{\bullet-}$and subsequently facilitated formation of *COOH intermediates on the Sn-N moieties. This may also account for the high selectivity and activity for CO formation on the Sn atoms modified N-doped carbon nanofibers.

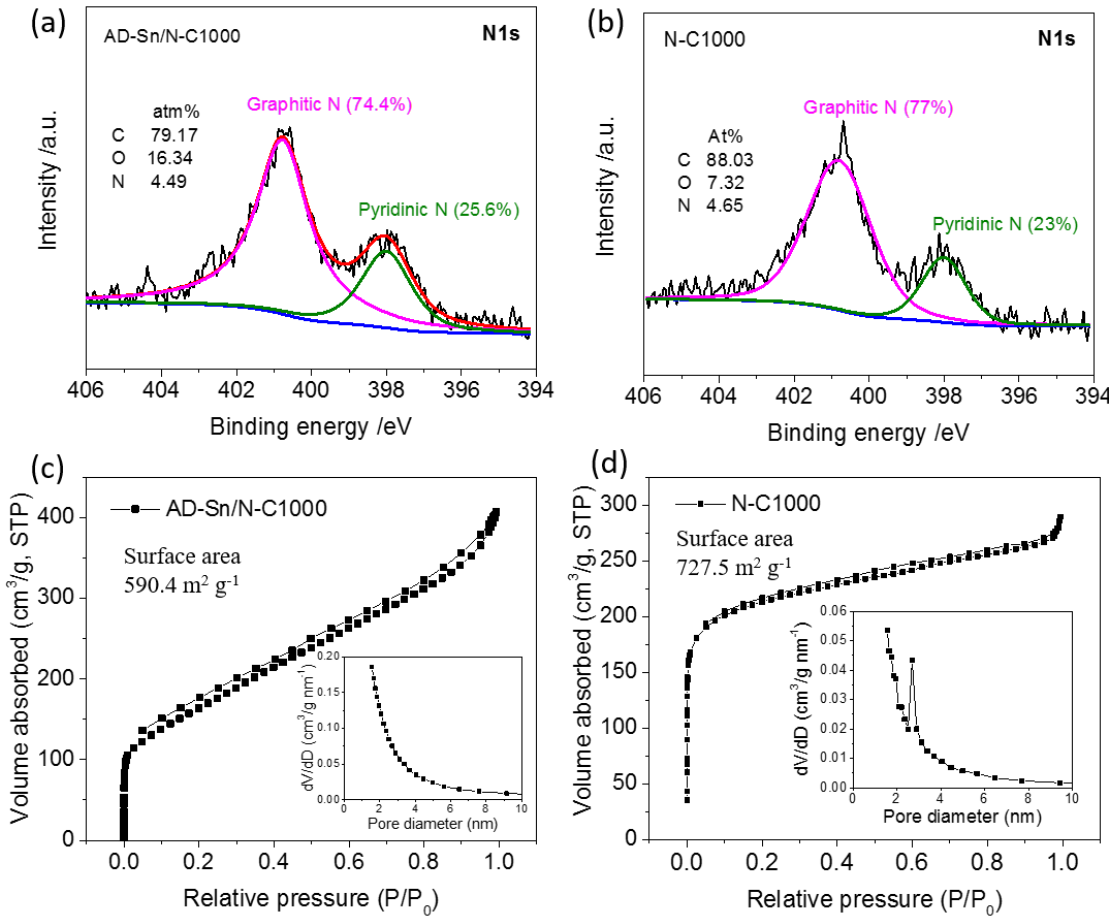

Figure 4.15 (a, b) N1s XPS spectra of the AD-Sn/N-C1000 and N-C1000. (c, d) Nitrogen adsorption/desorption curves of the AD-Sn/N-C1000 and N-C1000 composites and the corresponding BJH pore distribution curves.

4.4 Conclusion

In summary, a Sn modified N-doped porous carbon nanofiber (Sn-CF) catalyst has been developed using a straightforward electrospinning technique in combination with a pyrolysis method. The interaction between Sn species and carbon nanofiber supports has been investigated by simply controlling the pyrolysis temperature. It has been found that the electrocatalytic activity of this hybrid catalyst can be tuned by the structure and content of Sn and N species. The abundance of Sn active sites and the strong electronic interaction between pyridinic-N doped carbon and Sn NPs may contribute to the promoted CO_2-to-$HCOO^-$ conversion on Sn-CF1000 by improving the binding strength of $CO_2^{\bullet -}$ intermediate. The high activity and selectivity for CO production over the Sn atoms modified nanofibers may have arisen from the intrinsically high activity of the formed Sn-N_x moieties. Future mechanistic studies by *in situ* characterization techniques coupled with theoretical calculation are needed to understand the reaction kinetics behind it. This work not only demonstrates that engineering the metal-carbon interfaces is an effective way to tune the CO_2ER performance of Sn based catalysts, but also provides a route to the development of switchable non-precious metal hybrid electrodes for conversion of CO_2 to valuable $HCOO^-$ or CO as demanded. It should also be pointed out that this well-established electrospinning technology can also be readily employed to produce other metal-based hybrid catalysts integrated with heteroatom-doped carbon nanofibers (i.e. N, B, P) for CO_2ER, further expanding the materials family and promoting the research.

Chapter 5 Engineering Amine Modifiers of Ultrasmall Au Nanoparticles on Reduced Graphene Oxide Sheets for Enhanced CO_2-to-CO Electroreduction

This chapter is adapted from the article, "Engineering Surface Amine Modifiers of Ultrasmall Gold Nanoparticles Supported on Reduced Graphene Oxide for Improved Electrochemical CO_2 Reduction", by Yong Zhao, Caiyun Wang, Yuqing Liu, Douglas R. MacFarlane, Gordon G. Wallace, which was published in Adv. Energy Mater. (2018, 8, 1801400). Adapted with permission from Wiley-VCH.

5.1 Introduction

The major challenges of CO_2ER are the poor energy efficiency and product selectivity due to the large overpotential for CO_2 activation, complicated CO_2 reduction pathway and competitive H_2 evolution reaction (HER).[22] Au is one of the best electrocatalysts that can overcome these barriers for the CO_2-to-CO conversion.[30] Nanostructured Au such as nanoparticles (NPs)[68], mesoporous inverse opals[219], ultrathin nanowires[67] and field-enhanced needles[72] have demonstrated impressive electrocatalytic activity and selectivity. However, the majority of Au atoms are restrained in the particle core where no reaction occurs, resulting in poor utilization.

Downsizing the Au particle to sub-5 nm can significantly increase Au utilization efficiency, which is highly desirable for reducing cost and promoting large-scale application.[300-302] However, such small Au NPs are typically obtained from complicated colloidal synthesis coupled with a tedious surfactant-removal process. The residual surfactants often deteriorate the catalytic activity as well.[303,304] Moreover, the increased low-coordinated corner sites are more favourable for the competitive HER, lowering the CO selectivity.[68,305]

As discussed in Chapter 1, the CO selectivity of small Au NPs may be improved by tuning their binding ability to reaction intermediates (*COOH or *CO) via tailoring the electronic structure and catalytic environment of Au active sites. Apart from the strategy of modulating metal-support interfaces applied in Chapters 3 and 4, engineering the surface modifiers of

metal catalysts is a simple and effective approach to achieve this goal. In fact, it has demonstrated impressive capability to tune the electrocatalytic selectivity of Au catalysts. For example, a thiol-tethered pyridinium monolayer modification on Au foil improved the selectivity for formate formation via a proton-induced desorption mechanism.[246] The phenylethanethiol-protected Au_{25} clusters provided an anionic charge environment facilitating CO_2 adsorption and C=O bond activation, showing a promoted onset potential (< 90 mV) and a superior FE_{CO} of ~ 100% (at -1.0 V vs. RHE).[306] The N-heterocyclic-carbene functionalized 7 nm Au NPs exhibited improved reaction kinetics for CO formation due to the strong electronic donation from carbene to the Au NP surface.[244] Recently the adsorbed CN^- and Cl^- anions were demonstrated as promoters for CO production on Au nanostructured electrodes because of the improved stabilization of the *COOH intermediates.[249]

Amine species with the ability of promoting CO_2 adsorption and suppressing HER have great potential in this regard.[141,307-309] Their modifications have remarkably promoted the CO_2ER on Cu,[241,254] Ag,[74,247,309] MoS_x,[141] and N-doped carbon nanotubes.[144] However, the influence from amines with different molecular structures has not been revealed. Amine-modified Au for CO_2ER has not been reported either. Therefore, systematic research on amine-modified sub-5 nm Au NPs is highly desirable. It may not only provide an opportunity to remedy the selectivity problem of ultrasmall Au NPs but also a deeper insight into the effect of ligand-induced surface functionalization for CO_2ER on Au.

In this chapter, work has been carried out to develop a reduced graphene oxide (rGO) sheets supported ultrasmall Au NPs catalyst for CO_2-to-CO conversion with high Au utilization. This rGO-Au composite was synthesized via a facile and surfactant-free wet chemistry method. It not only delivered a high Au utilization efficiency, but also provided a clean platform to investigate the influence of surface modification on CO_2ER. Five common primary amines with different structures were selected to modify the rGO-Au composite to systematically investigate the influence of amine structures on CO_2ER. An amine-structure-dependent surface modification effect has been revealed. Linear amines promoted the CO formation whereas the branched polyamine greatly depressed it. Among them, the linear oleylamine exhibited the best promotion effect with more than 20% increase in the CO selectivity while not deteriorating the catalytic activity. Ultrahigh Au-specific mass activities (> 100 A g^{-1}) coupled with improved CO faradaic efficiencies (> 60%) were achieved at the moderate overpotential range of 450-600 mV.

5.2 Experimental

5.2.1 Synthesis of rGO-Au Catalysts

Synthesis of rGO dispersion: The GO was prepared according to the modified Hummers method.[310] The rGO dispersions were synthesized by a simple thermal reduction method: GO (62.5 mg) was dispersed in ultrapure water (250 mL) to obtain a 0.025 wt % solution, followed by addition of ammonia solution (25 wt%, 1 mL). This mixture was heated at 95 °C and stirred for 3 h. After cooling to room temperature, the rGO dispersion was obtained. The mass concentration of the rGO dispersion was measured by a freeze-drying method, and it was about 0.17 mg/mL.

Synthesis of rGO-Au composite: Au NPs were synthesized on rGO sheets according to a previous report with some modifications.[300] The $HAuCl_4$ aqueous solution (50 mM, 100 µL) was added to the freshly-prepared rGO dispersion (10 mL) under vigorous stirring at room temperature. After 15 min, the resultant products were collected by centrifugation and rinsed three times with ethanol/water (1:3 v/v) solution to remove the residual $HAuCl_4$. Sponge-like rGO-Au composite (1.67 mg) was obtained after a freeze-drying process. The content of gold in the composite was evaluated by TGA analysis to be about 42 wt%. The composite of rGO-Au120 was obtained by annealing the freshly lyophilized rGO-Au composite in an oven at 120°C for 10 h in air atmosphere. In this process, the ultrasmall Au NPs aggregated and grew into relatively large NPs.

Synthesis of rGO-Au-amine composite: Amine solutions with a concentration of 0.15 M were firstly prepared by dissolving the pure amines in water (for EDA, PA and PEI) or ethanol (for HA and OLA). The obtained rGO-Au wet composite was then dispersed into the amine solution (3 mL) and stirred for 10 min to obtain a uniform dispersion. It was collected by centrifugation and washed with ethanol three times to remove the weakly-attached amine molecules. The rGO-Au-amine composite was finally obtained via lyophilisation. No obvious mass loss or gain was found after amine modification.

Synthesis of rGO-amine composites: To prepare rGO composites, the $KHCO_3$ solution (0.1 M, 2 mL) was first added into the rGO aqueous dispersion (10 mL). The flocculated rGO sheets were collected by centrifugation at 8,000 rpm for 10 min and then washed with water twice. They were modified with different amine solutions using the same procedure to the

rGO-Au-amine composites. The rGO and rGO-amine composites were obtained via lyophilisation.

5.2.2 Fabrication of Working Electrode

A microporous carbon black layer was painted on the surface of carbon paper (1 × 1 cm^2) by brushing an ink containing Vulcan XC72R carbon black (CB) and polytetrafluoroethylene (PTFE). The CB loading was ~0.9 mg cm^{-2}, and the PTFE content was ~15 wt%. The catalyst ink was prepared by mixing 1.67 mg of rGO, rGO-amine, rGO-Au or rGO-Au-amine composite, 1.8 mL of ethanol/water (2:3 v/v) solution and 0.1 mL Nafion solution (5 wt%) with ultrasonication for 15 min. An aliquot of the catalyst ink (70 µL) was dropped evenly on the CB layer (1cm^2) and kept at room temperature overnight to evaporate most of the solvents. Working electrodes were obtained by annealing them at 70 ℃ for 3 h. The loading mass of composite catalyst was about 71 µg cm^{-2}, and the Au loading in Au-containing electrodes was then calculated to be about 30 µg cm^{-2}. For the rGO-Au120 and rGO-Au120-OLA electrodes, the loading mass of composites was increased to 112 µg cm^{-2} to improve the response current due to the poor catalytic activity of large Au NPs.

5.2.3 Electrochemical Measurements and Product Analysis

All the electrochemical measurements and product analysis of bulk electrolysis experiments were performed according to the methods and procedures presented in Chapter 2.

5.3 Results and Discussion

5.3.1 Structural Analysis of rGO-Au Catalysts

Partially reduced graphene oxide sheet with high surface area and abundant defective sites was used as a template for the growth of Au NPs. The reaction between the oxidative $AuCl_4^-$ ions and reductive O- and N-containing functional groups on rGO leads to the spontaneous formation of ultrasmall Au NPs on rGO sheets.[300] The defective sites of rGO may act as the adsorption and nucleation sites, and their strong interactions with Au atoms lead to the stabilization of Au NPs. The formed rGO-Au composite was then modified with propylamine (PA), hexylamine (HA), oleylamine (OLA), ethylenediamine (EDA) or polyethyleneimine (PEI) to further tune the electrocatalytic properties (**Figure 5.1**a). These

amines with different molecular structures or functionality density may induce different Au-amine interactions and lead to different influences on CO_2ER.

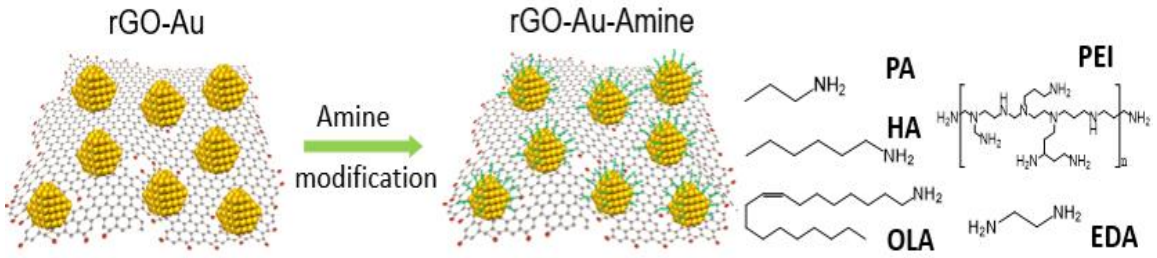

Figure 5.1 Schematic illustration of amine modification on the rGO-Au composite.

The rGO-Au composite was investigated by X-ray diffraction (XRD), which confirmed a face-centred cubic (fcc) crystal structure of Au NPs (**Figure 5.2**a). The scanning electron microscopy (SEM) and transmission electron microscopy (TEM) studies revealed a sheet-like morphology and a uniform dispersion of Au NPs on rGO (Figure 5.2b-d). The size distribution of Au NPs exhibited a typical Gaussian shape with an average diameter of 2.4 nm and a narrow dispersion of 0.5 nm (inset of Figure 1e). These Au NPs were nearly spherical in shape without clearly exposed facets (high-resolution TEM image, HRTEM, Figure 1f). The discerned lattice spacing of 0.23 nm can be ascribed to the (111) plane of fcc-Au, consistent with XRD analysis. Most of the particles smaller than 2 nm are Au clusters without specific crystal structure (high-angle annular dark field scanning TEM image, HAADF-STEM, Figure 1g). Au atoms were also detected, which may be stabilized at the defective sites of rGO owing to Au-O or Au-N interactions.[300] The Au content in the composite was evaluated by thermo-gravimetric analysis, and was ~42 wt% (**Figure 5.3**a). According to an Au cuboctahedra model, the fraction of surface atoms on such small NPs should be close to that of bulk atoms, indicating that this Au catalyst may deliver a high mass activity for CO_2ER.[68]

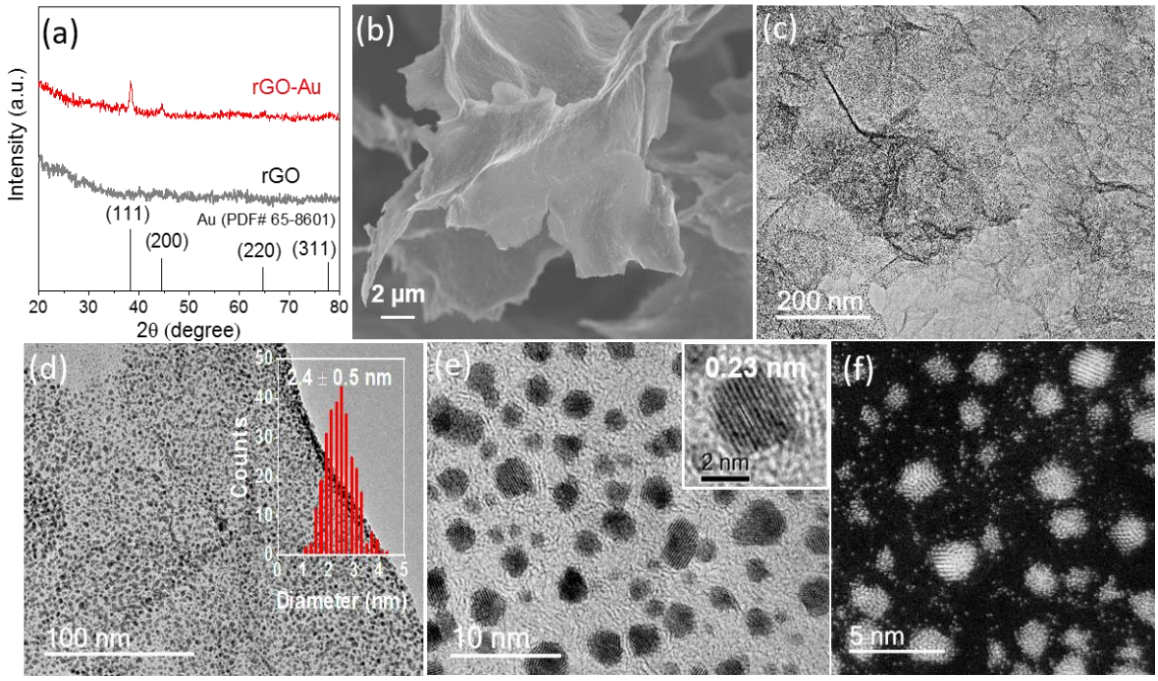

Figure 5.2 (a) XRD patterns of rGO-Au and rGO; (b) SEM and (c-d) TEM images of rGO-Au, inset of (d) histogram of Au NP sizes; (e) HRTEM and (f) HAADF-STEM images of rGO supported ultrasmall Au NPs.

With the amine modification, a moderate aggregation of the composite sheets occurred, which may be caused by the electrostatic interaction between the positively charged amine molecules and the negatively charged rGO sheets (**Figure 5.3**b). The presence of Au clusters and single atoms were also observed after amine modification (Figure 5.3c), indicating that the interaction between Au and rGO was strong and could inhibit the detachment or severe aggregation of these Au species during amine modification. The morphology, crystallinity and size distribution of Au NPs were nearly unchanged, as shown in **Figure 5.4**. Therefore, the influences of particle size could be ruled out, and the effect of different amine modifiers on rGO supported ultrasmall Au NPs could be demonstrated by investigating their CO_2ER performances.

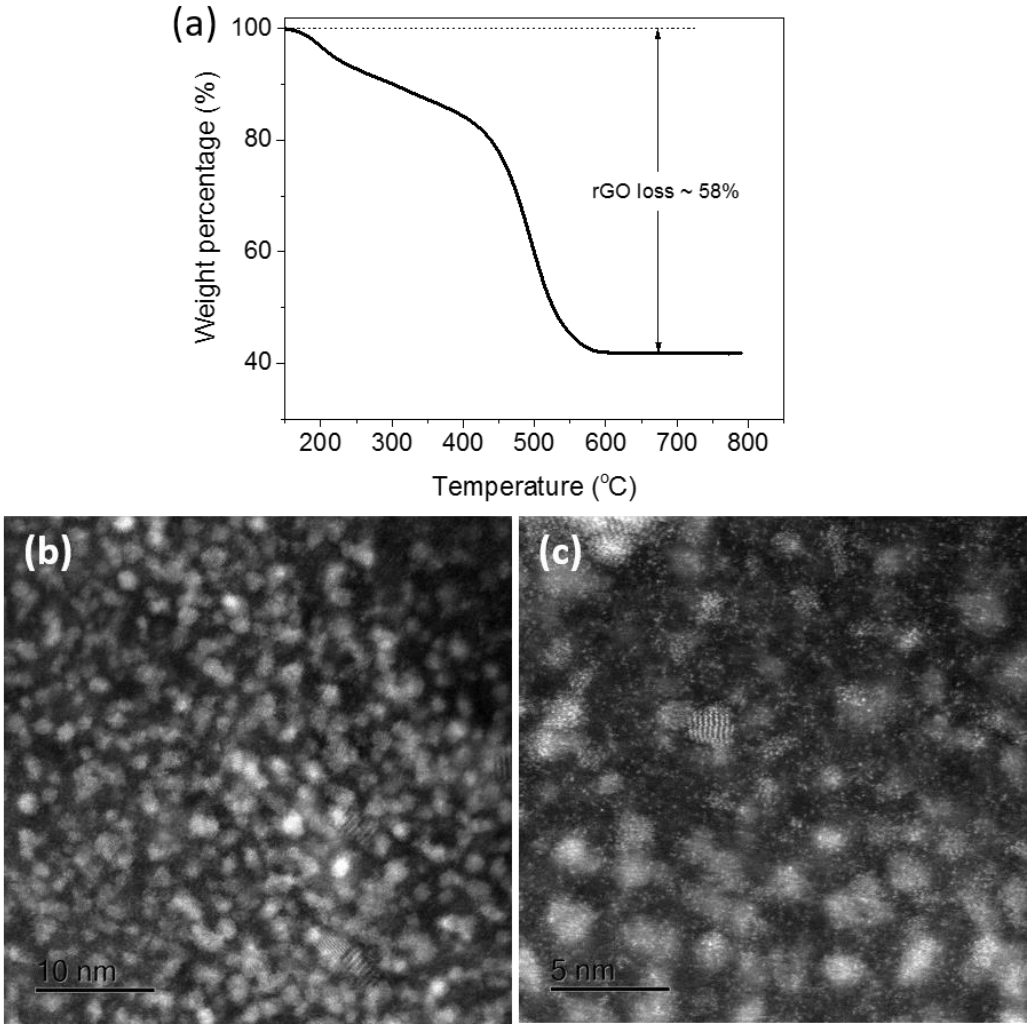

Figure 5.3 (a) TGA analysis of the lyophilized rGO-Au composite. (b-c) dark field STEM images of oleylamine modified rGO-Au sample (rGO-Au-OLA).

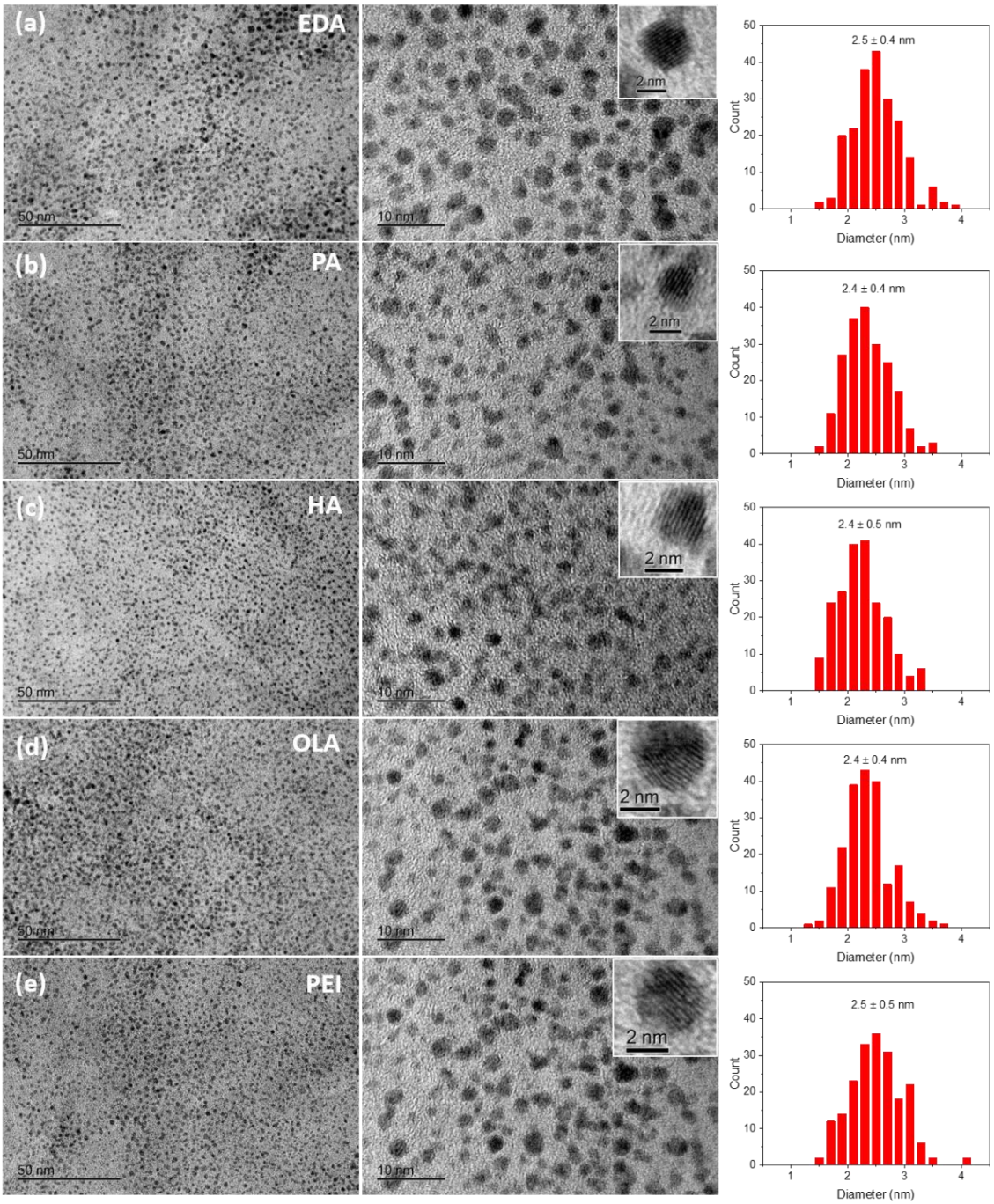

Figure 5.4 TEM and HRTEM images of five different rGO-Au/amine composites and their particle size distribution. Statistical histograms were obtained by manually counting 200 particles.

It was also noticed that the structural defects on rGO were slightly reduced after amine modification, as evidenced by the decreased I_D/I_G ratio in their Raman spectra in comparison with that for rGO-Au (**Figure 5.5**a). This may be attributed to the decreased oxygen content on the rGO via the amine-induced ring-opening reaction or nucleophilic substitution of the

residual hydroxyl, epoxide and carboxyl groups.[311] Among them, OLA modified rGO-Au (simply denoted as Au-OLA) exhibited the lowest I_D/I_G ratio of 1.29, indicating its relatively low oxygen content on rGO after modification. The attachments of amines were firstly verified by Fourier transform infrared spectroscopy (FTIR) (Figure 5.5b). The samples modified with bidentate EDA and polydentate PEI clearly demonstrate the characteristic bands of amines: N-H bending vibrations at 1640 - 1556 cm^{-1} and C-N stretching vibration at ~1316 cm^{-1}. The monodentate PA, HA and OLA could be discerned by the characteristic bands of C-H stretching vibration of alkane at 2840 - 2930 cm^{-1}.

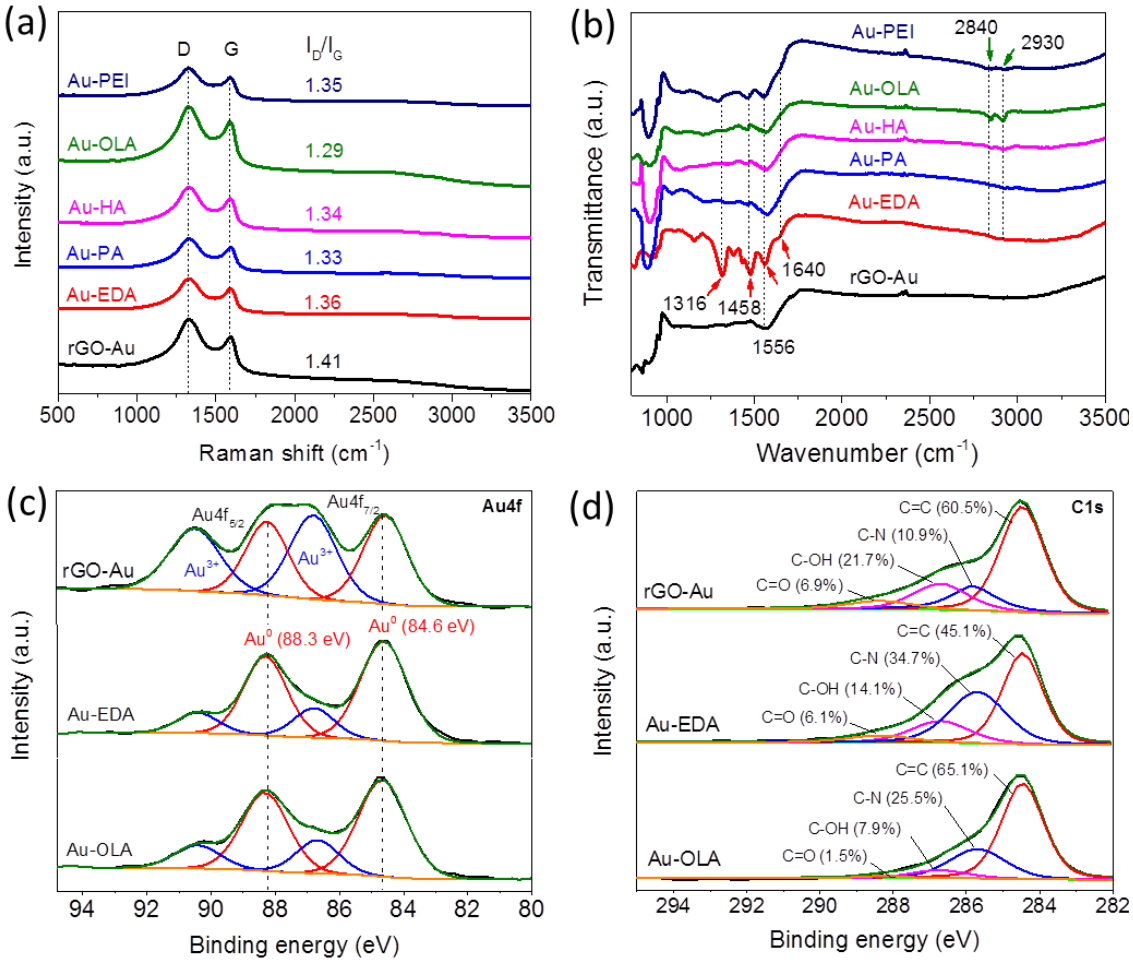

Figure 5.5 (a) Raman and (b) FTIR spectra of the pristine rGO-Au and five different amine modified rGO-Au; (c) Deconvoluted Au4f and (d) C1s XPS spectra of rGO-Au, Au-EDA and Au-OLA.

The surface chemical state of Au was elucidated by X-ray photoelectron spectroscopy (XPS) analysis on three representative samples, rGO-Au, Au-EDA and Au-OLA (Figure 5.5c). With the EDA and OLA modification, no significant binding energy shift was

observed on Au^0 and Au^{3+} peaks, as that reported for N-containing ligands-functionalized Pt, Au and Ag nanostructures.[240,245,247] The decreased relative percentage of Au^{3+} ions might be ascribed to the strong electron donation from amine groups inducing a partial reduction.[18] The anchored amine modifiers may not be protonated in aqueous environment within the pH range of 6~8 due to the covalent-bond-like strong interaction between the amine functionality and Au NPs.[312-314] The XPS quantification analysis demonstrated a decreased content of oxygen and an increased content of nitrogen after the EDA and OLA modification (**Table 5.1**). The deconvoluted C1s spectra of Au-EDA and Au-OLA also exhibited an obvious increase in the relative percentage of C-N functionality compared with that of rGO-Au (Figure 5.5d). These results further evidenced the presence of amine molecules. The decreased relative content of C-OH functionality may be attributed to the reactions between amine and hydroxyl groups mentioned above.[311] This may also explain the reduced I_D/I_G ratio in the Raman analysis after amine modification.

Table 5.1 Relative content of C, O, N and Au in four representative samples estimated from XPS analysis.

Atomic content (%)	**C**	**O**	**N**	**Au**
rGO	67.20	29.90	2.90	0
rGO-Au	68.17	27.07	3.49	1.27
Au-EDA	67.63	22.98	8.00	1.38
Au-OLA	69.26	22.71	6.55	1.49

5.3.2 CO_2ER Performance of rGO-Au Catalysts

The CO_2ER performance of rGO-Au and the amine-modified rGO-Au catalysts were firstly evaluated by linear sweep voltammetry (LSV) studies using rGO and amine modified rGO as controls (**Figure 5.6**). All the catalysts containing Au exhibited much higher current densities and more positive onset potentials compared with rGO and rGO-amine samples, excluding the possibility that the superior electrocatalytic activities had arisen from rGO supports or amine modifiers. The Au-EDA and Au-PA showed similar current-voltage profiles to rGO-Au, while lower current responses were observed for HA-, OLA- and PEI-

modified rGO-Au (Figure 5.6a). The LSV trends of amine modified rGO was slightly different from that of amine modified rGO-Au (Figure 5.6b). They exhibited a similar LSV trend as the pristine rGO. The linear amines (EDA, PA, HA and OLA) modified rGO exhibited lower current densities compared with the pristine rGO, whereas the branched PEI modified rGO exhibited a higher current density. This may be attributed to their different influence of molecular structures on rGO restacking during the catalyst drying process. The branched PEI molecules with relatively large steric structures probably inhibited the restacking of rGO and led to a larger electrochemically active surface area, affording a higher current density compared with other small amine modifiers under the same conditions.

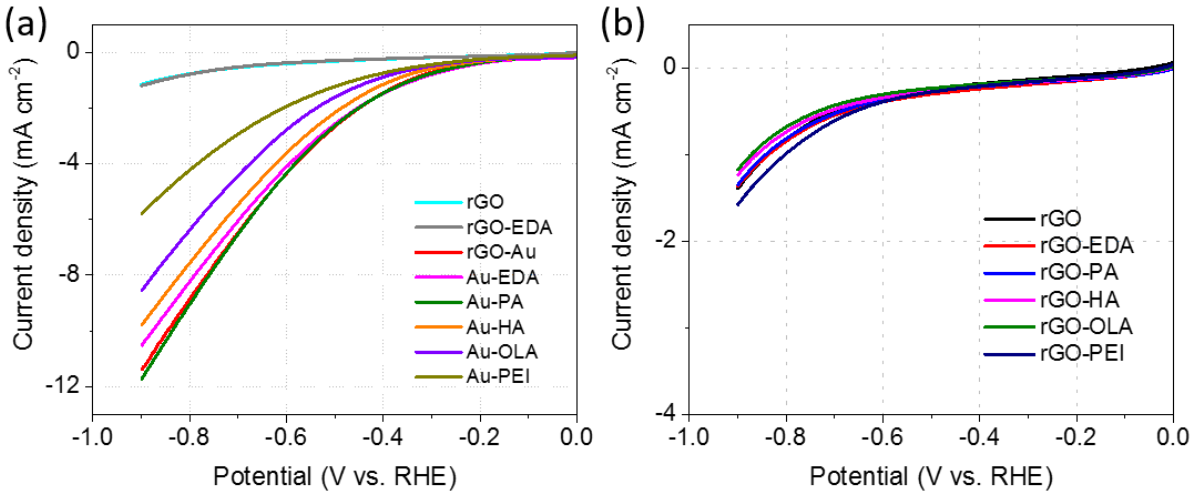

Figure 5.6 (a) LSV scans of rGO, rGO-EDA, rGO-Au composites and amine modified rGO-Au composites in CO_2-saturated 0.1 M $KHCO_3$; (b) LSV curves of rGO and amine modified bare rGO sheets.

To clarify the role of amine modification, controlled-potential electrolysis was performed (**Figure 5.7**). Each sample exhibited almost stable current-time profiles under different applied potentials, indicating the nearly stable catalytic properties of these catalysts.

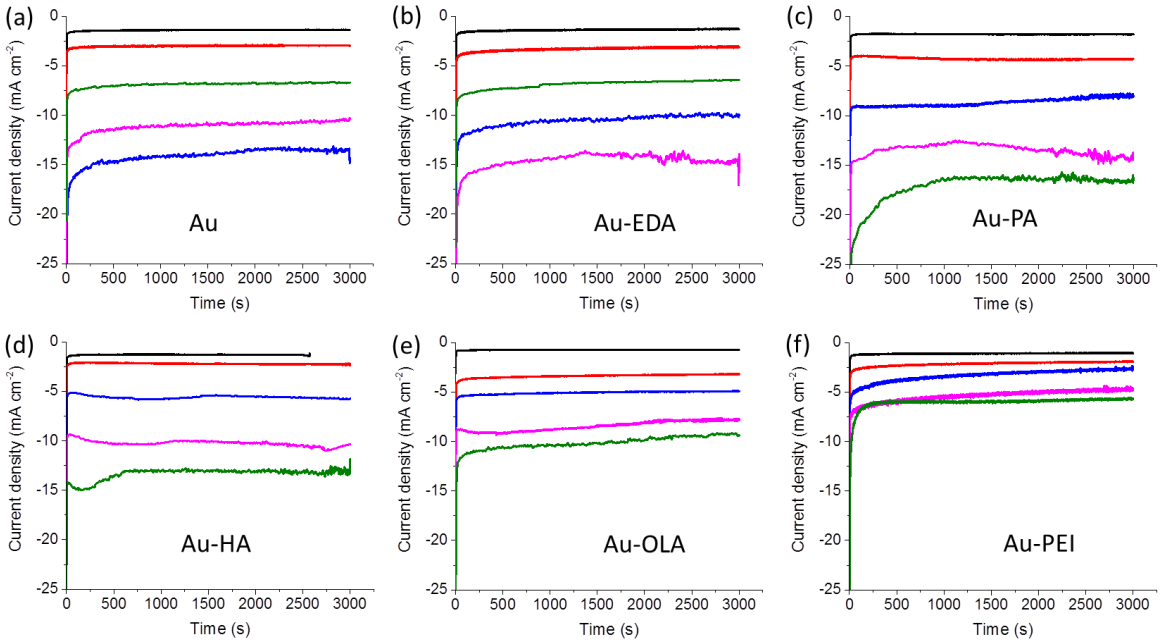

Figure 5.7 Chronoamperometry curves of rGO-Au and Au-amine catalysts at various potentials in CO_2-saturated 0.1 M $KHCO_3$ solution. The applied potential from top to bottom was -0.4 V, -0.5 V, -0.6 V, -0.7 V and -0.8 V (vs. RHE), respectively.

The iR-corrected total current densities of Au-containing samples showed a similar trend to the LSV results (**Figure 5.8**a). They decreased with increasing alkyl length of amine modifiers at potentials more negative than -0.5 V (all the potentials are referenced to RHE herein) except that Au-PA exhibited the highest current densities. The products generated were H_2 and CO. The linear amines (EDA, PA, HA and OLA) modified catalysts exhibited observably improved CO faradaic efficiencies (FE_{CO}) compared with bare rGO-Au, while the branched polyamine PEI modified catalyst (Au-PEI) remarkably hindered CO formation and improved H_2 evolution (Figure 5.8b-c). Among these linear amines, OLA with the longest alkyl chain exhibited the best promotion effect: FE_{CO} was improved by over 20% at potentials more negative than -0.5 V. Specifically, at -0.6 V, the FE_{CO} of rGO-Au was only 32% and was remarkably enhanced to 59% after the OLA modification, which is even comparable to that ~60% for ultrathin Au nanowires with high density of reactive edge sites (2.1 nm width).[67] Moreover, the linear amine modification did not depress but rather, slightly enhanced the rate of CO_2 reduction, as evidenced by the increased geometric CO partial current density (j_{CO}), in contrast to that greatly decreased j_{CO} on Au-PEI (Figure 5.8d). This depression effect of PEI is different from the promotion effect reported for N-doped carbon nanotubes and rGO/MoS_x,[141,144] which may be related to the intrinsic properties of these active sites. The direct and strong interaction between PEI and ultrasmall Au NPs with

abundant low-coordinated sites may induce a severe surface poisoning effect, blocking the catalytic sites for CO_2 adsorption and reduction.

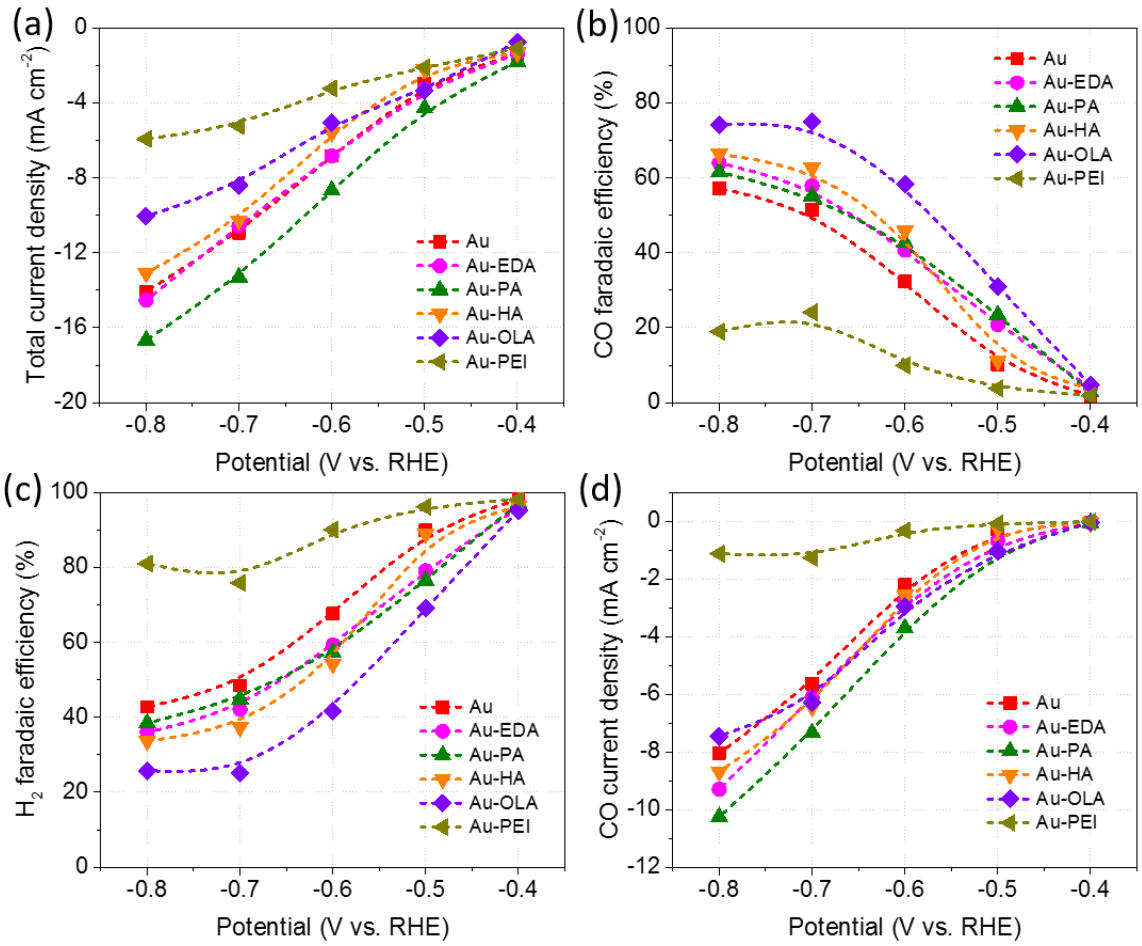

Figure 5.8 (a) Geometric total current densities, (b) FE_{CO}, (c) FE_{H2} and (d) j_{CO} at various potentials for rGO-Au and Au-amine catalysts.

Figure 5.9a highlights the dependence of FE_{CO} and j_{CO} on the structure of amine modifiers at -0.7 V. It clearly reveals an amine-dependent modification effect: linear amines promoted CO formation whereas the branched amine depressed it; the CO selectivity increased with the increasing alkyl chain length of linear amine modifiers. Electrochemical impedance spectroscopy was used to investigate the electron transfer and mass transportation properties of different amine modified Au catalysts, but no clear clues were observed (Figure 5.9b).

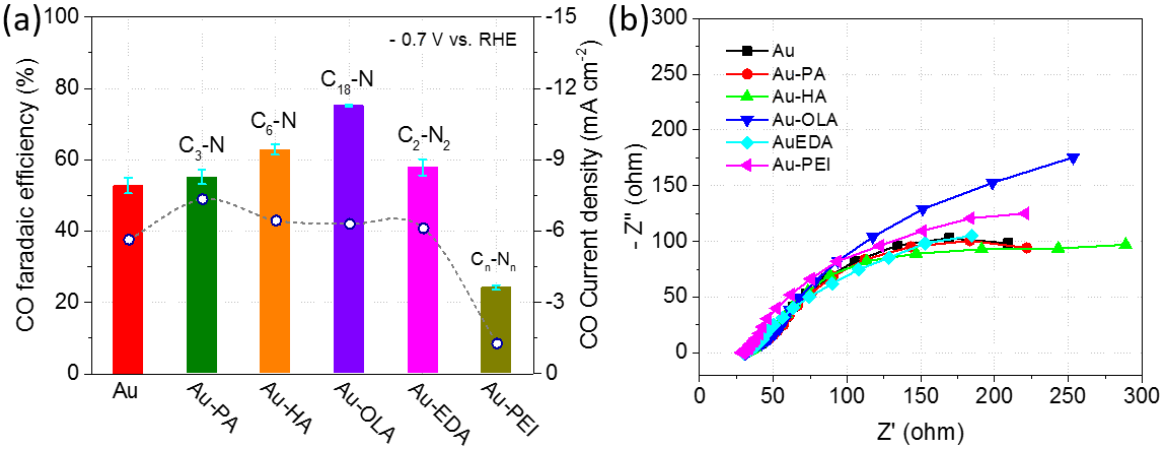

Figure 5.9 (a) The FE_{CO} (column) and j_{CO} (circle) at -0.7 V; (b) Electrochemical impedance spectroscopy investigation of rGO-Au and Au-amine catalysts at -0.3 V vs. RHE in CO_2-saturated 0.1 M $KHCO_3$ solution in a two-compartment gastight cell. It was performed by applying an AC voltage with 10 mV amplitude in a frequency range from 20 mHz to 100 kHz.

The mass activity is one of the most important parameters to assess noble metallic catalysts for practical application. The OLA modified ultrasmall Au NPs delivered remarkably high mass activities for the CO_2-to-CO conversion at moderate overpotentials ranging from -0.6 to -0.8 V vs. RHE due to the intrinsic high electrocatalytic activity and high surface atom fraction (**Figure 5.10**). A metal-specific mass activity of 102, 217 and 257 A g^{-1} was respectively obtained at -0.6, -0.7 and -0.8 V, which surpassed most of the reported noble metal catalysts such as 8 nm Au NPs on graphene nanoribbons (GNR),[71] 4 nm Au NPs on carbon black (CB),[68] 3.7 nm Pd NPs,[79] 5 nm Ag NPs,[247] 2 nm Au ultrathin nanowires,[67] and the benchmark catalyst 8 nm Au-Fe NPs.[124]

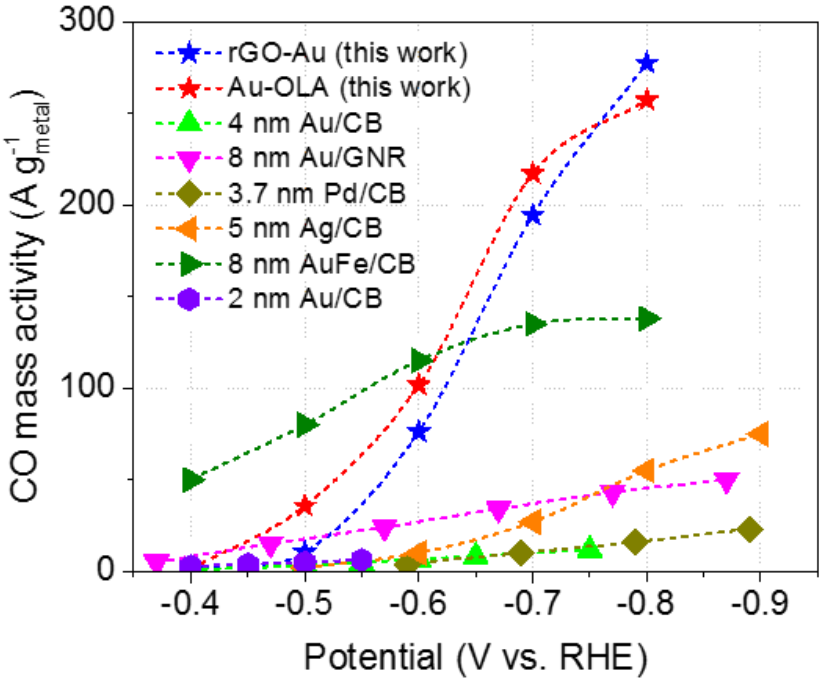

Figure 5.10 Comparison of the mass activities for CO production with the reported noble metal catalysts.

Stability of the amine modification on rGO-Au for CO_2ER was investigated by comparing the Au-OLA and rGO-Au catalysts at -0.65 V, and the chronoamperometry (i-t) profiles and product selectivity are shown in **Figure 5.11**a-b. Both Au-OLA and rGO-Au exhibited slightly decreasing current densities during the 10 h electrolysis with an increased FE_{CO} in the first 2 h: an increase from 64% to 68% for Au-OLA and 37% to 44% for rGO-Au. These changes may be ascribed to the slow growth of Au particle size related with aggregation.[315] The smaller change for Au-OLA indicates that OLA may stabilize the ultrasmall Au NPs. It should be pointed out that the Au-OLA catalyst did not exhibit a good stability at a more negative potential of -0.75 V, namely, both the current density and FE_{CO} decreased gradually during the 10 h electrolysis (Figure 5.11c). This deteriorated stability may be ascribed to the relatively severe NPs aggregation or rapid size increase at this potential. This is consistent with the reported potential-dependent growth of ligand-capped Au NPs supported on carbon blacks, in which the growth of Au NPs in size occurred more rapidly at a more negative potential.[315]

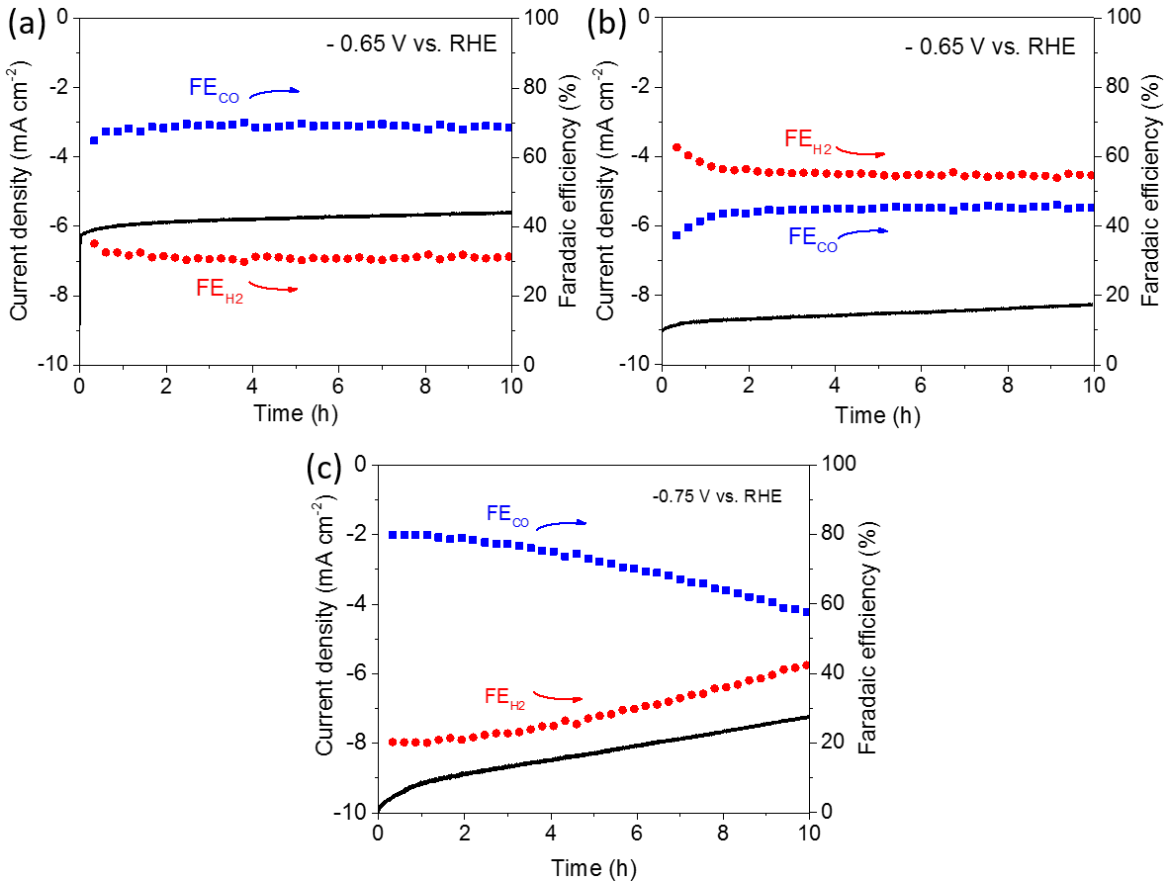

Figure 5.11 Stability analysis of (a) Au-OLA and (b) rGO-Au at -0.65 V for 10 h, and (c) Au-OLA at -0.75 V for 10 h in CO_2-saturated 0.1 M $KHCO_3$.

To reveal the site-specific electrocatalytic activity, the electrochemically active surface areas (ECSAs) of Au before and after amine modification were evaluated using the Pb underpotential deposition (UPD) method.[244] The EDA modified rGO-Au (Au-EDA) was used as an example (**Figure 5.12**). No obviously sharp peaks were presented on their UPD voltammograms precluding the accurate calculation of ECSAs, which is probably related to the ultrasmall size of these Au NPs. Nevertheless, Au-amine exhibited much weaker intensity compared with rGO-Au, revealing a decreased ECSA after amine modification. It can be qualitatively inferred that the ECSA-normalized j_{CO} of Au-amine is higher than that of rGO-Au, that is, the presence of amine molecules improves the site-specific catalytic activity for CO production. This is in agreement with the results for carbene-functionalized 7 nm Au NPs catalyst.[244]

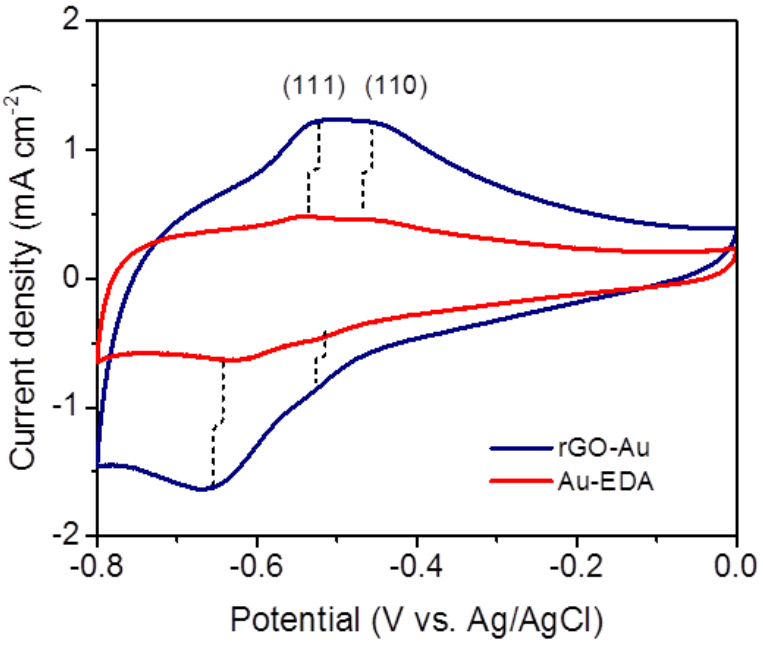

Figure 5.12 Pb underpotential deposition (UPD) analysis of the electrochemically active surface areas (ECSAs) before and after amine modification.

All the above results demonstrate that both the amine group and its molecular configuration greatly affect the CO_2-to-CO conversion on ultrasmall Au NPs. The promotion effect from linear amines may be explained by referencing to the reported theoretical calculation for amine-anchored Ag_{147} NPs:[247] amine groups are more readily adsorbed on the under-coordinated corner sites of ultrasmall Au NPs, making the surrounding sites to favour the stabilization of *COOH intermediates, inhibiting the adsorption of *H and thus promoting the CO formation. To probe this further, annealing of the rGO-Au at 120 ^{o}C in air atmosphere was done to obtain a new composite rGO-Au120 containing large Au NPs (11.7 nm, **Figure 5.13**a-b); which were deficient in under-coordinated sites compared with ultrasmall Au NPs. As expected, the OLA modification on rGO-Au120 did not exhibit an obvious promotion effect, as revealed by the similar FE_{CO}, FE_{H2}, j_{H2} and j_{CO} values as the pristine samples at all the applied potentials (Figure 5.14c-f). This demonstrates the important role of Au surface structure in the amine functionalization for CO_2ER, which may be attributed to the different binding ability of amine functionality on various Au active sites such as corners, edges and facets.

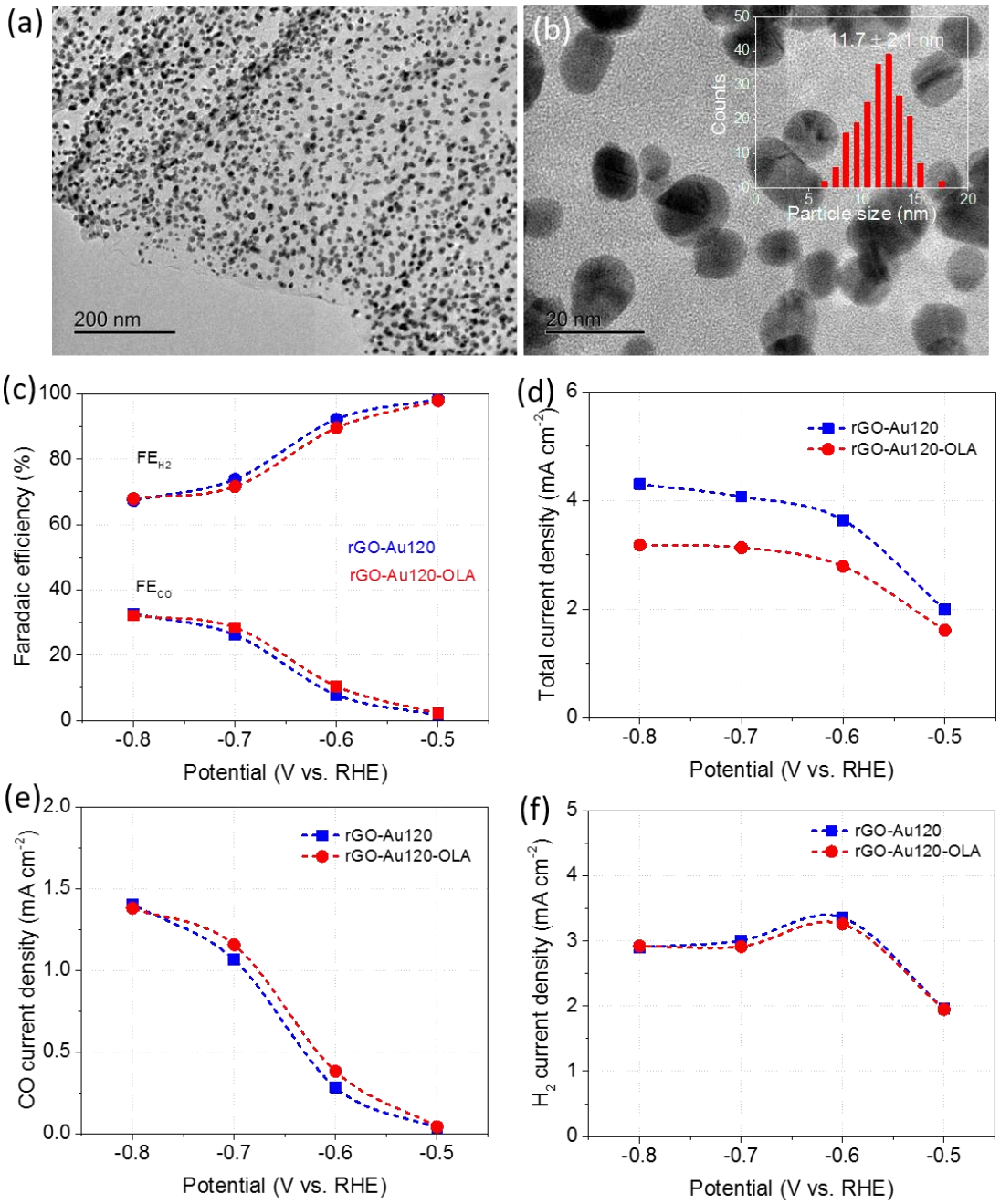

Figure 5.13 (a,b) TEM images of rGO-Au120 under different magnifications, inset of (b) the size distribution of Au NPs; (c) FE_{CO} and FE_{H2}, (d) j_{total}, (e) j_{CO} and (f) j_{H2} at various potentials for rGO-Au120 and rGO-Au120-OLA catalysts.

The influence of amine molecules on the CO formation may also be related to their coverage on the ultrasmall Au NPs. As reported for CN^- and Cl^- functionalized Au electrodes, only a proper coverage of anions on Au(111) surface could benefit the CO_2ER, and higher coverages negatively affect the stabilization of *COOH and lower the activity.[249] The amine functionality has strong electron-donating ability as well, and may induce a similar effect. However, it is challenging to quantify the amine coverage on these ultrasmall Au NPs due

to the complexity of the rGO-Au-amine system. Alternatively, probing of this amine-coverage effect was done by manipulating the purification process of the Au-OLA catalyst to remove the loosely bound surface modifier. It is reasonable to infer that the Au-OLA composite via one-time ethanol purification (Au-OLA-1) had a higher OLA coverage compared with that via three times (Au-OLA-3) or seven times (Au-OLA-7). Au-OLA-1 exhibited significantly depressed CO formation compared with the latter two catalysts (**Figure 5.14**), verifying the adverse effect of higher amine coverage for CO_2-to-CO conversion. Au-OLA-3 and Au-OLA-7 exhibited almost the same performance, indicating that three times of ethanol washing was sufficient to remove the excessive OLA molecules on the composite. This was the condition used to prepare all the samples for CO_2ER characterizations. The PEI molecule has a branched polyamine configuration. It may induce a much higher coverage on Au sites compared with the other linear amines due to the strong Au-amine interactions related with its much higher density of amine functionality, thus resulting in the greatly depressed CO formation. For the linear amines, their coverage on the Au NPs may decrease with the increasing alkyl chain length, as reported for linear thiol-ligands on Au NPs.[316] The increased CO selectivity with alkyl chain length may correlate with the decreased amine coverage on ultrasmall Au NPs.

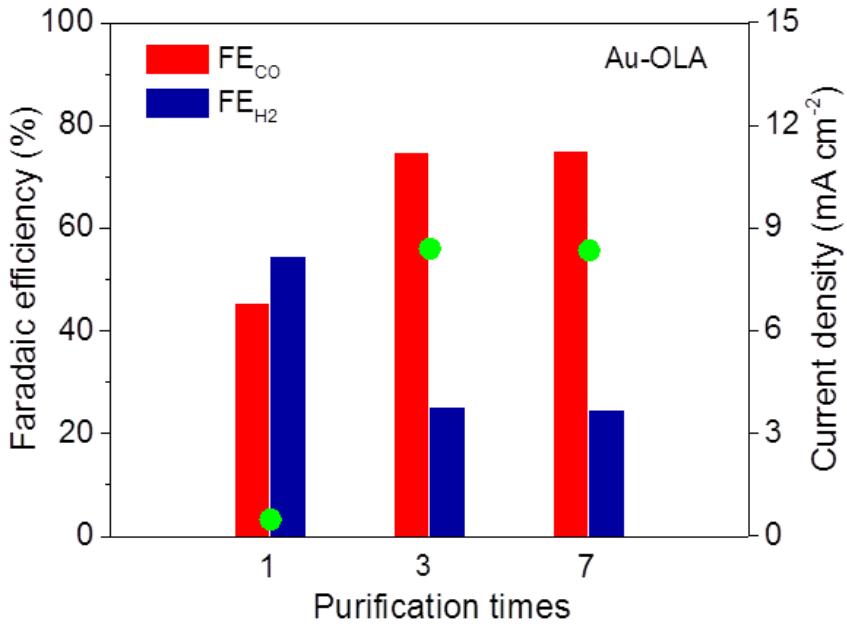

Figure 5.14 The CO_2ER performance of rGO-Au-OLA that was purified with ethanol for different times. Columns are the faradaic efficiencies and solid circles are the corresponding total current densities.

5.4 Conclusion

In summary, an ultrasmall ligand-free Au NP catalyst has been developed by a scalable rGO-assisted wet chemistry method for CO_2 electrochemical reduction with high mass activity. A simple amine modification strategy was applied to depress the severe hydrogen evolution reaction on these ultrasmall Au NPs and promote the CO_2-to-CO conversion. The amine functionality as well as the molecular configuration played important roles in tuning the electrocatalytic activity of ultrasmall Au NPs with abundant low-coordinated sites. Among all the modifiers, the linear oleylamine exhibited the most effective promotion effect on the CO selectivity, probably due to its optimal coverage on the Au NPs. These oleylamine molecules may adsorb on the low-coordinated sites of the ultrasmall Au NPs, making the surrounding sites favour the stabilization of *COOH intermediates and inhibiting the adsorption of *H. Thus, the H_2 evolution was depressed while the CO formation was promoted. In addition, the surface structure of Au NPs such as morphology and particle size had an impact on amine functionalization due to the different binding ability of amine functionality on Au active sites. This work demonstrates that engineering the metal-organic ligand interface is a simple and effective way to tune the electrocatalytic property of nanostructured metal catalysts. It may shed light on the rational design of highly efficient and selective electrocatalysts for CO_2 conversion by engineering the catalyst surface at a molecular level.

Chapter 6 Conclusions and Outlook

6.1 Conclusions

This thesis work aims to develop high-performance catalysts for CO_2 electrochemical reduction by exploring the interfacial factors that can manipulate the reactivity of this electrocatalytic reaction. A simple strategy of engineering the interface of nanostructured metals has been adopted to realize this goal. Three different types of interfaces have been engineered to design and develop inexpensive and efficient electrocatalysts, including metal-metal interface, metal-carbon interface, and metal-organic ligand interface. The catalysts developed include Sn NPs decorated Cu NWs, N-doped carbon nanofiber supported Sn NPs, and amine modified ultrasmall Au NPs on rGO sheets. Facile wet chemistry techniques are utilized to fabricate these catalysts, affording them great potential for practical and large-scale application. The greatly improved electrocatalytic performance offered from these catalysts prove that engineering the interface of metal catalysts is an effective and facile strategy to tune their catalytic properties for enhanced CO_2 electroreduction.

The Sn NPs decorated Cu NWs hybrid catalyst fabricated by the electrochemical anodization coupled with an electroless deposition process exhibits excellent electrocatalytic activity towards the electroreduction of CO_2 to CO (Chapter 3). High CO Faradaic efficiencies and current densities can be reached under low overpotentials by simply tuning the coverage of Sn NPs on the Cu NWs. The interaction between the nanoscale Cu and Sn phases has been identified as the major factor for the improved CO formation. Engineering the Cu-Sn interfaces by controlling the interface density or introducing a third metal in-between are able to further manipulate the interaction and thus tune the electrocatalytic performance. This study may not only provide a facile and scalable way to fabricate non-precious metal hybrid catalysts, but also shed light on the rational design of other Cu-based bimetallic catalysts for improved CO_2 electroreduction.

Following the metal-metal interface, this thesis work has been extended to regulating the metal-carbon interfaces for electrocatalyst design (Chapter 4) by using a low cost sustainable organic matter to replace metal. The Sn NPs modified N-doped porous carbon nanofibers (CFs) catalyst has been developed via a straightforward electrospinning technique coupled with a pyrolysis process. The pyridinic-N component in the N-doped CFs demonstrates an obvious promotion effect on formate formation over the supported Sn NPs. This hybrid

catalyst exhibits high electrocatalytic activity and selectivity for formate production at low overpotentials. This work reveals that the electronic structure of carbon supports plays a crucial role in tuning the electrocatalytic property of the supported Sn nanocrystals. Interestingly, after a simple acidic leaching treatment, the atomically dispersed Sn species remaining on the N-doped CFs switches to drive the CO_2 electroreduction to CO with high selectivity at low overpotentials. Structural and performance analyses have indicated that these Sn atoms may be stabilized by the pyridinic N sites to form Sn-N_x moieties that promote CO_2-to-CO conversion. This finding reveals that the interaction between Sn and N-doped carbon at atomic level can also be manipulated to design improved CO_2ER catalysts. The drastic shift of product selectivity induced by a simple acidic leaching treatment represents a practical strategy for the development of earth-abundant CO_2ER catalysts for target products as demanded. Moreover, the electrospinning-pyrolysis method used in this work can be readily applied to produce other metal-based hybrid catalysts integrated with heteroatom-doped CFs (i.e., N, B, P), further expanding the materials family and promoting the research.

Finally, this thesis expands the interfacial strategies towards tuning the metal-organic ligand interaction (Chapter 5). The influence of amine modification has been investigated upon the ultrasmall Au NPs on rGO sheets that is fabricated by a simple rGO-assisted wet chemistry method. It has been found that some amine modifiers on those ultrasmall Au NPs are capable of depressing the H_2 evolution reaction and promoting the CO_2-to-CO conversion. Their molecular configurations are crucial for tuning the electrocatalytic activity: linear amines promote the CO formation whereas the branched polyamine greatly depresses it; the increasing alkyl chain length boosts the promotion effect of linear amines. In addition, the promotion effect for the large Au NPs with a lack of low-coordinated sites is not as evident as that for the ultrasmall Au NPs, indicating that the surface structure of Au NPs has a remarkable impact on amine functionalization; probably due to the different binding ability of amine functionality on various Au active sites such as corners, edges and facets. This surface molecule functionalization provides an effective way to suppress the hydrogen evolution induced by downsizing the metal catalysts for high metal atom utilizations. The findings in this work may shed light on the rational design of improved CO_2ER catalysts by engineering the catalyst surface at a molecular level.

All in all, this thesis work has successfully developed three different kinds of inexpensive and efficient electrocatalysts by engineering the interface of metal catalysts. Detailed control

experiments and structural analyses have been performed to verify these effects. The results indicate that engineering the interfaces of nanostructured metal catalysts is a simple and effective way to tune the binding ability to key intermediates or the catalytic environment of metal active sites for enhancing the performance of CO_2ER. The work in this thesis offers a deep understanding of the interfacial process of CO_2ER, and sheds lights on the rational design of inexpensive and efficient electrocatalysts for CO_2ER.

6.2 Outlook

The ultimate goal of the research on CO_2ER is to realize the practical transformation of CO_2 into target products on a large scale. In this thesis, catalysts developed in the powder form such as Sn modified N-doped carbon nanofibers and amine-modified ultrasmall Au NPs on rGO sheets have exhibited excellent CO_2ER performances. However, these performances are evaluated in a static "H-cell" in which the performance is limited by the low solubility of CO_2 in aqueous solution and the low CO_2 diffusion rate to the catalyst surface.

To overcome these limitations and improve the CO_2ER performance, it is essential to perform electrode-electrolyte interface engineering by creating unobstructed and robust three-phase contact for CO_2, electrolyte, and catalyst.[317] A gas-diffusion layer composed of hydrophobic polytetrafluoroethylene (PTFE) and carbon black powder can be employed to support the catalyst. The hydrophobic PTFE can also be used to create an abrupt reaction interface or modify the nanostructured metal catalysts.[32,318] These interface engineering strategies have demonstrated excellent capability of controlling the reaction kinetics and the product selectivity of CO_2ER in aqueous solution.

To further boost the catalytic performance, the gas-diffusion electrode should be integrated into a flow cell, which is commonly used in commercial-scale electrochemical reactors such as fuel cells and water electrolyzers. This kind of continuous reactors can offer more control over reagent delivery, and enable the use of a gaseous CO_2 feed to the cathodic catalysts and thus generate much higher current densities by reducing the mass transport issues inherent to the H-cells.[319] They are more relevant to a scalable CO_2 electrolyzer system. In this regard, the next step of this study should focus on the integration of catalysts into the porous microstructure of a gas diffusion electrode in a dynamic flow reactor, which aims to minimize the limitations related to mass and charge transfer as well as achieve stable long-term operation under industrially-relevant conditions.

On the other hand, although the interfacial engineering strategies have been proven effective in modulating the catalytic behaviours of nanostructured metal catalysts, the intermediate process of CO_2ER is still unclear. Additional efforts should be exerted to deepen the understanding of these effects at the molecular level under both static and dynamic electrolysis conditions so as to promote the rational design of high-performance catalysts for large scale application. Given the multicomponent nature of the electrocatalysts and the possibility of undergoing structural and compositional changes under the reaction conditions, the development of this understanding should follow an approach of combining experimental *in situ* techniques with theoretical modelling. The *in situ* and *operando* microscopic and spectroscopic techniques should be powerful tools for identifying the adsorbed intermediates and the real state of the catalyst surface under the reaction conditions; while the theoretical studies may obtain a mechanistic interpretation of the experimental observations as well as predict new catalysts to guide the research.

In the recent decade, a variety of *in situ* techniques have been applied to study the CO_2ER. For example, the attenuated total reflection infrared spectroscopy (ATR-IR) has received intensive attention since it can directly provide molecular-level structural information about the electrode/electrolyte interface.[320] It is an ideal tool for studying CO_2ER mechanisms by identifying the chemical nature and geometries of the adsorbed molecules and/or intermediates as a function of potential or time. Similarly, *in situ* Raman spectroscopy can also monitor the surface species during the CO_2 electrolysis and thus help to explore the mechanism of this interfacial reaction.[224] Moreover, synchrotron-based ambient-pressure X-ray photoelectron spectroscopy has been widely used to identify the real catalytically active species for CO_2 reduction. *In-situ* and *operando* X-ray absorption spectroscopy (XAS) is particularly powerful, as the X-ray absorption near edge structure (XANES) can reveal the oxidation state of the element of interest, and extended X-ray absorption fine structure (EXAFS) is capable of probing the influence from the local coordination environment.[321] With the advance of microscopy technology, the interfacial process of CO_2 reduction may be directly observed by *in situ* scanning transmission electron microscopy (STEM) with atomic resolution in the future. The surface restructuring phenomena[322] induced by potential, adsorbates or reactants will be clearly demonstrated then.

Meanwhile, the computational study of the CO_2ER process has also achieved significant advances due to the rapid development of computer science and related computational theories. For the CO_2 electroreduction, the density function theory (DFT) method has been

identified as a powerful tool to explain experimental results and predict new catalysts as well.[4] These computational efforts coupled with the advanced *in situ* characterization techniques will help to derive accurate structure-performance relationships that can guide the optimization of these types of catalysts. This will pave the way for the rational design of new catalysts by combining the interfacial engineering strategies with other strategies such as surface engineering to achieve breakthrough in performance.

With the increasingly worldwide input into CO_2ER research, it is highly expected that this promising technique will be put into practical large-scale application in the future so as to realize the goal of simultaneously curbing anthropogenic CO_2 emissions and providing sustainable pathways for fuel generation.

References

[1] S. Chu and A. Majumdar. Opportunities and challenges for a sustainable energy future. *Nature*. **2012**, 488: 294.

[2] M. Dresselhaus and I. Thomas. Alternative energy technologies. *Nature*. **2001**, 414: 332.

[3] J. G. Canadell, C. Le Quéré, M. R. Raupach, C. B. Field, E. T. Buitenhuis, P. Ciais, T. J. Conway, N. P. Gillett, R. Houghton and G. Marland. Contributions to accelerating atmospheric CO_2 growth from economic activity, carbon intensity, and efficiency of natural sinks. *Proceedings of the National Academy of Sciences*. **2007**, 104: 18866-18870.

[4] D.D. Zhu, J.L. Liu and S.Z. Qiao. Recent advances in inorganic heterogeneous electrocatalysts for reduction of carbon dioxide. *Advanced Materials*. **2016**, 28: 3423-3452.

[5] E. D. a. P. Tans. NOAA/ESRL. www.esrl.noaa.gov/gmd/ccgg/trends/.

[6] Z.-L. Wang, C. Li and Y. Yamauchi. Nanostructured nonprecious metal catalysts for electrochemical reduction of carbon dioxide. *Nano Today*. **2016**, 11: 373-391.

[7] D. R. Feldman, W. D. Collins, P. J. Gero, M. S. Torn, E. J. Mlawer and T. R. Shippert. Observational determination of surface radiative forcing by CO_2 from 2000 to 2010. *Nature*. **2015**, 519: 339.

[8] R. S. Haszeldine. Carbon capture and storage: how green can black be? *Science*. **2009**, 325: 1647-1652.

[9] S. Chu, Carbon capture and sequestration, *Science*. **2009**, 325: 1599.

[10] M. Aresta, A. Dibenedetto and A. Angelini. Catalysis for the valorization of exhaust carbon: from CO_2 to chemicals, materials, and fuels. Technological use of CO_2. *Chemical Reviews.* **2013**, 114: 1709-1742.

[11] T. Bruhn, H. Naims, B. Olfe-Kräutlein. Separating the debate on CO_2 utilisation from carbon capture and storage. *Environmental Science & Policy*. **2016**, 60: 38-43.

[12] J. S. Rhodes and D. W. Keith. Biomass with capture: negative emissions within social and environmental constraints: an editorial comment. *Climatic Change*. **2008**, 87: 321-328.

[13] M. Aresta and A. Dibenedetto, Carbon Dioxide Fixation into Organic Compounds, in: M. Aresta (Ed.) Carbon Dioxide Recovery and Utilization, Springer Netherlands, Dordrecht, **2003**, pp. 211-260.

[14] R. Quadrelli and S. Peterson. The energy-climate challenge: Recent trends in CO_2 emissions from fuel combustion. *Energy Policy*. **2007**, 35: 5938-5952.

[15] D. T. Whipple and P. J. Kenis. Prospects of CO_2 utilization via direct heterogeneous electrochemical reduction. *The Journal of Physical Chemistry Letters*. **2010**, 1: 3451-3458.

[16] D. Mignard, M. Sahibzada, J. Duthie and H. Whittington. Methanol synthesis from flue-gas CO_2 and renewable electricity: a feasibility study. *International Journal of Hydrogen Energy*. **2003**, 28: 455-464.

[17] D. Mignard and C. Pritchard. Processes for the synthesis of liquid fuels from CO_2 and marine energy. *Chemical Engineering Research and Design*. **2006**, 84: 828-836.

[18] C. Costentin, M. Robert and J.-M. Savéant. Catalysis of the electrochemical reduction of carbon dioxide. *Chemical Society Reviews*. **2013**, 42: 2423-2436.

[19] O. S. Bushuyev, P. De Luna, C. T. Dinh, L. Tao, G. Saur, J. van de Lagemaat, S. O. Kelley and E. H. Sargent. What Should We Make with CO_2 and How Can We Make It? *Joule*. **2018**, 2: 825-832.

[20] A. M. Appel, J. E. Bercaw, A. B. Bocarsly, H. Dobbek, D. L. DuBois, M. Dupuis, J. G. Ferry, E. Fujita, R. Hille and P. J. Kenis. Frontiers, opportunities, and challenges in biochemical and chemical catalysis of CO_2 fixation. *Chemical Reviews*. **2013**, 113: 6621-6658.

[21] J. Qiao, Y. Liu, F. Hong and J. Zhang. A review of catalysts for the electroreduction of carbon dioxide to produce low-carbon fuels. *Chemical Society Reviews*. **2014**, 43: 631-675.

[22] E. E. Benson, C. P. Kubiak, A. J. Sathrum and J. M. Smieja. Electrocatalytic and homogeneous approaches to conversion of CO_2 to liquid fuels. *Chemical Society Reviews*. **2009**, 38: 89-99.

[23] C. Costentin, M. Robert, J.-M. Savéant and A. Tatin. Efficient and selective molecular catalyst for the CO_2-to-CO electrochemical conversion in water. *Proceedings of the National Academy of Sciences*. **2015**, 112: 6882-6886.

[24] K. A. Grice and C. P. Kubiak, Recent studies of rhenium and manganese bipyridine carbonyl catalysts for the electrochemical reduction of CO_2, in: *Advances in Inorganic Chemistry*, Elsevier, **2014**, pp. 163-188.

[25] J. A. Keith, K. A. Grice, C. P. Kubiak and E. A. Carter. Elucidation of the selectivity of proton-dependent electrocatalytic CO_2 reduction by fac-Re(bpy)$(CO)_3$Cl. *Journal of the American Chemical Society*. **2013**, 135: 15823-15829.

[26] J. Schneider, H. Jia, J. T. Muckerman and E. Fujita. Thermodynamics and kinetics of CO_2, CO, and H^+ binding to the metal centre of CO_2 reduction catalysts. *Chemical Society Reviews*. **2012**, 41: 2036-2051.

[27] B. J. Fisher and R. Eisenberg. Electrocatalytic reduction of carbon dioxide by using macrocycles of nickel and cobalt. *Journal of the American Chemical Society*. **1980**, 102: 7361-7363.

[28] L. Chen, Z. Guo, X.-G. Wei, C. Gallenkamp, J. Bonin, E. Anxolabéhère-Mallart, K.-C. Lau, T.-C. Lau and M. Robert. Molecular catalysis of the electrochemical and photochemical reduction of CO_2 with earth-abundant metal complexes. Selective production of CO vs

HCOOH by switching of the metal center. *Journal of the American Chemical Society*. **2015**, 137: 10918-10921.

[29] K. Manthiram, B. J. Beberwyck and A. P. Alivisatos. Enhanced electrochemical methanation of carbon dioxide with a dispersible nanoscale copper catalyst. *Journal of the American Chemical Society*. **2014**, 136: 13319-13325.

[30] Y. i. Hori, Electrochemical CO_2 reduction on metal electrodes, in: *Modern aspects of electrochemistry*, Springer, **2008**, pp. 89-189.

[31] Z. Sun, T. Ma, H. Tao, Q. Fan and B. Han. Fundamentals and Challenges of Electrochemical CO_2 reduction using two-dimensional materials. *Chem*. **2017**, 3: 560-587.

[32] C.-T. Dinh, T. Burdyny, M. G. Kibria, A. Seifitokaldani, C. M. Gabardo, F. P. G. de Arquer, A. Kiani, J. P. Edwards, P. De Luna and O. S. Bushuyev. CO_2 electroreduction to ethylene via hydroxide-mediated copper catalysis at an abrupt interface. *Science*. **2018**, 360: 783-787.

[33] C. W. Li and M. W. Kanan. CO_2 reduction at low overpotential on Cu electrodes resulting from the reduction of thick Cu_2O films. *Journal of the American Chemical Society*. **2012**, 134: 7231-7234.

[34] Y. Chen, C. W. Li and M. W. Kanan. Aqueous CO_2 reduction at very low overpotential on oxide-derived Au nanoparticles. *Journal of the American Chemical Society*. **2012**, 134: 19969-19972.

[35] J. Durst, A. Rudnev, A. Dutta, Y. Fu, J. Herranz, V. Kaliginedi, A. Kuzume, A. A. Permyakova, Y. Paratcha and P. Broekmann. Electrochemical CO_2 reduction-A critical view on fundamentals, materials and applications. *CHIMIA International Journal for Chemistry*. **2015**, 69: 769-776.

[36] M. Hammouche, D. Lexa, M. Momenteau and J. M. Saveant. Chemical catalysis of electrochemical reactions. Homogeneous catalysis of the electrochemical reduction of carbon dioxide by iron porphyrins. Role of the addition of magnesium cations. *Journal of the American Chemical Society*. **1991**, 113: 8455-8466.

[37] Q. Lu, J. Rosen and F. Jiao. Nanostructured metallic electrocatalysts for carbon dioxide reduction. *ChemCatChem*. **2015**, 7: 38-47.

[38] B. Kumar, V. Atla, J. P. Brian, S. Kumari, T. Q. Nguyen, M. Sunkara and J. M. Spurgeon. Reduced SnO_2 porous nanowires with a high density of grain boundaries as catalysts for efficient electrochemical CO_2-into-HCOOH conversion. *Angewandte Chemie International Edition*. **2017**, 56: 3645-3649.

[39] S. A. Akhade, W. Luo, X. Nie, N. J. Bernstein, A. Asthagiri and M. J. Janik. Poisoning effect of adsorbed CO during CO_2 electroreduction on late transition metals. *Physical Chemistry Chemical Physics*. **2014**, 16: 20429-20435.

[40] Y. Hori, K. Kikuchi and S. Suzuki. Production of CO and CH_4 in electrochemical reduction of CO_2 at metal electrodes in aqueous hydrogencarbonate solution. *Chemistry Letters*. **1985**, 14: 1695-1698.

[41] Y. Hori, H. Wakebe, T. Tsukamoto and O. Koga. Electrocatalytic process of CO selectivity in electrochemical reduction of CO_2 at metal electrodes in aqueous media. *Electrochimica Acta*. **1994**, 39: 1833-1839.

[42] K. P. Kuhl, T. Hatsukade, E. R. Cave, D. N. Abram, J. Kibsgaard and T. F. Jaramillo. Electrocatalytic conversion of carbon dioxide to methane and methanol on transition metal surfaces. *Journal of the American Chemical Society*. **2014**, 136: 14107-14113.

[43] A. Wuttig and Y. Surendranath. Impurity ion complexation enhances carbon dioxide reduction catalysis. *ACS Catalysis*. **2015**, 5: 4479-4484.

[44] J. He, N. J. Johnson, A. Huang and C. P. Berlinguette. Electrocatalytic Alloys for CO_2 Reduction. *ChemSusChem*. **2018**, 11: 48-57.

[45] F. Li, D. R. MacFarlane and J. Zhang. Recent advances in the nanoengineering of electrocatalysts for CO_2 reduction. *Nanoscale*. **2018**, 10: 6235-6260.

[46] S. Zhang, P. Kang and T. J. Meyer. Nanostructured tin catalysts for selective electrochemical reduction of carbon dioxide to formate. *Journal of the American Chemical Society*. **2014**, 136: 1734-1737.

[47] F. Lei, W. Liu, Y. Sun, J. Xu, K. Liu, L. Liang, T. Yao, B. Pan, S. Wei and Y. Xie. Metallic tin quantum sheets confined in graphene toward high-efficiency carbon dioxide electroreduction. *Nature Communications*. **2016**, 7: 12697.

[48] J. Wu, F. G. Risalvato, S. Ma and X.-D. Zhou. Electrochemical reduction of carbon dioxide III. The role of oxide layer thickness on the performance of Sn electrode in a full electrochemical cell. *Journal of Materials Chemistry A*. **2014**, 2: 1647-1651.

[49] J. Medina-Ramos, R. C. Pupillo, T. P. Keane, J. L. DiMeglio and J. Rosenthal. Efficient conversion of CO_2 to CO using tin and other inexpensive and easily prepared post-transition metal catalysts. *Journal of the American Chemical Society*. **2015**, 137: 5021-5027.

[50] F. Li, L. Chen, G. P. Knowles, D. R. MacFarlane and J. Zhang. Hierarchical mesoporous SnO_2 nanosheets on carbon cloth: a robust and flexible electrocatalyst for CO_2 reduction with high efficiency and selectivity. *Angewandte Chemie International Edition*. **2017**, 56: 505-509.

[51] Z. Chen, S. Yao and L. Liu. 3D hierarchical porous structured carbon nanotube aerogel-supported Sn spheroidal particles: an efficient and selective catalyst for electrochemical reduction of CO_2 to formate. *Journal of Materials Chemistry A*. **2017**, 5: 24651-24656.

[52] L. Fan, Z. Xia, M. Xu, Y. Lu and Z. Li. 1D SnO_2 with Wire-in-Tube Architectures for Highly Selective Electrochemical Reduction of CO_2 to C1 Products. *Advanced Functional Materials*. **2018**, 28: 1706289.

[53] Y. Zhao, J. Liang, C. Wang, J. Ma and G. G. Wallace. Tunable and efficient tin modified nitrogen-doped carbon nanofibers for electrochemical reduction of aqueous carbon dioxide. *Advanced Energy Materials*. **2018**, 8: 1702524.

[54] Z. Zhang, M. Chi, G. M. Veith, P. Zhang, D. A. Lutterman, J. Rosenthal, S. H. Overbury, S. Dai and H. Zhu. Rational design of Bi nanoparticles for efficient electrochemical CO_2 reduction: the elucidation of size and surface condition effects. *ACS Catalysis*. **2016**, 6: 6255-6264.

[55] J. Medina-Ramos, J. L. DiMeglio and J. Rosenthal. Efficient reduction of CO_2 to CO with high current density using in situ or ex situ prepared Bi-based materials. *Journal of the American Chemical Society*. **2014**, 136: 8361-8367.

[56] N. Han, Y. Wang, H. Yang, J. Deng, J. Wu, Y. Li and Y. Li. Ultrathin bismuth nanosheets from in situ topotactic transformation for selective electrocatalytic CO_2 reduction to formate. *Nature Communications*. **2018**, 9: 1320.

[57] P. Su, W. Xu, Y. Qiu, T. Zhang, X. Li and H. Zhang. Ultrathin Bismuth nanosheets as highly efficient electrocatalyst for CO_2 reduction. *ChemSusChem*. **2018**, 11: 848.

[58] Y. Qiu, J. Du, W. Dong, C. Dai and C. Tao. Selective conversion of CO_2 to formate on a size tunable nano-Bi electrocatalyst. *Journal of CO_2 Utilization*. **2017**, 20: 328-335.

[59] C. Ding, A. Li, S.-M. Lu, H. Zhang and C. Li. In Situ Electrodeposited indium nanocrystals for efficient CO_2 reduction to CO with low overpotential. *ACS Catalysis*. **2016**, 6: 6438-6443.

[60] C. I. Shaughnessy, D. T. Jantz and K. C. Leonard. Selective electrochemical CO_2 reduction to CO using in situ reduced In_2O_3 nanocatalysts. *Journal of Materials Chemistry A*. **2017**, 5: 22743-22749.

[61] Z. Xia, M. Freeman, D. Zhang, B. Yang, L. Lei, Z. Li and Y. Hou. Highly Selective Electrochemical conversion of CO_2 to HCOOH on dendritic indium foams. *ChemElectroChem*. **2018**, 5: 253-259.

[62] A. Rabiee and D. Nematollahi. Electrochemical reduction of CO_2 to formate ion using nanocubic mesoporous $In(OH)_3$/carbon black system. *Materials Chemistry and Physics*. **2017**, 193: 109-116.

[63] Z. M. Detweiler, J. L. White, S. L. Bernasek and A. B. Bocarsly. Anodized indium metal electrodes for enhanced carbon dioxide reduction in aqueous electrolyte. *Langmuir*. **2014**, 30: 7593-7600.

[64] S. Gao, Y. Lin, X. Jiao, Y. Sun, Q. Luo, W. Zhang, D. Li, J. Yang and Y. Xie. Partially oxidized atomic cobalt layers for carbon dioxide electroreduction to liquid fuel. *Nature*. **2016**, 529: 68.

[65] S. Gao, X. Jiao, Z. Sun, W. Zhang, Y. Sun, C. Wang, Q. Hu, X. Zu, F. Yang and S. Yang. Ultrathin Co_3O_4 layers realizing optimized CO_2 electroreduction to formate. *Angewandte Chemie International Edition*. **2016**, 55: 698-702.

[66] P. Sekar, L. Calvillo, C. Tubaro, M. Baron, A. Pokle, F. Carraro, A. Martucci and S. Agnoli. Cobalt Spinel Nanocubes on N-Doped Graphene: A synergistic hybrid electrocatalyst for the highly selective reduction of carbon dioxide to formic acid. *ACS Catalysis*. **2017**, 7: 7695-7703.

[67] W. Zhu, Y.-J. Zhang, H. Zhang, H. Lv, Q. Li, R. Michalsky, A. A. Peterson and S. Sun. Active and selective conversion of CO_2 to CO on ultrathin Au nanowires. *Journal of the American Chemical Society*. **2014**, 136: 16132-16135.

[68] W. Zhu, R. Michalsky, O. n. Metin, H. Lv, S. Guo, C. J. Wright, X. Sun, A. A. Peterson and S. Sun. Monodisperse Au nanoparticles for selective electrocatalytic reduction of CO_2 to CO. *Journal of the American Chemical Society*. **2013**, 135: 16833-16836.

[69] X. Feng, K. Jiang, S. Fan and M. W. Kanan. Grain-boundary-dependent CO_2 electroreduction activity. *Journal of the American Chemical Society*. **2015**, 137: 4606-4609.

[70] S. Zhao, N. Austin, M. Li, Y. Song, S. D. House, S. Bernhard, J. Yang, G. Mpourmpakis and R. Jin. Influence of atomic-level morphology on catalysis: the case of sphere and rod-like gold nanoclusters for CO_2 electroreduction. *ACS Catalysis*. **2018**, 8: 4996-5001.

[71] C. Rogers, W. S. Perkins, G. Veber, T. E. Williams, R. R. Cloke and F. R. Fischer. Synergistic enhancement of electrocatalytic CO_2 reduction with gold nanoparticles embedded in functional graphene nanoribbon composite electrodes. *Journal of the American Chemical Society*. **2017**, 139: 4052-4061.

[72] M. Liu, Y. Pang, B. Zhang, P. De Luna, O. Voznyy, J. Xu, X. Zheng, C. T. Dinh, F. Fan and C. Cao. Enhanced electrocatalytic CO_2 reduction via field-induced reagent concentration. *Nature*. **2016**, 537: 382.

[73] C. Kim, H. S. Jeon, T. Eom, M. S. Jee, H. Kim, C. M. Friend, B. K. Min and Y. J. Hwang. Achieving selective and efficient electrocatalytic activity for CO_2 reduction using immobilized silver nanoparticles. *Journal of the American Chemical Society*. **2015**, 137: 13844-13850.

[74] Y.-C. Hsieh, S. D. Senanayake, Y. Zhang, W. Xu and D. E. Polyansky. Effect of chloride anions on the synthesis and enhanced catalytic activity of silver nanocoral electrodes for CO_2 electroreduction. *ACS Catalysis*. **2015**, 5: 5349-5356.

[75] Q. Lu, J. Rosen, Y. Zhou, G. S. Hutchings, Y. C. Kimmel, J. G. Chen and F. Jiao. A selective and efficient electrocatalyst for carbon dioxide reduction. *Nature Communications*. **2014**, 5: 3242.

[76] W. Xi, R. Ma, H. Wang, Z. Gao, W. Zhang and Y. Zhao. Ultrathin Ag nanowires electrode for electrochemical syngas production from carbon dioxide. *ACS Sustainable Chemistry & Engineering*. **2018**, 6: 7687-7694.

[77] M. Ma, K. Liu, J. Shen, R. Kas and W. A. Smith. In-situ fabrication and reactivation of highly selective and stable Ag catalysts for electrochemical CO_2 conversion. *ACS Energy Letters*. **2018**, 3: 1301-1306.

[78] S. Liu, H. Tao, L. Zeng, Q. Liu, Z. Xu, Q. Liu and J.-L. Luo. Shape-dependent electrocatalytic reduction of CO_2 to CO on triangular silver nanoplates. *Journal of the American Chemical Society*. **2017**, 139: 2160-2163.

[79] D. Gao, H. Zhou, J. Wang, S. Miao, F. Yang, G. Wang, J. Wang and X. Bao. Size-dependent electrocatalytic reduction of CO_2 over Pd nanoparticles. *Journal of the American Chemical Society*. **2015**, 137: 4288-4291.

[80] X. Min and M. W. Kanan. Pd-catalyzed electrohydrogenation of carbon dioxide to formate: high mass activity at low overpotential and identification of the deactivation pathway. *Journal of the American Chemical Society*. **2015**, 137: 4701-4708.

[81] H. Huang, H. Jia, Z. Liu, P. Gao, J. Zhao, Z. Luo, J. Yang and J. Zeng. Understanding of strain effects in the electrochemical reduction of CO_2: using Pd nanostructures as an ideal platform. *Angewandte Chemie International Edition*. **2017**, 129: 3648-3652.

[82] A. Klinkova, P. De Luna, C.-T. Dinh, O. Voznyy, E. M. Larin, E. Kumacheva and E. H. Sargent. Rational design of efficient palladium catalysts for electroreduction of carbon dioxide to formate. *ACS Catalysis*. **2016**, 6: 8115-8120.

[83] J. Rosen, G. S. Hutchings, Q. Lu, R. V. Forest, A. Moore and F. Jiao. Electrodeposited Zn dendrites with enhanced CO selectivity for electrocatalytic CO_2 reduction. *ACS Catalysis*. **2015**, 5: 4586-4591.

[84] X. Jiang, F. Cai, D. Gao, J. Dong, S. Miao, G. Wang and X. Bao. Electrocatalytic reduction of carbon dioxide over reduced nanoporous zinc oxide. *Electrochemistry Communications*. **2016**, 68: 67-70.

[85] F. Quan, D. Zhong, H. Song, F. Jia and L. Zhang. A highly efficient zinc catalyst for selective electroreduction of carbon dioxide in aqueous NaCl solution. *Journal of Materials Chemistry A*. **2015**, 3: 16409-16413.

[86] D. H. Won, H. Shin, J. Koh, J. Chung, H. S. Lee, H. Kim and S. I. Woo. Highly efficient, selective, and stable CO_2 electroreduction on a hexagonal Zn catalyst. *Angewandte Chemie International Edition.* **2016**, 55: 9297-9300.

[87] M. Ma, K. Djanashvili and W. A. Smith. Selective electrochemical reduction of CO_2 to CO on CuO-derived Cu nanowires. *Physical Chemistry Chemical Physics*. **2015**, 17: 20861-20867.

[88] J.-F. Xie, Y.-X. Huang, W.-W. Li, X.-N. Song, L. Xiong and H.-Q. Yu. Efficient electrochemical CO_2 reduction on a unique chrysanthemum-like Cu nanoflower electrode and direct observation of carbon deposit. *Electrochimica Acta*. **2014**, 139: 137-144.

[89] A. Dutta, M. Rahaman, N. C. Luedi, M. Mohos and P. Broekmann. Morphology matters: tuning the product distribution of CO_2 electroreduction on oxide-derived Cu foam catalysts. *ACS Catalysis*. **2016**, 6: 3804-3814.

[90] A. Loiudice, P. Lobaccaro, E. A. Kamali, T. Thao, B. H. Huang, J. W. Ager and R. Buonsanti. Tailoring copper nanocrystals towards C2 products in electrochemical CO_2 reduction. *Angewandte Chemie International Edition*. **2016**, 55: 5789-5792.

[91] M. Ma, K. Djanashvili and W. A. Smith. Controllable hydrocarbon formation from the electrochemical reduction of CO_2 over Cu nanowire arrays. *Angewandte Chemie International Edition*. **2016**, 55: 6680-6684.

[92] D. Gao, I. Zegkinoglou, N. J. Divins, F. Scholten, I. Sinev, P. Grosse and B. Roldan Cuenya. Plasma-activated copper nanocube catalysts for efficient carbon dioxide electroreduction to hydrocarbons and alcohols. *ACS Nano*. **2017**, 11: 4825-4831.

[93] C. Reller, R. Krause, E. Volkova, B. Schmid, S. Neubauer, A. Rucki, M. Schuster and G. Schmid. Selective electroreduction of CO_2 toward ethylene on nano dendritic copper catalysts at high current density. *Advanced Energy Materials*. **2017**, 7: 1602114.

[94] O. Baturina, Q. Lu, F. Xu, A. Purdy, B. Dyatkin, X. Sang, R. Unocic, T. Brintlinger and Y. Gogotsi. Effect of nanostructured carbon support on copper electrocatalytic activity toward CO_2 electroreduction to hydrocarbon fuels. *Catalysis Today*. **2017**, 288: 2-10.

[95] F.S. Ke, X.-C. Liu, J. Wu, P. P. Sharma, Z.Y. Zhou, J. Qiao and X.D. Zhou. Selective formation of C2 products from the electrochemical conversion of CO_2 on CuO-derived copper electrodes comprised of nanoporous ribbon arrays. *Catalysis Today*. **2017**, 288: 18-23.

[96] D. Ren, N. T. Wong, A. D. Handoko, Y. Huang and B. S. Yeo. Mechanistic insights into the enhanced activity and stability of agglomerated Cu nanocrystals for the electrochemical reduction of carbon dioxide to n-propanol. *The Journal of Physical Chemistry Letters*. **2015**, 7: 20-24.

[97] Y. Li, F. Cui, M. B. Ross, D. Kim, Y. Sun and P. Yang. Structure-sensitive CO_2 electroreduction to hydrocarbons on ultrathin 5-fold twinned copper nanowires. *Nano Letters*. **2017**, 17: 1312-1317.

[98] K. Jiang, R. B. Sandberg, A. J. Akey, X. Liu, D. C. Bell, J. K. Nørskov, K. Chan and H. Wang. Metal ion cycling of Cu foil for selective C–C coupling in electrochemical CO_2 reduction. *Nature Catalysis*. **2018**, 1: 111-119.

[99] R. Kas, K. K. Hummadi, R. Kortlever, P. De Wit, A. Milbrat, M. W. Luiten-Olieman, N. E. Benes, M. T. Koper and G. Mul. Three-dimensional porous hollow fibre copper electrodes for efficient and high-rate electrochemical carbon dioxide reduction. *Nature Communications*. **2016**, 7: 10748.

[100] Z. P. Jovanov, H. A. Hansen, A. S. Varela, P. Malacrida, A. A. Peterson, J. K. Nørskov, I. E. Stephens and I. Chorkendorff. Opportunities and challenges in the electrocatalysis of CO_2 and CO reduction using bifunctional surfaces: A theoretical and experimental study of Au-Cd alloys. *Journal of Catalysis*. **2016**, 343: 215-231.

[101] M. Watanabe, M. Shibata, A. Kato, M. Azuma and T. Sakata. Design of alloy electrocatalysts for CO_2 reduction III. The selective and reversible reduction of on Cu alloy electrodes. *Journal of the Electrochemical Society*. **1991**, 138: 3382-3389.

[102] Z. Xu, E. Lai, S.-H. Yang and H.-S. Kimberly. Compositional dependence of the stability of AuCu alloy nanoparticles. *Chemical Communications*. **2012**, 48: 5626-5628.

[103] F. Jia, X. Yu and L. Zhang. Enhanced selectivity for the electrochemical reduction of CO_2 to alcohols in aqueous solution with nanostructured Cu-Au alloy as catalyst. *Journal of Power Sources*. **2014**, 252: 85-89.

[104] D. Kim, J. Resasco, Y. Yu, A. M. Asiri and P. Yang. Synergistic geometric and electronic effects for electrochemical reduction of carbon dioxide using gold-copper bimetallic nanoparticles. *Nature Communications*. **2014**, 5: 4948.

[105] S. Rasul, D. H. Anjum, A. Jedidi, Y. Minenkov, L. Cavallo and K. Takanabe. A highly selective copper-indium bimetallic electrocatalyst for the electrochemical reduction of aqueous CO_2 to CO. *Angewandte Chemie International Edition*. **2015**, 127: 2174-2178.

[106] N. Artrith and A. M. Kolpak. Understanding the composition and activity of electrocatalytic nanoalloys in aqueous solvents: A combination of DFT and accurate neural network potentials. *Nano Letters*. **2014**, 14: 2670-2676.

[107] P. Hirunsit. Electroreduction of carbon dioxide to methane on copper, copper-silver, and copper-gold catalysts: a DFT study. *The Journal of Physical Chemistry C*. **2013**, 117: 8262-8268.

[108] P. Hirunsit, W. Soodsawang and J. Limtrakul. CO_2 electrochemical reduction to methane and methanol on copper-based alloys: theoretical insight. *The Journal of Physical Chemistry C*. **2015**, 119: 8238-8249.

[109] M. Karamad, V. Tripkovic and J. Rossmeisl. Intermetallic alloys as CO electroreduction catalysts: Role of isolated active sites. *ACS Catalysis*. **2014**, 4: 2268-2273.

[110] R. Kortlever, I. Peters, C. Balemans, R. Kas, Y. Kwon, G. Mul and M. Koper. Palladium-gold catalyst for the electrochemical reduction of CO_2 to C1-C5 hydrocarbons. *Chemical Communications*. **2016**, 52: 10229-10232.

[111] D. A. Torelli, S. A. Francis, J. C. Crompton, A. Javier, J. R. Thompson, B. S. Brunschwig, M. P. Soriaga and N. S. Lewis. Nickel-gallium-catalyzed electrochemical reduction of CO_2 to highly reduced products at low overpotentials. *ACS Catalysis*. **2016**, 6: 2100-2104.

[112] C. Hahn, D. N. Abram, H. A. Hansen, T. Hatsukade, A. Jackson, N. C. Johnson, T. R. Hellstern, K. P. Kuhl, E. R. Cave and J. T. Feaster. Synthesis of thin film AuPd alloys and their investigation for electrocatalytic CO_2 reduction. *Journal of Materials Chemistry A*. **2015**, 3: 20185-20194.

[113] X. Bai, W. Chen, C. Zhao, S. Li, Y. Song, R. Ge, W. Wei and Y. Sun. Exclusive formation of formic acid from CO_2 electroreduction by tunable Pd-Sn alloy. *Angewandte Chemie International Edition*. **2017**, 129: 12387-12391.

[114] M. Li, J. Wang, P. Li, K. Chang, C. Li, T. Wang, B. Jiang, H. Zhang, H. Liu and Y. Yamauchi. Mesoporous palladium-copper bimetallic electrodes for selective electrocatalytic reduction of aqueous CO_2 to CO. *Journal of Materials Chemistry A*. **2016**, 4: 4776-4782.

[115] S. Sarfraz, A. T. Garcia-Esparza, A. Jedidi, L. Cavallo and K. Takanabe. Cu-Sn bimetallic catalyst for selective aqueous electroreduction of CO_2 to CO. *ACS Catalysis*. **2016**, 6: 2842-2851.

[116] C. Wang, M. Cao, X. Jiang, M. Wang and Y. Shen. A catalyst based on copper-cadmium bimetal for electrochemical reduction of CO_2 to CO with high faradaic efficiency. *Electrochimica Acta*. **2018**, 271: 544-550.

[117] X. Guo, Y. Zhang, C. Deng, X. Li, Y. Xue, Y.-M. Yan and K. Sun. Composition dependent activity of Cu-Pt nanocrystals for electrochemical reduction of CO_2. *Chemical Communications*. **2015**, 51: 1345-1348.

[118] T. T. Hoang, S. Verma, S. Ma, T. T. Fister, J. Timoshenko, A. I. Frenkel, P. J. Kenis and A. A. Gewirth. Nanoporous copper-silver alloys by additive-controlled electrodeposition for the selective electroreduction of CO_2 to ethylene and ethanol. *Journal of the American Chemical Society*. **2018**, 140: 5791-5797.

[119] S. Ma, M. Sadakiyo, M. Heima, R. Luo, R. T. Haasch, J. I. Gold, M. Yamauchi and P. J. Kenis. Electroreduction of carbon dioxide to hydrocarbons using bimetallic Cu-Pd catalysts with different mixing patterns. *Journal of the American Chemical Society*. **2016**, 139: 47-50.

[120] D. Ren, B. S.-H. Ang and B. S. Yeo. Tuning the selectivity of carbon dioxide electroreduction toward ethanol on oxide-derived Cu_xZn catalysts. *ACS Catalysis*. **2016**, 6: 8239-8247.

[121] Y. Wang, D. Wang, C. J. Dares, S. L. Marquard, M. V. Sheridan and T. J. Meyer. CO_2 reduction to acetate in mixtures of ultrasmall $(Cu)_n$,$(Ag)_m$ bimetallic nanoparticles. *Proceedings of the National Academy of Sciences*. **2017**, 1713962.

[122] S. Lee, G. Park and J. Lee. Importance of Ag-Cu biphasic boundaries for selective electrochemical reduction of CO_2 to ethanol. *ACS Catalysis*. **2017**, 7: 8594-8604.

[123] J. He, K. E. Dettelbach, A. Huang and C. P. Berlinguette. Brass and bronze as effective CO_2 reduction electrocatalysts. *Angewandte Chemie International Edition*. **2017**, 56: 16579-16582.

[124] K. Sun, T. Cheng, L. Wu, Y. Hu, J. Zhou, A. Maclennan, Z. Jiang, Y. Gao, W. A. Goddard III and Z. Wang. Ultrahigh mass activity for carbon dioxide reduction enabled by gold-iron core-shell nanoparticles. *Journal of the American Chemical Society*. **2017**, 139: 15608-15611.

[125] W. Luc, C. Collins, S. Wang, H. Xin, K. He, Y. Kang and F. Jiao. Ag-Sn bimetallic catalyst with a core-shell Structure for CO_2 reduction. *Journal of the American Chemical Society*. **2017**, 139: 1885-1893.

[126] Q. Lai, N. Yang and G. Yuan. Highly efficient In-Sn alloy catalysts for electrochemical reduction of CO_2 to formate. *Electrochemistry Communications*. **2017**, 83: 24-27.

[127] X. Sun, Q. Zhu, X. Kang, H. Liu, Q. Qian, Z. Zhang and B. Han. Molybdenum-bismuth bimetallic chalcogenide nanosheets for highly efficient electrocatalytic reduction of carbon dioxide to methanol. *Angewandte Chemie International Edition*. **2016**, 55: 6771-6775.

[128] R. Arrigo, M. E. Schuster, S. Wrabetz, F. Girgsdies, J. P. Tessonnier, G. Centi, S. Perathoner, D. S. Su and R. Schlögl. New insights from microcalorimetry on the FeO_x/CNT-based electrocatalysts active in the conversion of CO_2 to fuels. *ChemSusChem*. **2012**, 5: 577-586.

[129] A. N. Grace, S. Y. Choi, M. Vinoba, M. Bhagiyalakshmi, D. H. Chu, Y. Yoon, S. C. Nam and S. K. Jeong. Electrochemical reduction of carbon dioxide at low overpotential on a polyaniline/Cu_2O nanocomposite based electrode. *Applied Energy*. **2014**, 120: 85-94.

[130] N. Kumari, N. Sinha, M. A. Haider and S. Basu. CO_2 reduction to methanol on CeO_2 (110) surface: A density functional theory study. *Electrochimica Acta*. **2015**, 177: 21-29.

[131] N. Ullah, I. Ali, M. Jansen and S. Omanovic. Electrochemical reduction of CO_2 in an aqueous electrolyte employing an iridium/ruthenium-oxide electrode. *The Canadian Journal of Chemical Engineering*. **2015**, 93: 55-62.

[132] S. Ma, Y. Lan, G. M. Perez, S. Moniri and P. J. Kenis. Silver supported on titania as an active catalyst for electrochemical carbon dioxide reduction. *ChemSusChem*. **2014**, 7: 866-874.

[133] D. Chu, G. Qin, X. Yuan, M. Xu, P. Zheng and J. Lu. Fixation of CO_2 by electrocatalytic reduction and electropolymerization in ionic liquid-H_2O solution. *ChemSusChem*. **2008**, 1: 205-209.

[134] G. K. Ramesha, J. F. Brennecke and P. V. Kamat. Origin of catalytic effect in the reduction of CO_2 at nanostructured TiO_2 films. *ACS Catalysis*. **2014**, 4: 3249-3254.

[135] Y. Oh, H. Vrubel, S. Guidoux and X. Hu. Electrochemical reduction of CO_2 in organic solvents catalyzed by MoO_2. *Chemical Communications*. **2014**, 50: 3878-3881.

[136] T. Sekimoto, M. Deguchi, S. Yotsuhashi, Y. Yamada, T. Masui, A. Kuramata and S. Yamakoshi. Highly selective electrochemical reduction of CO_2 to HCOOH on a gallium oxide cathode. *Electrochemistry Communications*. **2014**, 43: 95-97.

[137] A. Yamaguchi, M. Yamamoto, K. Takai, T. Ishii, K. Hashimoto and R. Nakamura. Electrochemical CO_2 reduction by Ni-containing iron sulfides: how is CO_2 electrochemically reduced at bisulfide-bearing deep-sea hydrothermal precipitates? *Electrochimica Acta*. **2014**, 141: 311-318.

[138] K. Chan, C. Tsai, H. A. Hansen and J. K. Nørskov. Molybdenum sulfides and selenides as possible electrocatalysts for CO_2 reduction. *ChemCatChem*. **2014**, 6: 1899-1905.

[139] M. Asadi, B. Kumar, A. Behranginia, B. A. Rosen, A. Baskin, N. Repnin, D. Pisasale, P. Phillips, W. Zhu and R. Haasch. Robust carbon dioxide reduction on molybdenum disulphide edges. *Nature Communications*. **2014**, 5: 4470.

[140] M. Asadi, K. Kim, C. Liu, A. V. Addepalli, P. Abbasi, P. Yasaei, P. Phillips, A. Behranginia, J. M. Cerrato and R. Haasch. Nanostructured transition metal dichalcogenide electrocatalysts for CO_2 reduction in ionic liquid. *Science*. **2016**, 353: 467-470.

[141] F. Li, S.-F. Zhao, L. Chen, A. Khan, D. R. MacFarlane and J. Zhang. Polyethylenimine promoted electrocatalytic reduction of CO_2 to CO in aqueous medium by graphene-supported amorphous molybdenum sulphide. *Energy & Environmental Science*. **2016**, 9: 216-223.

[142] J. Lee, J. Kim and T. Hyeon. Recent progress in the synthesis of porous carbon materials. *Advanced Materials*. **2006**, 18: 2073-2094.

[143] B. Kumar, M. Asadi, D. Pisasale, S. Sinha-Ray, B. A. Rosen, R. Haasch, J. Abiade, A. L. Yarin and A. Salehi-Khojin. Renewable and metal-free carbon nanofiber catalysts for carbon dioxide reduction. *Nature Communications*. **2013**, 4: 2819.

[144] S. Zhang, P. Kang, S. Ubnoske, M. K. Brennaman, N. Song, R. L. House, J. T. Glass and T. J. Meyer. Polyethylenimine-enhanced electrocatalytic reduction of CO_2 to formate at nitrogen-doped carbon nanomaterials. *Journal of the American Chemical Society*. **2014**, 136: 7845-7848.

[145] J. Wu, R. M. Yadav, M. Liu, P. P. Sharma, C. S. Tiwary, L. Ma, X. Zou, X.-D. Zhou, B. I. Yakobson and J. Lou. Achieving highly efficient, selective, and stable CO_2 reduction on nitrogen-doped carbon nanotubes. *ACS Nano*. **2015**, 9: 5364-5371.

[146] P. P. Sharma, J. Wu, R. M. Yadav, M. Liu, C. J. Wright, C. S. Tiwary, B. I. Yakobson, J. Lou, P. M. Ajayan and X. D. Zhou. Nitrogen-doped carbon nanotube arrays for high-efficiency electrochemical reduction of CO_2: on the understanding of defects, defect density, and selectivity. *Angewandte Chemie International Edition*. **2015**, 54: 13701-13705.

[147] J. Wu, M. Liu, P. P. Sharma, R. M. Yadav, L. Ma, Y. Yang, X. Zou, X.-D. Zhou, R. Vajtai and B. I. Yakobson. Incorporation of nitrogen defects for efficient reduction of CO_2 via two-electron pathway on three-dimensional graphene foam. *Nano Letters*. **2015**, 16: 466-470.

[148] J. Wu, S. Ma, J. Sun, J. I. Gold, C. Tiwary, B. Kim, L. Zhu, N. Chopra, I. N. Odeh and R. Vajtai. A metal-free electrocatalyst for carbon dioxide reduction to multi-carbon hydrocarbons and oxygenates. *Nature Communications*. **2016**, 7: 13869.

[149] Y. Liu, S. Chen, X. Quan and H. Yu. Efficient electrochemical reduction of carbon dioxide to acetate on nitrogen-doped nanodiamond. *Journal of the American Chemical Society*. **2015**, 137: 11631-11636.

[150] Y. Song, W. Chen, C. Zhao, S. Li, W. Wei and Y. Sun. Metal-free nitrogen-doped mesoporous carbon for electroreduction of CO_2 to ethanol. *Angewandte Chemie International Edition*. **2017**, 129: 10980-10984.

[151] Y. Liu, Y. Zhang, K. Cheng, X. Quan, X. Fan, Y. Su, S. Chen, H. Zhao, Y. Zhang and H. Yu. Selective electrochemical reduction of carbon dioxide to ethanol on a boron-and nitrogen-Co-doped nanodiamond. *Angewandte Chemie International Edition*. **2017**, 56: 15607-15611.

[152] K. Nakata, T. Ozaki, C. Terashima, A. Fujishima and Y. Einaga. High-yield electrochemical production of formaldehyde from CO_2 and seawater. *Angewandte Chemie International Edition*. **2014**, 53: 871-874.

[153] N. Sreekanth, M. A. Nazrulla, T. V. Vineesh, K. Sailaja and K. L. Phani. Metal-free boron-doped graphene for selective electroreduction of carbon dioxide to formic acid/formate. *Chemical Communications*. **2015**, 51: 16061-16064.

[154] J. Xu, Y. Kan, R. Huang, B. Zhang, B. Wang, K. H. Wu, Y. Lin, X. Sun, Q. Li and G. Centi. Revealing the origin of activity in nitrogen-doped nanocarbons towards electrocatalytic reduction of carbon dioxide. *ChemSusChem*. **2016**, 9: 1085-1089.

[155] F. Li, M. Xue, G. P. Knowles, L. Chen, D. R. MacFarlane and J. Zhang. Porous nitrogen-doped carbon derived from biomass for electrocatalytic reduction of CO_2 to CO. *Electrochimica Acta*. **2017**, 245: 561-568.

[156] X. Sun, X. Kang, Q. Zhu, J. Ma, G. Yang, Z. Liu and B. Han. Very highly efficient reduction of CO_2 to CH_4 using metal-free N-doped carbon electrodes. *Chemical Science*. **2016**, 7: 2883-2887.

[157] H. Wang, J. Jia, P. Song, Q. Wang, D. Li, S. Min, C. Qian, L. Wang, Y. F. Li and C. Ma. Efficient electrocatalytic reduction of CO_2 by ntrogen-doped nanoporous carbon/carbon nanotube membranes-A step towards the electrochemical CO_2 refinery. *Angewandte Chemie International Edition*. **2017**, 129: 7955-7960.

[158] A. S. Varela, N. Ranjbar Sahraie, J. Steinberg, W. Ju, H. S. Oh and P. Strasser. Metal-doped nitrogenated carbon as an efficient catalyst for direct CO_2 electroreduction to CO and hydrocarbons. *Angewandte Chemie International Edition*. **2015**, 54: 10758-10762.

[159] A. Bagger, W. Ju, A. S. Varela, P. Strasser and J. Rossmeisl. Single site porphyrin-like structures advantages over metals for selective electrochemical CO_2 reduction. *Catalysis Today*. **2017**, 288: 74-78.

[160] C. Yan, H. Li, Y. Ye, H. Wu, F. Cai, R. Si, J. Xiao, S. Miao, S. Xie and F. Yang. Coordinatively unsaturated nickel-nitrogen sites towards selective and high-rate CO_2 electroreduction. *Energy & Environmental Science*. **2018**, 11: 1204-1210.

[161] X. Wang, Z. Chen, X. Zhao, T. Yao, W. Chen, R. You, C. Zhao, G. Wu, J. Wang and W. Huang. Regulation of coordination number over single Co sites: triggering the efficient electroreduction of CO_2. *Angewandte Chemie International Edition*. **2018**, 130: 1962-1966.

[162] Y. Pan, R. Lin, Y. Chen, S. Liu, W. Zhu, X. Cao, W. Chen, K. Wu, W.-C. Cheong and Y. Wang. Design of single-atom Co-N_5 catalytic site: a robust electrocatalyst for CO_2 reduction with nearly 100% CO selectivity and remarkable stability. *Journal of the American Chemical Society*. **2018**, 140: 4218-4221.

[163] W. Ju, A. Bagger, G.P. Hao, A. S. Varela, I. Sinev, V. Bon, B. R. Cuenya, S. Kaskel, J. Rossmeisl and P. Strasser. Understanding activity and selectivity of metal-nitrogen-doped carbon catalysts for electrochemical reduction of CO_2. *Nature Communications*. **2017**, 8: 944.

[164] E. Li, F. Yang, Z. Wu, Y. Wang, M. Ruan, P. Song, W. Xing and W. Xu. A Bifunctional highly efficient FeN_x/C electrocatalyst. *Small*. **2018**, 14: 1702827.

[165] T. N. Huan, N. Ranjbar, G. Rousse, M. Sougrati, A. Zitolo, V. Mougel, F. Jaouen and M. Fontecave. Electrochemical reduction of CO_2 catalyzed by Fe-NC materials: a structure-selectivity study. *ACS Catalysis*. **2017**, 7: 1520-1525.

[166] F. Pan, H. Zhao, W. Deng, X. Feng and Y. Li. A novel N, Fe-decorated carbon nanotube/carbon nanosheet architecture for efficient CO_2 reduction. *Electrochimica Acta*. **2018**, 273: 154-161.

[167] Q. Cheng, K. Mao, L. Ma, L. Yang, L. Zou, Z. Zou, Z. Hu and H. Yang. Encapsulation of iron nitride by Fe-N-C shell enabling highly efficient electroreduction of CO_2 to CO. *ACS Energy Letters*. **2018**, 3: 1205-1211.

[168] C. Yan, Y. Ye, L. Lin, H. Wu, Q. Jiang, G. Wang and X. Bao. Improving CO_2 electroreduction over ZIF-derived carbon doped with Fe-N sites by an additional ammonia treatment. *Catalysis Today*. **2018**, https://doi.org/10.1016/j.cattod.2018.03.062.

[169] C. Zhao, X. Dai, T. Yao, W. Chen, X. Wang, J. Wang, J. Yang, S. Wei, Y. Wu and Y. Li. Ionic exchange of metal-organic frameworks to access single nickel sites for efficient electroreduction of CO_2. *Journal of the American Chemical Society*. **2017**, 139: 8078-8081.

[170] X. Li, W. Bi, M. Chen, Y. Sun, H. Ju, W. Yan, J. Zhu, X. Wu, W. Chu and C. Wu. Exclusive Ni-N_4 sites realize near-unity CO selectivity for electrochemical CO_2 reduction. *Journal of the American Chemical Society*. **2017**, 139: 14889-14892.

[171] K. Jiang, S. Siahrostami, T. Zheng, Y. Hu, S. Hwang, E. Stavitski, Y. Peng, J. Dynes, M. Gangisetty and D. Su. Isolated Ni single atoms in graphene nanosheets for high-performance CO_2 reduction. *Energy & Environmental Science*. **2018**, 11: 893-903.

[172] H. B. Yang, S.-F. Hung, S. Liu, K. Yuan, S. Miao, L. Zhang, X. Huang, H.-Y. Wang, W. Cai and R. Chen. Atomically dispersed Ni (I) as the active site for electrochemical CO_2 reduction. *Nature Energy*. **2018**, 3: 140.

[173] P. Su, K. Iwase, S. Nakanishi, K. Hashimoto and K. Kamiya. Nickel-nitrogen-modified graphene: an efficient electrocatalyst for the reduction of carbon dioxide to carbon monoxide. *Small*. **2016**, 12: 6083-6089.

[174] W. Bi, X. Li, R. You, M. Chen, R. Yuan, W. Huang, X. Wu, W. Chu, C. Wu and Y. Xie. Surface immobilization of transition metal ions on nitrogen-doped graphene realizing high-efficient and selective CO_2 reduction. *Advanced Materials*. **2018**, 30: 1706617.

[175] P. Su, K. Iwase, T. Harada, K. Kamiya and S. Nakanishi. Covalent triazine framework modified with coordinatively-unsaturated Co or Ni atoms for CO_2 electrochemical reduction. *Chemical Science*. **2018**, 9: 3941-3947.

[176] C. Costentin, M. Robert and J.-M. Savéant. Molecular catalysis of electrochemical reactions. *Current Opinion in Electrochemistry*. **2017**, 2: 26-31.

[177] B. Kumar, M. Llorente, J. Froehlich, T. Dang, A. Sathrum and C. P. Kubiak. Photochemical and photoelectrochemical reduction of CO_2. *Annual Review of Physical Chemistry*. **2012**, 63: 541-569.

[178] R. M. Bullock, A. K. Das and A. M. Appel. Surface immobilization of molecular electrocatalysts for energy conversion. *Chemistry-A European Journal*. **2017**, 23: 7626-7641.

[179] S. Meshitsuka, M. Ichikawa and K. Tamaru. Electrocatalysis by metal phthalocyanines in the reduction of carbon dioxide. *Journal of the Chemical Society, Chemical Communications*. **1974**, 5: 158-159.

[180] S. Chardon-Noblat, A. Deronzier, R. Ziessel and D. Zsoldos. Electroreduction of CO_2 catalyzed by polymeric [Ru(bpy)$(CO)_2$] n films in aqueous media: parameters influencing the reaction selectivity. *Journal of Electroanalytical Chemistry*. **1998**, 444: 253-260.

[181] S. A. Yao, R. E. Ruther, L. Zhang, R. A. Franking, R. J. Hamers and J. F. Berry. Covalent attachment of catalyst molecules to conductive diamond: CO_2 reduction using "smart" electrodes. *Journal of the American Chemical Society*. **2012**, 134: 15632-15635.

[182] P. Kang, S. Zhang, T. J. Meyer and M. Brookhart. Rapid selective electrocatalytic reduction of carbon dioxide to formate by an iridium pincer catalyst immobilized on carbon nanotube electrodes. *Angewandte Chemie International Edition*. **2014**, 53: 8709-8713.

[183] J. Shen, R. Kortlever, R. Kas, Y. Y. Birdja, O. Diaz-Morales, Y. Kwon, I. Ledezma-Yanez, K. J. P. Schouten, G. Mul and M. T. Koper. Electrocatalytic reduction of carbon dioxide to carbon monoxide and methane at an immobilized cobalt protoporphyrin. *Nature Communications*. **2015**, 6: 8177.

[184] C. Costentin, S. Drouet, M. Robert and J.-M. Savéant. A local proton source enhances CO_2 electroreduction to CO by a molecular Fe catalyst. *Science*. **2012**, 338: 90-94.

[185] Z. Weng, J. Jiang, Y. Wu, Z. Wu, X. Guo, K. L. Materna, W. Liu, V. S. Batista, G. W. Brudvig and H. Wang. Electrochemical CO_2 reduction to hydrocarbons on a heterogeneous molecular Cu catalyst in aqueous solution. *Journal of the American Chemical Society*. **2016**, 138: 8076-8079.

[186] X. Zhang, Z. Wu, X. Zhang, L. Li, Y. Li, H. Xu, X. Li, X. Yu, Z. Zhang and Y. Liang. Highly selective and active CO_2 reduction electrocatalysts based on cobalt phthalocyanine/carbon nanotube hybrid structures. *Nature Communications*. **2017**, 8: 14675.

[187] B. Reuillard, K. H. Ly, T. E. Rosser, M. F. Kuehnel, I. Zebger and E. Reisner. Tuning product selectivity for aqueous CO_2 reduction with a Mn(bipyridine)-pyrene catalyst immobilized on a carbon nanotube electrode. *Journal of the American Chemical Society*. **2017**, 139: 14425-14435.

[188] S. Sato, K. Saita, K. Sekizawa, S. Maeda and T. Morikawa. Low-energy electrocatalytic CO_2 reduction in water over Mn-complex catalyst electrode aided by a nanocarbon support and K^+ cations. *ACS Catalysis*. **2018**, 8: 4452-4458.

[189] S. Lin, C. S. Diercks, Y.-B. Zhang, N. Kornienko, E. M. Nichols, Y. Zhao, A. R. Paris, D. Kim, P. Yang and O. M. Yaghi. Covalent organic frameworks comprising cobalt porphyrins for catalytic CO_2 reduction in water. *Science*. **2015**, 349: 1208-1213.

[190] I. Hod, M. D. Sampson, P. Deria, C. P. Kubiak, O. K. Farha and J. T. Hupp. Fe-porphyrin-based metal-organic framework films as high-surface concentration, heterogeneous catalysts for electrochemical reduction of CO_2. *ACS Catalysis*. **2015**, 5: 6302-6309.

[191] L. Ye, J. Liu, Y. Gao, C. Gong, M. Addicoat, T. Heine, C. Wöll and L. Sun. Highly oriented MOF thin film-based electrocatalytic device for the reduction of CO_2 to CO exhibiting high faradaic efficiency. *Journal of Materials Chemistry A*. **2016**, 4: 15320-15326.

[192] N. Kornienko, Y. Zhao, C. S. Kley, C. Zhu, D. Kim, S. Lin, C. J. Chang, O. M. Yaghi and P. Yang. Metal-organic frameworks for electrocatalytic reduction of carbon dioxide. *Journal of the American Chemical Society*. **2015**, 137: 14129-14135.

[193] A. Rodes, E. Pastor and T. Iwasita. Structural effects on CO_2 reduction at Pt single-crystal electrodes: Part 1. The Pt(110) surface. *Journal of Electroanalytical Chemistry*. **1994**, 369: 183-191.

[194] B. Nikolic, H. Huang, D. Gervasio, A. Lin, C. Fierro, R. Adzic and E. Yeager. Electroreduction of carbon dioxide on platinum single crystal electrodes: electrochemical and in situ FTIR studies. *Journal of Electroanalytical Chemistry and Interfacial Electrochemistry*. **1990**, 295: 415-423.

[195] S. Taguchi and A. Aramata. Surface-structure sensitive reduced CO_2 formation on Pt single crystal electrodes in sulfuric acid solution. *Electrochimica Acta*. **1994**, 39: 2533-2537.

[196] N. Hoshi, T. Mizumura and Y. Hori. Significant difference of the reduction rates of carbon dioxide between Pt(111) and Pt(110) single crystal electrodes. *Electrochimica Acta*. **1995**, 40: 883-887.

[197] N. Hoshi, M. Kato and Y. Hori. Electrochemical reduction of CO_2 on single crystal electrodes of silver Ag(111), Ag(100) and Ag(110). *Journal of Electroanalytical Chemistry*. **1997**, 440: 283-286.

[198] N. Hoshi, M. Noma, T. Suzuki and Y. Hori. Structural effect on the rate of CO_2 reduction on single crystal electrodes of palladium. *Journal of Electroanalytical Chemistry*. **1997**, 421: 15-18.

[199] Y. Hori, I. Takahashi, O. Koga and N. Hoshi. Selective formation of C2 compounds from electrochemical reduction of CO_2 at a series of copper single crystal electrodes. *The Journal of Physical Chemistry B*. **2002**, 106: 15-17.

[200] B. P. Sullivan, K. Krist and H. Guard, *Electrochemical and electrocatalytic reactions of carbon dioxide*, Elsevier, **2012**.

[201] Y. Hori, H. Wakebe, T. Tsukamoto and O. Koga. Adsorption of CO accompanied with simultaneous charge transfer on copper single crystal electrodes related with electrochemical reduction of CO_2 to hydrocarbons. *Surface Science*. **1995**, 335: 258-263.

[202] H. Mistry, A. S. Varela, S. Kühl, P. Strasser and B. R. Cuenya. Nanostructured electrocatalysts with tunable activity and selectivity. *Nature Reviews Materials*. **2016**, 1: 16009.

[203] K. J. P. Schouten, Z. Qin, E. Pérez Gallent and M. T. Koper. Two pathways for the formation of ethylene in CO reduction on single-crystal copper electrodes. *Journal of the American Chemical Society*. **2012**, 134: 9864-9867.

[204] K. Schouten, Y. Kwon, C. Van der Ham, Z. Qin and M. Koper. A new mechanism for the selectivity to C1 and C2 species in the electrochemical reduction of carbon dioxide on copper electrodes. *Chemical Science*. **2011**, 2: 1902-1909.

[205] J. H. Montoya, C. Shi, K. Chan and J. K. Nørskov. Theoretical insights into a CO dimerization mechanism in CO_2 electroreduction. *The Journal of Physical Chemistry Letters*. **2015**, 6: 2032-2037.

[206] F. Calle-Vallejo and M. Koper. Theoretical considerations on the electroreduction of CO to C2 species on Cu(100) electrodes. *Angewandte Chemie International Edition*. **2013**, 125: 7423-7426.

[207] R. Reske, H. Mistry, F. Behafarid, B. Roldan Cuenya and P. Strasser. Particle size effects in the catalytic electroreduction of CO_2 on Cu nanoparticles. *Journal of the American Chemical Society*. **2014**, 136: 6978-6986.

[208] O. A. Baturina, Q. Lu, M. A. Padilla, L. Xin, W. Li, A. Serov, K. Artyushkova, P. Atanassov, F. Xu and A. Epshteyn. CO_2 electroreduction to hydrocarbons on carbon-supported Cu nanoparticles. *ACS Catalysis*. **2014**, 4: 3682-3695.

[209] F. S. Roberts, K. P. Kuhl and A. Nilsson. High selectivity for ethylene from carbon dioxide reduction over copper nanocube electrocatalysts. *Angewandte Chemie International Edition*. **2015**, 127: 5268-5271.

[210] C. S. Chen, A. D. Handoko, J. H. Wan, L. Ma, D. Ren and B. S. Yeo. Stable and selective electrochemical reduction of carbon dioxide to ethylene on copper mesocrystals. *Catalysis Science & Technology*. **2015**, 5: 161-168.

[211] D. Kim, C. S. Kley, Y. Li and P. Yang. Copper nanoparticle ensembles for selective electroreduction of CO_2 to C2-C3 products. *Proceedings of the National Academy of Sciences*. **2017**, 114: 10560-10565.

[212] H.-E. Lee, K. D. Yang, S. M. Yoon, H.-Y. Ahn, Y. Y. Lee, H. Chang, D. H. Jeong, Y.-S. Lee, M. Y. Kim and K. T. Nam. Concave rhombic dodecahedral Au nanocatalyst with multiple high-index facets for CO_2 reduction. *ACS Nano*. **2015**, 9: 8384-8393.

[213] C. W. Li, J. Ciston and M. W. Kanan. Electroreduction of carbon monoxide to liquid fuel on oxide-derived nanocrystalline copper. *Nature*. **2014**, 508: 504.

[214] A. Verdaguer-Casadevall, C. W. Li, T. P. Johansson, S. B. Scott, J. T. McKeown, M. Kumar, I. E. Stephens, M. W. Kanan and I. Chorkendorff. Probing the active surface sites for CO reduction on oxide-derived copper electrocatalysts. *Journal of the American Chemical Society*. **2015**, 137: 9808-9811.

[215] X. Feng, K. Jiang, S. Fan and M. W. Kanan. A direct grain-boundary-activity correlation for CO electroreduction on Cu nanoparticles. *ACS Central Science*. **2016**, 2: 169-174.

[216] R. G. Mariano, K. McKelvey, H. S. White and M. W. Kanan. Selective increase in CO_2 electroreduction activity at grain-boundary surface terminations. *Science*. **2017**, 358: 1187-1192.

[217] K.-S. Kim, W. J. Kim, H.-K. Lim, E. K. Lee and H. Kim. Tuned chemical bonding ability of Au at grain boundaries for enhanced electrochemical CO_2 reduction. *ACS Catalysis*. **2016**, 6: 4443-4448.

[218] H. Mistry, F. Behafarid, R. Reske, A. S. Varela, P. Strasser and B. Roldan Cuenya. Tuning catalytic selectivity at the mesoscale via interparticle interactions. *ACS Catalysis*. **2016**, 6: 1075-1080.

[219] A. S. Hall, Y. Yoon, A. Wuttig and Y. Surendranath. Mesostructure-induced selectivity in CO_2 reduction catalysis. *Journal of the American Chemical Society*. **2015**, 137: 14834-14837.

[220] Y. Yoon, A. S. Hall and Y. Surendranath. Tuning of silver catalyst mesostructure promotes selective carbon dioxide conversion into fuels. *Angewandte Chemie International Edition*. **2016**, 128: 15508-15512.

[221] X. Zheng, P. De Luna, F. P. G. de Arquer, B. Zhang, N. Becknell, M. B. Ross, Y. Li, M. N. Banis, Y. Li and M. Liu. Sulfur-modulated tin sites enable highly selective electrochemical reduction of CO_2 to formate. *Joule*. **2017**, 1: 794-805.

[222] K. W. Frese. Electrochemical reduction of CO_2 at intentionally oxidized copper electrodes. *Journal of the Electrochemical Society*. **1991**, 138: 3338-3344.

[223] R. Kas, R. Kortlever, A. Milbrat, M. T. Koper, G. Mul and J. Baltrusaitis. Electrochemical CO_2 reduction on Cu_2O-derived copper nanoparticles: controlling the catalytic selectivity of hydrocarbons. *Physical Chemistry Chemical Physics*. **2014**, 16: 12194-12201.

[224] D. Ren, Y. Deng, A. D. Handoko, C. S. Chen, S. Malkhandi and B. S. Yeo. Selective electrochemical reduction of carbon dioxide to ethylene and ethanol on copper(I) oxide catalysts. *ACS Catalysis*. **2015**, 5: 2814-2821.

[225] Y.-J. Zhang and A. A. Peterson. Oxygen-induced changes to selectivity-determining steps in electrocatalytic CO_2 reduction. *Physical Chemistry Chemical Physics*. **2015**, 17: 4505-4515.

[226] D. Kim, S. Lee, J. D. Ocon, B. Jeong, J. K. Lee and J. Lee. Insights into an autonomously formed oxygen-evacuated Cu_2O electrode for the selective production of C_2H_4 from CO_2. *Physical Chemistry Chemical Physics*. **2015**, 17: 824-830.

[227] H. Mistry, A. S. Varela, C. S. Bonifacio, I. Zegkinoglou, I. Sinev, Y.-W. Choi, K. Kisslinger, E. A. Stach, J. C. Yang and P. Strasser. Highly selective plasma-activated copper catalysts for carbon dioxide reduction to ethylene. *Nature Communications*. **2016**, 7: 12123.

[228] A. Eilert, F. Cavalca, F. S. Roberts, J. r. Osterwalder, C. Liu, M. Favaro, E. J. Crumlin, H. Ogasawara, D. Friebel and L. G. Pettersson. Subsurface oxygen in oxide-derived copper electrocatalysts for carbon dioxide reduction. *The Journal of Physical Chemistry Letters*. **2016**, 8: 285-290.

[229] M. Ma, B. J. Trześniewski, J. Xie and W. A. Smith. Selective and efficient reduction of carbon dioxide to carbon monoxide on oxide-derived nanostructured silver electrocatalysts. *Angewandte Chemie International Edition*. **2016**, 55: 9748-9752.

[230] Y. Chen and M. W. Kanan. Tin oxide dependence of the CO_2 reduction efficiency on tin electrodes and enhanced activity for tin/tin oxide thin-film catalysts. *Journal of the American Chemical Society*. **2012**, 134: 1986-1989.

[231] D. L. T. Nguyen, M. S. Jee, D. H. Won, H. Jung, H.-S. Oh, B. K. Min and Y. J. Hwang. Selective CO_2 reduction on zinc electrocatalyst: the effect of zinc oxidation state induced by pretreatment environment. *ACS Sustainable Chemistry & Engineering*. **2017**, 5: 11377-11386.

[232] C. H. Lee and M. W. Kanan. Controlling H^+ vs CO_2 reduction selectivity on Pb electrodes. *ACS Catalysis*. **2014**, 5: 465-469.

[233] Y. Yang, M. Luo, W. Zhang, Y. Sun, X. Chen and S. Guo. Metal surface and interface energy electrocatalysis: fundamentals, performance engineering, and opportunities. *Chem*. **2018**, https://doi.org/10.1016/j.chempr.2018.05.019.

[234] D. Gao, Y. Zhang, Z. Zhou, F. Cai, X. Zhao, W. Huang, Y. Li, J. Zhu, P. Liu and F. Yang. Enhancing CO_2 electroreduction with the metal-oxide interface. *Journal of the American Chemical Society*. **2017**, 139: 5652-5655.

[235] W. Zhang, Q. Qin, L. Dai, R. Qin, X. Zhao, X. Chen, D. Ou, T. T. Chuong, B. Wu and N. Zheng. Electrochemical Reduction of CO_2 to CH_3OH on hierarchical Pd/SnO_2 nanosheets with abundant Pd-O-Sn interfaces. *Angewandte Chemie International Edition*. **2018**, 57: 9475-9479.

[236] Q. Li, W. Zhu, J. Fu, H. Zhang, G. Wu and S. Sun. Controlled assembly of Cu nanoparticles on pyridinic-N rich graphene for electrochemical reduction of CO_2 to ethylene. *Nano Energy*. **2016**, 24: 1-9.

[237] T. Bligaard and J. K. Nørskov. Ligand effects in heterogeneous catalysis and electrochemistry. *Electrochimica Acta*. **2007**, 52: 5512-5516.

[238] P. Strasser, S. Koh, T. Anniyev, J. Greeley, K. More, C. Yu, Z. Liu, S. Kaya, D. Nordlund and H. Ogasawara. Lattice-strain control of the activity in dealloyed core-shell fuel cell catalysts. *Nature Chemistry*. **2010**, 2: 454.

[239] J. J. Humphrey, D. Plana, V. Celorrio, S. Sadasivan, R. P. Tooze, P. Rodríguez and D. J. Fermín. Electrochemical reduction of carbon dioxide at gold-palladium core-shell nanoparticles: product distribution versus shell thickness. *ChemCatChem*. **2016**, 8: 952-960.

[240] G. Chen, C. Xu, X. Huang, J. Ye, L. Gu, G. Li, Z. Tang, B. Wu, H. Yang and Z. Zhao. Interfacial electronic effects control the reaction selectivity of platinum catalysts. *Nature Materials*. **2016**, 15: 564.

[241] M. S. Xie, B. Y. Xia, Y. Li, Y. Yan, Y. Yang, Q. Sun, S. H. Chan, A. Fisher and X. Wang. Amino acid modified copper electrodes for the enhanced selective electroreduction of carbon dioxide towards hydrocarbons. *Energy & Environmental Science*. **2016**, 9: 1687-1695.

[242] S. Ahn, K. Klyukin, R. J. Wakeham, J. A. Rudd, A. R. Lewis, S. Alexander, F. Carla, V. Alexandrov and E. Andreoli. Poly-amide modified copper foam electrodes for enhanced electrochemical reduction of carbon dioxide. *ACS Catalysis*. **2018**, 8: 4132-4142.

[243] A. A. Peterson and J. K. Nørskov. Activity descriptors for CO_2 electroreduction to methane on transition-metal catalysts. *The Journal of Physical Chemistry Letters*. **2012**, 3: 251-258.

[244] Z. Cao, D. Kim, D. Hong, Y. Yu, J. Xu, S. Lin, X. Wen, E. M. Nichols, K. Jeong and J. A. Reimer. A molecular surface functionalization approach to tuning nanoparticle electrocatalysts for carbon dioxide reduction. *Journal of the American Chemical Society*. **2016**, 138: 8120-8125.

[245] Z. Cao, J. S. Derrick, J. Xu, R. Gao, M. Gong, E. M. Nichols, P. T. Smith, X. Liu, X. Wen and C. Copéret. Chelating N-heterocyclic carbene ligands enable tuning of electrocatalytic CO_2 reduction to formate and carbon monoxide: surface organometallic chemistry. *Angewandte Chemie International Edition*. **2018**, 130: 5075-5079.

[246] Y. Fang and J. C. Flake. Electrochemical reduction of CO_2 at functionalized Au electrodes. *Journal of the American Chemical Society*. **2017**, 139: 3399-3405.

[247] C. Kim, T. Eom, M. S. Jee, H. Jung, H. Kim, B. K. Min and Y. J. Hwang. Insight into electrochemical CO_2 reduction on surface-molecule-mediated Ag nanoparticles. *ACS Catalysis*. **2016**, 7: 779-785.

[248] W. Gao, W. Gou, X. Zhou, J. C. Ho, Y. Ma and Y. Qu. Amine-modulated/engineered interfaces of NiMo electrocatalysts for improved hydrogen evolution reaction in alkaline solutions. *ACS Applied Materials & Interfaces*. **2018**, 10: 1728-1733.

[249] M. Cho, J. T. Song, S. Back, Y. Jung and J. Oh. The role of adsorbed CN and Cl on an Au electrode for electrochemical CO_2 reduction. *ACS Catalysis*. **2018**, 8: 1178-1185.

[250] J. Fu, Y. Wang, J. Liu, K. Huang, Y. Chen, Y. Li and J.-J. Zhu. Low Overpotential for electrochemically reducing CO_2 to CO on nitrogen-doped graphene quantum dots-wrapped single-crystalline gold nanoparticles. *ACS Energy Letters*. **2018**, 3: 946-951.

[251] C.Y. Lee, Y. Zhao, C. Wang, D. R. Mitchell and G. G. Wallace. Rapid formation of self-organised Ag nanosheets with high efficiency and selectivity in CO_2 electroreduction to CO. *Sustainable Energy & Fuels*. **2017**, 1: 1023-1027.

[252] F. Li, L. Chen, M. Xue, T. Williams, Y. Zhang, D. R. MacFarlane and J. Zhang. Towards a better Sn: efficient electrocatalytic reduction of CO_2 to formate by Sn/SnS_2 derived from SnS_2 nanosheets. *Nano Energy*. **2017**, 31: 270-277.

[253] K. Ogura, J. R. Ferrell III, A. V. Cugini, E. S. Smotkin and M. D. Salazar-Villalpando. CO_2 attraction by specifically adsorbed anions and subsequent accelerated electrochemical reduction. *Electrochimica Acta*. **2010**, 56: 381-386.

[254] A. S. Varela, W. Ju, T. Reier and P. Strasser. Tuning the catalytic activity and selectivity of Cu for CO_2 electroreduction in the presence of halides. *ACS Catalysis*. **2016**, 6: 2136-2144.

[255] D. Gao, F. Scholten and B. Roldan Cuenya. Improved CO_2 Electroreduction performance on plasma-activated Cu catalysts via electrolyte design: halide effect. *ACS Catalysis*. **2017**, 7: 5112-5120.

[256] S. Zhao, Z. Tang, S. Guo, M. Han, C. Zhu, Y. Zhou, L. Bai, J. Gao, H. Huang and Y. Li. Enhanced activity for CO_2 electroreduction on a highly active and stable ternary Au-CDots-C_3N_4 electrocatalyst. *ACS Catalysis*. **2017**, 8: 188-197.

[257] P. A. Tipler and R. Llewellyn, *Modern Physics*, Macmillan, **2003**.

[258] B. Fultz and J. M. Howe, *Transmission Electron Microscopy and Diffractometry of Materials*, Springer Science & Business Media, **2012**.

[259] E. P. Bertin, *Principles and practice of X-ray spectrometric analysis*, Springer Science & Business Media, **2012**.

[260] N. Colthup, *Introduction to Infrared and Raman spectroscopy*, Elsevier, **2012**.

[261] R. B. Prime, H. E. Bair, S. Vyazovkin, P. K. Gallagher and A. Riga. Thermogravimetric analysis (TGA). in *Thermal Analysis of Polymers: Fundamentals and Applications*. **2009**, pp. 241-317.

[262] G. Fagerlund. Determination of specific surface by the BET method. *Matériaux et Construction*. **1973**, 6: 239-245.

[263] R. Kortlever, J. Shen, K. J. P. Schouten, F. Calle-Vallejo and M. T. Koper. Catalysts and reaction pathways for the electrochemical reduction of carbon dioxide. *The Journal of Physical Chemistry Letters*. **2015**, 6: 4073-4082.

[264] Y. Hori, A. Murata, R. Takahashi and S. Suzuki. Electroreduction of carbon monoxide to methane and ethylene at a copper electrode in aqueous solutions at ambient temperature and pressure. *Journal of the American Chemical Society*. **1987**, 109: 5022-5023.

[265] K. Klier, Methanol synthesis, in: *Advances in Catalysis*, Elsevier, **1982**, pp. 243-313.

[266] R. Burch, S. E. Golunski and M. S. Spencer. The role of copper and zinc oxide in methanol synthesis catalysts. *Journal of the Chemical Society, Faraday Transactions*. **1990**, 86: 2683-2691.

[267] C. K. Rofer-DePoorter. A comprehensive mechanism for the Fischer-Tropsch synthesis. *Chemical Reviews*. **1981**, 81: 447-474.

[268] P. Vennestrøm, C. M. Osmundsen, C. Christensen and E. Taarning. Beyond petrochemicals: the renewable chemicals industry. *Angewandte Chemie International Edition*. **2011**, 50: 10502-10509.

[269] Y. Zhang, G. Jacobs, D. E. Sparks, M. E. Dry and B. H. Davis. CO and CO_2 hydrogenation study on supported cobalt Fischer-Tropsch synthesis catalysts. *Catalysis Today*. **2002**, 71: 411-418.

[270] Y. Hori, R. Takahashi, Y. Yoshinami and A. Murata. Electrochemical reduction of CO at a copper electrode. *The Journal of Physical Chemistry B*. **1997**, 101: 7075-7081.

[271] M. Watanabe, M. Shibata, A. Katoh, T. Sakata and M. Azuma. Design of alloy electrocatalysts for CO_2 reduction: improved energy efficiency, selectivity, and reaction rate for the CO_2 electroreduction on Cu alloy electrodes. *Journal of Electroanalytical Chemistry and Interfacial Electrochemistry*. **1991**, 305: 319-328.

[272] A. Katoh, H. Uchida, M. Shibata and M. Watanabe. Design of electrocatalyst for CO_2 reduction V. effect of the microcrystalline structures of Cu-Sn and Cu-Zn Alloys on the Electrocatalysis of Reduction. *Journal of the Electrochemical Society*. **1994**, 141: 2054-2058.

[273] S. Rasul, D. H. Anjum, A. Jedidi, Y. Minenkov, L. Cavallo and K. Takanabe. A highly selective copper-indium bimetallic electrocatalyst for the electrochemical reduction of aqueous CO_2 to CO. *Angewandte Chemie International Edition*. **2015**, 54: 2146-2150.

[274] H.-K. Lim, H. Shin, W. A. Goddard III, Y. J. Hwang, B. K. Min and H. Kim. Embedding covalency into metal catalysts for efficient electrochemical conversion of CO_2. *Journal of the American Chemical Society*. **2014**, 136: 11355-11361.

[275] X. Huang, Z. Zhao, L. Cao, Y. Chen, E. Zhu, Z. Lin, M. Li, A. Yan, A. Zettl and Y. M. Wang. High-performance transition metal-doped Pt_3Ni octahedra for oxygen reduction reaction. *Science*. **2015**, 348: 1230-1234.

[276] Q. Lu, G. S. Hutchings, W. Yu, Y. Zhou, R. V. Forest, R. Tao, J. Rosen, B. T. Yonemoto, Z. Cao and H. Zheng. Highly porous non-precious bimetallic electrocatalysts for efficient hydrogen evolution. *Nature Communications*. **2015**, 6: 6567.

[277] D. H. Won, C. H. Choi, J. Chung, M. W. Chung, E. H. Kim and S. I. Woo. Rational design of a hierarchical tin dendrite electrode for efficient electrochemical reduction of CO_2. *ChemSusChem*. **2015**, 8: 3092-3098.

[278] R. Czerw, M. Terrones, J.-C. Charlier, X. Blase, B. Foley, R. Kamalakaran, N. Grobert, H. Terrones, D. Tekleab and P. Ajayan. Identification of electron donor states in N-doped carbon nanotubes. *Nano Letters*. **2001**, 1: 457-460.

[279] Q. Wei, X. Tong, G. Zhang, J. Qiao, Q. Gong and S. Sun. Nitrogen-doped carbon nanotube and graphene materials for oxygen reduction reactions. *Catalysts*. **2015**, 5: 1574-1602.

[280] Y. Liu, N. Zhang, L. Jiao and J. Chen. Tin nanodots encapsulated in porous nitrogen-doped carbon nanofibers as a free-standing anode for advanced sodium-ion batteries. *Advanced Materials*. **2015**, 27: 6702-6707.

[281] Y. Yu, L. Gu, C. Zhu, P. A. Van Aken and J. Maier. Tin nanoparticles encapsulated in porous multichannel carbon microtubes: preparation by single-nozzle electrospinning and application as anode material for high-performance Li-based batteries. *Journal of the American Chemical Society*. **2009**, 131: 15984-15985.

[282] Y. Zhao, Y. Meng and P. Jiang. Carbon@MnO_2 core-shell nanospheres for flexible high-performance supercapacitor electrode materials. *Journal of Power Sources*. **2014**, 259: 219-226.

[283] Y. Li, J. Qiao, X. Zhang, T. Lei, A. Girma, Y. Liu and J. Zhang. Rational design and synthesis of SnO_x electrocatalysts with coralline structure for highly improved aqueous CO_2 reduction to formate. *ChemElectroChem*. **2016**, 3: 1618-1628.

[284] Y. Liu, N. Zhang, L. Jiao, Z. Tao and J. Chen. Ultrasmall Sn nanoparticles embedded in carbon as high-performance anode for sodium-ion batteries. *Advanced Functional Materials*. **2015**, 25: 214-220.

[285] V. Tripkovic, M. Vanin, M. Karamad, M. r. E. Björketun, K. W. Jacobsen, K. S. Thygesen and J. Rossmeisl. Electrochemical CO_2 and CO reduction on metal-functionalized porphyrin-like graphene. *The Journal of Physical Chemistry C*. **2013**, 117: 9187-9195.

[286] W. Lv, R. Zhang, P. Gao and L. Lei. Studies on the faradaic efficiency for electrochemical reduction of carbon dioxide to formate on tin electrode. *Journal of Power Sources*. **2014**, 253: 276-281.

[287] Q. Wang, H. Dong and H. Yu. Development of rolling tin gas diffusion electrode for carbon dioxide electrochemical reduction to produce formate in aqueous electrolyte. *Journal of Power Sources*. **2014**, 271: 278-284.

[288] G. S. Prakash, F. A. Viva and G. A. Olah. Electrochemical reduction of CO_2 over Sn-Nafion® coated electrode for a fuel-cell-like device. *Journal of Power Sources*. **2013**, 223: 68-73.

[289] Q. Wang, H. Dong, H. Yu, H. Yu and M. Liu. Enhanced electrochemical reduction of carbon dioxide to formic acid using a two-layer gas diffusion electrode in a microbial electrolysis cell. *RSC Advances*. **2015**, 5: 10346-10351.

[290] D. Kopljar, A. Inan, P. Vindayer, N. Wagner and E. Klemm. Electrochemical reduction of CO_2 to formate at high current density using gas diffusion electrodes. *Journal of Applied Electrochemistry*. **2014**, 44: 1107-1116.

[291] H. Li and C. Oloman. Development of a continuous reactor for the electro-reduction of carbon dioxide to formate-Part 2: Scale-up. *Journal of Applied Electrochemistry*. **2007**, 37: 1107-1117.

[292] C. Oloman and H. Li. Electrochemical processing of carbon dioxide. *ChemSusChem*. **2008**, 1: 385-391.

[293] E. Irtem, T. Andreu, A. Parra, M. Hernandez-Alonso, S. Garcia-Rodriguez, J. Riesco-Garcia, G. Penelas-Pérez and J. Morante. Low-energy formate production from CO_2 electroreduction using electrodeposited tin on GDE. *Journal of Materials Chemistry A*. **2016**, 4: 13582-13588.

[294] Q. Wang, H. Dong and H. Yu. Fabrication of a novel tin gas diffusion electrode for electrochemical reduction of carbon dioxide to formic acid. *RSC Advances*. **2014**, 4: 59970-59976.

[295] J. Wu, F. Risalvato and X.D. Zhou. Effects of the electrolyte on electrochemical reduction of CO_2 on Sn electrode. *ECS Transactions*. **2012**, 41: 49-60.

[296] S. Zhang, Y. Shao, H.-g. Liao, J. Liu, I. A. Aksay, G. Yin and Y. Lin. Graphene decorated with PtAu alloy nanoparticles: facile synthesis and promising application for formic acid oxidation. *Chemistry of Materials*. **2011**, 23: 1079-1081.

[297] G. Panomsuwan, N. Saito and T. Ishizaki. Nitrogen-doped carbon nanoparticle-carbon nanofiber composite as an efficient metal-free cathode catalyst for oxygen reduction reaction. *ACS Applied Materials & Interfaces*. **2016**, 8: 6962-6971.

[298] Y. Zhao, C. Wang and G. G. Wallace. Tin nanoparticles decorated copper oxide nanowires for selective electrochemical reduction of aqueous CO_2 to CO. *Journal of Materials Chemistry A*. **2016**, 4: 10710-10718.

[299] H. R. M. Jhong, C. E. Tornow, B. Smid, A. A. Gewirth, S. M. Lyth and P. J. Kenis. A nitrogen-doped carbon catalyst for electrochemical CO_2 conversion to CO with high selectivity and current density. *ChemSusChem*. **2017**, 10: 1094-1099.

[300] H. Yin, H. Tang, D. Wang, Y. Gao and Z. Tang. Facile synthesis of surfactant-free Au cluster/graphene hybrids for high-performance oxygen reduction reaction. *ACS Nano*. **2012**, 6: 8288-8297.

[301] X.-F. Yang, A. Wang, B. Qiao, J. Li, J. Liu and T. Zhang. Single-atom catalysts: a new frontier in heterogeneous catalysis. *Accounts of Chemical Research*. **2013**, 46: 1740-1748.

[302] Y.-J. Wang, D. P. Wilkinson and J. Zhang. Noncarbon support materials for polymer electrolyte membrane fuel cell electrocatalysts. *Chemical Reviews*. **2011**, 111: 7625-7651.

[303] Z. Wu, D. Jiang, A. K. Mann, D. R. Mullins, Z.-A. Qiao, L. F. Allard, C. Zeng, R. Jin and S. H. Overbury. Thiolate ligands as a double-edged sword for CO oxidation on CeO_2 supported $Au_{25}(SCH_2CH_2Ph)_{18}$ nanoclusters. *Journal of the American Chemical Society*. **2014**, 136: 6111-6122.

[304] D. Li, C. Wang, D. Tripkovic, S. Sun, N. M. Markovic and V. R. Stamenkovic. Surfactant removal for colloidal nanoparticles from solution synthesis: the effect on catalytic performance. *ACS Catalysis*. **2012**, 2: 1358-1362.

[305] H. Mistry, R. Reske, Z. Zeng, Z.-J. Zhao, J. Greeley, P. Strasser and B. R. Cuenya. Exceptional size-dependent activity enhancement in the electroreduction of CO_2 over Au nanoparticles. *Journal of the American Chemical Society*. **2014**, 136: 16473-16476.

[306] D. R. Kauffman, D. Alfonso, C. Matranga, H. Qian and R. Jin. Experimental and computational investigation of Au25 clusters and CO_2: a unique interaction and enhanced electrocatalytic activity. *Journal of the American Chemical Society*. **2012**, 134: 10237-10243.

[307] C. Kim, H. S. Cho, S. Chang, S. J. Cho and M. Choi. An ethylenediamine-grafted Y zeolite: a highly regenerable carbon dioxide adsorbent via temperature swing adsorption without urea formation. *Energy & Environmental Science*. **2016**, 9: 1803-1811.

[308] B. Rezaei, S. Mallakpour and M. Taki. Application of ionic liquids as an electrolyte additive on the electrochemical behavior of lead acid battery. *Journal of Power Sources*. **2009**, 187: 605-612.

[309] B. A. Rosen, W. Zhu, G. Kaul, A. Salehi-Khojin and R. I. Masel. Water enhancement of CO_2 conversion on silver in 1-ethyl-3-methylimidazolium tetrafluoroborate. *Journal of The Electrochemical Society*. **2013**, 160: H138-H141.

[310] Y. Liu, B. Weng, J. M. Razal, Q. Xu, C. Zhao, Y. Hou, S. Seyedin, R. Jalili, G. G. Wallace and J. Chen. High-performance flexible all-solid-state supercapacitor from large free-standing graphene-PEDOT/PSS films. *Scientific Reports*. **2015**, 5: 17045.

[311] L. Lai, L. Chen, D. Zhan, L. Sun, J. Liu, S. H. Lim, C. K. Poh, Z. Shen and J. Lin. One-step synthesis of NH_2-graphene from in situ graphene-oxide reduction and its improved electrochemical properties. *Carbon*. **2011**, 49: 3250-3257.

[312] A. Kumar, S. Mandal, P. Selvakannan, R. Pasricha, A. Mandale and M. Sastry. Investigation into the interaction between surface-bound alkylamines and gold nanoparticles. *Langmuir*. **2003**, 19: 6277-6282.

[313] M. Aslam, L. Fu, M. Su, K. Vijayamohanan and V. P. Dravid. Novel one-step synthesis of amine-stabilized aqueous colloidal gold nanoparticles. *Journal of Materials Chemistry*. **2004**, 14: 1795-1797.

[314] D. V. Leff, L. Brandt and J. R. Heath. Synthesis and characterization of hydrophobic, organically-soluble gold nanocrystals functionalized with primary amines. *Langmuir*. **1996**, 12: 4723-4730.

[315] J. A. Trindell, J. Clausmeyer and R. M. Crooks. Size stability and H_2/CO selectivity for Au nanoparticles during electrocatalytic CO_2 reduction. *Journal of the American Chemical Society*. **2017**, 139: 16161-16167.

[316] H. Hinterwirth, S. Kappel, T. Waitz, T. Prohaska, W. Lindner and M. Lämmerhofer. Quantifying thiol ligand density of self-assembled monolayers on gold nanoparticles by inductively coupled plasma-mass spectrometry. *ACS Nano*. **2013**, 7: 1129-1136.

[317] Z. Lu, W. Xu, J. Ma, Y. Li, X. Sun and L. Jiang. Superaerophilic carbon-nanotube-array electrode for high-performance oxygen reduction reaction. *Advanced Materials.* **2016**, 8: 7155-7161.

[318] C. Zhao, Y. Zhang, Y. Zhao, Y. Wu, W. Xu, X. Wen, Y. Zhong, Y. Zhang, W. Liu, H. Wang, Y. Kuang and X. Sun. Selectivity regulation of CO_2 electroreduction through contact interface engineering on superwetting Cu nanoarray electrodes. *Nano Research.* **2019**, 12: 345-349.

[319] D. M. Weekes, D. A. Salvatore, A. Reyes, A. Huang and C. P. Berlinguette. Electrolytic CO_2 reduction in a flow cell. *Accounts of Chemical Research*. **2018**, 51: 910-918.

[320] H. Wang, Y.-W. Zhou and W.-B. Cai. Recent applications of in situ ATR-IR spectroscopy in interfacial electrochemistry. *Current Opinion in Electrochemistry*. **2017**, 1: 73-79.

[321] Z. Weng, Y. Wu, M. Wang, J. Jiang, K. Yang, S. Huo, X.-F. Wang, Q. Ma, G. W. Brudvig and V. S. Batista. Active sites of copper-complex catalytic materials for electrochemical carbon dioxide reduction. *Nature Communications*. **2018**, 9: 415.

[322] J. Huang, N. Hörmann, E. Oveisi, A. Loiudice, G. L. De Gregorio, O. Andreussi, N. Marzari and R. Buonsanti. Potential-induced nanoclustering of metallic catalysts during electrochemical CO_2 reduction. *Nature Communications*. **2018**, 9: 3117.

Appendix A List of Publications and Presentations

Publications

1. **Y. Zhao**, C. Wang, Y. Liu, D. R. MacFarlane, G. G. Wallace, Engineering surface amine modifiers of ultrasmall gold nanoparticles supported on reduced graphene oxide for improved electrochemical CO_2 reduction, *Adv. Energy Mater.* **2018**, 8, 1801400.

2. **Y. Zhao**, J. Liang, C. Wang, J. Ma, G. G. Wallace, Tunable and efficient tin modified nitrogen-doped carbon nanofibers for electrochemical reduction of aqueous carbon dioxide, *Adv. Energy Mater.* **2018**, 8, 1702524.

3. **Y. Zhao**, C. Wang, G. G. Wallace, Tin nanoparticles decorated copper oxide nanowires for selective electrochemical reduction of aqueous CO_2 to CO, *J. Mater. Chem. A* **2016**, 4, 10710.

4. Z. Zhu, H. Yin, C.T. He, M. A. Mamun, P. Liu, L. Jiang, **Y. Zhao**, Y. Wang, H. Yang, Z. Tang, D. Wang, X. Chen, H. Zhao, Ultrathin transition metal dichalcogenide/3d metal hydroxide hybridized nanosheets to enhance hydrogen evolution activity, *Adv. Mater.* **2018**, 30, 1801171.

5. Y. Ge, C. Gonzalo, **Y. Zhao**, X. Jia, R. Kerr, C. Wang, P. Howlett, G. G. Wallace, Towards thermally stable high performance lithium-ion batteries: the combination of a phosphonium cation ionic liquid and a 3D porous molybdenum disulfide/graphene electrode, *Chem. Comm.* **2018**, 54, 5338.

6. Y. Ge, C. Wang, **Y. Zhao**, Y. Liu, Y. Chao, T. Zheng, G. G Wallace, An electrosynthesized 3D porous molybdenum sulfide/graphene film with enhanced electrochemical performance for lithium storage, *Small* **2018**, 14, 1703096.

7. Y. Chao, Y. Ge, **Y. Zhao**, C. Qin, A. Vijayakumar, C. Yu, G. G. Wallace, Tuning the structure of three dimensional nanostructured molybdenum disulfide/nitrogen-doped carbon composite for high lithium storage, *Electrochimica Acta* **2018**, 291, 197.

8. C. Lee, **Y. Zhao**, C. Wang, G. G. Wallace et al. Rapid formation of self-organised Ag nanosheets with high efficiency and selectivity in CO_2 electroreduction to CO, *Sustainable Energy Fuels* **2017**, 1, 1023.

9. Z. Lu, Y. Chao, Y. Ge, J Foroughi, **Y. Zhao**, C. Wang, G. G Wallace et al., High-performance hybrid carbon nanotube fibers for wearable energy storage, *Nanoscale* **2017**, 9, 5063.

10. Y. Wang, X. Zhang, X. Li, X. Li, **Y. Zhao**, P. Jiang et al. Highly dispersed ultrasmall $Ni(OH)_2$ aggregated particles on a conductive support as a supercapacitor electrode with superior performance, *J. Colloid Interface Sci.* **2017**, 490, 252.

11. X. Li, Z. Song, **Y. Zhao**, Y. Wang, X. Zhao et al. Vertically porous nickel thin film supported Mn_3O_4 for enhanced energy storage performance, *J. Colloid Interface Sci.*

2017, 483,17.

12. X. Li, **Y. Zhao**, W. Chu et al. Vertically aligned carbon nanotube@MnO_2 nanosheet arrays grown on carbon cloth for high performance flexible electrodes of supercapacitors, *RSC Adv.* **2015**, 5, 77437.

13. **Y. Zhao**, Y. Meng, P. Jiang et al. In-situ anchoring uniform MnO_2 nanosheets on three-dimensional macroporous graphene thin-films for supercapacitor electrodes, *RSC Adv.* **2015**, 5, 90307.

Presentations

1. **Invited talk**: Interface engineering of nanostructured metal catalysts for enhanced CO_2 electroreduction, *Northwestern Polytechnical University 4th Aoxiang Forum for Distinguished Young Scholars*, Xi'an, China, 09/2018.

2. **Poster**: Engineering amine modifiers of ultrasmall gold nanoparticles for enhanced CO_2 electroreduction, *ARC Centre of Excellence for Electromaterials Science Full Centre Meeting*, Melbourne, Australia, 07/2018.

3. **Oral**: Tunable and efficient tin modified nitrogen-doped carbon nanofibers for CO_2 electroreduction, *233rd ECS Meeting*, Seattle, USA, 05/2018.

4. **Poster**: Tin modified nitrogen-doped carbon nanofibers for CO_2 electroreduction, *International Conference on Nanoscience and Nanotechnology*, Wollongong, Australia, 02/2018.

5. **Invited talk**: Interfacial engineering of Sn-based electrocatalysts for selective CO_2 electroreduction, School of Chemistry, Qingdao Agricultural University, Qingdao, China, 01/2018.

6. **Invited talk**: Functionalized nanomaterials for energy storage and conversion applications, *Qingdao University 1st Laoshan Forum for International Young Scholars*, Qingdao, China, 12/2017.

7. **Seminar talk**: Tin modified nitrogen-doped carbon nanofibers for tunable CO_2 electroreduction, Intelligent Polymer Research Institute, University of Wollongong, Wollongong, Australia, 12/2017.

8. **Seminar talk**: Tin decorated copper nanowires for selective electroreduction of CO_2 to CO, Intelligent Polymer Research Institute, University of Wollongong, Wollongong, Australia, 04/2016.

9. **Poster**: Cu-Sn core-shell nanowires for electrochemical reduction of carbon dioxide in aqueous solution, *ARC Centre of Excellence for Electromaterials Science Full Centre Meeting*, Melbourne, Australia, 08/2015.

Appendix B Permission Letters

JOHN WILEY AND SONS LICENSE TERMS AND CONDITIONS

Aug 16, 2018

This Agreement between Mr. Yong Zhao ("You") and John Wiley and Sons ("John Wiley and Sons") consists of your license details and the terms and conditions provided by John Wiley and Sons and Copyright Clearance Center.

License Number	4410660307483
License date	Aug 16, 2018
Licensed Content Publisher	John Wiley and Sons
Licensed Content Publication	Advanced Energy Materials
Licensed Content Title	Tunable and Efficient Tin Modified Nitrogen-Doped Carbon Nanofibers for Electrochemical Reduction of Aqueous Carbon Dioxide
Licensed Content Author	Yong Zhao, Jiaojiao Liang, Caiyun Wang, et al
Licensed Content Date	Jan 5, 2018
Licensed Content Volume	8
Licensed Content Issue	10
Licensed Content Pages	9
Type of use	Dissertation/Thesis
Requestor type	Author of this Wiley article
Format	Electronic
Portion	Full article
Will you be translating?	No
Title of your thesis / dissertation	Interface engineering of nanostructured metal catalysts for improved CO2 electroreduction
Expected completion date	Dec 2018
Expected size (number of pages)	180
Requestor Location	Mr. Yong Zhao
Publisher Tax ID	EU826007151
Total	0.00 AUD
Terms and Conditions	

TERMS AND CONDITIONS

This copyrighted material is owned by or exclusively licensed to John Wiley & Sons, Inc. or one of its group companies (each a"Wiley Company") or handled on behalf of a society with which a Wiley Company has exclusive publishing rights in relation to a particular work (collectively "WILEY"). By clicking "accept" in connection with completing this licensing transaction, you agree that the following terms and conditions apply to this transaction (along with the billing and payment terms and conditions established by the Copyright Clearance Center Inc., ("CCC's Billing and Payment terms and conditions"), at the time that you opened your RightsLink account (these are available at any time at http://myaccount.copyright.com).

JOHN WILEY AND SONS LICENSE TERMS AND CONDITIONS

Aug 16, 2018

This Agreement between Mr. Yong Zhao ("You") and John Wiley and Sons ("John Wiley and Sons") consists of your license details and the terms and conditions provided by John Wiley and Sons and Copyright Clearance Center.

License Number	4410651335440
License date	Aug 16, 2018
Licensed Content Publisher	John Wiley and Sons
Licensed Content Publication	Advanced Energy Materials
Licensed Content Title	Engineering Surface Amine Modifiers of Ultrasmall Gold Nanoparticles Supported on Reduced Graphene Oxide for Improved Electrochemical CO2 Reduction
Licensed Content Author	Yong Zhao, Caiyun Wang, Yuqing Liu, et al
Licensed Content Date	Jul 5, 2018
Licensed Content Volume	0
Licensed Content Issue	0
Licensed Content Pages	9
Type of use	Dissertation/Thesis
Requestor type	Author of this Wiley article
Format	Electronic
Portion	Full article
Will you be translating?	No
Title of your thesis / dissertation	Interface engineering of nanostructured metal catalysts for improved CO2 electroreduction
Expected completion date	Dec 2018
Expected size (number of pages)	180
Requestor Location	Mr. Yong Zhao
Publisher Tax ID	EU826007151
Total	0.00 AUD
Terms and Conditions	

TERMS AND CONDITIONS

This copyrighted material is owned by or exclusively licensed to John Wiley & Sons, Inc. or one of its group companies (each a"Wiley Company") or handled on behalf of a society with which a Wiley Company has exclusive publishing rights in relation to a particular work (collectively "WILEY"). By clicking "accept" in connection with completing this licensing transaction, you agree that the following terms and conditions apply to this transaction (along with the billing and payment terms and conditions established by the Copyright Clearance Center Inc., ("CCC's Billing and Payment terms and conditions"), at the time that you opened your RightsLink account (these are available at any time at http://myaccount.copyright.com).